Award Number: W81XWH-11-2-0125

TITLE: The Use of Inhibitors of Mechanosensitive Ion Channels as Local Inhibitors of Peripheral Pain

PRINCIPAL INVESTIGATOR: Frederick Sachs

CONTRACTING ORGANIZATION: Research Foundation of State University of Buffalo
BUFFALO, NY 14260

REPORT DATE: January 2015

TYPE OF REPORT: Final

PREPARED FOR: U.S. Army Medical Research and Materiel Command
Fort Detrick, Maryland 21702-5012

REPORT DOCUMENTATION PAGE

Form Approved
OMB No. 0704-0188

1. REPORT DATE	2. REPORT TYPE	3. DATES COVERED
January 2015	Final	25 Feb 2011 - 24 Oct 2014

4. TITLE AND SUBTITLE
The Use of Inhibitors of Mechanosensitive Ion Channels as Local Inhibitors of Peripheral Pain

5a. CONTRACT NUMBER

5b. GRANT NUMBER
W81XWH-11-2-0125

5c. PROGRAM ELEMENT NUMBER

6. AUTHOR(S)
Frederick Sachs

Email: sachs@buffalo.edu

5d. PROJECT NUMBER

5e. TASK NUMBER

5f. WORK UNIT NUMBER

7. PERFORMING ORGANIZATION NAME(S) AND ADDRESS(ES)
.
Research Foundation of State University of Buffalo
BUFFALO, NY 14260

8. PERFORMING ORGANIZATION REPORT NUMBER

9. SPONSORING / MONITORING AGENCY NAME(S) AND ADDRESS(ES)
U.S. Army Medical Research and Materiel Command
Fort Detrick, Maryland 21702-5012

10. SPONSOR/MONITOR'S ACRONYM(S)

11. SPONSOR/MONITOR'S REPORT NUMBER(S)

12. DISTRIBUTION / AVAILABILITY STATEMENT
Approved for Public Release; Distribution Unlimited

13. SUPPLEMENTARY NOTES

14. ABSTRACT

Mechanical pain is a major factor in the medical care of soldiers and veterans, whether in acute or chronic injury. Current analgesics, while effective, suffer from a potential for addiction and a variety of negative side effects. We have developed a new class of analgesics based on a peptide that is specific for inhibiting mechanosensitive ion channels. It is non toxic, acts peripherally, may be administered locally or systemically and may be non-addictive. This proposal is to explore the mechanism of action at the cell and molecular level and correlate nerve activation by mechanical stimulation *in vitro* with pain sensation in animals

15. SUBJECT TERMS-

16. SECURITY CLASSIFICATION OF:			17. LIMITATION OF ABSTRACT	18. NUMBER OF PAGES	19a. NAME OF RESPONSIBLE PERSON
a. REPORT	b. ABSTRACT	c. THIS PAGE			USAMRMC
U	U	U	UU	133	19b. TELEPHONE NUMBER *(include area code)*

Table of Contents

Introduction: The focus of this grant was to understand the molecular mechanisms of mechanical transduction in dorsal root ganglia cells (DRGs) that give rise to the sensation of pain. The first goal was to understand how the specific peptide inhibitor of mechanosensitive ion channels (MSCs), GsMTx4, acts to suppress mechanotransduction. The studies for this goal incorporated synthetic mutant peptides, single channel patch clamp electrophysiology and multiple physicochemical membrane binding assays to elaborate the contributions of specific amino acids. A second goal was to understand the mechanism of MSC activation and inactivation properties that control the mechanosensing response in DRGs. For these studies we expressed and characterized mutants of the newly cloned MSCs Piezo1 and 2. We extend the single channel patch experiments to whole cell recordings where the cytoskeleton is more intact to understand the contribution of the cytoskeleton in MSC regulation. A third goal is understand how external mechanical stress is distributed in proteins of the cytoskeleton since those mechanics affect the stress in the lipid bilayer where the channels reside. Finally, we tested GsMTx4 to determine its therapeutic use as a peripheral analgesic in intact rats.

Aim 1) GsMTx4 Mechanism of Inhibition

GsMTx4 Lysine to Glutamate Mutations Reveal New Mechanism of Inhibition:

GsMTx4 is a peptide inhibitor of MSCs that may be useful as a peripheral analgesic. The goal of this aim was to understand the mechanism of inhibition by determining the amino acids important to GsMTx4 interactions with MSCs and the membrane. The long term goal is to use this information to selectively modify its structure to improve its potency and change its affinity for different targets. A unique feature of GsMTx4 is its high positive charge, which we suspected was important to the peptides mechanism of action. So we constructed 6 lysine to glutamate mutants and measured changes in their inhibition strength on exogenously expressed Piezo 1 channels in outside-out patches from HEK cells, and used a host of physicochemical assays to measure the membrane binding differences among these mutants. The findings from these studies are described in the accompanying manuscript that has been submitted to the Journal of Physiology (**Appendix A**) and summarized below.

Bilayer stretching does work on MSCs favoring states with larger in-plane areas [1-3]. The fundamental difference between channels activated by tension and channels modulated by tension, such as voltage and ligand gated channels [4], lies in the significantly larger increase of in-plane area of MSCs during opening [5]. GsMTx4 is an inhibitory gating modifier peptide [6], similar in structure to other venom derived channel inhibitory peptides, but notable because of its high selectivity for cationic mechanosensitive channels (MSCs) [7]. It represents the first compound in a new category of pharmaceuticals for treating diseases related to mechanical dysregulation [8]. The studies described in **Appendix A** support a new model of inhibition (**Fig. 1**) where the peptide is envisioned as providing a tension dependent equilibrium between a surface absorbed shallow mode and a deeply adsorbed mode. The key to GsMTx4 activity is the stability of the shallow mode. At resting tension, the shallow mode occupies less area. As tension increases, GsMTx4 slips in deeper, increasing the monolayer area and acting as a tension clamp by holding surface area constant. The high content of lysine plays an important role in stabilizing the shallow state, where some lysines are more critical in stabilizing the surface absorbed state. Deeper penetration at resting tension reduces the amount of material extruded

and reduces the tension buffering capacity. In this model, membrane tension increases the free volume of the membrane so that peptide partitioning and the tension activating the MSCs [9] overlap and the details of GsMTx4 reaction kinetics probably involves both processes.

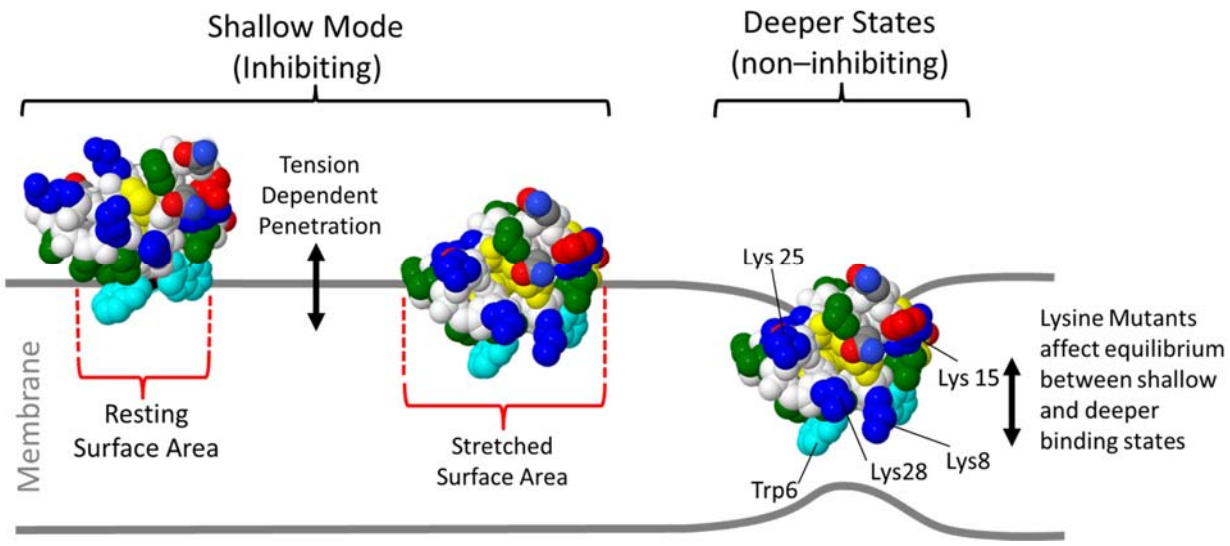

Figure 1 Model for GsMTx4 tension clamping. MD simulations predict shallow and deeper binding states for ICK peptides. For GsMTx4 Trp6, Lys 8, and Lys 28 are predicted to promote deeper binding by forming interactions with the lipid head groups of the inner leaflet while other lysines maintain association with the outer leaflet [10]. The shallow mode is depicted as superficial association where the penetration depth is tension sensitive with its surface area contribution increasing with stretch. One property expected to reduce inhibitory activity is increased occupancy of the deeper binding states which may be promoted by specific lysine mutants. Residues are colored as: basic residues (blue), acidic residues (red), hydrophobic residues (green), polar residues (blue/red/gray), Tryptophan (cyan), cysteine (yellow), backbone (white).

Simulation of GsMTx4 Bilayer Association:

Molecular dynamics simulations of GsMTx4 binding to lipid bilayers performed by Dr. Kazu Nishizawa's laboratory at Teikyo University confirm that the wt peptide enters a shallow (interaction with outer leaflet, **Fig. 2**) and a deep (interaction with both inner and outer leaflets) binding mode. Dr. NIshizawa'a simulations of the lysine to glutamate mutants confirmed our experimental results by showing that lysines that stabilize shallow binding were associated with compromised activity, while lysines that promote deep binding had no effect on inhibition (**Appendix B**). These studies revealed the paradoxical property of GsMTx4 that tighter/deeper biniding reduced its inhibitory function, suggesting that GsMTx4, unlike many other venom peptides, is more stable in the surface absorbed states providing it with its unique inhibitory activity against MSCs.

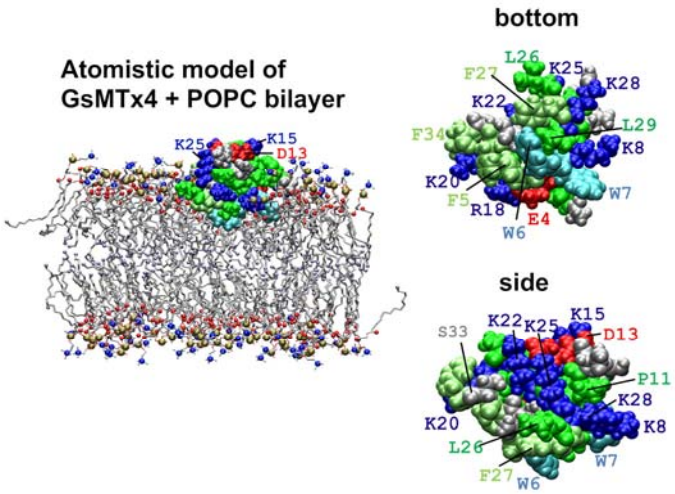

Figure 2. Van der Waals rendering of GsMTx4 structure and the simulation configuration. *Left*: a representative snapshot from an AT 60/64-WT free simulation of WT GsMTx4 and a POPC bilayer membrane. Trp residues are cyan, Phe residues are lime, other hydrophobic residues (Ala, Cys, Ile, Leu, Met, Pro and Val) are green, basic residues (Arg ad Lys) are blue, and acidic residues (Asp and Glu) are red. For the POPC head group, the nitrogen atoms are blue, phosphorus atoms are ocher, and carbonyl oxygen atoms are red spheres. The terminal carbon atoms of the lipid acyl tails are ice blue spheres. Water molecules and chloride ions are not shown. *Right:* a bottom and side view of WT GsMTx4 sampled from an in-water simulation. The bottom view illustrates the hydrophobic protrusion that contains W6. The graphical representation is similar to the panel on the left.

Aim 2) MSC Properties and Sensitivity to Inflammatory Reagents

The goals of this aim were to study the gating kinetics of MSCs in both the patch and in whole cell currents from isolated differentiated DRG neurons and from HEK cells expressing exogenous putative MSCs. To do this we are incorporating a variety of techniques to mechanically stimulate cells and to measure the channel activity. We also created mutations to investigate the inactivation properties of MSCs which has been shown to be a major contributor to neuronal sensitivity to mechanical stimulation [11]. We also worked to identify the MSC protein subunits in DRGs involved in the inflammatory response and to investigate how their gating properties are affected by inflammatory mediators.

Piezo channel inactivation:

The role of PIEZO1 inactivation is critical to the function of the PIEZO channels. This is evident from recent work that has shown that mutations that affect the kinetics of inactivation (slower inactivation) are associated with disease states such as Xerocytosis (Stomatocytosis) [12, 13] for PIEZO1 and Arthrogryposis (PIEZO2) [14]. In the case of DRGs currents that are elicited by a stimulus the inactivation rates can vary. Recently, the Lewin group showed that these currents may come from PIEZO2 channels whose response is modified by proteins (STOML3) tuning the response of the channel [15].

We have examined inactivation of PIEZO1 using two mutations M2225R and R2456K (called DhPIEZO1) that completely removes inactivation [5] (**Appendices C and D**). The loss of inactivation was accompanied by ~30 mmHg shift of the activation curve to lower pressures and slower rates of deactivation. The slope sensitivity of gating was the same for WT and mutants indicating that the

dimensional changes between the closed and open state are unaffected by the mutations. These are not associated with pore since the unitary channel conductance was unchanged. DhPIEZO1 was reversibly inhibited by the peptide GsMTx4 that acted as a gating modifier. The channel kinetics were solved using complex stimulus waveforms and the data fit to a three state loop in detailed balance. The reaction had two pressure dependent rates, *closed* to *open*, and *inactivated* to *closed*. Pressure sensitivity of the opening rate with no sensitivity of the closing rate means that the energy barrier between them is located near the open state. Mutant-cycle-analysis of inactivation showed that the two sites interacted strongly, even though they are postulated to be on opposite sides of the membrane. A key observation is that even in whole cell recordings the PIEZO channel does not inactivate indicating that there is no contribution to channel inactivation by adaptive response of the cell.

Piezo channel domain structure:

We constructed a number of PIEZO1 proteins tagged with fluorescent proteins to observe its domain structure and monitor its trafficing. An important use of this fluorescent construct was to image the channels in cells especially when mutations are made to the channel. We imaged the PIEZO1 protein distributed in HEK293 cells using Structured Illumination Microscopy. **Figure 3** shows the image of a cell that was cotransfected with 1591-mCherry-PIEZO1 and TREK-GFP, both mechanical channels. The large red clusters are PIEZO1 channels. Notice that there is no significant spatial overlap between the two types of channels so they are likely in different mechanical domains that likely have different stresses. The mechanical responses of the cells could span a wide range of stimulus magnitudes regardless of the intrinsic channel gating properties as they are presumably located in cellular domains of different stress.

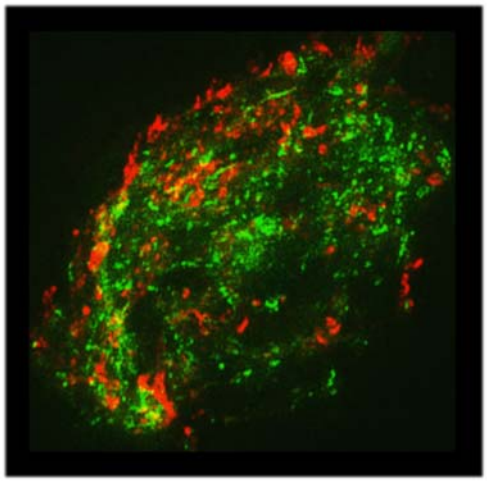

Figure 3 PIEZO1 channels form clusters and TREK-1 is more widely distributed. PIEZO1 (red) and TREK1 (green) are located on the surface of HEK cells. PIEZO1 is tagged with internal mCherry and TREK-1 is linked at its C-terminus to GFP. Cells were transfected and after 24 hours fixed with 4% paraformaldehyde. Data were collected by Structured Illumination Microscopy (24 level z-stack) and reconstructed into a 3D model using ImageJ. TREK-1 forms bead like domains that appear to follow the underlying cytoskeleton. In contrast, PIEZO1 forms large clusters domains. There is no significant spatial overlap between the two types of channels.

Next we split the sequence at the mCherry site and made a vector that expressed both the N- and C-terminal fragments separately but simultaneously (fragments 1-1591 and 1592 -2521). To allow us to monitor expression, the N-terminal fragment was labeled with mCherry at its C-terminal and the C-terminal fragment was labeled with GFP at its N-terminal (**Fig. 4**). We then expressed both components

in cells and measured the responses in whole-cell and cell-attached modes. The two independent parts of the expressed channel clearly reassembled into a functional unit with kinetics similar to the wild type (**Fig. 5**). Notice that inactivation normally slows with depolarization. We have tested each fragment individually and we were unable to generate whole-cell or patch currents. This argues that some elements in each fragment are needed to reconstitute a functional channel or that the channel requires elements to be transported to the plasma membrane.

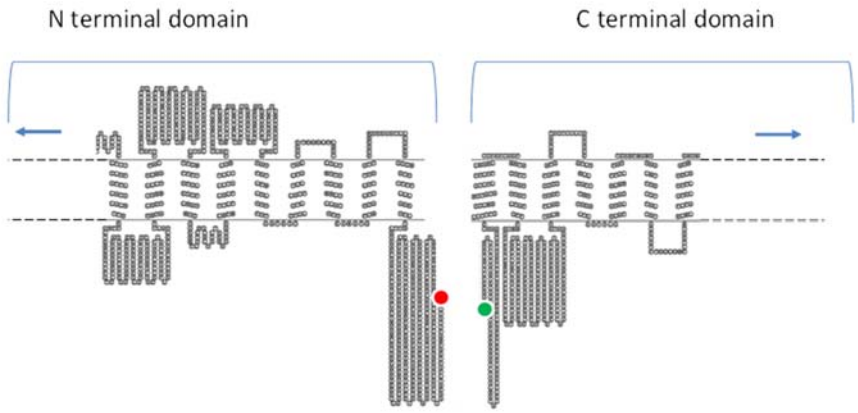

Figure 4 Two PIEZO1 fragments when coexpressed produced an active channel. This construct allows access to internal transmembrane domains where we can delete sequences to produce smaller channels. Fluorescent tags are indicated by colored circles.

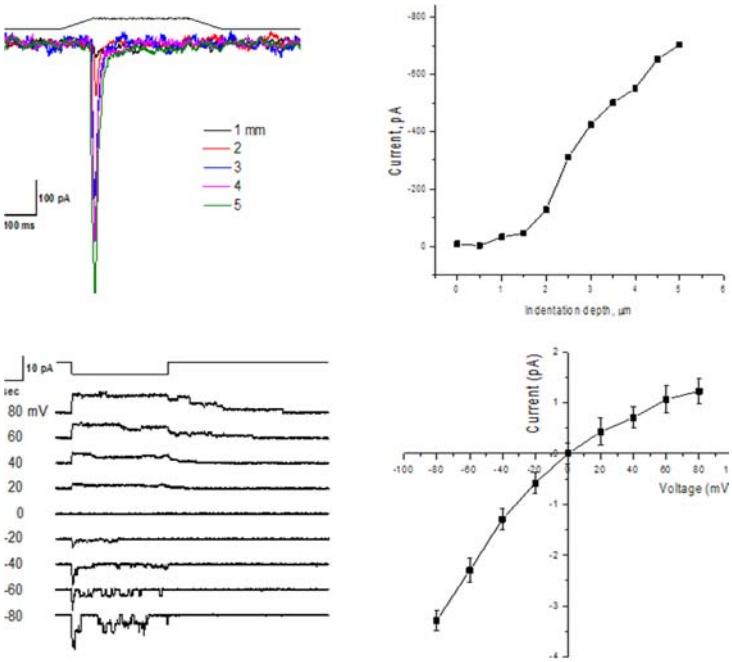

Figure 5 Reassembly of PIEZO1 fragments into a functional channel. The plasmid created expression of two independent protein segments in HEK293T cells. Cells were identified by both green and red fluorescence. Panel A shows whole cell currents elicited by indenting the cell with a fire polished probe at a holding potential of -60 mV. Panel B is a dose-response curve of mechanical sensitivity with increasing depths of penetration producing more current. Panel C is a recording of single channel currents from a cell-attached patch at the indicated voltages showing inactivation with depolarization. This emphasizes that the channels couple mechanical stress to membrane potential in time dependent ways. Panel D is an IV curve derived from the cell-attached single channel traces.

DRG MSCs sensitivity to inflammatory agents:

We have observed that treatment of DRG neurons with inflammatory agents affect indentation induced phasic currents (**Fig. 6**). Similar to that reported for Piezo 2 channels after Bradykinin treatment, we see an increase in current amplitude and slowing of the inactivation/adaptation rates. There are currently no reports showing modulation of MS currents as a result of changes in slope sensitivity to membrane tension, suggesting the intrinsic tension sensing structures are not likely significant points of regulation. Regulation of MSC activity most likely occurs by controlling the tension that reaches the channels and by modification of inactivation properties, typically slowing. Both these properties appear to be under the control of the local cytoskeleton, and actin and tubulin networks may both be involved.

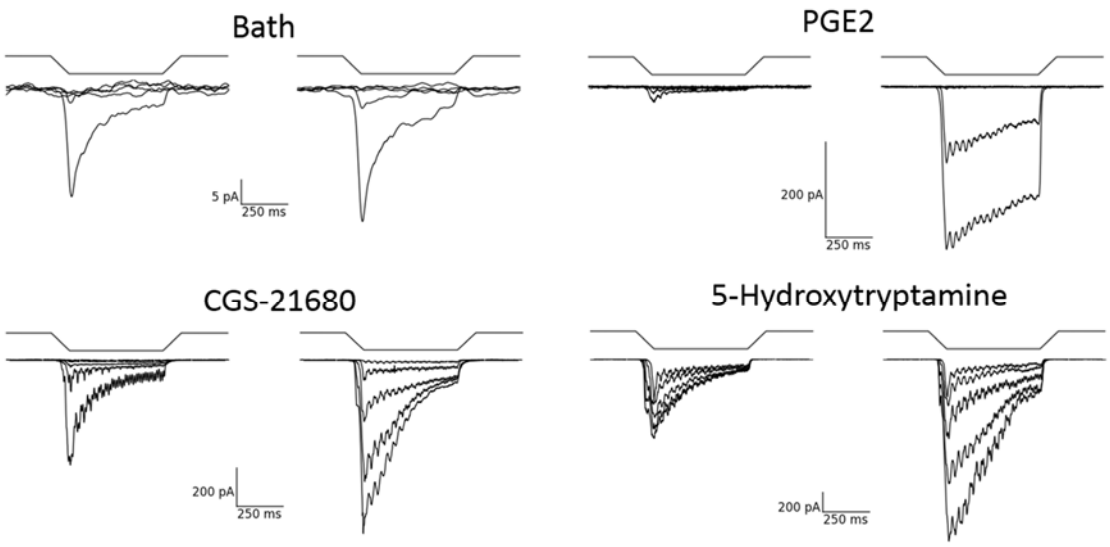

Agent tested	Δτ (increase or decrease)	fold increase in current
Bath	-25 ms	0.22
5-HT	328 ms	1.3
CGS	153 ms	1.6
PGE2	592 ms	10

Figure 6 Inflammatory agents increase the amplitude and slow inactivation of MS currents in DRG neurons. Voltage-clamped DRG neurons were mechanically indented to 5 depths from 6-10 µm with a fire polished glass probe to elicit MS currents. The mean MS currents at each depth from 5-6 cells were averaged to produce the ensemble currents shown. Recordings on the left show the average control MS currents before treatment, while traces to the right show currents 4-8 min after perfusion with new saline alone (Bath), or saline containing inflammatory agents (100 µM 5-HT or PGE2) or an adenosine A2A GPCR agonist (100 µM CGS-21680). CGS-21680 agonist mimics many of the inflammatory agents by activating cAMP dependent pathways. The time constants determined by exponential fits to the decaying current of the largest responses before and after treatment are shown with the peak amplitudes in the table below. Only neurons that produced MS currents without treatment were used for testing. Differences in the amplitude and inactivation rates of the initial currents among the four groups represents the heterogeneity of the DRGs selected from the cultured neurons. Mechanically perturbing the DRGs with saline changes alone (Bath -control) produced no change in the inactivation properties or

amplitude of the MS currents. When inflammatory mediators (100uM 5-HT or PGE2) or CGS-21680 were added to the saline change there was a significant increase in current amplitude and slowing of inactivation.

Di-8-ANEPPS voltage sensitive dye used to monitor whole cell DRG MSC currents:

An impediment to efficiently determining the sensitvity of MS currents to different inflammatory agents is that we are limited to one neuron per dish when performing electrophysiology recordings due to the length of recordings and treatment contamination of other cells. In order to increase the number of DRGs tested per coverslip we have incorporated the use of the membrane voltage sensitive fluorescent dye di-8-ANEPPS to measure MS currents. Di-8-ANEPPS and other environmentally sensitive dyes have been used for many years to measure neuronal currents, and this technology has recently been used to monitor whole cell currents with sub millisecond resolution [16]. It is non-invasive and multiple cells per coverslip can be tested since we are not tethered to the position of the electrode.

We observed that the signal to noise ratio was significantly better when we used an ROI to restrict the measurement to the membrane alone (**Fig. 5A and C**). We also learned that the signal becomes too muted past 30 min to accurately determine the response to different treatments (**Fig. 5D**). However,

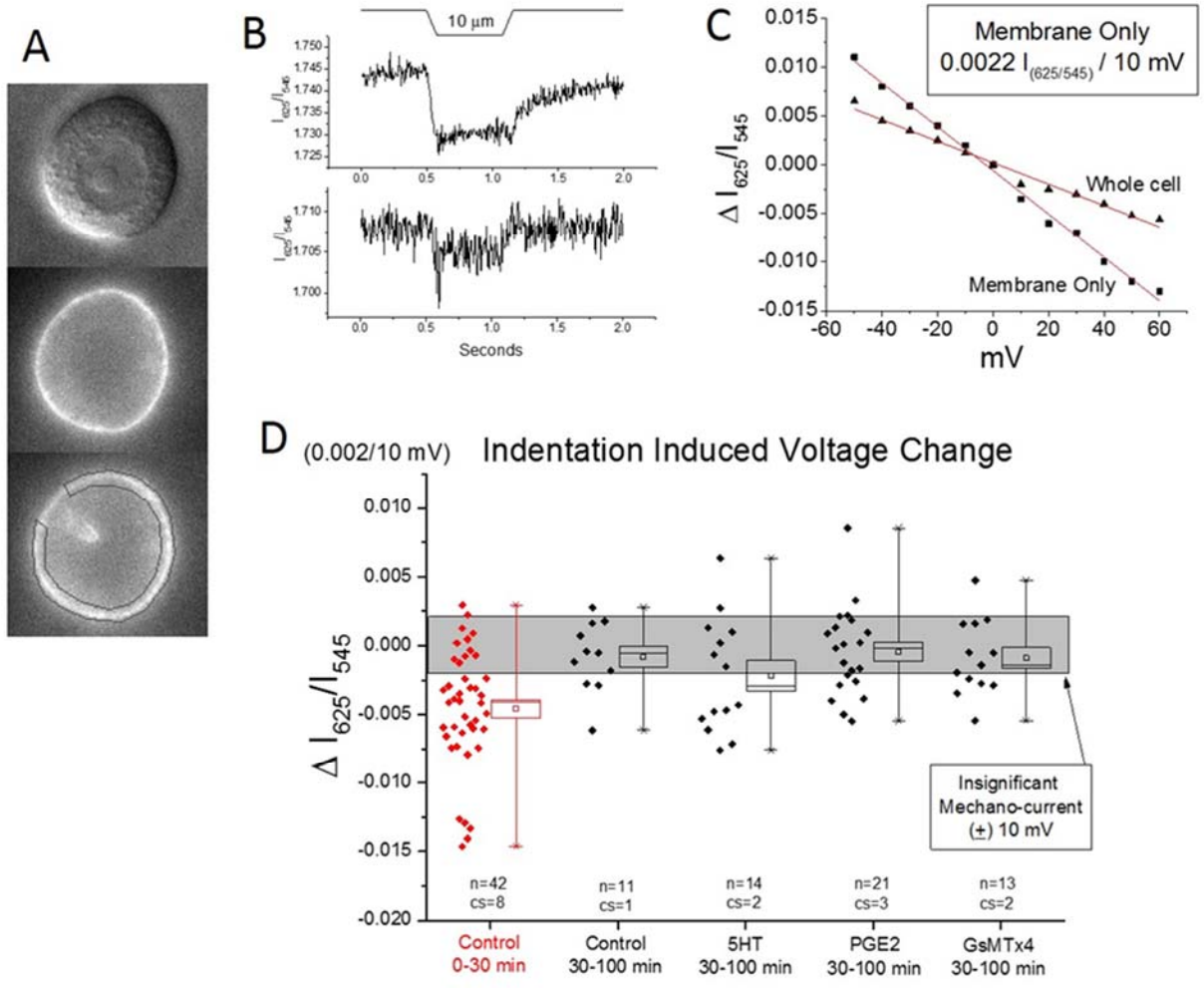

Figure 7 Monitoring MSC current using the voltage sensitive dye di-8-ANEPPS in the presence of inflammatory mediators. DRGs were loaded for 5 min with di-8-ANEPPS. (A) Representative DRG soma showing DIC image at the top, and 625nm

fluorescence emission images below showing the cell at rest and indented 10 µm with a 3-4 µm probe. The gray outline of the membrane in the bottom panel shows the ROI used to calculate the 625/545 nm ratio (voltage change). (B) Representative ratio recordings at 200 fr/sec shows that rapid inactivation properties can be observed. Records are averaged from 8 individual indentation events. (C) 625/545 nm ratio change in a voltage clamped cell shows that the dye response is linear over a 110 mV range and that the response is larger if only the membrane is included in the measurement by using a ROI that outlines this region. (D) The voltage change ($\Delta I_{625}/I_{545}$) is shown for control cells and cells treated with different inflammatory agents and MSC inhibitors. Box plots showing the mean, median, standard error and min-max response sizes are shown next to all data from each treatment group. Ordinarily, control cell experiments were performed in the first 30 min and followed by experiments with inflammatory mediators and inhibitors over the next hour. After 30 min the dye tends to internalize and the plasma membrane voltage response becomes significantly muted due to the high background fluorescence from dye not in the voltage field [compare red control responses (0-30 min) with black control group (30-100 min)]. The 0-30 min control cells show robust voltage changes in response to indentation and two different sized responses. The majority of cells show an ~-20mV depolarization, while a subgroup shows a large -70-80mV response. Past 30 minutes the large responders are never observed and most cells have an undetectable response.

during the first 30 min after loading cells there was a robust MSC response in control cells that appears to show at least three different cell types. Most voltage responses were -10-40 mV, but another well-defined larger response was observed at -70-80 mV. There is also a significant group of cells that do not respond. We were unable to determine if PGE2, 5HT or GsMTx4 had an effect because the response were too muted after 30 min which is when we applied these test substances. These experiments will need to be repeated with treatments within the first 30 min. Alternatively, Di-4-ANEPPS has a longer residency time in the plasma membrane which we may test to determine if it can significantly extend the experimental time frame. These studies are near completion and will be published in 2015.

DRG MSC sensitivity to inhibitors:

Four types of mechanoreceptor currents have been identified based on the rate of the decay of the phasic (inactivation/adaptation) response [11]. There are rapidly adapting (RA - ~3-6 ms), intermediate adapting (IA - ~15-30 ms), slowly adapting (SA – ~200-300 ms) and ultra-slowly adapting (uSA - ~1000 ms) currents generated by pressing on peripheral afferents. It has been proposed that neurons expressing the RA currents would provide better spatial and temporal resolution and are likely involved in light touch sensitivity, while the SA type currents are more closely associated with nociception. Although the current associated with the two main types of pain are not restricted to a specific type, modulation of neurons with RA currents is more commonly linked to allodynia, while hyperalgesia more likely emanates from SA type cells. Although different reports have suggested involvement of multiple channel types as potential mechanotransducers in somatosensory neurons, TRPA1, TRPV4 and Piezo 2 have emerged as leading candidates.

We have expressed Piezo 2 channels in HEK cells and observed rapidly inactivating currents in both outside-out patches (Fig. 8A and B) and whole-cell indentation currents that are blocked by GsMTx4 (Fig. 8C). However, GsMTx4 appears to have little effect on HC030031 sensitive SA currents (Fig. 8D) which are likely produced by TRPA1. Thus GsMTx4 may selectively inhibit RA currents though further experiments on specific DRG subtypes will be required.

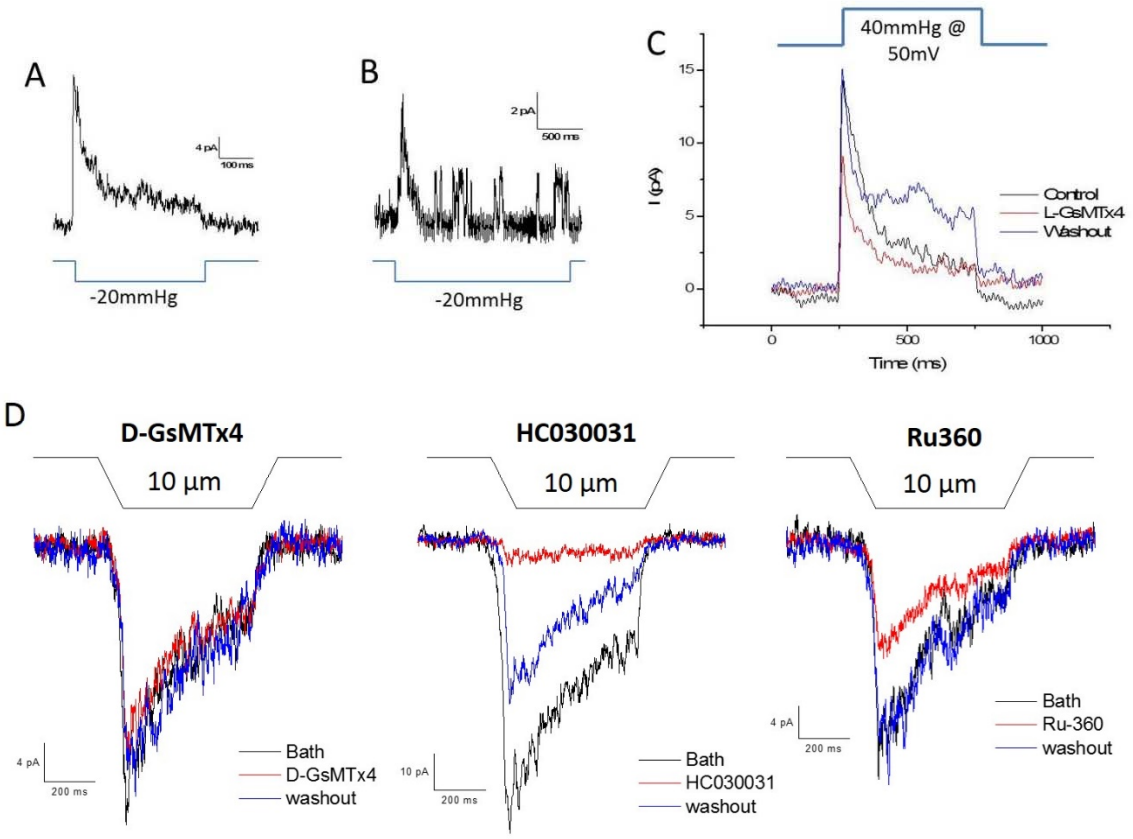

Figure 8 GsMTx4 blocks Piezo 2 currents expressed in HEK cells, but not slowly adapting currents in DRGs. A Piezo 2 pIRES vector was expressed in HEK cells so that GFP was an indicator of expression. (A) Shows rapidly inactivating average current from a cell-attached patch from a green fluorescent cell. (B) Individual trace showing inactivation of single channels. (C) Average currents from an outside-out patch from a Piezo 2 expressing cell is >50% inhibited by 5 µM GsMTx4. (D) SA currents induced by indentation from a cultured DRG. All three recordings are from a single cell with each record representing the average current from 5 indentations before, during and after application of different inhibitors. Three compounds were tested: GsMTx4 – 24% inhibition, HC030031 (TRPA1 inhibitor) – 94% inhibition, and Ru360 (TRRP V and C blocker) – 47% inhibition.

The evidence of MSC sensitivity to inflammatory agents is nearly complete and will be the first report of sensitivity to these specific agents. The last piece of data needed is to determine the sensitivity of the different whole cell currents (rapid, intermediate and slowly adapting) to different inhibitors such as GsMTx4, HC030031 and Ruthenium Red to provide an assessment of the channels involved. The changes in channel properties will be presented together in a report with the cytoskeletal data in Aim 3 which demonstrates that the changes in channel properties may be linked to modification of cytoskeletal distribution.

Aim 3) Cytoskeletal Membrane Tension Control in DRGs

In this aim we are investigating the stress distribution on different cytoskeletal proteins in DRGs using the FRET based stress reporting probes we have developed. Constitutive stress levels in the cell body and neurites will be measured and changes in stress after treatment with inflammatory agents. We will also induce macroscopic stress in the DRGs with probe pressure in different regions of the cell and monitor the currents and the GsMTx4 sensitive Ca^{2+} influx.

Actinin and Filamin sensitivity to inflammatory agents:

The cytoskeleton can control MSCs on multiple levels. The cytoskeleton is responsible for controlling bilayer stress and the localization of membrane proteins in lipid domains, or near adapter proteins. Stresses in the cytoskeleton are complicated by their three dimensional distribution and non-uniformity. Identifying the specific cytoskeletal elements responsible for controlling bilayer stress has been hampered by the lack of tools to study cytoskeletal stresses in individual elements. We have create multiple FRET based stress sensors, but in the early stages of this grant award we designed a FRET pair that changes angle suring stress changes called cpstFRET (**Appendix E**). It has become the workhhorse for all our latest studies due to its high dynamic range and compact nature. We have also designed and tested a new chimeric sensor in actin by inserting the sensor between α and β monomers forming an actin dimer and demonstrated its sensitivity to force in stem cells and cancer cells responding to variying surface stiffnesses (**Appendix F**). This probe will be useful in future studies of the stress sensitivity of the actin network in neurites of DRGs. We have also developed probes to vinculin, talin and the intermediate nuclear filament lamin A during this grant period.

Using the cpstFRET probe we have characterized the resting and dynamic responses of filamin and actinin chimeras in DRG neurons when treated with inflammatory agents (**Figs. 9 and 10**). Although actinin and filamin have similar affinities for actin, they modulate the stiffness of actin networks differently because they crosslink fibers in different orientations. Filamin has a pronounced role in crosslinking the actin network to other membrane proteins and has been implicated in regulating membrane signaling complexes in a stress-dependent manner, including modifying MSC gating.

In the resting cells stresss response (**Fig. 9**), control experiments examined the effect of simply exchanging the saline, and we observed a change in tension. Interestingly, actinin consistently showed a transient increase in stress while filamin showed a prolonged decrease in stress. These responses were

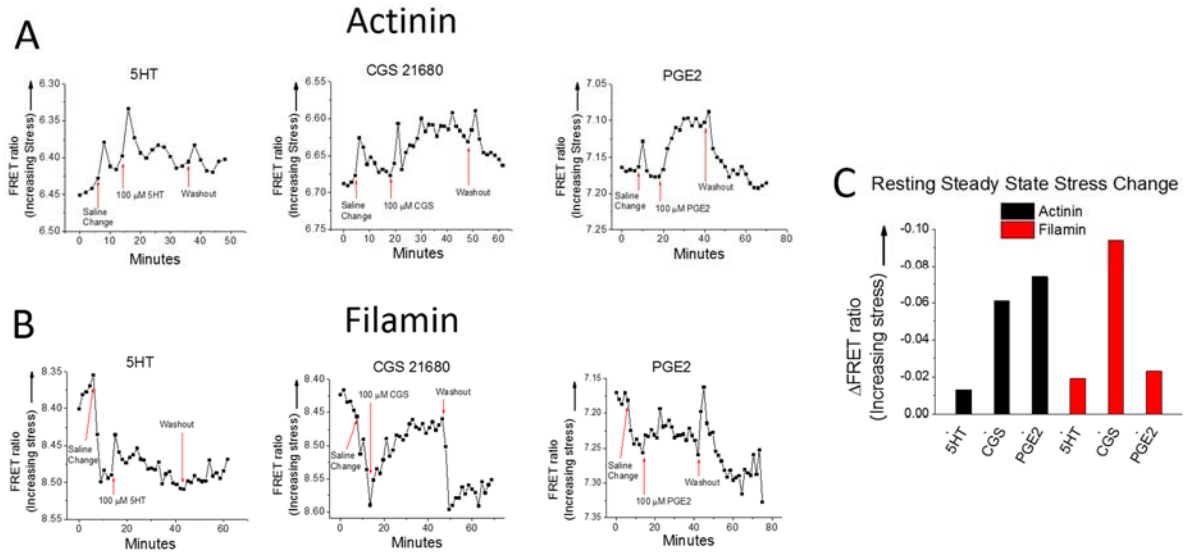

Figure 9. Inflammatory Agents Cause Resting Stress Changes. The resting FRET ratio was monitored for cpstFRET-actinin (A) and cpstFRET-filamin (B) chimeras expressed in DRG neurons. Each trace shows the average response from 15-20 neurons. The cells were challenged with a saline change alone, followed by a saline change including 100 µm of an inflammatory agent indicated by the red arrows. After 20-30 minutes of treatment the inflammatory agent was washed out. 5HT - serotonin, CGS 21680 - adenosine A2A receptor agonist, PGE2 - prostaglandin E2. Saline changes alone mechanically disturb cells probably by fluid shear stress and/or possibly by subtle osmotic changes. Actinin showed a transient stress increase, while filamin showed a sustained decrease in stress in response to saline changes. Cells also show sustained differential sensitivity to the

three inflammatory agents. The mean stress changes after 10-15 min treatment with the inflammatory agents is shown in (C). 5HT induces a small change in stress, CGS 21680 induces a large changes in both cytoskeletal elements, and PGE2 selectively induces a large change only in actinin.

likely caused by minor osmolarity changes or shear stress from the fluid movement. Neither chimera showed significant changes in resting tension from 5-HT exposure. Both showed an increase in stress in response to cAMP induction by CGS-21680, but only actinin had a strong increase in resting tension from PGE2.

We also examined dynamic stress changes in cells expressing the two chimeras by indenting the soma of neurons to a depth that normally elicited MS currents in electrophysiology recordings (**Fig. 10**). Again both chimeras showed weak sensitivity to 5-HT treatment (no change from control response), but strong stress increase in response to PGE2 treatment. Only filamin showed a response CGS-21680.

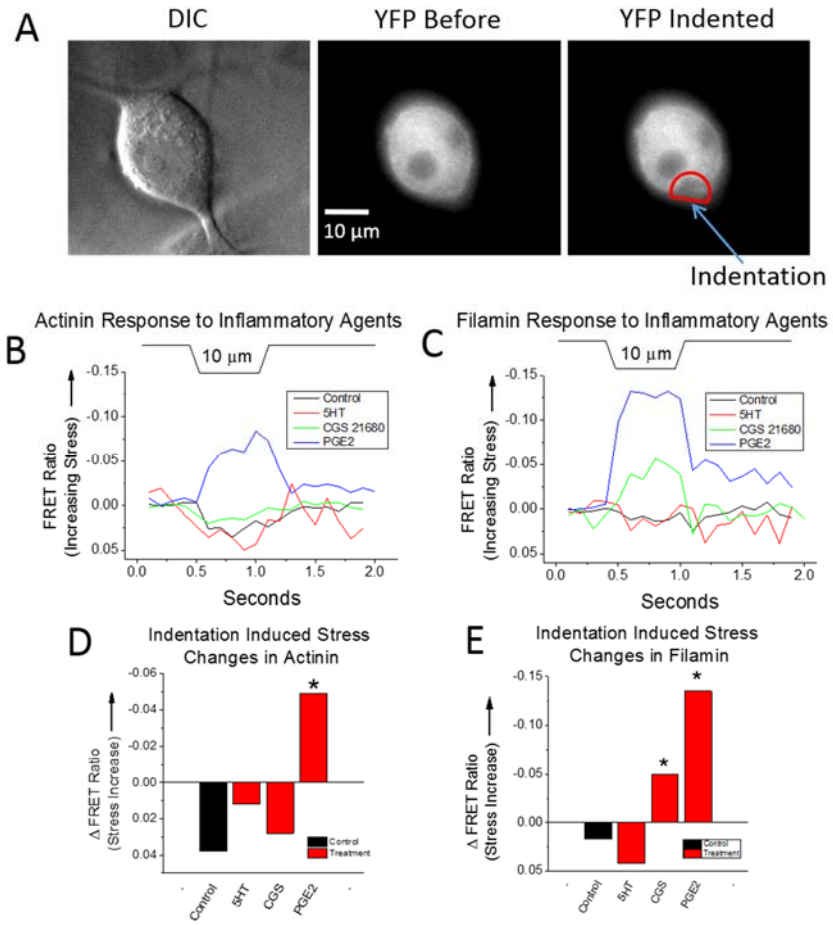

Figure 10. Inflammatory agents cause changes in the cytoskeleton sensitivity to stress. DRGs transfected with cpstFRET chimeras of actinin and filamin were indented with a blunt glass probe – tip ~3-4 µm diameter. The cell were indented ~10 µm with a trapezoidal shaped 0.5 sec long stimulus, a depth that produced maximal MSC currents in whole-cell recordings. (A) Shows a DIC image of a DRG soma, and the YFP fluorescence images before and at the peak of the indentation to show the change in distribution of the stress probe. The red semicircle outlines the region of the interest (ROI) used to analyze the FRET changes during indentation. Cells were indented 9 times before and during treatment with inflammatory agents, and the signals averaged. Images were acquired at a rate of 10 frames/sec. The mean response from 15-20 cells was averaged in the ensemble responses shown in (B and C). The FRET response was measured before (black control traces) and after 20-60

min in the presence of inflammatory mediators. Both cytoskeletal elements responded with a small decrease in stress during control indentations (D and E). Treatment with 5HT produced little change in the stress response. CGS 21680 selectively induced stress sensitivity in filamin. PGE2 treatment caused both actinin and filamin to show a robust increase in stress to indentations.

The filamin results are intriguing in light of the role this protein plays in cellular remodeling. Filamin and talin (another cortical adapter protein) compete for binding integrins. Talin association with integrins tends to stabilize long lasting focal adhesion complexes. Filamin tends to destabilize integrin association with the extracellular matrix for cortical remodeling and cell motility. Thus, the internal cytoskeleton bears the majority of cortical stress when filamin-integrin associations are dominant. Thus greater membrane compliance is a likely product of increased filamin associations which would increase MSC activity [17].

The data in **Figure 10** was aquired at low temporal resolution (10 Hz) with respect to MSC inactivation kinetics. To determine how the mechanical response of these chimeras compares to MSC kinetics we need much higher temporal resolution. Preliminary data on the filamin cells treated with PGE2 collected at 100 Hz shows the same general increase in stress as observed at the lower frame rates. However, we can now begin to see the time dependent changes in the stress durng the 500 ms indentation.

To complete the study on inflammatory sensitivity of the MSCs and cytoskeleton, we will test the dynamic response of actinin and filamin at higher temporal imaging resolution for PGE2 only; the strongest inflammatory agent. This data will then be combined with the MSC data in Aim 2 and published as a single manuscript.

Aim 4) In vivo analgesic properties of GsMTx4

The goal of this aim was to determine the potential analgesic properties of GsMTx4 for pain by in-vivo testing in rats. Initial tests preformed in the beginning of the grant period were not able to reproduce the results in the literature. However, recent PK analysis by Tonus Therapeutics (company licenced for pharmaceutical development of GsMTx4) may shed light on dosing that will achieve the peripheral tissue concentrations necessary to observe analgesic properties in a more consistent manner. We would like to point out that the Sachs lab in collaboration with Dr. Ji Li of the the Dept. of Pharmacology at the University of Buffalo have submitted a manuscript showing in vivo efficacy of GsMTx4-D in treating ischemic reperfusion injury. This paper shows suggests that there is an optimal tissue concentration for achieving the greatest cardio-protection. This may be relevant to the case of GsMTx4 use as an analgesic. Future analgesic testing will be undertaken once an new comprehesive PK/PD analysis of GsMTx4 is completed by Tonus which is planned to begin in the next several months.

Key Accomplishments/Impacts:

Aim 1)

1) We showed that the method of inhibition for GsMTx4 stems from its stability in a shallow bound mode at resting membrane tension where it occupies only a small surface area. When tension increases in the bilayer due to stretching, GsMTx4 binds deeper and takes up more surface area, acting as and area, or tension, clamp.

2) This new mechanistic data provides a basis for the developing other molecules with similar properties that could be developed into pharmaceuticals to inhibit MSCs. If other MSCs have different sensitivities to membrane stress, mutants of GsMTx4 could be created that match the sensitivities of the different channel types to increase tehir selectivity.

3) This new mechanistic data could also lead to new studies of endogenous secreted factors that bind to membranes and could possibly modulate membrane tension. There are a host of intracellular proteins, such as caveolin and cavins, that are surface absorbed to the inner bilayer acting as scaffolding proteins.

Aim 2)

1) Mutations to Piezo channels that lead to Xerocytosis and Arthrogryposis cause slower inactivation which effectively increases cation current in the effected cells of these disorders.

2) Fluorescent labeling of Piezo channels was achieved without disrupting channel function. Chimeric channel proteins containing roughly either the N or C terminal halves of the piezo 1 channel fused with fluorescent proteins at internal sites (instead of termini) showed that the channel gating requires both halves of the protein.

3) Inflammatory agents generally lead to increased MS current aplitude and slower inactivation rates, both of which would increase sensitivity of neuronal response to mechanical stimulation.

4) GsMTx4 effectively inhibits rapidly adapting MS currents such as those produced by PIEZO channels. However, it was less effective at inhibiting slow adapting MS currents which are thought to be associated with TRPA1 channels.

5) We can observe MS currents in DRGs with using voltage sensitive membrane dyes which will significantly increase the efficiency of testing MSC activity in the future.

Aim 3)

1) Demonstrated important general concents of cpstFRET chimeras expressed in DRGs:

    a. Inflammatory agents can “increase” static and dynamic stress.

    b. Cytoskeletal elements can be differentially affected by test substances (CGS produced indentation sensitivity only in filamin).

    c. Stress on a specific cytoskeletal element responds differentially to different reagents (actinin showed sensitivity to indentation after treatment with PGE2 but not 5-HT or CGS).

    d. Stress distributions are complicated since changes in static stress do not necessarily translate into dynamic changes (PGE2 induced little change in the static stress on filamin, but caused high sensitivity to indentation stress).

2) The dynamic response of filamin, an important adaptor protein in controlling membrane mechanics, shows a large increase in stress sensitivity after treatment with PGE2. In correlation with this finding, PGE2 also produced the largest increase in MS current amplitude and decay rate.

Conclusions:

We have made considerable progress these 3.5 years in 1) understanding the mechanism of GsMTx4 inhibition, 2) the properties of Piezo channel inactivation, and 3) how inflammatory agents increase DRG sensitivity to mechanical stimulation. We have gone beyond functional testing of GsMTx4, and incorporated physicochemical analyses that has shed light on the mechanism of GsMTx4 interaction with membranes. This is precisely the type of information we need to design different types of MSC inhibitors, whether by increasing selelctivity for specific channel types (since it is likely different MSCs reside in different membrane domains) or by increasing potency of inhibition (mutations stabilizing its depth of penetration will likely increase potency).

We have shown that naturally occurring mutations in Piezo 1 channels that cause disease in humans are associated with reduced inactivation of the channel and not the pore. This empahasizes the importance of understanding the factors that control this inactivation of the channel. Inactivation modulation has also been associated with hypersensitivity of peripheral somatic neurons to mechanical stimulation. We have also determined sites in Piezo 1 amenable to flourescent labeling which will aide us in our studies of the channel. In so doing we have learned that elements necessary for channel conduction of ions and/or gating reside in both halves (N and C termini).

We have developed considerable expertise in expression of exogenous proteins in DRG neurons and in monitoring their mechanotransducers (MSCs) and the mechanical controlling agents (cytoskeleton). We have shown that in general, natural inflammtory agents, or synthetic agents that elicit the inflammatory pathways, increase MSC current amplitude and slow inactivation. It was also shown that the cytoskeleton reacts to these same agents by absorbing greater amounts of stress. Though not all inflammatory agents were equivalent in potency of eliciting mechanical sensitivity. Filamin, an important regulator of cortical remodeling, was shown to be particularly sensitive to dynamic stress changes of the magnitude that activate MSCs.

The findings have strongly positioned us to advance the understanding of mechanical pain sensation, and provide a basis for future grant applications to study this sensation in more detail.

References:

1. Sachs, F. and C.E. Morris, *Mechanosensitive ion channels in non-specialized cells*, in *Reviews of Physiology and Biochemistry and Pharmacology*, M.P. Blaustein, et al., Editors. 1998, Springer: Berlin. p. 1-78.
2. Sukharev, S. and A. Anishkin, *Mechanosensitive channels: what can we learn from 'simple' model systems?* Trends Neurosci, 2004. **27**(6): p. 345-51.
3. Sukharev, S. and F. Sachs, *Molecular force transduction by ion channels: diversity and unifying principles.* J Cell Sci, 2012. **125**(Pt 13): p. 3075-83.
4. Morris, C., *Why are so many ion channels mechanosensitive.* Cell physiology source book, 4th ed. Amsterdam: Elsevier, 2011: p. 493-505.
5. Bae, C., P.A. Gottlieb, and F. Sachs, *Human PIEZO1: removing inactivation.* Biophys J, 2013. **105**(4): p. 880-6.
6. Suchyna, T.M., et al., *Bilayer-dependent inhibition of mechanosensitive channels by neuroactive peptide enantiomers.* Nature, 2004. **430**(6996): p. 235-240.

7. Suchyna, T.M., et al., *Identification of a peptide toxin from Grammostola spatulata spider venom that blocks stretch activated channels.* Journal of General Physiology, 2000. **115**: p. 583-598.
8. Bowman, C.L., et al., *Mechanosensitive ion channels and the peptide inhibitor GsMTx-4: history, properties, mechanisms and pharmacology.* Toxicon, 2007. **49**(2): p. 249-270.
9. Bae, C., F. Sachs, and P.A. Gottlieb, *The mechanosensitive ion channel Piezo1 is inhibited by the peptide GsMTx4.* Biochemistry, 2011. **50**(29): p. 6295-300.
10. Nishizawa, M. and K. Nishizawa, *Molecular dynamics simulations of a stretch-activated channel inhibitor GsMTx4 with lipid membranes: two binding modes and effects of lipid structure.* Biophys J, 2007. **92**(12): p. 4233-43.
11. Hao, J. and P. Delmas, *Multiple desensitization mechanisms of mechanotransducer channels shape firing of mechanosensory neurons.* J Neurosci, 2010. **30**(40): p. 13384-95.
12. Andolfo, I., et al., *Multiple clinical forms of dehydrated hereditary stomatocytosis arise from mutations in PIEZO1.* Blood, 2013. **121**(19): p. 3925-35, S1-12.
13. Albuisson, J., et al., *Dehydrated hereditary stomatocytosis linked to gain-of-function mutations in mechanically activated PIEZO1 ion channels.* Nat Commun, 2013. **4**: p. 1884.
14. Coste, B., et al., *Piezo1 and Piezo2 are essential components of distinct mechanically activated cation channels.* Science, 2010. **330**(6000): p. 55-60.
15. Poole, K., et al., *Tuning Piezo ion channels to detect molecular-scale movements relevant for fine touch.* Nat Commun, 2014. **5**: p. 3520.
16. Michel, K., et al., *Fast calcium and voltage-sensitive dye imaging in enteric neurones reveal calcium peaks associated with single action potential discharge.* J Physiol, 2011. **589**(Pt 24): p. 5941-7.
17. Suchyna, T.M. and F. Sachs, *Mechanosensitive channel properties and membrane mechanics in mouse dystrophic myotubes.* J.Physiol, 2007. **581**(Pt 1): p. 369-387.

Reportable Outcomes:

Publications

1. Bae C, Sachs F, Gottlieb PA. The mechanosensitive ion channel Piezo1 is inhibited by the peptide GsMTx4. *Biochemistry* 2011;**50**:6295-6300.
2. Gottlieb PA, Sachs F. Cell biology: The sensation of stretch. *Nature* 2012;**483**:163-164.
3. Meng F, Sachs F. Orientation-based FRET sensor for real-time imaging of cellular forces. *J Cell Sci* 2012;**125**:743-750.
4. Bae C, Gnanasambandam R, Nicolai C, Sachs F, Gottlieb PA. Xerocytosis is caused by mutations that alter the kinetics of the mechanosensitive channel PIEZO1. *Proc Natl Acad Sci U S A* 2013;**110**:E1162-1168.
5. Bae C, Gottlieb PA, Sachs F. Human PIEZO1: removing inactivation. *Biophys J* 2013;**105**:880-886.
6. Gnanasambandam R, Ghatak C, Yasmann A, Sachs F, Ladokhin AS, Sukharev S, Suchyna TM. GsMTx4 mutagenesis reveals dynamic membrane binding properties that confer selective inhibition of Piezo1. *Journal of Physiology* 2015 (submitted).
7. Nishizawa K, Nishizawa M, Gnanasambandam R, Sachs F, Ladokhin AS, Sukharev S, Suchyna TM. Effects of Lys to Glu mutations in GsMTx4 on membrane binding, peptide orientation, and self-association propensity, as analyzed by molecular dynamics simulations. *Journal of Membrane Biology* 2015 (submitted).
8. Guo J, Wang Y, Sachs F, Meng F. Actin stress in cell reprogramming. *Proceedings of the National Academy of Sciences* 2014;**111**:E5252-E5261.

Conference Abstracts:

Biophysics conference, San Diego, CA, Feb. 25-29, 2012:

1. P. Gottlieb, C. Bae, F. Sachs " Piezo1 Gating: Comparison Between Whole Cell Current and the Patch", Biophysical Society Annual Meeting, San Diego, CA, Feb. 25-29, 2012

2. C. Bae, P. Gottlieb, F. Sachs "Effect of Temperature on the Piezo1 Mechanosensitive Ion Channel Currents", Biophysical Society Annual Meeting, San Diego, CA, Feb. 25-29, 2012

Biophysics conference, Philadelphia, PA, Feb. 2-6, 2013:

1) Radhakrishnan Gnanasambandam, Chilman Bae, Philip A. Gottlieb, Frederick Sachs. **Pore Properties of the Human Piezo1 Channel Based on Cation Permeation**, 2806-Pos Board B498.

2) Philip A. Gottlieb, Chilman Bae, Thomas Suchyna, Frederick Sachs. **Two Segments of the Human PIEZO1 Mechanosensitive Ion Channel Can Reassemble into a Functional Unit**, 1572-Pos Board B302.

3) Radhakrishnan Gnanasambandam, Frederick Sachs, Thomas Suchyna. **Effect of Inflammatory Mediators on Cytoskeletal Stress and Endogenous Mechanosensitive Currents in Dorsal Root Ganglion Neurons**, 2807-Pos Board B499.

Grants Submitted:

DoD Clinical and Rehabilitative Medicine Neurosensory Research Award, Opportunity Number: W81XWH-13-DMRDP-CRMRP-NSRA, Sachs - PI, Suchyna and Gottlieb – CoPIs. Title: Regulation of Mechanosensitive Ion channels in Nocioceptive Neurons and the Mechanism of Action of Peptide Inhibitor GsMTx4, 9/1/2014 – 8/31/2017.

Personnel:

Frederick Sachs, PI
Thomas Suchyna, CoPI
Philip Gottlieb, CoPI
Stephen Besch, Tech
Fanjie Meng, Postdoc
Chilman Bae, Postdoc
Radhakrishnan Gnanasambandam, Postdoc
Mary Teeling, Tech
Beverly Harlos, Tech
Marian Pazik, Tech
JoAnne Pazik, Tech
Tara Barone, Tech

Appendix A

GsMTx4 mutagenesis reveals dynamic membrane binding properties that confer selective inhibition of Piezo1.

Radhakrishnan Gnanasambandam[1*], Chiranjib Ghatak[2*], Anthony Yasmann[3*], Frederick Sachs[1†], Alexey S. Ladokhin[2†], Sergei I. Sukharev[3†], Thomas M. Suchyna[1†]

1) Department of Physiology and Biophysics, State University of New York at Buffalo, Buffalo, NY

2) Department of Biochemistry and Molecular Biology, The University of Kansas Medical Center, Kansas City, KS

3) Department of Biology, University of Maryland, College Park, MD

*) Co-primary authors

†) Co-Principle Investigators

Key words: peptide inhibitor, mutagenesis, mechanotransduction

Key Points:

- GsMTx4, a selective peptide inhibitor of cation selective mechanosensitive ion channels, is rich in lysine residues that play an important role in stabilizing the peptide at the membrane interface.
- Lysine to glutamate mutations have differential effects on the inhibition of Piezo1 channels, but only weakly affect membrane binding energy.
- GsMTx4 inhibition is dependent on the equilibrium depth of penetration and its surface area contribution at resting membrane tension.
- Peptide penetration depth increases with membrane tension as the free volume is increased by bilayer stretching creating a “tension clamp”.

Abstract:

GsMTx4 is a spider venom derived peptide selective for cationic mechanosensitive channels (MSCs). It has six lysine residues that have been proposed to affect membrane binding. We mutated each of the six lysines to glutamate and tested them against Piezo1 channels in outside-out patches and measured lipid binding using a variety of physicochemical assays. Mutant peptides had lower efficacy (0-40%) in general compared to wild type (WT). Increased association rates for some of the mutants did not correlate with increased inhibition. Tryptophan fluorescence quenching and isothermal titration calorimetry showed that the free energy of binding to lipid vesicles was largely unaffected by the mutations, with the exception of the most compromised mutant, K15E, which actually bound more tightly. Fluorescence quenching assays showed that WT and mutant peptides bound near the lipid-water interface, but the mutants penetrated 1-2Å deeper than WT. Peptide association as a function of lipid tension was investigated in monolayers in a Langmuir trough. As amphipaths, the peptides bound to the membrane water interface and as the monolayer area is reduced to the monolayer-bilayer equivalence pressure, the compliance increased. Mutants with compromised efficacy had steeper slopes in this region suggesting deeper association. These data place GsMTx4 at the membrane surface where it is stabilized by the lysines, and it occupies a small fraction of membrane area at normal tension. As surface pressure decreases during membrane stretching, the peptides penetrate deeper acting as "area reservoirs", effectively clamping the outer monolayer tension and reducing the stress on the channels.

List of Abbreviations

10-DN – 10-doxylnonadecane

CD – Circular Dichroism

C_s^{-1} – inverse compressibility modulus

DLS – Dynamic Light Scattering

GsMTx4 – Grammostola Mechanotoxin 4

ICK – Inhibitory Cysteine Knot

I_{max} – Maximum Quench of I_o/I ratio

ITC – Isothermal Calorimentry

k_a – association rate constant

k_d – dissociation rate constant

K_D – equilibrium inhibition constant

K_{SV} – Stern-Volmer quenching constant

LUV – Large Unilamellar Vesicle

MD – Molecualr Dynamic simulations

MSC – Mechanosensitive Ion Channel

POPC – 1-palmitoyl-2-oleoyl-sn-glycero-3-phophocholine

POPG – 1-palmitoyl-2-oleoyl-sn-glycero-3-phosphoglycerol

π_B – monolayer-bilayer equivalence pressure

WT – Wild Type

Introduction

Many channel-active peptides isolated from spider venom are small (3-5 kD) amphipathic molecules built on a conserved inhibitory cysteine-knot (ICK) backbone (Norton & Pallaghy, 1998; Craik *et al.*, 2001). Most of them partition into lipid bilayers and inhibit their target channels by modifying gating kinetics (Lee & MacKinnon, 2004; Suchyna *et al.*, 2004). Examples of well-studied gating modifiers are the Hanatoxins, SGTx1, and VSTx1 that inhibit voltage gated K_v channels by interacting with the gating paddle (Lee *et al.*, 2003; Wang *et al.*, 2004; Jung *et al.*, 2005; Wee *et al.*, 2010a). These peptides have a hydrophobic face that presumably facilitates interfacial adsorption to the lipid bilayer increasing the likelihood of direct interaction with intra-membrane channel gating elements (Lee *et al.*, 2003).

GsMTx4 is an inhibitory gating modifier (Suchyna *et al.*, 2004) notable because of its high selectivity for cationic mechanosensitive channels (MSCs) (Suchyna *et al.*, 2000). It represents the first compound in a new category of pharmaceuticals for treating diseases related to mechanical dysregulation (Bowman *et al.*, 2007). These MSCs are gated by in-plane bilayer tension (Sachs, 2010), not voltage (Catterall, 2012), suggesting that GsMTx4 modifies gating by a different mechanism. Most ICK peptides have stereospecific interactions with the receptors (Bosmans & Swartz, 2010), but GsMTx4 is active as either an L or D enantiomer (Suchyna *et al.*, 2004). This means that, although GsMTx4 acts within a Debye length of the channel pore, it likely inhibits MSCs by modulating local membrane stress rather than via chiral interactions with the protein. GsMTx4 has two other distinct physical properties among ICK peptides, namely a high net positive charge (8 positive and 3 negative residues for a net of $+5e$), and strong hydrophobicity characterized by a long RP-HPLC elution time (Suchyna *et al.*, 2000).

We have tested the contributions of hydrophobicity and charge to the free energy of membrane partitioning using intrinsic tryptophan quenching of different peptides in the presence of vesicles composed of lipids with different charge (Posokhov *et al.*, 2007b). Surprisingly, the strongly cationic GsMTx4 had only weak selectivity for anionic over zwitterionic membranes. Other ICK peptides, like GsMTx1 and SGTx1, with lower net positive charge (both 6 positive and 3 negative residues for a net $+3e$), showed a strong preference for anionic lipids. This suggests that, in contrast

to other ICK peptides where electrostatic interactions govern the strength of lipid binding, other factors dominate GsMTx4 partitioning.

Molecular dynamic simulations (MD) of ICK peptide interactions with membranes suggest that they partition into the bilayer with an energy minimum at the interfacial boundary with the hydrophobic face toward the membrane interior (Bemporad *et al.*, 2006; Nishizawa & Nishizawa, 2007; Wee *et al.*, 2007; Wee *et al.*, 2010b; Chen & Chung, 2013). Simulated (Wee *et al.*, 2008; Chen & Chung, 2013) and experimental (Posokhov *et al.*, 2007b; Jung *et al.*, 2010) studies of membrane binding suggest nothing unusual about GsMTx4 partitioning since binding affinity is similar across ICK peptides. However, MD suggests that membrane dimpling caused by GsMTx4 insertion may be greater and extend over larger areas than the other peptides (Wee *et al.*, 2008; Chen & Chung, 2013). The stability of GsMTx4 interaction with the membrane interface may inhibit deeper penetration than predicted for the other ICK peptides (Nishizawa & Nishizawa, 2007; Nishizawa, 2011; Chen & Chung, 2013). While the hydrophobic face is clearly important for membrane insertion, simulations suggest that the large positive charge on GsMTx4 was important in determining the strength of bilayer interfacial association, the depth of penetration, and the lipid displacement (Chen & Chung, 2013). We tested this hypothesis by creating six charge mutants changing lysine to glutamate (KtoE) thereby reducing the net charge to +3*e*.

We looked first at the functional differences in the mutants by determining the kinetics of inhibition of Piezo1 in patches from transfected HEK cells. We observed different degrees of steady state inhibition that did not correlate simply with changes in the association and dissociation rate constants. We also observed that two of the mutants had no effect on inhibition, and these were the same lysines identified by MD to stabilize deeper binding modes. We investigated the lipid partitioning properties of the mutants using a variety of physical chemistry techniques including circular dichroism, tryptophan fluorescence quenching, isothermal titration calorimetry, Langmuir monolayers, dynamic light scattering, and native gel electrophoresis. We found that 1) WT GsMTx4 is superficially bound at resting membrane tension, and the mutants tended to bind deeper, 2) tension-dependent transitions between deep and shallow adsorption states gave GsMTx4 a tension clamping property, and 3) the reduction of charge tended to increase peptide aggregation in solution that may affect bilayer interactions. We have proposed a new model of efficacy whereby the distribution of charges influences the orientation and the equilibrium of

shallow and deeply bound states. An increase in membrane tension (an increase in free volume) favors the deeper state, and we predict that the partition coefficients are tension sensitive.

Methods

Peptide synthesis and folding: WT GsMTx4 (synthetic L amino acid form) and glutamate substitution mutant peptides of the 6 lysine residues at positions 8, 15, 20, 22, 25 and 28 were acquired from (CSBio Company, CA, USA). In this manner six mutant peptides were generated; henceforth, we refer to the mutant peptides as K8E, K15E, K20E, K22E, K25E and K28E. The wild-type (WT) and mutant peptides were chemically synthesized and folded commercially (the peptide was folded in 0.1 M Tris, pH 7.9 with the oxidized/reduced glutathione ratio = 1/10 (Ostrow *et al.*, 2003)). Peptide concentrations determined by HPLC analysis of the perfusates were between 1.5-6 μM, and the average value of the peptide concentrations from all patches for a given peptide was used for the K_D calculations.

Circular Dichroism: CD measurements were performed on peptides at 5 μM using an upgraded Jasco-720 spectropolarimeter (Japan Spectroscopic Company, Tokyo). Normally 80-100 scans were recorded in order to increase the signal to noise ratio to between 200-260 nm using a 1 nm optical path. Spectra were corrected for background scattering by subtracting a vesicle-only spectra. Temperature was controlled by a Peltier unit.

Electrophysiology: HEK cells were transfected with 1 μg of mouse Piezo1 cDNA cloned into a pIRES vector and we used outside-out patches. An Axopatch 200B amplifier (Axon Instruments) recorded mechanically activated Piezo currents. Patches were stretched by hydrostatic pressure applied to the pipette using an HSPC-1 pressure clamp (ALA Scientific Instruments, NY). We applied 500 ms pressure steps every 4 seconds to patches held at +50 mV pipette potential, and analyzed the currents from patches that showed consistent currents at 40-50 mmHg of pressure. Wild Type (WT) and KtoE mutant GsMTx4 peptides were perfused onto the patches using an ALA MP285 perfusion system. Acquisition of electrical recordings, stimulus generation and peptide application were controlled by QuBio software, analyzed using QuB Express (http://www.qub.buffalo.edu/wiki/index.php/QUB_Express) and Origin 8.5 graphical software. The extracellular solution contained 145 mM NaCl, 5 mM KCl, 3 mM $MgCl_2$, 0.1 mM $CaCl_2$ and

10 mM HEPES. The pipette solution contained 133 mM CsCl, 10 mM HEPES, 3 mM $MgCl_2$ and 0.5 mM EGTA. The pH of these solutions was adjusted to pH 7.4. Peptide solutions were made fresh daily, and the peptide concentration emerging from the perfusion tip was sampled and quantified in an Agilent 1100 series HPLC prior to use.

Fluorescence measurements of membrane binding: The interaction between these tryptophan-containing peptides and lipid vesicles were studied as described in (Posokhov *et al.*, 2007a). Briefly, tryptophan (Trp) fluorescence from 2 μM peptide was measured using a SPEX Flurolog FL 3-22 steady state fluorescence spectrometer (Jobin Yvon, Edison, NJ) equipped with double grating excitation and emission monochromators. Trp residues were excited at 280 nm and emission spectra were recorded between 290 nm and 500 nm using excitation and emission spectral slits of 2 and 4 nm, respectively. Measurements were made at 25°C in 2x10 mm cuvettes oriented perpendicular to the excitation beam. Quenching of Trp emission by aqueous iodide was measured in the presence of increasing concentrations of large unilamellar vesicles (LUVs) composed of 1-palmitoyl-2-oleoyl-sn-glycero-3-phosphocholine (POPC) and 1-palmitoyl-2-oleoyl-sn-glycero-3-phosphoglycerol (POPG) (Avanti, Alabaster, AL). All spectra were recorded after equilibration of the sample. Corrections for background and the fitting of spectra were performed as described previously (Ladokhin *et al.*, 2000).

Fluorescence quenching measurements of membrane penetration: We used two types of quenching: quenching with water-soluble (acrylamide) and membrane-bound quenchers (10-DN, and brominated lipids, Avanti, Alabaster, AL). All measurements were performed as described above with the exception of acrylamide quenching, for which 295 nm excitation was used in order to reduce inner filter effects. For depth-dependent quenching we used a series of lipids with bromine atoms attached at positions 6,7 and 9,10 and 11,12 along one of the acyl chains (6,7; 9,10; and 11,12-BRPCs). Depth-dependent quenching profiles were generated by taking the ratio of tryptophan intensity F, to that in the absence of quenchers, F_0, as a function of the depth of the bromolipids. The profiles were analyzed by Distribution Analysis (Ladokhin, 1999a; Ladokhin, 2014) which approximates the quenching profile as Gaussian.

Langmuir monolayer experiments: All experiments were conducted in a buffer made with 50 mM KCl, 10 mM KPi, titrated to pH 7.2. In both liposome and monolayer experiments, the

lipid was composed of POPG-POPC (3:1 mole/mole). The peptides were dissolved in buffer to make stock solutions of 150 μM and stored for no more than 2 days at 4 °°C; samples were never frozen. Langmuir monolayer experiments were done with a two-barrier, rectangular (22×6cm) trough (Kibron MicroTrough XS) housed in an AirClean enclosure. A Dyneprobe metal alloy needle was used as the Wilhelmy plate. A POPG-POPC mixture (both from Avanti Polar Lipids, Alabaster, AL) was dissolved in chloroform to a final concentration of 0.2 mg/ml. The lipids were deposited onto the subphase using a gastight 50 μL Hamilton® syringe; the measurements started after 10 min to allow the solvent to evaporate. Pressure/ area (π-A) isotherms of monolayers were measured at room temperature (~ 20 °C) from 114 cm^2 to 18 cm^2 at a barrier rate of 20 mm/min. For each mutant, isotherms were measured at least six times. The inverse lateral compressibility moduli $Cs^{-1} = A(d\pi/dA)$ were determined from the isotherms (Smaby *et al.*, 1997).

Isothermal Titration Calorimetry (ITC): POPG-POPC (3:1) liposomes were prepared by rehydrating 2 mg of dried lipid mixture in a round-bottom glass tube with buffer. After which they were vortexed, and sonicated in a Branson-type bath sonicator for 1 minute. ITC experiments were carried out using a Microcal VP-ITC Microcalorimenter. The heat of the high peptide dilution pre-defined the titration configuration in which 10-30 μM peptide was in the cell and a 0.3-1 mM liposome suspension was in the syringe. 20 μL injections were spaced by 300s intervals. For all peptides, interactions with POPG-POPC liposomes were exothermic. After minor baseline adjustments, the thermograms were fitted with single-site binding curves to determine the mean parameters (usually defined by the major low-affinity population of sites). Then, guided by this first fit, we fit to a two-site model. The two-site fittings were significantly better suggesting the presence of a second, higher affinity population of sites.

Dynamic Light Scattering: These experiments examined the tendency of the peptides to aggregate. The peptides were diluted to 20 μM in the standard 50 mM KCl buffer and within one hour were subjected to dynamic light scattering (DLS) measurements on a 90 Plus Particle Size Analyzer (Brookhaven Instruments Corp.) pre-calibrated with 92nm nanospheres (Duke Scientific Corp.). Autocorrelation data were collected during five 1-min intervals and averaged.

Non-denaturing gel electrophoresis: Three concentrations (1, 3 and 10 μM) of WT peptide and mutant peptides (K8E and K28E) were run on 10-20% gradients of Tris/Tricine

polyacrylamide gels from Biorad. The gels were run at 100 V and 400 mA for 1 hour. The markers were Precision Plus dual extra protein standard marker from Biorad containing SDS. Tris Tricine running buffer contained 100 mM Tris and 100 mM Tricine at pH 8.3. Tricine loading buffer contained 100 mM TrisCl, pH 8.3, 30% glycerol, and 0.25% Coomassie Brilliant blue G 250. The G250 stain is sensitive to 10 ng of protein.

Statistical Analysis:

Statistical significance of channel inhibition strength was determined using a Student's t-test on the mean steady state current levels with α at 0.05.

Results

Structural analysis of Lysine Mutants: At pH of 7.4, lysine residues are deprotonated and contribute substantially to the net positive charge on GsMTx4. MD predicts interactions between the lysine residues and the oxygens of the lipid head group carbonyls (Nishizawa & Nishizawa, 2007; Chen & Chung, 2013). To disrupt electrostatic interactions, we sequentially mutated lysines to glutamate giving all mutant peptides a net charge of +3*e,* since glutamate has a charge of -1 at pH 7.4.

Mass spectrometer measurements with single proton resolution showed the mutant peptides all had masses consistent with three disulfides having formed. RP-HPLC analysis showed that all mutant peptides eluted at similar times to WT (data not shown). As an additional check of the secondary structure, we measured the absorption spectrum using circular dichroism (CD). The spectra for the L and D forms of WT GsMTx4 in solution showed the opposite polarity as expected (Supporting Fig. S1A). The shape of the WT GsMTx4 spectrum was relatively unchanged by the addition of either 100% POPC (zwitterionic) or 3:1 POPG:POPC (negatively charged) LUVs, though a general increases in intensity was observed when bound to POPG:POPC, likely due to stabilization of the secondary structure. In solution, the spectrum of the mutants was similar to the WT, except for a distinct negative peak at ~228 nm that was present in all mutants (Fig. 1A). This peak disappeared when the peptides were allowed to bind to POPG:POPC LUVs, and the spectra of all mutants now showed the basic WT profile (Fig. 1B). However, the peak was unchanged after binding to POPC LUVs (Supporting Fig. S1B). We believe that the 228 nm peak arose from the

formation of multimers or aggregates due to inter-peptide hydrophobic interactions in solution or when weakly bound to membranes (see peptide aggregation studies below). Stronger association to membranes, as with the negatively charged POPG:POPC LUVs appears to cause dissociation of aggregates (see spectroscopic analysis below).

Functional analysis of MSC inhibition: The WT and KtoE mutants were tested on outside-out patches from HEK cells transfected with cDNA for mouse Piezo1. The stimulus was a pulse train of 500ms positive pressure step separated by 1500ms interpulse intervals. We measured the current elicited by the pressure steps before, during perfusion with ~5 μM peptide (until the current reached steady state inhibition), and after washout (Fig. 2A). As controls for variations in the patch geometry, the mutant tests episodes were followed by ~30-60 seconds of washout and an episode of WT peptide application. The association (k_a) and dissociation (k_d) rates were fit with single exponentials (Fig. 2B, and Supporting Fig. S2). The ratio of the rate constants for current decay and recovery for each peptide were used to calculate the equilibrium inhibition constant (K_D) (Fig. 2C). The k_as of most mutants were only weakly affected with the exception of K15E that was nearly double WT. The k_ds also showed little difference with the exceptions of K15E (~2X slower) and K28E (~3X faster). Most mutants had K_Ds in the low μM range, similar to WT (3.2 μM). However, two notable mutants were K15E and K28E which had equilibrium constants ~5X lower (higher affinity) and 2Xs higher (lower affinity) than WT respectively. Since GsMTx4 does not inhibit MSCs by a lock-and-key association (Suchyna *et al.*, 2004) but modifies the channel environment, differences in K_D values are difficult to interpret. K_D likely represents a combination of membrane partitioning and diffusion to the channel periphery followed by interaction with the channel.

The level of Piezo1 inhibition was determined from the steady state current from the association rate fits (Fig 3). K8E and K28E mutations had no effect on the level of inhibition, while the others all showed a 20-40% decrease in efficacy compared to WT. WT produces a 30 mmHg shift to higher pressures in the gating curve (Bae *et al.*, 2011). The percent loss in activity observed for these mutants is equivalent to a 6-12 mmHg increase in the midpoint pressure. As suggested above, the steady state inhibition was not generally correlated with a change in K_D. For example, the K_D

of K15E indicated higher affinity than WT, but it also had the greatest loss of inhibition. This suggests that, the K_D represents more than a typical two-state (free/inhibited) binding reaction.

As an alternative method of determining K_D, we calculated K_D from a direct measure of the concentration dependence of inhibition (Fig 4). Fitting the data with the Hill equation gave a calculated K_D of 2 μM, similar to that calculated from the rate constants. (*The K_D's determined here are slightly higher than the previously determined K_D (~0.5 μM) (Suchyna et al., 2000; Bae et al., 2011) which may be due to differences in the pressure step protocols used in the different studies*). The Hill coefficient was 1.5, suggesting that inhibition may involve more than one peptide.

Spectroscopic determination of Vesicle binding: Tryptophan (Trp) is a useful intrinsic fluorophore to study peptide binding to lipids. These measurements can be used to measure the free energy (ΔG) of bilayer partitioning using equilibrium titration. In our earlier work (Posokhov *et al.*, 2007b), we found that the addition of LUVs to a GsMTx4 solution led to minor changes in Trp emission limiting the use of the technique to calculate ΔG. To improve sensitivity, we developed a protocol based on the accessibility of GsMTx4 to aqueous iodide ion in solution and in membrane-bound states. KI will quench Trp fluorescence, but only in the aqueous phase where the Trps are exposed. We used 50 mM KI to accurately measured ΔG (Posokhov *et al.*, 2007a; Posokhov *et al.*, 2007b).

L-GsMTx4, and its D enantiomer have two adjacent Trp residues that have a peak emission intensity at 365 nm in solution (Supporting Fig. S3 and Table 1). The KtoE mutants all showed nearly identical blue shifts of ~8nm, suggesting a common effect of net charge on the environment of the Trp's. The blue shift is correlated with a more hydrophobic environment. In solution, the shift likely represents enhanced peptide aggregation that partially shields the Trp residues from the aqueous environment.

Peptides	Fluorescence λ_{max} (nm)			ΔG, kJ/mole		I_{max}		Z_{eff}
	Buffer	100% POPC	75% POPG 25% POPC	100% POPC	75% POPG 25% POPC	100% POPC	75% POPG 25% POPC	
L-GsMTx4	**365**	**365**	**365**	**-26.8**	**-31.4**	**1.4**	**2.6**	**+0.5**

D-GsMTx4	**365**	**365**	**365**	**-25.9**	**-31.0**			**+0.5**
K8E	**357**	**357**	**352**	**-26.4**	**-27.6**	**2.1**	**3.0**	**+0.2**
K15E	**357**	**357**	**352**	**-26.4**	**-31.4**	**2.9**	**3.5**	**+0.5**
K20E	**357**	**357**	**353**	**-26.4**	**-34.3**	**2.3**	**3.6**	**+0.8**
K22E	**357**	**357**	**351**	**-26.4**	**-29.3**	**2.3**	**3.4**	**+0.3**
K25E	**357**	**357**	**351**	**-25.1**	**-32.6**	**3.4**	**2.1**	**+0.7**
K28E	**357**	**357**	**349**	**-25.9**	**-31.8**	**1.7**	**3.2**	**+0.6**

Table 1. Trp fluorescence changes associated with mutagenesis and vesicle binding.

As shown previously (Posokhov *et al.*, 2007a), both the D and L enantiomers of WT GsMTx4 were *not* blue shifted in the presence of either POPC or POPG-POPC LUVs, even though I_{max} showed a robust association with both vesicle compositions (Supporting Fig. S3 and Table 1). The interpretation of I_{max} is addressed below. The mutants had a blue shift in the presence of POPG-POPC LUV, but not POPC (Table 1). We have suggested that the lack of blue shift for the WT and D-enantiomer may be related to incomplete dehydration of the Trp residues upon binding (Posokhov *et al.*, 2007a). The presence of the shift for the mutants in anionic vesicles suggests a less polar environment for the Trps, possibly related to a deeper membrane penetration. This was further investigated with membrane-resident fluorescent quenchers.

The free energy of partitioning can be calculated from the fluorescence intensity changes upon lipid titration. As shown previously, the WT D and L enantiomers bind only slightly stronger to POPG-POPC than to POPC LUVs (Table 1, and Fig. 5A and B). That stands in contrast to other ICK peptides that have weak affinity for POPC vesicles (Posokhov *et al.*, 2007b). This weak dependence of the binding energy in differently charged lipids serves as a striking example of the non-additivity of hydrophobic and electrostatic interactions. ΔG for the mutant peptides was similar to WT for both POPC and POPG-POPC LUVs. The lack of any substantial effect by the six different charge mutants on ΔG emphasizes the dominance of hydrophobicity in partitioning. The strong hydrophobic interaction is consistent with the long elution time of GsMTx4 compared to other venom derived peptides in RP-HPLC (Suchyna *et al.*, 2000).

The significant differences in the maximum quenching, I_{max}, for the different peptides suggests that it arises from differences in peptide tilt and the depth of penetration, or possibly local lipid packing. There was a general trend for all the mutants to have higher I_{max} values than WT suggesting those Trps were better penetrate deeper into the membrane. K8E and K28E whose

inhibitory activity was unaffected, had low I_{max} values similar to WT in both types of vesicles, while the least active mutant (K15E) had a significantly higher I_{max} suggesting greater protection of the Trp residues and deeper binding.

Peptide-vesicle affinity determined by isothermal titration calorimetry: As an independent measure of the binding energy to POPG:POPC vesicles, we performed isothermal titration calorimetry (ITC - Fig. 6). These enthalpy measurements are fundamentally different from the Trp quenching experiments since they have different sensitivities to the binding processes. A single-site binding model rarely produced a satisfactory fit to the ITC isotherms, but a two-site model was a good fit. In most cases, the smaller of the two binding constants was between $8 \bullet 10^4$ to $8 \bullet 10^5$ M^{-1} (Table 2), corresponding to interaction energies of 28 to 32 kJ/mol, that was consistent with the spectroscopic data (27-34 kJ/mol). However, curve fitting identified the presence of a second higher-affinity site(s) with constants in the range of $2 \bullet 10^6$ to $3 \bullet 10^7$ M^{-1} of comparable density as shown by N_1 and N_2. These higher affinity sites were not seen in the spectroscopic analysis. Similar chemistry of binding to both types of sites is suggested by their similar negative enthalpies (-0.9 to -1.5 kcal/mol) and positive entropies (20-30 cal/molK). The two mutants with the most compromised activity (K15E and K25E) had some unique characteristics. K15E had a significantly higher first binding constant ($8.6 \bullet 10^6$ M^{-1} or 40 kJ/mol) consistent with the stronger association constant calculated from the inhibition data. It also had a positive ΔH_1 and high ΔS_1, meaning that the low-affinity binding mode is quite different for this mutant. K25E had the highest affinity for the second site. The positive entropies probably signify partial desolvation. The experiment does not exclude the possibility of more sites, especially as we recall that the binding site is not chiral, however the simplest model with two sites seems to be adequate.

Peptides	N_1	K_1 (M^{-1}/min)	ΔH_1 (Cal/mol)	ΔS_1 (Cal/mol/deg)	N_2	K_2 (M^{-1}/min)	ΔH_2 (Cal/mol)	ΔS_2 (Cal/mol/deg)
L-GsMTx4	**1.9**	**2.4×10^5**	**-1078**	**21.0**	**2.4**	**2.7×10^6**	**-1565**	**24.2**
K8E	**0.3**	**8.0×10^4**	**-1580**	**17.2**	**0.8**	**8.8×10^6**	**-1566**	**26.6**
K15E	**0.8**	**8.6×10^6**	**971**	**63.8**	**0.8**	**2.2×10^7**	**-5073**	**16.5**
K22E	**1.9**	**2.3×10^5**	**-934**	**21.5**	**3.1**	**5.4×10^6**	**-1501**	**25.8**
K25E	**1.4**	**2.4×10^5**	**-448**	**23.1**	**2.4**	**3.1×10^7**	**-773**	**31.7**
K28E	**0.9**	**8.3×10^5**	**-498**	**25.4**	**1.0**	**2.1×10^7**	**-853**	**30.7**

Table 2. ITC Fitting Parameters. Based on the density values (N), the low- and high-affinity sites are occur in comparable amounts/densities. Of the two most compromised mutants, K25E shows the highest K2, and the K15E has positive ΔH1 and high ΔS1 meaning that the low-affinity binding mode is quite different for this mutant.

Peptide penetration depth: Two different quenching methods were used to determine the depth of peptide penetration into LUVs. In the first method, we employed dual quenching analysis which involves quenching Trp with two different quenchers residing either in solution or in the membrane. Acrylamide was the *aqueous* quencher and is unable to quench the fluorescence of residues deeply embedded in the bilayer. The other is 10-doxylnonadecane (10-DN) that is hydrophobic and efficiently quenches Trp residues residing near the bilayer center. The slope of the quenching agent concentration vs the ratio of quenched fluorescence is the Stern-Volmer quenching constant (K_{SV}). Comparisons of these constants provided a useful measure of the mean penetration depth.

Trp fluorescence decreased linearly with the concentration of acrylamide increased in saline (Fig. 7A), or when peptides were bound to POPC (Fig. 7B) or POPG-POPC LUVs (Fig. 7C). Quenching was greater in saline than in the presence of vesicles confirming membrane binding. The sensitivity of Trp fluorescence to 10-DN incorporated in POPC (Fig. 7D) and POPG-POPC (Fig. 7E) was also concentration dependent, but with a much shallower slope. Comparing the quenching constants of the mutants to WT in the membrane-bound state (Table 2) clearly indicates that mutants have lower accessibility for water-soluble acrylamide and higher accessibility to membrane-soluble 10-DN suggesting increased shielding of mutant Trp residues by deeper penetration. This correlates with the KI data where the mutants have higher I_{max} values suggesting greater protection of the Trps from aqueous quenchers. The WT appears to be more sensitive to

the charge on the membrane. For WT, the ratio of the K_{SV} in POPG:POPC vs that in POPC vesicles (POPG:POPC/POPC) was ~0.4 for acrylamide while in 10-DN the ratio was ~1.3. The difference between the ratios of the constants for the mutants was smaller for the two types of vesicles (~0.6 in acrylamide and ~1.0 in 10-DN). This suggests the greater positive charge on the WT peptide stabilizes a more superficial bilayer association.

Peptides	Buffer	Acrylamide 100%POPC	Acrylamide 75:25% POPG:POPC	10-DN 100%POPC	10-DN 75:25% POPG:POPC
WT	**20.4±0.6**	**14.9±0.5**	**5.8±0.2**	**2.1±0.1**	**2.7±0.5**
K8E	**10.9±0.2**	**4.8±0.6**	**2.9±0.1**	**3.3±0.2**	**3.8±0.6**
K25E	**11.4±0.4**	**5.8±0.3**	**3.8±0.2**	**3.8±0.1**	**3.6±0.2**
K28E	**10.4±0.3**	**5.0±0.5**	**3.1±0.4**	**3.7±0.1**	**4.1±0.4**

Table 3. Stern-Volmer quenching constant (K_{SV}) calculated from the slopes of Trp fluorescence quenching data in Fig. 7. K_{SV} values for water the soluble quencher acrylamide are expressed in units of M^{-1} and for membrane soluble 10-DN in dimensionless units.

The second approach to determining membrane penetration relies on Trp fluorescence quenching by bromine atoms attached to the lipids at different positions on the aliphatic chains between carbons 6-7 (11 Å from bilayer center), 9-10 (8 Å) and 11-12 (6 Å). We used both 100% BrPC and 50:50% POPG:BrPC LUVs. Trp quenching increased for all peptides with shallower bromines [Fig. 8A (100% BrPC) and B (50:50% POPG:BrPC)]. Because the maximum of the quenching profile is shallower than the depths of available bromolipids, we used *a priori* constraints to estimate the depth. We used the method of Distribution Analysis (Ladokhin, 1997; Kyrychenko & Ladokhin, 2014) which approximates a quenching profile with a Gaussian. Because the quenching profile is poorly defined, no unique solution exists when all three fitting parameters are varied. One can estimate the average position assuming a particular width of the distribution. Based on our previous experience with quenching of various peptides, we assumed a value of 5 Å for the dispersion of the Gaussian distribution (Ladokhin, 1999b). Note, that narrower distributions would be inconsistent with the presence of the two neighboring tryptophan residues while a wider distribution would have little effect on our conclusions. The results support the conclusions of the acrylamide/10-DN quenching which indicated a deeper penetration of the mutants compared to

WT. We emphasize however, that because the quenching profile is not well defined, the results of the analysis presented in Fig. 8 should be regarded as rough estimates of depth but unequivocally shallow.

Surface pressure dependent monolayer association: Because GsMTx4 inhibits channels that are sensitive to membrane tension, we characterized membrane binding as a function of lipid tension. The peptides were injected into the subphase of a Langmuir trough containing monolayer films composed of POPG:POPC (3:1) which could be compressed. The control pressure-area (π-A) isotherms (Fig. 9, green line) show no inflections, rising smoothly with compression until the monolayer collapses at about 44 mN/m. The control curve passes 40 mN/m at a molecular area of 68 $Å^2$, which would correspond to the lipid density in pure POPC bilayers (68.3 $Å^2$) (Kučerka *et al.*, 2006). The surface pressure that packs lipids at this bilayer density is called the monolayer-bilayer equivalence pressure (πB). Although as traditionally defined, πB for many lipids is in the range 30-35 mN/m (Marsh, 2006), according to Brockman (Dahim *et al.*, 2002), πB for a similar SOPC lipid is nearer to 40.5 mN/m, i.e. closer to the collapse pressure.

Addition of 0.1 μM WT peptide into the subphase visibly increased surface pressure over a wide range of areas. At 1 μM or above, GsMtx4 increased surface pressure immediately, i.e. without compression, signifying massive intercalation into the disorganized monolayer. As seen from the family of curves (Fig. 7), the increase in surface pressure is concentration dependent. Up to ~37 mN/m, the compression curves are above the controls, however, above that pressure the curves bend. The bend could be due to re-partitioning of the peptide from the film into the subphase or due to the peptide moving from a deeper penetration depth to a more superficial surface state. The peptide pressure curves intersect the control curve in the vicinity of 40 mN/m, i.e., near πB. The flattening of the curves at that level marks the expulsion of the peptide, which apparently continues during a gradual collapse of the monolayer. The area at which the transition point occurs increases with peptide concentration, while the pressure at the bending point decreases. Thus, the untreated monolayer can withstand ~7 mN/m more pressure before collapsing than it can in the presence of 1 μM peptide. The shape of the curve gets more complicated at 3 μM, so we focused on 1 μM where a strong inflection occurs but the curves maintained a similar shape. The bending of the isotherm near the monolayer-bilayer equivalence pressure (Fig. 9, arrows) suggests that the

peptide-harboring film undergoes a change resembling a phase transition. Reversible partitioning of the peptide between the aqueous phase (or loosely bound state, see calorimetry and discussion) and the deeper state(s) suggests that, near πB, changes in the area will not change lateral pressure/tension significantly, producing a pressure (or tension) clamp effect.

We compared the compression isotherms of WT with four mutants that had different levels of inhibitory activity. As was shown in the electrophysiology experiments (Fig. 3), K8E and K28E exhibited WT-like activity, while the K15E and K25E showed partial activity. The compression isotherms for the active peptides intersect with the control curves near 40 mN/m. As with WT, the isotherms are much shallower than the control curve near πB. Converting the pressure to the inverse compressibility modulus (C_s^{-1} – See Methods and Fig. 10 legend) and plotting it against the area change (Fig. 10, lower panels), shows that the flattened region at the left top end of the compression isotherms signifies the lower compressibility near the πB. This behavior shows specifically that the peptide residence in the lipid film in this region is strongly dependent on lateral pressure. The clear break of the isotherm for WT GsMTx4 in the region between 36 and 40 mN/m corresponding to πB shows that WT will tend to 'clamp' the tension near the monolayer-bilayer equivalence pressure. K8E and K28E pretty much follow the WT isotherm in that region and show uncompromised biological activity.

In contrast, the partially active peptides exhibited a different behavior near πB (Fig. 10). The curves for K15E and K25E had additional peaks that do not intersect the control curve. This indicates that the peptides have greater stability in the lipid film and never completely leave it. There is no visible 'phase transition' as observed in the WT from near 37 mN/m until collapse, which is observed near 45-47 mN/M as in the control. Importantly, in the vicinity of the density of 72 $Å^2$/lipid, i.e. between the πB and the collapse pressure, K15E and K25E isotherms have a steeper slope. The compressibility parameter C_s^{-1} exhibits a local maximum in that region, being considerably higher than that of the WT peptide or the active mutants (Fig. 10, asterisk), however, it is still lower than control membranes. Based on the compression isotherms, the K15E and K25E mutants will not be able to clamp pressure (tension) in the membrane as effectively as WT.

The presence of the peptide in the monolayer is reflected by an increase in area at a given pressure. To visualize the area occupied by the peptide we re-plotted the pressure-area curves in area-

pressure coordinates and presented the area difference in log scale (Fig. 10). Assuming that the area change is proportional to the probability of a peptide inserting into lipid p_{lip} while p_{bulk} (concentration in the bulk) is constant, one can write

$$K_{eq} = \frac{p_{lip}}{p_{bulk}} = e^{-(\Delta G + \pi a)/kT}, \quad \text{so that} \quad kT(\ln p_{lip} - \ln p_{bulk}) = -\Delta G - \pi a$$

Differentiating with respect to π we obtain, $-kTd(\ln p_{lip})/d\pi = a$

where a is the area occupied by the peptide molecule in the plane of the lipid film.

The bottom row in Figure 11 is a plot of the log of the area difference vs pressure for the WT and four variants with a range of inhibitory properties. The obvious difference between WT, K8E, and K28E and the two weakened activity peptides is the character of the intersection of the corresponding isotherms with the control. The slope of the logarithmic difference area plot near that intersection also reflects that difference. The flattening of the isotherms for active peptides occurring in the vicinity of the πB is the property that means high compressibility in that region.

For WT GsMTx4 (Fig. 11, bottom panel), one can see that there is minimal total area change at pressures below 20 mN/m. However, above 20 mN/m, the monolayer with the peptide starts compacting faster showing two compaction rates. A shallow-slope "*slow expulsion*" with an area change of 0.26 nm^2 is observed at pressures between 25-37 mN/m. At 37mN/m the WT-harboring monolayer undergoes a sharp transition reflecting a massive displacement/expulsion of the peptide. The slope corresponds to a particle with a cross-sectional area a = 3.3 nm^2. The two mutants with normal activity (K8E and K28E) also show relatively large changes in cross-sectional area. In contrast, no sharp transitions were observed in compromised K15E or K25E, but near the πB, particles were effectively displaced with the slopes corresponding to smaller characteristic areas between 0.87 and 1.5 nm^2, respectively. Figure 11 D shows that the K25E mutant is apparently not completely expelled as it shallowly approaches the control curve.

Peptide aggregation: Peptide aggregation is suggested by the CD results and aggregation can reduce the effective concentration (activity) of the peptide in experiments (Lee *et al.*, 2014). It can also modify the partitioning of the peptide with the membrane. The aggregation properties were investigated using DLS and native gel electrophoresis. DLS data was taken at a 30 µM. The volume placed in the cuvette was 1.0 mL. All mutants were tested independently three times. All peptides showed aggregate particle sizes represented by single peaks of 50-400 nm in size (Fig. 12), corresponding to aggregation numbers between 1.6×10^4 for K8E and 1.4×10^7 for the most compromised K15E mutant (assuming that molecular volume of GsMTx4 is ~6.7 nm^3/monomer.). Only WT and K22E produced smaller peaks of larger particles near 700 nm, whereas K15E particles showed their main peak near 570 nm. It is obvious that inactive mutants form larger aggregates at 30 µM, where most of the peptide might be sequestered. We should note that the monomer-aggregate equilibrium is concentration-dependent and the sensitivities to aggregate sizes was low at 3 µM. To increase the intensity of scattered light we used about an order of magnitude higher concentration than in the electrophysiological experiments.

To determine the concentration dependence of aggregation size at lower concentrations, we ran WT, K15E, and K28E at 1, 3, and 10 µM on non-denaturing gels using migration rate to estimate particle sizes. SDS denatured samples of 10 µM WT and mutant peptides dissociated into the 4096 Da monomeric form and all material ran with G250 dye in the loading buffer. However, under non-denaturing conditions we observed similar results to the DLS experiments, where larger aggregates (slowly migrating) were present for the mutants compared to WT (Fig. 13). The aggregate size was concentration dependent with no visible aggregates detected at 1 µM (40 ng of peptide), and only weakly retarded species at 3 µM. Significantly larger aggregates were observed at 10 µM. Due to the non-denaturing conditions we were unable to determine the aggregate sizes, but clearly some aggregation is occurring at lower concentrations and users should e mindful of this property.

Discussion

A model for GsMTx4 tension-area clamping and the role of lysines: Our previous model of GsMTx4 inhibition of MSCs (Suchyna *et al.*, 2004) suggested that association of the peptide with the bilayer changed local curvature and stress near the channel in such a way as to translate the gating curve to higher tension. MD studies predict that GsMTx4 and other ICK peptides will produce local membrane perturbations such as changes in thickness and curvature (Nishizawa & Nishizawa, 2007; Nishizawa, 2011; Chen & Chung, 2013). However, our previous model did not take into account the predicted shallow and deeper binding modes, nor dynamic changes in peptide position with changing stress. These, and other properties of GsMTx4 and the lysine mutants are revealed in a blind MD companion study (Nishizawa *et al.*, 2015) supporting our new model.

The findings in this study, in combination with MD simulations suggest a new model for GsMTx4 inhibition, where GsMTx4 occupies a shallow binding site at low tension and a deeper binding location at higher tension (Fig. 14). Unlike other ICK peptides, GsMTx4 is more stable in the shallow, surface absorbed, mode (Nishizawa, 2011; Chen & Chung, 2013; Nishizawa *et al.*, 2015) where it acts as an area clamp by penetrating more deeper during stretching. Charge mutations that shift the equilibrium toward longer lived and/or more frequent excursions to deeper binding reduce the area clamping property and efficacy.

Lysines are key amino acids in the stabilization of proteins at the membrane interface (Killian & von Heijne, 2000; Caputo & London, 2003a). The six lysines on GsMTx4 are distinctive since they cover most of the hydrophilic surface and are likely to stabilize the shallow position. Lysines comprise 18% of the peptide so we suspected that single mutations would produce relatively modest changes in efficacy and that in general proved true. The differential effects among the mutants were not due to specific interactions with the channel since the peptide was equally efficacious in the D and L forms (Suchyna *et al.*, 2004). An important observation was that the calculated K_Ds based on the ratio of the association/dissociation rates did not correlate with the degree of inhibition. This suggests that the observed rates include multiple processes, perhaps the equilibrium between the shallow and deeper modes.

Lys8, and Lys28 interactions with the head groups of the inner monolayer are predicted to promote penetration to deeper binding states (Nishizawa & Nishizawa, 2007) (Fig. 14). Since K8E and

K28E showed no loss of activity suggests that the deeper modes do not contribute to MSC inhibition, and may in fact suppress occupancy of deeper states. The other four lysines are predicted to stabilize the shallow binding mode, and mutating these did reduce inhibition. The NMR structure of GsMTx4 shows K15 and K25 on the same side of the peptide as K8 and K28 (Oswald *et al.*, 2002). Simulations suggest that K15 and K25, which showed the most compromised inhibitory function, counteract deeper penetration of K8 and K28 by stabilizing the interactions with the outer leaflet (Nishizawa *et al.*, 2015).

Lysines mutants only weakly affect binding energy. Our model suggests that GsMTx4 partitioning into membranes is considered a key to its inhibitory activity, however the energy of binding was largely unaffected by the mutations. The *effective charge sensitivity* (Z_{eff}) for GsMTx4 and other peptides can be estimated from the slope of ΔG vs. surface potential (Posokhov *et al.*, 2007b). This serves as a useful measure of how much charge affects binding. GsMTx4 was unusual in that, despite having a relatively high net positive charge compared to other ICK peptides, it had a low Z_{eff} in zwitterionic POPC or anionic POPG:POPC (Posokhov *et al.*, 2007b). The weak contribution of charge to binding suggests that association may be driven by the positive entropic energy of desolvation as seen with Cyclosporin D (Schote *et al.*, 2002) or by dissociation of aggregates (*see below*). This suggests that the negative free energy from desolvating the hydrophobic face is relatively large compared to electrostatic repulsion from the methylamines of POPC.

Trp fluorescent quenching and ITC agreed on the level of binding energies showing ΔG for all peptides between 27-34 kJ/mol in POPG:POPC. The only outlier was the most compromised mutant, K15E, which had a binding constant of 40 kJ/mol using ITC. In the companion MD study (Nishizawa *et al.*, 2015), the predicted binding energies for all peptides to POPC membranes (18-27 kJ/mol) were in good agreement with the experimental values measured by Trp quenching (25-26 kJ/mol). This study also predicted K15E (27 kJ/mol) to have higher binding energies to POPC than WT (23 kJ/mol), and the lower binding energy of K28E (19 kJ/mol) correlates with the higher dissociation constant observed in the inhibition data. The higher affinity of K15E likely increases its area contribution at the resting membrane tension, but decreases the "area reservoir" during stretch.

GsMTx4 partitioning depth and tilt. Simulations suggest GsMTx4 is particularly stable at the shallow binding position when compared to Hanatoxin1 (Nishizawa & Nishizawa, 2006) and HpTx2 (Chen & Chung, 2013). If the binding depth is key to the inhibition, mutations that promote deeper associations are predicted to reduce efficacy. Quenching studies comparing aqueous and membrane resident quenchers showed that quenching of the WT Trp residues was only mildly attenuated in both POPC and POPG-POPC vesicles compared to free peptide suggesting that they reside near the interface. The quenching constants for the mutants all showed greater penetration depths that were comparable to depths observed for Trp residues in synthetic α-helices 10 residues (15 Å) from the bilayer center (Caputo & London, 2003b). However, even K28E which had WT levels of activity showed deeper penetration suggesting that this is not the only factor affecting efficacy. Bromine quenching also showed that the Trp residues of both WT and mutant peptides were shallow (<6 Å from interface), though the Gaussian fits to the data suggest only slightly deeper binding depth for the two mutants tested. However, the lack of shallower quenchers made the measurement a poor predictor of changes at shallow depths.

The tilt of the peptides with respect to the plane of the bilayer surface and binding depth in the shallow bound mode could significantly affect the surface area occupied by the peptide in resting membranes. While the binding energies were similar, the I_{max} values of Trp quenching, which represent the level of Trp protection, varied significantly. I_{max} is affected by the environment of the Trps, so that deeper penetration would tend to increase fluorescence and cause the blue shift that we observed for all mutants. The compromised mutants showed the highest equilibrium I_{max} values in both types of vesicles, while the mutants exhibiting WT efficacy had values closer to that of WT. An increase in peptide penetration depth and tilt that increased Trp depth of penetration, was also predicted by our companion MD studies. Most of the compromised mutants (K15E, K20E and K22E) tended to increase Trp depth, while mutants with WT activity (K8E and K28E) tended to tilt toward the outer monolayer. The increased depth in the shallow mode may promote the tendency for these peptides to transiently occupy deeper binding states (Nishizawa & Nishizawa, 2007; Chen & Chung, 2013) and are predicted to be stabilized by the interaction of Trp 6, Lys 8 and Lys 28 with the inner monolayer (Fig. 14).

The pressure/area isotherms suggest the existence of different binding states. Compared to other ICK peptides, MDS studies suggest GsMTx4 has a stronger tendency to occupy a superficial interface position with outer monolayer rather than the deeper binding states (Nishizawa, 2011). Absorption to the surface and subsequent penetration to a deeper state has been seen for antimicrobial, viral, and signaling peptide binding (Wieprecht *et al.*, 2002), though the tension dependence of this property has never been tested. Interestingly, the ITC isotherms suggest the presence of at least two binding sites for all peptides. The first constant likely represents the binding energy ΔG of monomers and/or multimers, while the second higher affinity site may represent a more deeply bound state, or the energy for dissolution of aggregates.

Tension dependent insertion. In the Langmuir experiments, the peptides showed strong interfacial partitioning as expected for amphipaths. They exhibited a decrease in compressibility above 20 mN/m. Between 25-37 mN/m, the WT transitions to a shallow compression slope corresponding to an area change of 0.22 nm^2 reflecting compaction of the peptides among the lipids by changes in tilt or depth. Upon reducing the surface area further, there was a shallow increase in pressure up to the rupture point. This strongly contrasts with the exponential increase in pressure in control monolayers. The massive expulsion of peptide at compressions approaching the monolayer-bilayer equivalence pressure (πB ~37-40 mN/m) creates the tension clamp. The steep slope transition in the WT compression curve predicts displacement or expulsion of the peptide that occupies an effective area of 3.3 nm^2. The structure of GsMTx4 (Oswald *et al.*, 2002) predicts that the maximal area that can be taken by the peptide in the plane of the membrane is ~4 nm^2 (Fig. 14). If the peptide occupies 3.3 nm^2 of surface area at pressures just below the πB, the hydrophobic face would be predicted to penetrate the interface ~1.5 nm. Applied tension will lower the lateral pressure in the membrane and lead to increased insertion of peptide and reduced local tension. This was supported by the companion MD study which showed that increasing membrane surface tension (60 to 75 mN/m) induced the WT peptide to penetrate deeper by ~1Å (Nishizawa *et al.*, 2015).

All mutant peptides have modified isotherms of pressure vs area compared to WT. The two most compromised mutants, K15E and K25E, have significantly lower compressibility near πB. If compressibility is related to peptide occupancy in the shallow mode, then peptides that transition

to the deeper mode will have reduce capacity to buffer area changes. We suspect that the depth increase of 1-2 Å would only slightly increase the likelihood of entering the deep binding mode. However, in the case of the two unaffected mutants, K8E and K28E, the MD simulations predict these mutations would be deficient in their ability to stabilize the deeper binding mode (Nishizawa *et al.*, 2015). It is reasonable to assume that stretch will promote transitions to the deeper states.

In the Langmuir studies the calculated cross-sectional areas may represent the expulsion of peptides from multiple states and even peptides leaving the membrane with lipids attached (expulsion accompanied with monolayer collapse). For instance, from the pressure midpoint of the last transition (π = 40 mN/m) for WT, we estimate the energy of insertion, ΔG = area × π = -79 kJ/mol which translates into a very high affinity of $K_D = 6.9 \bullet 10^{13}$ M^{-1}. Thus, the estimated insertion energy must be steeply dependent on the peptide-displaced lipid area. If we reduce the area by half (a = 1.65 nm^2), then the insertion energy drops to ΔG = -39 kJ/mol, giving $K_D = 8 \bullet 10^6$ M^{-1}, which is much closer to the measured affinities. From this calculation we might infer that the peptides are expelled as dimers (*see below*) or with clusters of lipids. If the process of expulsion is concomitant with collapse, then the peptide may induce non-lamellar structures that are in equilibrium with the lamellar part, precisely at πB. This would create another type of peptide/lipid material reservoir that could 'clamp' tension in the monolayer.

Aggregation may affect membrane binding kinetics. The tendency of the peptides to aggregate can lower the free concentration of peptide available for binding and may include multimers in the bound state. In our companion MD study we observed that a second free peptide in solution near a bilayer that has a bound peptide, had a greater tendency to bind to the bound peptide rather than the membrane (Nishizawa *et al.*, 2015). After binding the pair was then stable over 300 ns with one peptide inserted in the bilayer and the second peptide riding on top. This tendency to dimerize increased for the mutant peptides suggesting aggregation was promoted by the KtoE mutations which would fit with the lowering of net charge. When these bound dimers were subjected to bilayer stretching, the membrane bound peptide penetrated deeper, but additionally the top peptide rapidly inserted into the adjacent bilayer. These two mechanisms occurring simultaneously to clamp surface area might explain the Hill coefficient of 1.5 in the inhibition concentration dependence curve.

We observed that the size of the aggregates was concentration dependent, but it was difficult to assess the amount and size of aggregates at low concentrations (1-5 μM) using DLS where GsMTx4 is most effective. On native gels with lower peptide concentrations, two highly aggregated mutants in the DLS experiments (K15E and K28E) created slower migrating species compared to WT at 3 μM, suggesting aggregation may play a role even at lower concentrations. The aggregated states can explain the 228 nm peak in the CD spectra that disappears upon equilibration with POPG:POPC vesicles. A recent paper on MSCs in cartilage cells, showing that Piezo1 inhibition required 40 μM GsMTx4! This appears surprising but it may reflect peptide uptake by various proteins and lipids in the preparation (Lee *et al.*, 2014).

Conclusions

Bilayer stretching does work on MSCs favoring states with larger in-plane areas (Sachs & Morris, 1998; Sukharev & Anishkin, 2004; Sukharev & Sachs, 2012). The fundamental difference between channels activated by tension and channels modulated by tension, such as voltage and ligand gated channels (Morris, 2011), lies in the significantly larger increase of in-plane area of MSCs during opening (Bae *et al.*, 2013). In our new model (Fig. 14), the peptide is envisioned as providing a tension dependent equilibrium between a surface absorbed state and a deeply adsorbed state. At resting tension, the surface absorbed state occupies less area. As tension increases, GsMTx4 slips in deeper, increasing the monolayer area and acting as a force clamp. The high content of lysine plays an important role in stabilizing the surface absorbed state. Deeper penetration reduces the amount of material extruded and reduces the tension buffering capacity. The energy of the electrostatic interactions appears similar to hydrophobic binding energy as occurs for other ICK peptides. Membrane tension increases the free volume of the membrane so that peptide partitioning and the tension activating the channels (Bae *et al.*, 2011) overlap and the details of GsMTx4 reaction kinetics probably involves both processes.

Competing Interests:

The authors claim no competing interests in the development of these studies nor the conclusions drawn from these findings.

Author Contributions

Radhakrishnan Gnanasambandan – Electrophysiological recordings of Piezo1 channels, testing sensitivity to GsMTx4 and mutant peptides, native gel electrophoresis of peptide aggregation, data analysis and manuscript editing.

Chiranjib Ghatak – Tryptophan quenching and vesicle protection experiments, binding affinity determination, depth of penetratin, CD spectrum of native structures, and editing of manuscript.

Anthony Yasmann – Langmuir Blodgett monolayers, tension dependent peptide depth measurements, isothermal calorimetry, dynamic light scattering assessment of aggregation, data analysis and manuscript editing.

Frederick Sachs – Conception and design of the experiments, interpretation of data, critically revising manuscript.

Alexey S. Ladokhin – Conception and design of the experiments, analysis and interpretation of data, drafting the manuscript and critically revising.

Sergei I. Sukharev – Conception and design of the experiments, analysis and interpretation of data, drafting the manuscript and critically revising.

Thomas M. Suchyna – Conception and design of the experiments, analysis and interpretation of data, drafting the manuscript and critically revising.

Funding

This work was funded by a DoD grant, project # DM102091, and NIH HL054887 to Dr. Frederick Sachs, an NIH RO1 GM069783 grant to Dr. Alexey Ladokhin, and NIH R01 GM107652 grant to Dr. Sergei Sukharev.

References

Bae C, Gottlieb PA & Sachs F. (2013). Human PIEZO1: removing inactivation. *Biophys J* 105, 880-886.

Bae C, Sachs F & Gottlieb PA. (2011). The mechanosensitive ion channel Piezo1 is inhibited by the peptide GsMTx4. *Biochemistry* 50, 6295-6300.

Bemporad D, Sands ZA, Wee CL, Grottesi A & Sansom MS. (2006). Vstx1, a modifier of Kv channel gating, localizes to the interfacial region of lipid bilayers. *Biochemistry* 45, 11844-11855.

Bosmans F & Swartz KJ. (2010). Targeting voltage sensors in sodium channels with spider toxins. *Trends Pharmacol Sci* 31, 175-182.

Bowman CL, Gottlieb PA, Suchyna TM, Murphy YK & Sachs F. (2007). Mechanosensitive ion channels and the peptide inhibitor GsMTx-4: history, properties, mechanisms and pharmacology. *Toxicon* 49, 249-270.

Caputo GA & London E. (2003a). Cumulative effects of amino acid substitutions and hydrophobic mismatch upon the transmembrane stability and conformation of hydrophobic alpha-helices. *Biochemistry* 42, 3275-3285.

Caputo GA & London E. (2003b). Using a novel dual fluorescence quenching assay for measurement of tryptophan depth within lipid bilayers to determine hydrophobic alpha-helix locations within membranes. *Biochemistry* 42, 3265-3274.

Catterall WA. (2012). Voltage-gated sodium channels at 60: structure, function and pathophysiology. *J Physiol* 590, 2577-2589.

Chen R & Chung SH. (2013). Effect of gating modifier toxins on membrane thickness: implications for toxin effect on gramicidin and mechanosensitive channels. *Toxins* 5, 456-471.

Craik DJ, Daly NL & Waine C. (2001). The cystine knot motif in toxins and implications for drug design. *Toxicon* 39, 43-60.

Dahim M, Mizuno NK, Li X-M, Momsen WE, Momsen MM & Brockman HL. (2002). Physical and photophysical characterization of a BODIPY phosphatidylcholine as a membrane probe. *Biophysical journal* 83, 1511-1524.

Jung HH, Jung HJ, Milescu M, Lee CW, Lee S, Lee JY, Eu YJ, Kim HH, Swartz KJ & Kim JI. (2010). Structure and orientation of a voltage-sensor toxin in lipid membranes. *Biophys J* 99, 638-646.

Jung HJ, Lee JY, Kim SH, Eu YJ, Shin SY, Milescu M, Swartz KJ & Kim JI. (2005). Solution structure and lipid membrane partitioning of VSTx1, an inhibitor of the KvAP potassium channel. *Biochemistry* 44, 6015-6023.

Killian JA & von Heijne G. (2000). How proteins adapt to a membrane-water interface. *Trends Biochem Sci* 25, 429-434.

Kučerka N, Tristram-Nagle S & Nagle JF. (2006). Structure of fully hydrated fluid phase lipid bilayers with monounsaturated chains. *The Journal of membrane biology* 208, 193-202.

Kyrychenko A & Ladokhin AS. (2014). Refining membrane penetration by a combination of steady-state and time-resolved depth-dependent fluorescence quenching. *Analytical biochemistry* 446, 19-21.

Ladokhin AS. (1997). [22] Distribution analysis of depth-dependent fluorescence quenching in membranes: A practical guide. *Methods in enzymology* 278, 462-473.

Ladokhin AS. (1999a). Analysis of protein and peptide penetration into membranes by depth-dependent fluorescence quenching: theoretical considerations. *Biophysical journal* 76, 946-955.

Ladokhin AS. (1999b). Evaluation of lipid exposure of tryptophan residues in membrane peptides and proteins. *Anal Biochem* 276, 65-71.

Ladokhin AS. (2014). Measuring membrane penetration with depth-dependent fluorescence quenching: distribution analysis is coming of age. *Biochim Biophys Acta* 1838, 2289-2295.

Ladokhin AS, Jayasinghe S & White SH. (2000). How to measure and analyze tryptophan fluorescence in membranes properly, and why bother? *Anal Biochem* 285, 235-245.

Lee HC, Wang JM & Swartz KJ. (2003). Interaction between extracellular Hanatoxin and the resting conformation of the voltage-sensor paddle in Kv channels. *Neuron* 40, 527-536.

Lee SY & MacKinnon R. (2004). A membrane-access mechanism of ion channel inhibition by voltage sensor toxins from spider venom. *Nature* 430, 232-235.

Lee W, Leddy HA, Chen Y, Lee SH, Zelenski NA, McNulty AL, Wu J, Beicker KN, Coles J & Zauscher S. (2014). Synergy between Piezo1 and Piezo2 channels confers high-strain mechanosensitivity to articular cartilage. *Proceedings of the National Academy of Sciences* 111, E5114-E5122.

Marsh D. (2006). Comment on interpretation of mechanochemical properties of lipid bilayer vesicles from the equation of state or pressure-area measurement of the monolayer at the air-water or oil-water interface. *Langmuir* 22, 2916-2919.

Morris C. (2011). Why are so many ion channels mechanosensitive. *Cell physiology source book, 4th ed Amsterdam: Elsevier*, 493-505.

Nishizawa K. (2011). Atomistic Molecular Simulation of Gating Modifier Venom Peptides - Two Binding Modes and Effects of Lipid Structure. In *Mechanosensitivity and Mechanotransduction*, ed. Kamkin A & Kiseleva I, pp. 167-190. Springer, Tokyo, Japan.

Nishizawa K, Nishizawa M, Gnanasambandam R, Sachs F, ladokhin AS, Sukharev S & Suchyna TM. (2015). Effects of Lys to Glu mutations in GsMTx4 on membrane binding, peptide orientation, and self-association propensity, as analyzed by molecular dynamics simulations. *Submitted*.

Nishizawa M & Nishizawa K. (2006). Interaction between K+ channel gate modifier hanatoxin and lipid bilayer membranes analyzed by molecular dynamics simulation. *European Biophysics Journal* 35, 373-381.

Nishizawa M & Nishizawa K. (2007). Molecular dynamics simulations of a stretch-activated channel inhibitor GsMTx4 with lipid membranes: two binding modes and effects of lipid structure. *Biophys J* 92, 4233-4243.

Norton RS & Pallaghy PK. (1998). The cystine knot structure of ion channel toxins and related polypeptides. *Toxicon* 36, 1573-1583.

Ostrow KL, Mammoser A, Suchyna T, Sachs F, Oswald R, Kubo S, Chino N & Gottlieb PA. (2003). cDNA sequence and in vitro folding of GsMTx4, a specific peptide inhibitor of mechanosensitive channels. *Toxicon* 42, 263-274.

Oswald RE, Suchyna T, McFeeters R, Gottlieb P & Sachs F. (2002). Solution Structure of Peptide Toxins that Block Mechanosensitive Ion Channels. *Journal of Biological Chemistry* 277, 34443-34450.

Posokhov YO, Gottlieb PA & Ladokhin AS. (2007a). Quenching-enhanced fluorescence titration protocol for accurate determination of free energy of membrane binding. *Anal Biochem* 362, 290-292.

Posokhov YO, Gottlieb PA, Morales MJ, Sachs F & Ladokhin AS. (2007b). Is lipid bilayer binding a common property of inhibitor cysteine knot ion-channel blockers? *Biophys J* 93, L20-22.

Sachs F. (2010). Stretch-activated ion channels: what are they? *Physiology (Bethesda)* 25, 50-56.

Sachs F & Morris CE. (1998). Mechanosensitive ion channels in non-specialized cells. In *Reviews of Physiology and Biochemistry and Pharmacology*, ed. Blaustein MP, Greger R, Grunicke H, Jahn R, Mendell LM, Miyajima A, Pette D, Schultz G & Schweiger M, pp. 1-78. Springer, Berlin.

Schote U, Ganz P, Fahr A & Seelig J. (2002). Interactions of cyclosporines with lipid membranes as studied by solid-state nuclear magnetic resonance spectroscopy and high-sensitivity titration calorimetry. *Journal of pharmaceutical sciences* 91, 856-867.

Smaby JM, Momsen MM, Brockman HL & Brown RE. (1997). Phosphatidylcholine acyl unsaturation modulates the decrease in interfacial elasticity induced by cholesterol. *Biophysical journal* 73, 1492-1505.

Suchyna TM, Johnson JH, Clemo HF, Huang ZH, Gage DA, Baumgarten CM & Sachs F. (2000). Identification of a peptide toxin from Grammostola spatulata spider venom that blocks stretch activated channels. *Journal of General Physiology* 115, 583-598.

Suchyna TM, Tape SE, Koeppe RE, Andersen OS, Sachs F & Gottlieb PA. (2004). Bilayer-dependent inhibition of mechanosensitive channels by neuroactive peptide enantiomers. *Nature* 430, 235-240.

Sukharev S & Anishkin A. (2004). Mechanosensitive channels: what can we learn from 'simple' model systems? *Trends Neurosci* 27, 345-351.

Sukharev S & Sachs F. (2012). Molecular force transduction by ion channels: diversity and unifying principles. *J Cell Sci* 125, 3075-3083.

Wang JM, Roh SH, Kim S, Lee CW, Kim JI & Swartz KJ. (2004). Molecular surface of tarantula toxins interacting with voltage sensors in K(v) channels. *J Gen Physiol* 123, 455-467.

Wee CL, Bemporad D, Sands ZA, Gavaghan D & Sansom MS. (2007). SGTx1, a Kv channel gating-modifier toxin, binds to the interfacial region of lipid bilayers. *Biophys J* 92, L07-09.

Wee CL, Gavaghan D & Sansom MS. (2008). Lipid bilayer deformation and the free energy of interaction of a Kv channel gating-modifier toxin. *Biophys J* 95, 3816-3826.

Wee CL, Gavaghan D & Sansom MS. (2010a). Interactions between a voltage sensor and a toxin via multiscale simulations. *Biophys J* 98, 1558-1565.

Wee CL, Ulmschneider MB & Sansom MSP. (2010b). Membrane/Toxin Interaction Energetics via Serial Multiscale Molecular Dynamics Simulations. *J Chem Theory Comput* 6, 966-976.

Wieprecht T, Beyermann M & Seelig J. (2002). Thermodynamics of the coil-alpha-helix transition of amphipathic peptides in a membrane environment: the role of vesicle curvature. *Biophys Chem* 96, 191-201.

Figure Legends

Figure 1. (A) CD spectrum from WT and KtoE mutants (2 μM) shows a distinct negative peak at 228 nm for all mutants compared to WT. Other regions of the spectrum are similar to WT. (B) CD spectra before and after binding to negatively charged POPG-POPC lipid vesicles. When bound, the 228 nm peak disappears and the spectrum more closely resembles that of the WT.

Figure 2. (A) Shows typical averaged currents in outside-out patches before, during and after application of 5 μM WT GsMTx4. (B) Shows the association (k_a) and dissociation (k_d) rate constants for WT calculated from exponential fits to the data (red curves). (C) Shows k_a and k_d for all peptides (calculated from the fits in Supporting Figure S1). Control WT GsMTx4 constants shown in black. The bottom chart shows the calculated equilibrium constants (K_D).

Figure 3. The mean reduction of Piezo 1 currents by the different peptides. The average currents from the 500 ms steps before peptide application were set to 100% to normalize the inhibition from different patches. The percent values represent the amount of current reduction at steady state. Asterisks represent significantly different means at $\alpha = 0.05$.

Figure 4. Concentration dependence of inhibition by WT GsMTx4. Each point represents the average Piezo1 current from 7-12 patches in the presence of the indicated GsMTx4 concentration. Red curve shows the Hill equation fit to the data.

Figure 5. Changes in Trp intensity measured upon titration with LUV in the presence of aqueous KI can be used to determine bilayer partitioning properties. As the LUV concentration increases, peptide association with the membrane increases leading to protection of Trp quenching by aqueous iodine. Significantly higher concentrations of zwitterionic POPC LUV (**A**) are required to titrate the KI quenching compared to anionic POPG-POPC LUVs (**B**), and maximum protection levels for POPG:POPC were greater. ΔG was calculated from single exponential fits to the titration data showing that the free energy of partitioning for all mutants were similar to WT GsMTx4 for both LUV compositions. However, the I_{max} values differed significantly.

Figure 6. Titration isotherms for WT and 4 KtoE mutants with different inhibitory capacity suggesting a variety of binding sites on vesicles. All titrations were done at 30°C with unilamellar POPG:POPC liposomes in the same buffer as the monolayer and spectroscopic experiments. The

peptide at 20-30 μM was present in the chamber and liposomes (0.5-1 mM of lipid) were injected (20 μl per step) from a syringe at 300 s intervals. The K2 constants suggest the inactive mutants bind with slightly higher affinities.

Figure 7. Acrylamide versus 10-DN quenching (K_{SV}) was used to compare penetration depth of WT and three different KtoE mutants. (A) Shows the ratio of the initial fluorescent intensity to the quenched intensity (I_o/I) for WT GsMTx4, and K8E, K25E, and K28E mutants vs the concentration of Acrylamide (λ_{ex} = 295 nm). Spectra for these peptides in the presence of either 100% POPC (B) or 75%POPG:25%POPC (C) are corrected for the inner filter effect determined in buffer alone. The quenching is linearly related to the quenching agent concentration. The color coded KSV values in buffer and in the presence of the different types of LUVs is shown above the quenching data. The I_o/I for WT and mutant peptides vs the concentration of the bilayer resident 10-DN quenching agent (λ_{ex} = 280 nm) is shown for POPC (D) and POPG/POPC (E) vesicles. At these concentrations quenching is linearly related to the concentration**.**

Figure 8. Depth-dependent fluorescence quenching profiles obtained for WT, K25E, and K28E GsMTx4 in bromolipid containing vesicles. Three bromo PC lipids (brominated at position 6-7, 9-10 and 11-12) were incorporated into LUVs. The quench ratio for the three peptides was plotted with respect to the bromolipid present for both 100BrPC (A) and 50POPG:50BrPC (B). Data were fitted with a Gaussian function (σ was fixed at 5.0). In the presence of 100BrPC LUV, the Gaussian parameters were: h_m = 16.0 ± 2.1 Å, s = 1.0 ± 0.1 for WT-GsMTx4, h_m = 15.2 ± 0.4 Å, s = 0.9 ± 0.1 for K25E and h_m = 14.6 ± 0.9 Å, s = 0.9 ± 0.2 for K28E. In the presence of 50POPG:50BrPC LUV: h_m = 14.0 ± 0.7 Å, s = 0.6± 0.1 for WT-GsMTx4, h_m = 12.4 ± 0.1 Å, s = 0.6 ± 0.1 for K25E and h_m = 12.7 ± 0.5 Å, s = 0.7 ± 0.1 for K28E. (h_m indicates the most probable location of the probe (here tryptophan) and s is proportional to quenchibility).

Figure 9. Pressure-area isotherms taken with different concentrations of WT GsMTx4 in the subphase. Qualitatively similar interactions of WT GsMTx4 with POPG-POPC monolayers at different concentrations are illustrated by compression isotherms. Visible monolayer 'swelling' is observed at subphase peptide concentrations of 0.1 μM and above. The peptide tightly binds to the expanded monolayer. There is no obvious effect of gradual 'squeezing-out' of the peptide from the monolayer at higher pressures. The monolayer instead has a tendency to collapse earlier

(arrows) as the peptide concentration increases and pressure approaches 37-40 mN/m. In the control, the monolayer collapses at 43-45 mN/m.

Figure 10. Compression and compression modulus isotherms of POPG-POPC monolayers in the presence of 1 μM WT with active K8E (A) and K28E (D), and partially active K15E (B) and K25E (C) peptides. The control monolayers, only lipids, compress smoothly (red curve) with no phase transition. The monolayer collapses near 45 mN/m. At the πB (traditionally taken as 35 mN/m according to (Marsh, 2006)) the molecular area per lipid is approximately 72 $Å^2$. Below the compression isotherms are plots of the inverse compressibility modulus (Cs^{-1}) calculated from: $Cs^{-1} = A\cdot(d\pi / dA)$. The Cs^{-1} plots for these peptides all exhibit low values near the πB (or ~72 $Å^2$/molecule) compared to the control monolayer. In the area marked by the asterisk, the isotherms for the less active peptides (K15E and K25E) are elevated higher above the control monolayer curves than K8E and K28E. Elevation above the WT curves shows greater stability at the πB and at the normal collapse pressures. Instead of a low plateau (green curves) an additional peak in Cs^{-1} is present indicating higher stiffness of the monolayer.

Figure 11. Plots of the area vs pressure (top panels) between the control and peptide curves for WT (A), normal activity mutants K8E (B) and K28E (E), and the two least active mutants K15E (C) and K25E (D). These plots illustrate partitioning of peptides into the monolayer in the expanded state (low pressures) and expulsion back to the subphase at higher pressures. The WT isotherm intersects with the control monolayer near the πB, while the least active mutant isotherms approach the control near the πB but never intersect. Conversion to the logarithm of the area vs pressure (bottom panels) provides a clearer representation of the transitions during compression. If we assume that the change of the log-area with increasing pressure represents either the displacement of the peptide to a shallower state or complete expulsion of the peptide to the subphase, the slope of the film compaction can be used to calculate the peptide contribution to cross-sectional area prior to the transition. The active peptides (A, B and E) are displaced by lateral pressure from positions with effective molecular areas of 3.3, 2.5 and 2.0 nm^2, whereas the transitions in inactive peptides (C and D) are shallower and show smaller molecular area changes.

Figure 12. The distributions of particle size measured by Dynamic Light Scattering in solutions of WT GsMTx4 and four mutants at 30 μM. The distributions show the KtoE mutations produce

different aggregation sizes for the peptides in aqueous solution. The least active peptide K15E shows the largest aggregates, while WT and the uncompromised K8E show the smallest aggregation sizes.

Figure 13. GsMTx4 WT and either K15E (A) or K28E (B) mutants run by nondenaturing PAGE suggesting peptide aggregation at higher concentrations. Three concentrations for each peptide show that aggregate size increases with concentration, and that the aggregate sizes are larger for the mutants than WT (red brackets). However, at 1 μM there is little evidence of aggregation. This is not due to sensitivity since we are able to detect <10 ng of protein with G250 dye (1 μM = 40 ng of protein in 10 μl).

Figure 14. Model for GsMTx4 tension clamping. MD simulations predict shallow and deeper binding states for ICK peptides. For GsMTx4 Trp6, Lys 8, and Lys 28 are predicted to promote deeper binding by forming interactions with the lipid head groups of the inner leaflet while other lysines maintain association with the outer leaflet (Nishizawa & Nishizawa, 2007). The shallow mode is depicted as superficial association where the penetration depth is tension sensitive with its surface area contribution increasing with stretch. One property expected to reduce inhibitory activity is increased occupancy of the deeper binding states which may be promoted by specific lysine mutants. Residues are colored as: basic residues (blue), acidic residues (red), hydrophobic residues (green), polar residues (blue/red/gray), Tryptophan (cyan), cysteine (yellow), backbone (white).

Figure 1

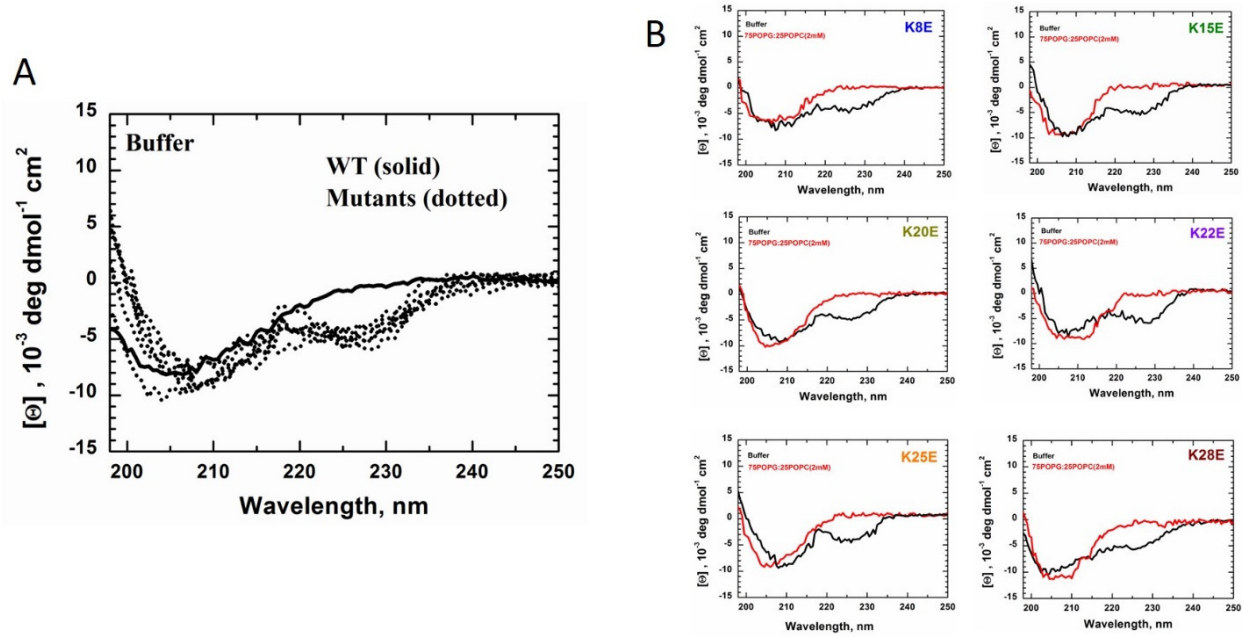

Figure 2.

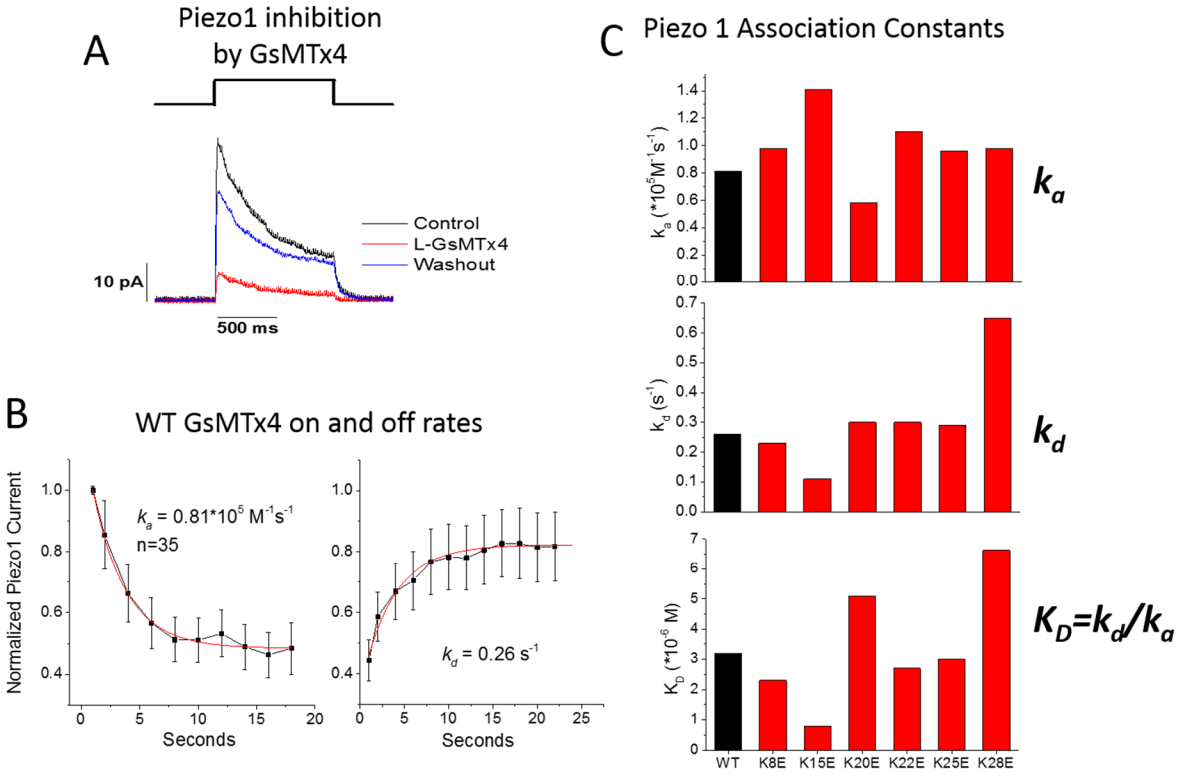

Figure 3.

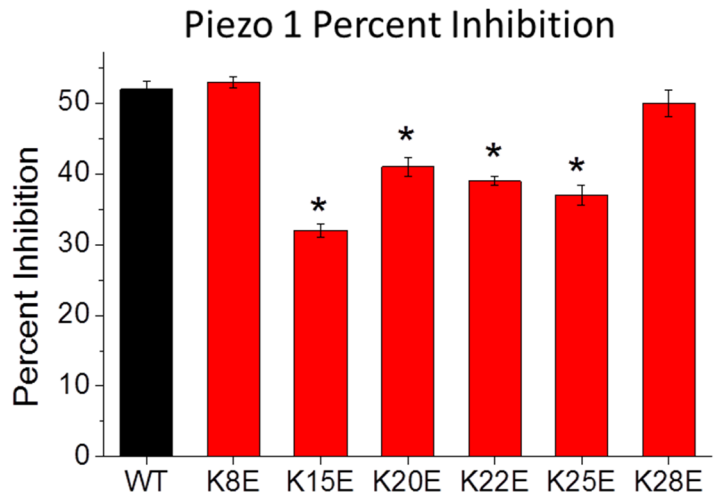

Figure 4.

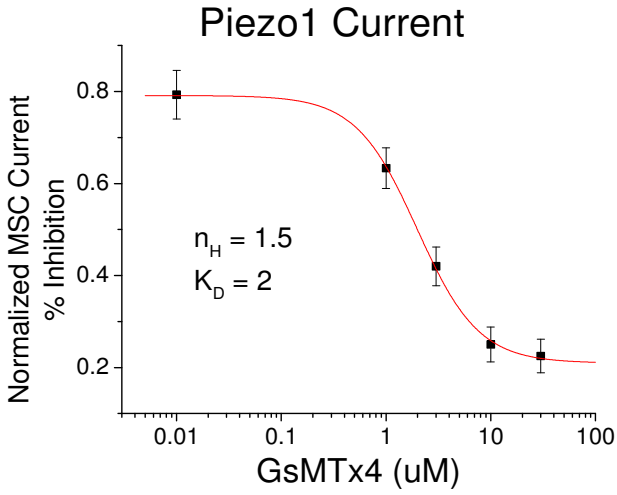

Figure 5.

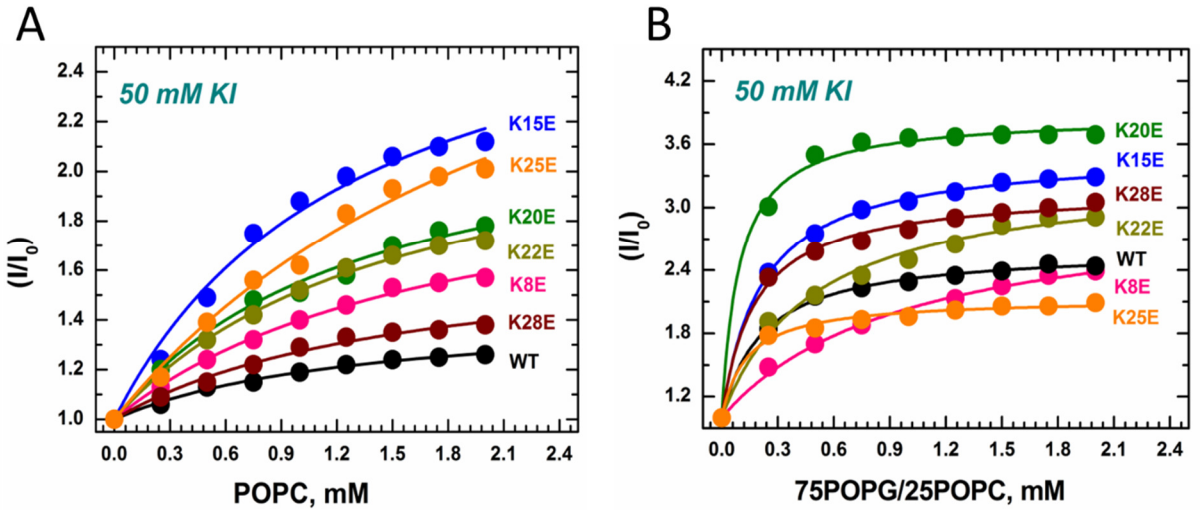
A
50 mM KI
K15E
K25E
K20E
K22E
K8E
K28E
WT
(I/I0)
POPC, mM
B
50 mM KI
K20E
K15E
K28E
K22E
WT
K8E
K25E
(I/I0)
75POPG/25POPC, mM

Figure 6.

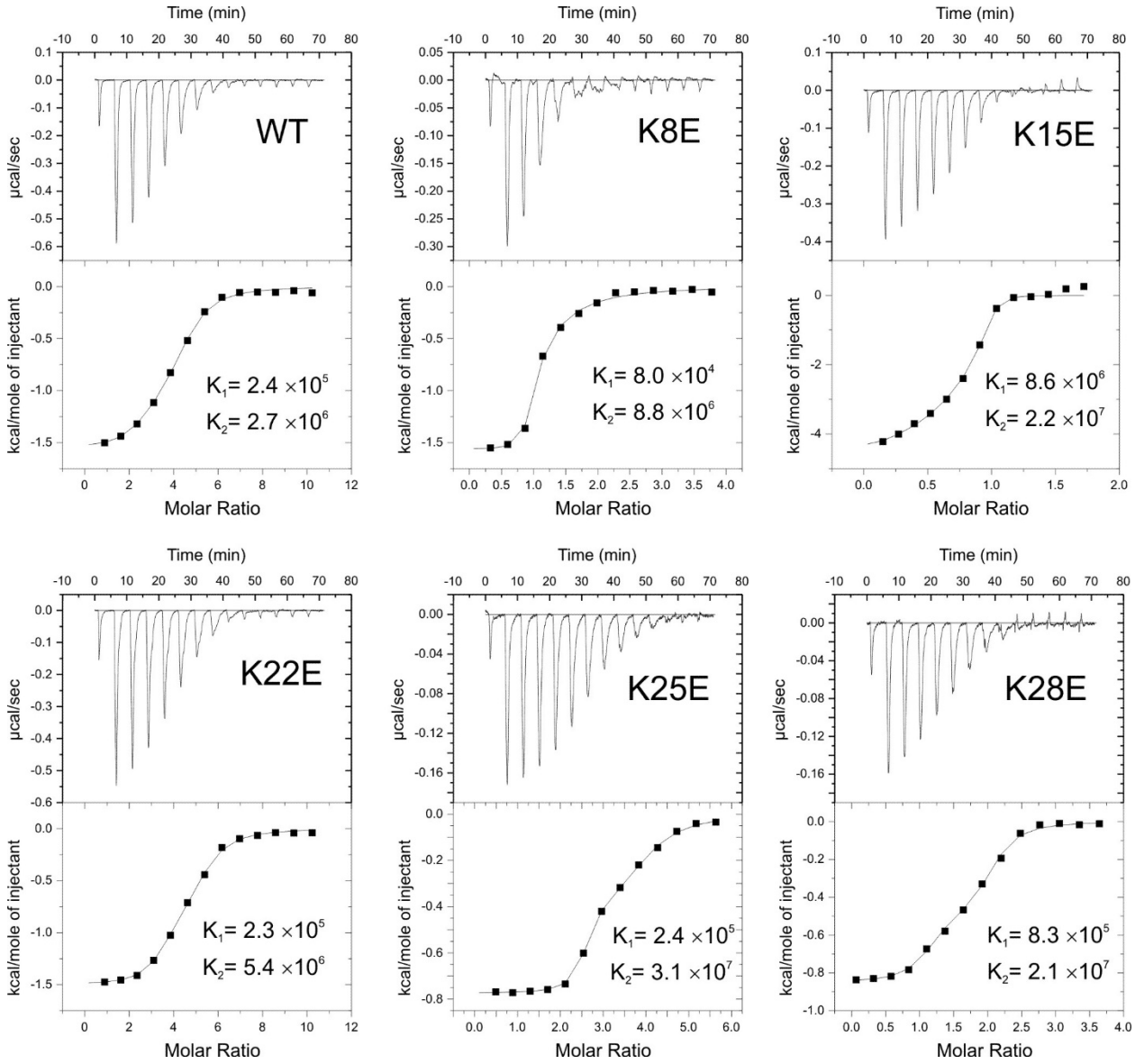
Time (min)
µcal/sec
kcal/mole of injectant
Molar Ratio
WT
K_1= 2.4 ×10^5
K_2= 2.7 ×10^6
K8E
K_1= 8.0 ×10^4
K_2= 8.8 ×10^6
K15E
K_1= 8.6 ×10^6
K_2= 2.2 ×10^7
K22E
K_1= 2.3 ×10^5
K_2= 5.4 ×10^6
K25E
K_1= 2.4 ×10^5
K_2= 3.1 ×10^7
K28E
K_1= 8.3 ×10^5
K_2= 2.1 ×10^7

Figure 7.

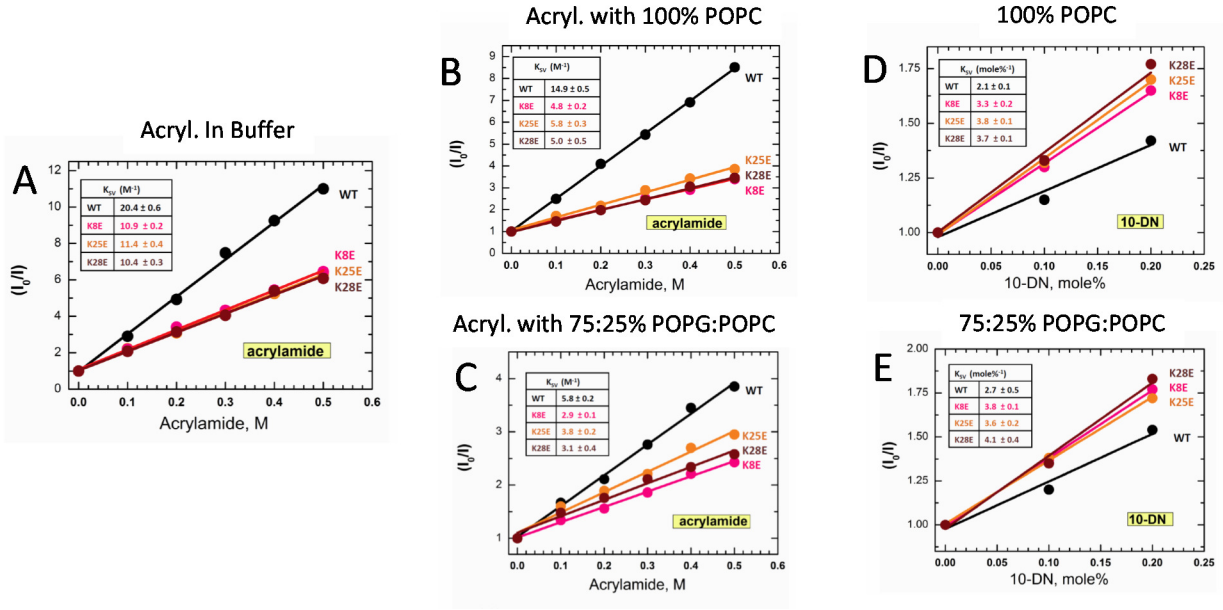

Figure 8.

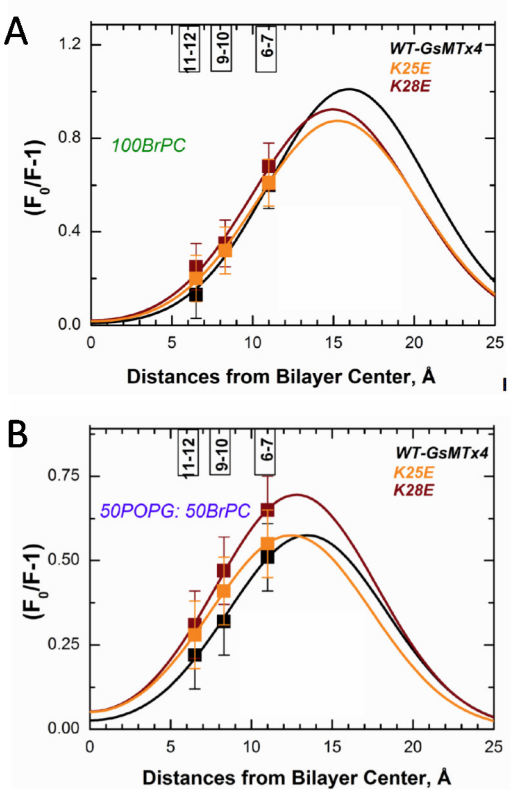

Figure 9.

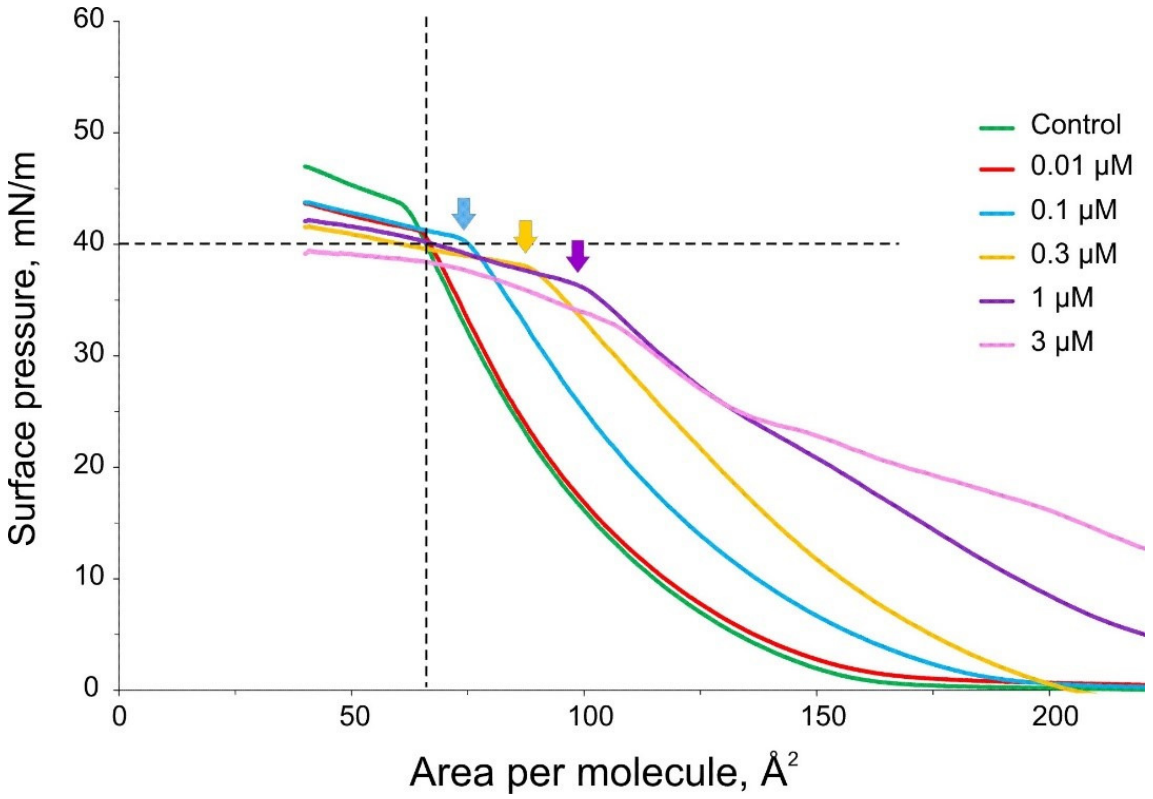

Figure 10

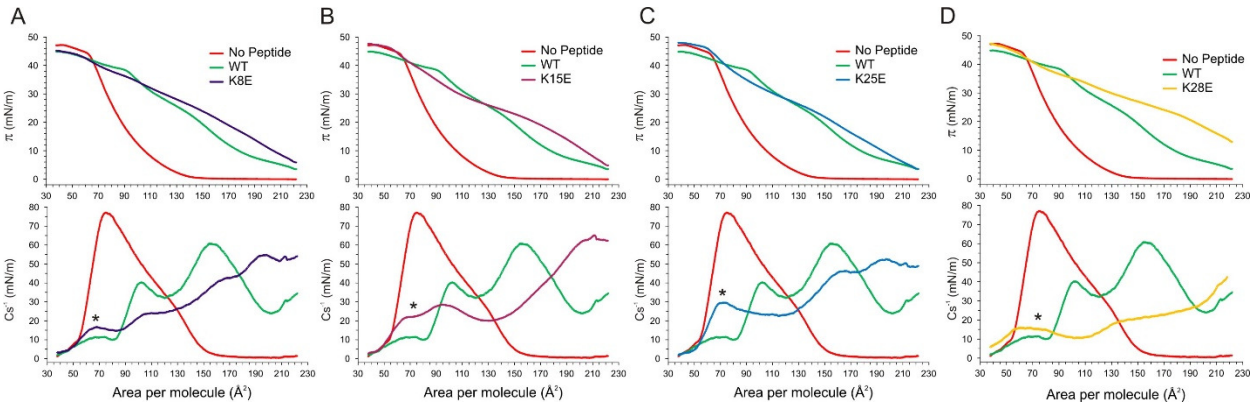

Figure 11.

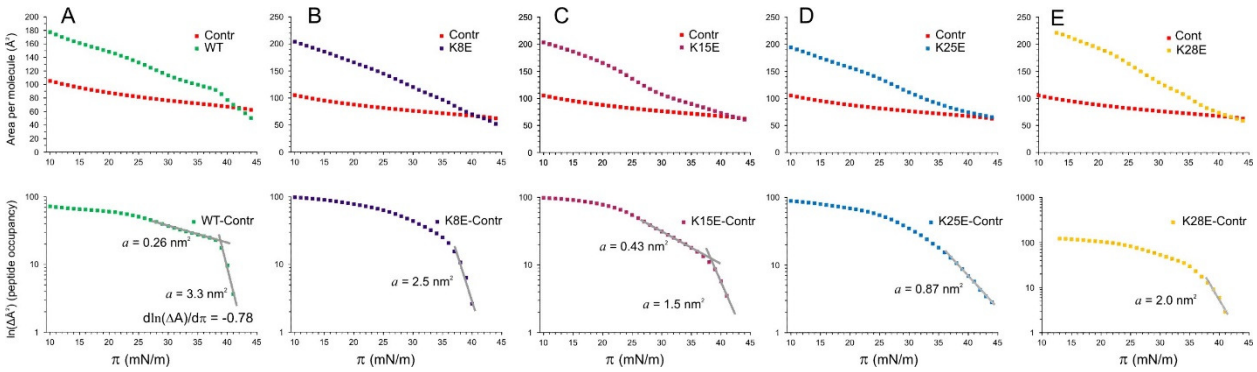

Figure 12.

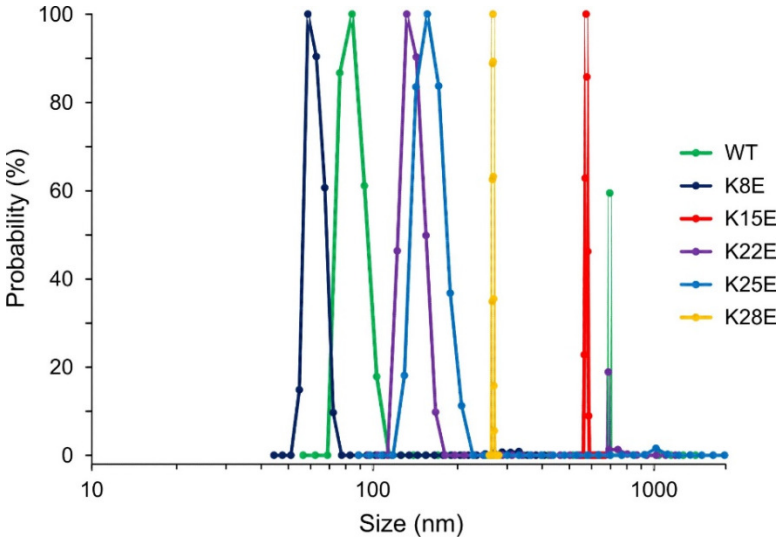

Figure 13.

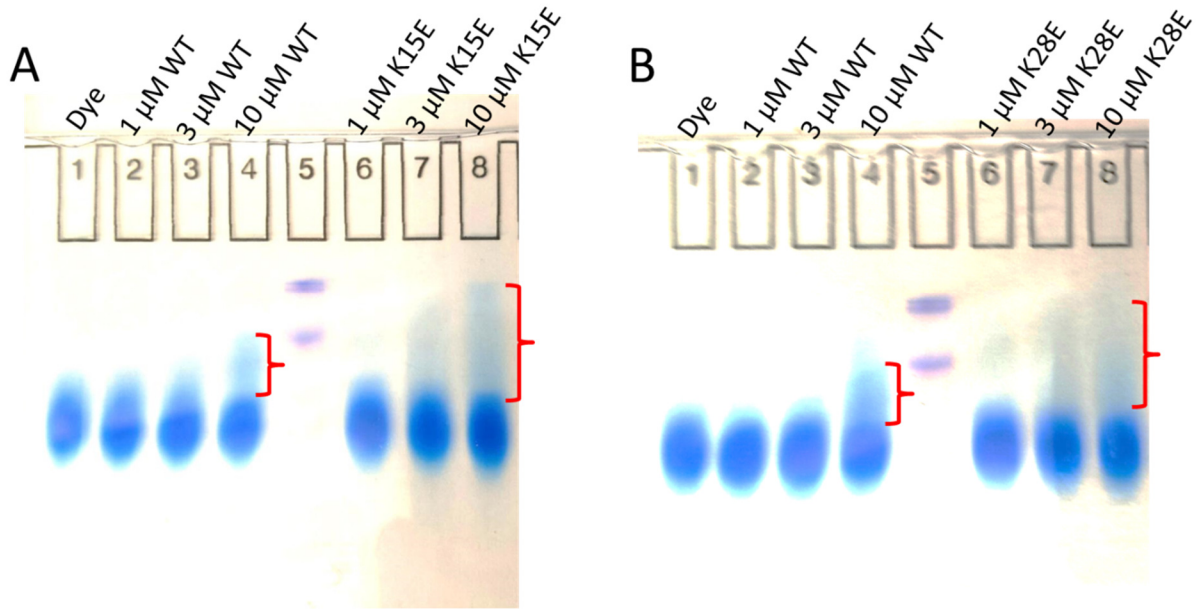

Figure 14.

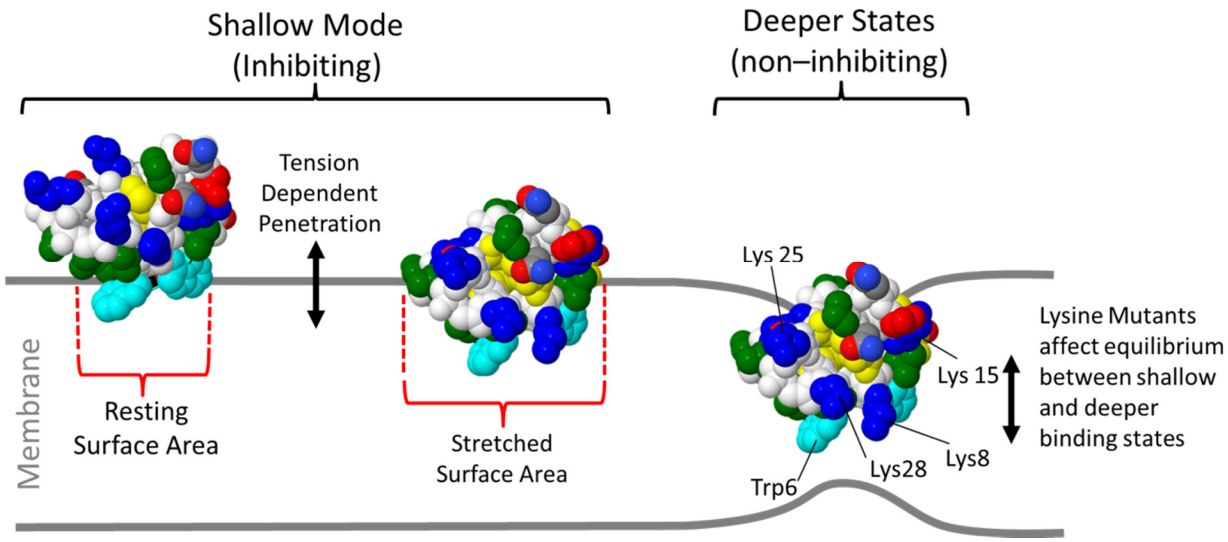

Appendix B

Effects of Lys to Glu mutations in GsMTx4 on membrane binding, peptide orientation, and self-association propensity, as analyzed by molecular dynamics simulations

Kazuhisa Nishizawa[1*†], Manami Nishizawa[1], Radhakrishnan Gnanasambandam[2†], Frederick Sachs[2], Alexey S. Ladokhin[3†], Sergei I. Sukharev[4†], and Thomas M. Suchyna[2†]

1) Teikyo University School of Medical Technology, Tokyo, Japan
2) Department of Physiology and Biophysics, State University of New York at Buffalo, Buffalo. NY
3) Department of Biochemistry and Molecular Biology, The University of Kansas, Lawrence, KS
4) Department of Biology, University of Maryland, College Park, MD

*Corresponding author,
† Co-Principal Investigators

Abstract

GsMTx4, a gating modifier peptide acting on cationic mechanosensitive channels, has a high positive charge (+5 *e*) due to six Lys residues. The peptide does not have a stereospecific binding site on the channel but acts from the boundary lipids within a Debye length of the pore probably by changing local stress. To gain insight into how these Lys residues interact with membranes, we performed molecular dynamics simulations of Lys to Glu (KtoE) mutants in parallel with our experimental work. *In silico*, K15E had higher affinity for 1-palmitoyl-2-oleoyl-glycero-3-phosphocholine (POPC) bilayers than wild-type (WT) peptide or any other mutant tested, and showed deeper penetration than WT, a finding consistent with the experimental data. Experimentally, the inhibitory activities of K15E and K25E were most compromised, whereas K8E and K28E inhibitory activities remained similar to WT peptide. Binding of WT in a shallow (interfacial) mode did not influence membrane thickness. With interfacial binding, the direction of the dipole moments of K15E

and K25E were predicted to differ from the WT, whereas the dipole moments of K8E and K28E oriented similarly to that of the WT. These results support a model in which binding of K15E to the membrane acts like an immersible wedge that serves as a membrane expansion buffer reducing local stress and thus inhibiting channel activity. The simulations showed that membrane-bound WT peptide attracted other WT peptides to form aggregates at the bilayer surface. This may account for the positive cooperativity observed in the ion channel experiments. The Lys residues seem to fine-tune the depth of membrane binding, the tilt angle, and the dipole moments.

Introduction

GsMTx4 is a 34-residue peptide isolated from tarantula (*Grammostola spatulata)* venom and acts as a gating inhibitor on mechanosensitive channels (MSCs) that are activated by membrane tension [1 Suchyna 2000, 2 Sachs 2010]. Although the molecular structure of eukaryotic MSCs is still underway, GsMTx4 has been shown to be a specific modulator with high specificity toward cationic MSCs like Piezo1 [6 Bae2011]. It may also have activity against TRPC5 [4 Gomis] and TRPC6 [5 Spassova] cation channels, but has no activity against the K-selective 2-P domain TREK-1 MSCs [6 Bae2011]. At low concentrations (10^{-7}-10^{-6} M), GsMTx4 inhibit cationic MSCs although it has shown some potentiation of the prokaryotic MSCs at higher concnetrations. GsMTx4 belongs to the inhibitory cysteine knot (ICK) family [7 Swartz 2007, 8 Gao] of venom peptides, and like other ICK peptides, it has a hydrophobic protrusion that is thought to facilitate bilayer penetration. While other ICK peptides interact stereospecifically with their targets, GsMTx4 is active in the L and D enantiomers [9 Suchyna 2004] and hence inhibits gating by shifting the gating curves to higher tension.

GsMTx4 has been subjected to several computational analyses [10 Nishzawa 2007, 11 Chen-Chung], but the interactions with membranes remain poorly understood. We expected that peptide binding would produce local deformation and local changes in membrane thickness and curvature [9 Suchyna 2004, 11 Chen-Chung], but these effects have not been systematically evaluated. One notable feature of GsMTx4 is that it has high net positive charge (+5 *e*). When the peptide is viewed from the side of the hydrophobic protrusion, six Lys residues and one Arg residue form a ring-like structure encircling the periphery (Figure 1). Our previous simulations suggested that GsMTx4 could interact with the lipid bilayer through a shallow (interfacial) binding mode and a deeper mode [10 Nishizawa 2007] wherein some Lys residues interacted with lipid head groups of the inner monolayer while the remaining Lys interacted with head groups of the outer monolayer. At low concentrations GsMTx4 inhibits bacterial channels MscS and MscL, but at higher concentrations there may be potentiation which might reflect a concentration-dependent transition from shallow to deep binding mode [12 Kamaraju, 13 Hurst].

To better understand the role of the positively charged residues, we mutated each Lys to Glu (KtoE: K8E, K15E, K20E, K22E, K25E, and K28E) and we examined the effect on channels and the physical chemistry of the peptide lipid interactions; these results are reported in another paper [14 Gnanasambandam et al., submitted]. Briefly, the six mutants

inhibited MSCs to variable degrees, but the bilayer affinities did not correlate with inhibition. For example, K15E had the most compromised inhibitory activity relative to WT, but had higher affinity for membranes. We also observed that, in general, all peptides reside at a shallow, apparently surface absorbed, position in membranes at resting tension occupying only a small surface area. The depth and surface area occupied by the peptides increases as the membrane tension increases so that the peptides act as "area clamps". The tension dependent penetration was the strongest predictor of inhibitory activity. The deeper penetration of the mutants at resting tensions would compromise their capacity to buffer changes in membrane free volume as tension changes during stretch.

To try and gain detailed insight into the interaction of GsMTx4 with the bilayer, we undertook a blinded simulation study of what the KtoE mutations would do to the bilayer. The simulations were done only knowing the mutations, but not the experimental results. Here, we discuss the blinded computational analyses in light of the experimental work {Gnanasambandam, 2015 #9031} [14 Gnanasanmbansdan]. The experiments also served as a test of the predictive power of the combined atomistic (AT) and coarse-grained (CG) molecular dynamics (MD) simulations.

In brief, we found that the most compromised mutant, K15E, bound more tightly to a POPC bilayer in the AT and CG simulations relative to the WT and the other mutants. Perturbation of membrane structure induced by WT binding in the shallow binding mode was not as intense as previously reported. Peptide penetration depth showed that mutants with compromised activity tended to penetrate deeper at resting membrane tension, consistent with experimental results. WT peptide penetrated deeper upon increasing membrane tension (increasing free volume) which was predicted by the experimental displacement of the peptide under changing monolayer compression. The dipole moments of compromised mutants tended to show greater directional differences with respect to the plane of the bilayer which may have greater significance in charged bilayers composed of POPG. The tendency to aggregate and the tension-dependent changes in binding were also consistent with experimental results. We conclude that the Lys residues are particularly important in controlling peptide tilt angle, penetration depth, and in defining the equilibrium between the shallow and deep binding modes.

Computational details

To ensure an unbiased study, the authors were blinded with respect to the outcome

of experiments when they performed computational analyses. GROMACS 4.5.4 [15 Hess et al. 2008] was used for simulations and data analysis. Graphical representations were created using Visual Molecular Dynamics [16 Humphery et al. 1996]. All the simulations in this study are described in Table 1. The size of the simulation box is represented by the x, y, and z-dimensions, and in simulations containing a bilayer, the z-axis was defined as the bilayer normal. We refer to the z-coordinate of an atom as the 'z-position' of the atom. The distance between two atoms projected onto the z-axis is referred to as the 'z-distance.' The GsMTx4 structural model contained 34 residues, including G47 to F80 of UniProt ID: Q7YT39 [17 The consortium; 18 Oswald].

Coarse-grained simulations

For coarse-grained (CG) simulations, we used the MARTINI force field (version 2.0) [19 Marrink et al. 2007]. CG POPC was modeled as done previously [20 Nishizawa 2013], and water was represented using the Yesylevskyy model [21 Yesylevskyy 2010]. For the peptides, atomistic models derived from structures produced in our previous work [10 Nishizawa 2007] were coarse-grained with Martinize (version 2.3) using the default topological parameters. As recommended by the developers [19 Marrink et al. 2007], elastic bonds with force constants of 500 kJ/nm^2/mol were applied to all those pairs of the backbone beads which were located within 0.7 nm. The Lennard-Jones interactions were shifted smoothly to zero between 0.9 and 1.2 nm, and the electrostatic interactions were smoothly shifted to zero between 0 and 1.2 nm. The relative dielectric constant was set to 2.5. The non-bonded neighbor list was updated every 10 steps. The integration time step was 20 fs, but for monolayer simulations (see below), we used 10 fs. The pressure was semi-isotropically coupled using the Berendsen algorithm at 1 bar with τ_P = 1 ps and compressibility at 3×10^{-4} bar^{-1}. The temperature was controlled at 320K with a constant τ_T of 1 ps. For this study, CG simulation time is presented after multiplication by a factor of four [19 Marrink et al. 2007]. POPC bond lengths were restrained using LINCS [22 Hess et al. 1997]. The protonation states of titratable side chains of amino acids were the same as for the AT simulations. The backbone of the N-terminal Gly was represented by a Qd bead and was assigned +1 charge. The backbone of the C-terminal amino acid was represented by an uncharged P5 bead.

Atomistic simulations

For the atomistic (AT) simulations, the united-atom Berger force field for lipids [23 Berger], in combination with an adapted Optimized Potentials for Liquid Simulations all-atom (OPLS-AA) force field [24 Neale] were used along with the simple-point charge (SPC) water model [25 Berendsen 1981]. The bond lengths for water and lipids were restrained using SETTLE and LINCS, respectively [26 Miyamoto; 22 Hess 1997]. The Particle-Mesh Ewald (PME) algorithm [27 Darden] was used with a real-space cutoff of 1.4 nm and a maximal grid size of 0.125 nm. Berendsen coupling was used to regulate the temperature [28 Berendsen 1984]. Other parameters were set as described previously [29 Nishizawa 2014]. The N-terminus was protonated and the C-terminus was capped with a carboxamide group. All titratable amino acid side chains were assumed to be in their ionized forms, because they were all solvent-exposed, and Glu residues introduced in place of Lys were predicted to have pKa values between 4.3 and 5.3, based on H++ calculations [30 Gordon]. Furthermore, our CG analyses suggested that membrane binding energy changed only slightly (0.5−8.0 kJ/mol) with changes in protonation state for all mutants tested, which would be insufficient energy to change the protonation state upon membrane binding [31 Sandberg].

Free energy for binding of peptides to membrane

The profiles of the potential of mean force (PMF) for peptide binding to the membrane were derived using a system containing a peptide and the POPC bilayer (Table 1). For both CG PMF and AT PMF analyses, z-position (i.e., the position along the membrane normal) of the center of mass (COM) of the peptide was restrained using the constraint mode of GROMACS; we measured the vertical mean force needed to impose this constraint. For CG PMF analysis, the target z-position from the bilayer midplane was varied from 2.2 to 5.4 nm in 0.2 nm intervals. For the CG PMF simulations, we performed a 200 ns equilibration run followed by a 800 ns production run for each z-position. For the AT PMF analysis, the z-positions were varied from 1.6 to 3.8 nm, in 0.2 nm intervals, plus an additional run at 1.5 nm. Two independent 300 ns production runs following a 100 ns equilibration run were performed for each z-position. Note that the thickness of the POPC bilayer is different between the CG and AT systems; the mean z-position of the PO_4 atoms of the CG bilayer was 2.1 nm whereas that of the phosphorus atoms of the AT bilayer was 1.85 nm above the bilayer center. For CG PMFs, the PMF curves were vertically shifted so that the 5.2−5.4 nm range, where the vertical mean force was negligible, was defined as zero. Binding free energy

was calculated using a method similar to the one used by Neale et al. [24 Neale 2011]. Briefly, the Boltzmann factor was integrated and the ratio of the integrals was calculated using the following equation:

$$\exp[-\beta\Delta G^{bind}] = \int_{min\_memb}^{max\_memb} \exp[-\beta G^{PMF}(z)]dz \; \} / \{ \int_{min\_water}^{max\_water} \exp[-\beta G^{PMF}(z)]dz \; \}$$

where ΔG^{bind} is the standard free energy of peptide binding to the bilayer, $G^{PMF}(z)$ is the PMF value at the given z, and β is $(RT)^{-1}$, where R is the gas constant and T is the temperature. For the CG PMFs, the min_memb and max_memb parameters were set to 0 and 4.0 nm, respectively, whereas min_water and max_water were set to 4.0 and 8.0 nm, respectively. Due to computational limitations, the PMF for 5.4−8.0 nm in the water layer, and for 0−1.4 nm in the membrane, were assumed to be zero. The z-range corresponding to the opposing monolayer was excluded from the calculation, as we regarded peptide residence at the upper (outer) lipid-water interface or within the upper monolayer as the only membrane-bound state relevant to this analysis. While this assumption appears drastic, the Boltzmann factor for the deep part of the membrane is very small; for example, a layer with zero PMF value has no more than 10^{-3}-fold of the Boltzmann factor for a layer with -25 kJ/mol. However, the width of the water layer affects ΔG^{bind}; a change in width from 3 to 4 nm leads to a $RT\ln(4/3)$ difference in ΔG^{bind}. As reported previously, the choice of the boundary height also has a non-negligible effect on ΔG^{bind} [24 Neale].

CG PMF of peptide dimerization in water

The CG PMF analysis for peptide aggregation and dimerization was carried out as described in Table 1. The inter-peptide distance (the distance between COMs) was used to define the reaction coordinate. The constraint mode in GROMACS was used to restrain distances, and the mean force between the COMs was monitored. The inter-peptide distance was varied from 1.4 to 2.8 nm, in 0.2 nm intervals, and the trapezoidal integration was performed to derive the PMF curves.

1-to-1 free runs

In 1-to-1 free runs, CG simulations were configured such that one peptide was introduced in a membrane-bound position (referred to as the pre-bound peptide), and a second peptide was introduced in bulk water (Table 1). Simulations were run free of restraints.

To prepare the initial system, the second peptide (WT or K28E) was placed at varying positions in the xy-plane located 4 nm above the bilayer midplane, and the overlapping water molecules were removed. The pre-bound peptide resided at about ~2.35 nm from the midplane of the CG POPC bilayer. We performed a 10-ns preparative run in which the position of each of the peptides was harmonically restrained, followed by 1μs of unrestrained production run.

CG model-based Langmuir-type simulations, with a configuration of vacuum/POPC monolayer/water (henceforth, 'monolayer simulations') were carried out and analyzed as described previously [32 Lopez; 33 Duncan]. Briefly, the surface tension was calculated using the formula $\gamma_s = h_z \{P_{zz} - (1/2)(P_{xx} + P_{yy})\}$, where h_z is the z-component of the box size and P_{zz} and $(1/2)(P_{xx} + P_{yy})$ are the pressures normal to the monolayer and tangential to the monolayer, respectively. For all monolayer simulations, surface tension coupling was used.

CG monolayer simulation systems contained a monolayer of 128 POPC molecules placed in the xy plane, 6435 water molecules [21 Yesylevskyy], chloride ions, and GsMTx4 in a box with a fixed z-component of 20 nm. For monolayer simulations, PMF was analyzed as above, but to reduce error due to the flexibility of the monolayer, we used the cylinder mode (radius of 1 nm), in which the COM of the lipids located within the cylinder was used for the calculation of monolayer-peptide distance.

Other analyses

The dipole moments for WT and mutant GsMTx4s were calculated using the g_dipole module of GROMACS using coordinates sampled from trajectories for either in-water or interfacial binding mode simulations. Ten structures each for the in-water and membrane-bound states were randomly sampled from trajectories. After aligning each set of structures, the dipole moment vectors were calculated and averaged.

Results

Compromised activity mutant K15E strongly binds to the POPC bilayer

To gain insight into the dynamics of WT and mutant peptide binding, we carried out CG and AT MD simulations (Table 1). To estimate the binding energy between the peptide and the surface of a POPC bilayer, we carried out potential of mean force (PMF) analyses using the distance (z) from the peptide center of mass (COM) to the bilayer center as the

reaction coordinate (CG-pmf series of Table 1). We calculated the depth of the PMF profile and the integrated binding energy ΔG^{bind} (Table 2, Figure 2). K15E interacted with the membrane with higher affinity than WT, and K25E and K28E interacted with lower affinity than WT. For all peptides, ΔG^{bind} fell within the range of 18-27 kJ/mol. These results are consistent with binding energies determined by fluorescence quenching in the physical experiments [Tables 1 of 14 Gnanasambandam].

Due to computational limitations, the AT simulation-based PMF analysis was performed only for the WT peptide, K28E, and K15E, and for z between 1.6 and 3.8 nm. For WT peptide, the CG and AT PMFs yielded similar PMF depths, which were also consistent with the results of the CHARMM36-based analysis by Chen and Chung, who reported a PMF depth of 26 *kT* [11 Chen-Chung]. Binding strengths for these peptides were also consistent with our AT and CG analyses, suggesting that these force fields are reliable, at least for this application. Overall, *in silico* binding energies were consistent with those in the experiment [14 Gnanasambandam]. In particular, the simulations correctly predicted the strongest binding of K15E (inhibition kinetics and ITC energies) and the weaker binding of K28E (inhibition kinetics). Hereafter, we will refer to the binding position of peptides (the depth in the membrane) in the unrestrained WT peptide and POPC bilayer runs, as the 'normal' binding position.

Peptide penetration depth

To examine membrane penetration depth and properties of the local bilayer in atomistic detail, we performed unrestrained atomistic simulations of membrane-bound peptide in a POPC bilayer system (60/64-WT etc., of Table 1; Figure 1, *left*). The distance of the peptide COM from the bilayer center differed among WT and mutant peptides; this measurement fluctuated greatly, producing large standard deviations (0.14-0.24 nm) suggesting the peptides position in the shallow mode may be available to transition to deeper modes during membrane stress (Table 3). Nonetheless, K15E, K20E, and K22E, all of which displayed compromised inhibitory activities [14 Gnanasambandam], exhibited relatively deep membrane penetration, while peptides that showed WT levels of inhibition (K8E and K28E) showed similar penetration depths to WT. K25E was an outlier in that, while showing compromised activity, it showed penetration depths similar to WT.

Quenching of Trp fluorescence by aqueous, and membrane, resident quenching agents is sensitive to the depth of the residues in the membrane. Gnanasambandam et.al.

measured the quenching of the two adjacent Trp residues (Trp6 and Trp7) in GsMTx4 WT and KtoE mutants, and found that, in general the Trp residues on KtoE mutants bound deeper, though the sensitivity of the measurements did not allow precise positioning [14 Gnanasambandam, Fig.s 7 & 8]. We determined the Trp COM in these simulations (i.e., the COM of the atoms belonging to Trp6 or Trp7), and found that, consistent with the fluorescence data, the Trp residues of compromised mutants (K15E, K20E, and K22E) showed deeper penetration than WT, and mutants with WT activity (K8E and K28E) had depths similar to WT (Table 3). As above, the compromised K25E mutant did not follow this pattern exhibiting Trp depths similar to WT. Also, K28E showed deeper binding depth in the fluorescence quenching experiments. These differences in the COM depth (either whole peptide or Trp residues) at resting tension is only one factor contributing to the inhibition mechanism.

Assuming the analysis of the tilt angle was statistically reliable (see below), we calculated the z-position of the Trp COM relative to the peptide COM (Trp-Pep z-distance) (the rightmost column of Table 3). Intriguingly, K8E showed a relatively short Trp-Pep z-distance (Table 3) with a large standard deviation (SD). This short Trp-Pep z-distance may be associated with the side of the peptide containing Trp6 and Trp7 tilting away from the membrane (see the next section). The large SD indicates large motions of the Trp residues relative to the peptide COM. In contrast, K15E and K25E, which have most compromised inhibitory activities, have Trp residues that are deeply buried in the membrane with relatively small SD. Given their small SD and the deep penetration of the Trps, we expect that K15E and K25E are stably oriented in the membrane, with the hydrophobic protrusion firmly sticking into the hydrophobic core (Table 3). The implication is that the Trp residues of K15E and K25E may be better engaged by lipids than those of the other mutants, an idea that is consistent with the fluorescence quenching data for K15E and K25E [Table 1 in 14 Gnanasambandam].

K to E mutations alter tilt orientation of GsMTx4 in the membrane-bound state

The tilt angle of the peptides was analyzed for the free simulations (AT 60/64 series of Table 1). The tilt is represented by the z-position of C γ (the carbon atom two bonds away from the Cα) of each amino acid residue relative to that of the peptide COM. Despite large fluctuations in the penetration depth, the tilt angle of the peptides exhibited an unexpectedly consistent trend (Table S1 of Supplementary Material). All KtoE mutations caused the

mutated side of the peptide to tilt away from the membrane, in a seesaw-like manner. Figure 3 summarizes the results of Table S1. For example, in the K8E simulation (AT 60/64-K8E), the z-position of C γ of the eighth (mutated) residue relative to the peptide COM was 2.25 Å shallower in the membrane than the corresponding value for WT peptide (in bold in Table S1), whereas the similarly analyzed z-positions of the residues on the opposite side (K22 and K25) were ~5 Å deeper in the membrane compared to WT (Table S1 and Figure 3). A similar trend was observed for the CG simulation tilt analysis (data not shown). The other mutant with WT like activity, K28E, also cause K8 to become shallower, which is the closest Lys to the Trp residues and is predicted to interact with lipid headgroups on the opposite leaflet in deeper bound states.

We also analyzed the dipole moments of the WT and mutant peptides. In Figure S1, the moment vector is represented as an arrow originating from the peptide COM. For the structures sampled from in-water simulations, the moment vector generally points from the mutated residue toward the opposite side of the peptide. For the structures sampled from the membrane bound state (shallow binding mode), the moment vectors were quite different among WT and mutant peptides (Figure 5). Intriguingly, K15E and K25E, which had the most compromised functional activity [Figure 3 of 14 Gnanasambandam], produced the greatest angular changes in their dipole moments, while K8E and K28E, whose activities were unaffected, produced the least change in moment vectors. This raises the possibility that the positioning of the charged residues in the membrane, in addition to the direction of the dipole moment vector, play an important role in the inhibitory activity of the peptide.

Binding of GsMTx4 causes a minor change in membrane thickness and undulations

To examine the effect of peptide binding on membrane thickness and dynamics, we analyzed the z-positions of the lipid phosphorus atoms averaged within a small vertical column of membrane for peptide-free (control), WT-bound, and K28E-bound POPC bilayers (Figure 5). There were minimal changes to membrane thickness for the K28E peptide in comparison to WT peptide, however, in comparison to the peptide-free POPC bilayer, a region of higher positioning was observed. For K28E, the upper-monolayer phosphorus heights averaged over nine adjacent 4 $Å^2$ bilayer patches ranged from 1.38 to 2.47 nm, whereas the corresponding values for the control bilayer ranged from 1.76 to 2.01 nm. Thus, K28E binding increased the heterogeneity in membrane thickness for the upper monolayer.

However, the heterogeneity in membrane thickness for the WT peptide-bound bilayer was similar to the peptide-free bilayer (Figure 7). The ratio of the average distance of the phosphorus atoms from the bilayer midline for the upper and lower monolayers, in nm was 1.88/1.88 for the control POPC bilayer, 1.90/1.84 for the WT peptide, and 1.93/1.86 for K28E. Together with the PMF results (Table 2) and discussions of the tension-induced change in binding [Figure 10 of 14 Gnanasambandam], the K28E-induced perturbation of the upper monolayer may explain the lower affinity of K28E for POPC (discussed below). Nonetheless, it is difficult to explain the inhibitory activity of the WT peptide and K28E against MSCs based solely on these small effects on the upper monolayer undulation or on membrane thickness. It is also difficult to imagine that the time-averaged thicknesses presented in Figure 7 would be a major determinant of inhibitory impact on channel conductance given the vertical fluctuations in peptide position, as well as the normal peristaltic and undulatory fluctuations of the lipid bilayer [e.g., 34 Tarazona]. Rather, pronounced membrane thinning induced by multiple peptides binding to the bilayer is more likely to have an impact on the peptide activity, as discussed below.

Propensity to form multimers/aggregates in water and on the membrane

Dynamic light scattering and nondenaturing electrophoresis suggested that GsMTx4 had a propensity to form large aggregates [Figure 13 in 14 Gnanasambandam]. In addition, an extra peak at 228 nm in the mutants' CD spectra suggested peptide aggregation in solution and when weakly bound to membranes [Figure 1 and S1 in 14 Gnanasambandam]. Aggregate size was concentration dependent and most mutants showed a greater tendency to form larger aggregates than WT. Dimer and/or multimer formations may affect peptide structure and possibly explain the 228 nm peak observed in the CD spectra for the aqueous and weakly bound mutant peptides to POPC vesicles. The 228 nm peak disappears when bound more strongly to negatively charged vesicles of POPG:POPC [Figure 1 in 14 Gnanasambandam] which may force the formation of bound monomers, though this was not tested here. Multimers of these peptides may also affect Trp quenching in solution and in superficially membrane bound states.

Here we assessed the tendency for peptides to dimerize using the CG simulation system ('in-water' series of Table 1). When two WT peptides were placed in water at varying distances from each other, the PMF profile of dimerization suggested that the mean force was attractive for ~1.6−2.6 nm. For WT peptide, the PMF depth was 36.3 kJ/mol (8.7 kcal/mol) at 2.7 nm, while for K28E, the PMF depth was 46.2 kJ/mol (11.0 kcal/mol). Thus, both WT

and K28E peptides had a propensity to self-associate in water, but K28E had a greater propensity, which is consistent with the experimental data [Figure 13 of 14 Gnanasambandam]. In contrast, membrane-bound peptides yielded largely flat PMF attraction profiles for WT and K28E, implying that dimerization was not favorable when these peptides were placed in the interfacial (shallow) binding mode (data not shown).

We then examined whether pre-bound peptides affected the subsequent binding of other peptide molecules from the bulk water. The simulation system contained a WT (or K28E) peptide in the pre-bound position and one additional WT (or K28E) peptide in the bulk water at varied xy-positions (1-to-1 free runs) (Figure 6A). For the WT peptide, a quarter of the 100 trials resulted in the acqueous peptide binding to the pre-bound peptide (Table 4; Figure 6C). For K28E, about half of the 100 runs resulted in peptide-peptide interaction. Once binding occurred (either peptide-peptide or peptide-bilayer), it persisted until the end of the simulation. Binding in cis-configuration (independent binding events of the two peptides to the bilayer) was less frequently observed than peptide-peptide binding. After the peptide-peptide binding event, the second peptide resided at a higher position (~3.5-3.9 nm above the bilayer center) than the normal binding position (~2.35 nm) for both the WT peptide and K28E. In these and other CG simulations, both WT and K28E peptides appeared to exert a trapping effect, in which the pre-bound peptide attracted a peptide from bulk water to the vicinity of the bilayer to form stable aggregates, hindering the second peptide from proceeding to the normal binding position. GsMTx4 shows weak cooperativity [n_H = 1.5, Figure 4 of 14 Gnanasambandam], so that this finding could be relevant to the inhibitory mechanism, but we have not yet explored this idea experimentally.

Impact of applied membrane tension on peptide binding in the shallow binding mode

In the Langmuir experiments [Figure 9-11 of 14 Gnanasambandam], the pressure-area curves for WT, K8E and K28E (active peptides) transitioned rapidly near the monolayer-bilayer equivalence pressure (πB = 40.5 mN/m) showing a remarkable increase in membrane compressibility compared to control monolayers for π = 37-45 mN/m, where π is the membrane pressure. This shows that, the area per molecule of membranes containing these peptides is responsive to small changes in membrane pressure. In contrast, K15E and K25E (compromised inhibitory activities) produced lower compressibilities in the latter range, meaning that for these mutants, the area per molecule was less responsive to membrane

pressure [Figure 11 of 14 Gnanasambandam]. The strong binding observed for K15E is likely related to the reduced compressibility modulus of the K15E-bound membranes that likely reduces K15E displacement during pressure changes compromising its inhibitory activity.

We performed several analyses in which membrane surface tension was varied. In a Langmuir-like CG monolayer system (a monolayer of 128 POPC surrounded by 6435 CG water molecules (Yesylevskyy model) on one side and a vacuum (air) on the other, for 2000 ns), a tension-dependent increase in xy-area was observed [33 Duncan, 32 Lopez]. When the monolayer was coupled to a surface tension of γ_s = 60mN/m (equivalent to the membrane pressure that brings the area per lipid of the peptide-free monolayer to 0.628 nm^2, close to 0.64 nm^2 reported for 1 bar, i.e. resting tension) [33 Duncan; 32 Lopez], the depth of the PMF profile for WT binding (derived similarly to Figure 2) was 70.7 kJ/mol. When the surface tension was raised to 75 mN/m (corresponding to an area per lipid of 0.721 nm^2, without peptide, i.e. stretched), the PMF depth increased to 77.4 kJ/mol. These results suggest that WT binding strength increased as the applied tension expanded the CG monolayer. We have not yet examined the mutants nor have we systematically addressed membrane compressibility.

The effect of applied tension on the WT penetration depth in a CG POPC *bilayer* was also examined. A WT peptide was placed at the water-bilayer interface and the membrane tension was coupled at 60 mN/m (Figure. 7). Note that the run with no applied tension (control run) and the run with tension of 60 mN/m produce an area per lipid of 0.664 and 1.130 nm^2, respectively, for the peptide-free bilayer. The mean ± SD of z-position of the peptide COM was 0.180 ± 0.14 nm above the z-position of PO_4 for the control run (Figure7A, black line) and the corresponding value was 0.075 ± 0.14 nm for the 60 mN/m run (Figure 7B). Similarly, for the control run, the z-position of the Trp6 and Trp7 COM was 0.11± 0.16 nm above the GL1/GL2 COM (Figure 7C), the corresponding value was only 0.02 ± 0.15 nm for the 60 mN/m run. Thus, the applied tension caused the deeper positioning of the WT. The change in COM appears small (~1Å), but may be associated with changes in the binding energy or transitions to deeper states in a different lipid envirionment.

The effects of applied tension were clear when the CG POPC bilayer carrying two WT peptides (dimer) was examined. Initial structures were representative of the 1-to-1 free runs, in which the second peptide was leaning on the upper surface of the first (pre-bound) peptide (Figure 6C). At 0 ns, the second peptide was placed at a high z-position, but, in the presence of high tension, it quickly (< ~300ns) moved to the height of the first peptide (black

line, Figure 7E). The two peptides remained attached to each other in the interface for the remainder of the simulation (data not shown), suggesting that dissociation occurs on a much longer timescale. In contrast, without the applied tension, the height of the two peptides remained unchanged (Figure 7D). Therefore, at least in this CG system, the applied tension facilitates the movement of the second peptide from the loosely associated state to the normal binding position. Further analyses are necessary to investigate whether the dimers observed in the 1-to-1 simulations merely represent a kinetic trap or whether they represent a relevant state in equilibrium with state(s) in which the aggregates are broken and individual peptides bind in the interfacial (shallow) binding mode.

Discussion

Before considering the *in silico* results, we'll provide a brief summary of the experimental results. The mutants exhibited differences of inhibitory activity against Piezo1 in outside-out patches [14 Gnanasambandam]. However, binding energies did not predict the inhibitory activities of mutants and were actually paradoxical to our expectations. For example, the compromised K15E had a lower equilibrium association constant (K_D – from Piezo1 inhibition rates) relative to WT peptide, while the unaffected mutant K28E exhibited a significantly higher K_D [Figure 2 of 14 Gnanasambandam]. Together with the results on membrane penetration depth and the effects of the tension on peptide binding, we propose a model in which the K8E and K28E mutations cause destabilization of the deeper binding states, thereby stabilizing the shallow mode binding, which is likely to be the mode with inhibitory activity [14 Gnanasambandam]. Since the WT peptide and K8E, but not K15E, were easily expelled from the monolayer/bilayer by lateral compression applied in the Langmuir experiment [Figure 10 of 14 Gnanasambandam], we also propose that the WT-like activity of K8E and K28E is enabled by their area-buffering ability, whereas K15E (tight binder) is poorly expelled from the membrane and may suffer the loss of the area-buffering function, causing the loss of the activity [14 Gnanasambandam].

Membrane Binding energy

Isothermal titration calorimetry (ITC) was used to show that K15E (lowest K_D) interacted with POPG (1-palmitoyl-2-oleoyl-phosphatidylglycerol):POPC (3:1) liposomes with a higher affinity than WT or any of the other mutants [Table 2 of 14 Gnanasambandam]. These results are consistent with the high affinity binding of K15E observed in our CG and

AT PMF analysis. On the other hand, liposome experiments showed that the binding energy to POPC was rather similar among all peptides (e.g., -26.8, -26.4 and -25.9 kJ/mol for the WT, K15E and K28E, respectively) [Table 1 of 14 Gnanasambandam]. While peptide binding to the POPG:POPC (3:1) liposomes produced a blue shift in Trp fluorescence, suggesting that Trp residues became buried in the hydrophobic interior of the membrane, binding to pure POPC liposomes caused no such blue-shift [14 Gnanasambandam]. It is possible that aggregation or loose binding to the membrane surface could be a confounding factors in the experiments using POPC liposomes.

Penetration depth

Although the penetration depth showed large fluctuations in the z-position of the peptides, AT simulations produced interesting results (Table 3). In particular, the Trp-Pep z-distance and its SD implied that K15E (with compromised activity) deeply penetrates and stably interacts with lipids compared to K8E and K28E (active mutants). Trp fluorescence quenching experiments suggested that K28E was more deeply positioned in the membrane than WT [Figure 8 of 14 Gnanasambandam]. Our preliminary analyses showed that a system with a thinner membrane (specifically 34/34 POPC) yielded better resolution and a result more consistent with the experimental data, likely because the small system can suppress membrane undulations [data not shown]. However, even though K28E appears to penetrate deeper experimentally, it has a significantly higher K_D than WT suggesting lower affinity that may be the result of altered tilt, local membrane heterogenieties and/or higher aggregation states..

Dipole moment and tilt orientation

The direction of the dipole moments of K15E and K25E (mutants with compromised functional activity) were quite different from WT, while those of K8E and K28E (with unaffected activity) were similar to that of the WT (Figure 4). We surmise that the position of the charged residues and the direction of the dipole moment vector may be critical determinants of inhibitory activity. Tilt angle analysis suggested that KtoE caused the mutated end of the peptide to tilt away from the membrane and the opposite side to tilt toward the membrane, like a seesaw. The distribution of the charged residues is thus a determinant of the orientation and position of the peptide in the membrane. Phosphatidylcholine bilayers

have a zone of high electrostatic potential at the level of the choline group [35 Tieleman 2004]. This zone may cause the shallow positioning of the Glu relative to Lys at the same position. Another possibility is that the Glu side chain is shorter than Lys and might favor the shallow positioning for better hydration. (POPG:POPC bilayers order water to a greater extent than POPC (Janosi and Gorf, J. of Chem. Theory and Computation, 6, p3267, 2010) and may have a more significant affect on peptide tilt and inhibitory activity).

Effects on membrane thickness

In our analysis of thickness, we obtained a 'negative' result in that no clear change in membrane thickness nor curvature was seen upon WT (and K28E) binding (Figure 5). arguing that such changes are not important for the inhibitory activity of the peptides. Using the CHARMM36 force field, Chen and Chung reported thickening of POPC bilayer in the proximity of GsMTx4 and thinning in more distal parts of the POPC bilayer [11 Chen-Chung]. However, our similar analyses using the CHARMM36 force field uncovered slow undulatory motions of the membrane and vertical drifts of the peptides, causing strong autocorrelation on time scales well beyond 100 ns (details not shown). Our CHARMM36 analyses produced inconsistent results for membrane thickening.

We replicated the findings of Chen and Chung related to membrane *thinning* with binding of multiple peptides to the membrane [11 Chen-Chung]. Using AT (Berger and OPLS-AA force fields), when two WT peptides were placed at normal binding positions at the center of a bilayer of 256 (125/131) DPPC (dipalmitoylphosphatidylcholine) molecules, thinning was prominent in the close vicinity of GsMTx4. The thickness of the bilayer (divided into cylinders with radius r parallel to the membrane normal) was 2.52 nm ($r < 2$nm), 2.70 nm ($r = 2$—3.5 nm), 2.71 nm ($r = 3.5$—5.5 nm), and 2.73 nm ($r > 5.5$ nm). Thickness was measured as the C2-C2 distance, where C2 is the carbon atom that is bonded to the carbon atom belonging to the carbonyl groups of the acyl chains of DPPC. The membrane thickness of the peptide-free bilayer was 2.73 nm. When four WT molecules were placed at r < 2.0 nm, in the normal binding position, the membrane thinning was pronounced near GxMTx4; the C2-C2 distance was 2.43 nm ($r < 3$ nm), 2.70 ($r = 3$—4.5 nm), 2.72 ($r = 4.5$—6.5 nm) and 2.74 ($r > 6.5$ nm). Our CG analysis also suggested similar thinning (data not shown). These data suggest that membrane thinning becomes prominent with increasing numbers of bound GsMTx4 peptides, which is in agreement with previous results [11 Chen and Chung]. This thinning effect may explain the phenomenon that potentiation, but not inhibition, becomes

prominent with very high concentrations of GsMTx4 [12 Karamaju, 13 Hurst].

The shallow and deep binding modes

We previously reported that GsMTx4 could bind in at least in two modes, shallow and deep [10 Nishizawa 2007]. As force fields have improved over time, the Lennard-Jones interactions between protein and lipid acyl chains atoms may have weakened [29 Nishizawa 2014, 36 Tieleman], and the deep binding mode currently appears to be less stable than with previous force fields (unpublished result). Using CHARMM36, the deep binding mode was found to be unstable relative to the shallow (interfacial) binding mode [11 Chen-Chung]. Nonetheless the deep binding mode could be relevant in some cases. The asymmetry of local pressure between the two monolayers generated by normal peptide binding at modest densities (~3-5 molecules per 100 nm^2 bilayer) may confer inhibitory activity to GxMTx4. At higher peptide densities, membrane thinning may become predominant, causing facilitation of channel opening as seen previously in prokaryotic channels [12 Kamaraju; 13 Hurst]. In this regime, the transition to the deep binding mode may be facilitated through both membrane thinning and local pressure asymmetries between the two monolayers. Intriguingly, in our additional AT simulations containing eight WT peptides and a 64/64 DPPC bilayer, two peptides moved to the membrane core and interacted in the deep binding mode spontaneously (data not shown). Furthermore, our experimental results support the view that the applied membrane tension facilitates the transition from the shallow binding mode to the deep binding mode [14 Gnanasambandam].

Prior to this work, we performed a self-reconstitution analysis in which lipids and peptides starting in randomized configurations were allowed to spontaneously aggregate during AT simulations. Bilayer defects formed in many runs due to the limited time length of simulations (100 ns), and water carrying pore(s) often emerged. If such cases are also counted as successful reconstitution events, WT assumed the deep binding mode in 61 out of 150 runs. Of note, ~59% of the 61 (deep mode) runs produced one of the following results: ~36% adopted the configuration in which K8, K25 and K28 were segregated from the other charged residues, and ~23% adopted the configuration in which K8, K15 and K28 were segregated from the other charged residues. K8 and K28 are probably important for the deep mode binding; These mutations which leave WT activity intact, introduce Glu side chains that are shorter than Lys side chains and contain partial negative charges, likely destabilize the deep binding mode.

Conclusion

We have described our computational and experimental work on GsMTx4, a peptide that modifies the gating of mechanosensitive channels. The computational simulations were overall consistent with experimental results, demonstrating the predictive power of MD simulations. Both the AT and CG simulations predicted high affinity binding of K15E to the membrane compared to WT and mutant peptides, which was similarly observed in both electrophysiological and calorimetric analyses. Self-reconstitution analyses indicated that K8 and K28 had a tendency to split from the other charged residues during the formation of the deep binding mode. This lends support to the view that K8E and K28E destabilize the deep binding mode [14 Gnanasambandam]. *In silico* measures of membrane penetration depth were consistent with fluorescence quenching results (Table 3). Tilt angle and the dipole moment analyses raised the possibility that appropriate tilt angle, dipole moment orientation and appropriate locations of charged residues on the peptide surface are important to inhibitory activity, but their relative impacts remain unclear. Of technical relevance, the AT PMF profiles were in agreement with the CG PMF profiles (Table 2A,B). Importantly, no gross membrane deformations or changes in thickness were observed upon a single WT peptide binding to the surface of the bilayer in the AT system.

As discussed in the accompanying paper, the shallow binding mode is likely the functionally relevant inhibitory mode. In the presence of applied tension, the peptide's action as an area buffer (i.e., reservoir that provides materials to fill free space) should be relevant because it would serve as a mechanism to maintain pressure asymmetry between the two monolayers in the presence of tension. The minimal amount of deep binding would be consistent with the observation that GsMtx4 acts from the extracellular surface and probably the gating mechanics of the channel are based in the outer monolayer. Future studies should address the possibility that peptides can loosely associated with membrane (or with pre-bound peptides) and act as reservoirs when the membrane is stretched. Our CG simulations support this interpretation, but much longer simulations are necessary to examine whether or not the loosely associated peptides are in equilibrium with the peptides that are independently residing in the shallow binding mode. The physiological relevance of the deep binding mode is also unclear. Future analyses should address the extent to which membrane tension stabilizes the deep binding mode relative to the shallow binding mode.

References

[1] T.M. Suchyna, J.H. Johnson, K. Hamer, J.F. Leykam, D.A. Gage, H.F. Clemo, C.M. Baumgarten, F. Sachs. Identification of a peptide toxin from Grammostola spatulata spider venom that blocks cation-selective stretch-activated channels. J. Gen. Physiol. 115 (2000) 583-598.

[2] F. Sachs. Stretch-activated ion channels: what are they? Physiology. 25 (2010) 50-56.

[3] Reed A, Kohl P, Peyronnet R. Molecular candidates for cardiac stretch-activated ion channels. Glob Cardiol Sci Pract. 2014 Jun 18;2014(2):9-25

[4] A. Gomis, S. Soriano, C. Belmonte and F. Viana Hypoosmotic- and pressure-induced membrane stretch activate TRPC5 channels The Journal of Physiology 586, 5633-5649, 2008

[5] M.A. Spassova, T.Hewavitharana, W. Xu, J. Soboloff, and D. L. Gill A common mechanism underlies stretch activation and receptor activation of TRP C6 channels PNAS, 103 (2006)16586-16591

[6] C. Bae, F. Sachs, and P.A. Gottlieb The Mechanosensitive Ion Channel Piezo1 Is Inhibited by the Peptide GsMTx4 Biochemistry, 50 (2011) 6295-6300

[7] K.J. Swartz. Tarantula toxins interacting with voltage sensors in potassium channels. Toxicon. 49 (2007) 213-230.

[8] B. Gao, P.J. Harvey, D.J. Craik, M. Ronjat, M. De Waard, S. Zhu. Functional evolution of scorpion venom peptides with an inhibitor cystine knot fold. Biosci. Rep. 33 (2013) e00047.

[9] T.M. Suchyna, S.E. Tape , R.E. Koeppe, O.S. Andersen, F. Sachs, P.A. Gottlieb. Bilayer-dependent inhibition of mechanosensitive channels by neuroactive peptide enantiomers Nature 430 (2004) 235–240.

[10] M. Nishizawa, K. Nishizawa. Molecular dynamics simulations of a stretch-

activated channel inhibitor GsMTx4 with lipid membranes: two binding modes and effects of lipid structure. Biophys J. 92 (2007) 4233-4243.

[11] R. Chen, S.H. Chung. Effect of gating modifier toxins on membrane thickness: implications for toxin effect on gramicidin and mechanosensitive channels. Toxins (Basel) 5 (2013) 456-471.

[12] K. Kamaraju, P.A. Gottlieb, F. Sachs, S. Sukharev, Effects of GsMTx4 on bacterial mechanosensitive channels in inside-out patches from giant spheroplasts. Biophys J. 99 (2010) 2870-2878.

[13] A.C. Hurst, P.A. Gottlieb, B. Martinac. Concentration dependent effect of GsMTx4 on mechanosensitive channels of small conductance in E. coli spheroplasts. Eur. Biophys. J. 38 (2009) 415-425.

[14] R. Gnanasambandam, C. Ghatak, A. Yasnamm, F. Sachs, A.S. Ladokhin, S.I.Sukharev, T.M. Suchyna. GsMTx4 superficial binding and tension dependent penetration of membranes confer inhibitory function of mechanosensitive ion channels. Submitted

[15] B. Hess, C. Kutzner, D. van der Spoel, E. Lindahl. GROMACS 4: Algorithms for Highly Efficient, Load-Balanced, and Scalable Molecular Simulation. J. Chem. Theory Comput. 4 (2008) 435.

[16] W. Humphery, A. Dalke, K. Schulten. VMD – visual molecular dynamics. J. Mol. Graph. 14 (2010) 33–38.

[17] The UniProt Consortium. Ongoing and future developments at the Universal Protein Resource. *Nucleic Acids Res*. 39, D214-D219 (2011)

[18] R.E. Oswald, T.M. Suchyna, R. Mcfeeters, P. Gottlieb, F. Sachs, Solution Structure of Peptide Toxins that Block Mechanosensitive Ion Channels. J.Biol.Chem. 277 (2002) 34443-34450.

[19] S.J. Marrink, H.J. Risselada, S. Yefimov, D.P. Tieleman, A.H. de Vries. The MARTINI force field: coarse-grained model for biomolecular simulations. J. Phys. Chem. B. 111 (2007) 7812-7824.

[20] M. Nishizawa, K. Nishizawa. Molecular dynamics simulation analysis of membrane defects and pore propensity of hemifusion diaphragms. Biophys. J. 104 (2013) 1038.

[21] S.O. Yesylevskyy, L.V. Schäfer, D. Sengupta, S.J. Marrink. Polarizable water model for the coarse-grained MARTINI force field. PLoS Comput. Biol. 6 (2010) e1000810.

[22] B. Hess, H. Bekker, H. J. C. Berendsen, J. G. E. M. Fraaije. LINCS: a linear constraint solver for molecular simulations. J. Comput. Chem. 18 (1997) 1463.

[23] O. Berger, O. Edholm, F. Jähnig. Molecular dynamics simulations of a fluid bilayer of dipalmitoylphosphatidylcholine at full hydration, constant pressure, and constant temperature. Biophys. J. 72 (1997) 2002-2013.

[24] C. Neale, W.F.D. Bennett, D.P. Tieleman, R. Pomès. Statistical Convergence of Equilibrium Properties in Simulations of Molecular Solutes Embedded in Lipid Bilayers. J. Chem. Theory Comput. 12 (2011) 4175–4188.

[25] H.J.C. Berendsen, J. P. M. Postma, W. F. van Gunsteren, J. Hermans. Intermolecular forces, interaction models for water in relation to protein hydration. D. Reidel Publishing, Dordrecht, The Netherlands, 1981, 331–342.

[26] S. Miyamoto, P.A. Kollman. SETTLE: an analytical version of the SHAKE and RATTLE algorithm for rigid water models. J. Comput. Chem. 13 (1992) 952.

[27] T. Darden, D. York, L. Pedersen. Particle mesh Ewald: an Nlog(N) method for Ewald sums in large systems. J. Chem. Phys. 98 (1993) 10089.

[28] H.J.C. Berendsen, J. P. M. Postma, W. F. van Gunsteren, A. DiNola, J. R. Haak, Molecular dynamics with coupling to an external bath. J. Chem. Phys. 81 (1984) 3684.

[29] M. Nishizawa, K. Nishizawa. Potential of mean force analysis of the self-association of leucine-rich transmembrane α-helices: difference between atomistic and coarse-grained simulations. J. Chem. Phys. 141 (2014) 075101.

[30] J.C. Gordon, J.B. Myers, T. Folta, V. Shoja, L.S.Heath, A. Onufriev. H++: a server for estimating pKas and adding missing hydrogens to macromolecules. Nucleic Acids Res. 33 (2005) W368-71.

[31] L. Sandberg, O. Edholm. Calculated Solvation Free Energies of Amino Acids in a Dipolar Approximation. J. Phys. Chem. B 105 (2001) 273-281.

[32] C.A. Lopez, A.H. de Vries, S.J. Marrink. Molecular mechanism of cyclodextrin mediated cholesterol extraction. PLoS Computational Biol. 7 (2011) e1002020.

[33] S.L. Duncan, R.G. Larson. Comparing experimental and simulated pressure-area isotherms for DPPC. 94 (2008) 2965-2986.

[34] P.Tarazona, E. Chacón, F. Bresme. Thermal fluctuations and bending rigidity of bilayer membranes. *J. Chem. Phys.* 139 (2013) 094902.

[35] D.P. Tieleman, The molecular basis of electroporation. BMC Biochem. 5 (2004) 10.

[36] D.P. Tieleman; J.L. MacCallum; W.L. Ash, C. Kandt, Z. Xu, L. Monticelli, Membrane protein simulations with a united-atom lipid and all-atom protein model: lipid–protein interactions, side chain transfer free energies and model proteins. J. Phys. Condens. Matter. 18, (2006) S1221–1234.

Table 1. Descriptions of performed molecular dynamics simulations

Simulation	Force field	Composition*	Initial box size (Å)	Run type /Configuration	Time
PMF analysis of membrane-binding energy					
CG-pmf-WT	MARTINI	124 POPC/2439 w/WT	65×65×110	z-restrained	4us for each z-position
CG-pmf-K8E	MARTINI	124 POPC/2439 w/K8E	65×65×110	z-restrained	4us for each z- position
CG-pmf-K15E	MARTINI	124 POPC/2439 w/K15E	65×65×110	z-restrained	4us for each z-position
CG-pmf-K20E	MARTINI	124 POPC/2439 w/K20E	65×65×110	z-restrained	4us for each z-position
CG-pmf-K22E	MARTINI	124 POPC/2439 w/K22E	65×65×110	z-restrained	4us for each z-position
CG-pmf-K25E	MARTINI	124 POPC/2439 w/K25E	65×65×110	z-restrained	4us for each z-position
CG-pmf-K28E	MARTINI	124 POPC/2439 w/K28E	65×65×110	z-restrained	4us for each z-position
AT-pmf-WT	Berger/OPLS-AA	124 POPC /8317 w /WT	66×66×98	z-restrained at 1.5-2.8nm	300ns for each z-position
AT-pmf-K15E	Berger/OPLS-AA	124 POPC /8317 w /K15E	66×66×98	z-restrained at 1.5-2.8nm	300ns for each z-position
AT-pmf-K28E	Berger/OPLS-AA	124 POPC /8317 w /K28E	66×66×98	z-restrained at 1.5-2.8nm	300ns for each z-position
AT free run					
60/64-WT	Berger/OPLS-AA	124 POPC/5696 w/WT	66×66×80	free run	300ns
60/64-K8E	Berger/OPLS-AA	124 POPC/5696 w/K8E	66×66×80	free run	300ns
60/64-K15E	Berger/OPLS-AA	124 POPC/5696 w/K15E	66×66×80	free run	300ns
60/64-K20E	Berger/OPLS-AA	124 POPC/5696 w/K20E	66×66×80	free run	300ns
60/64-K22E	Berger/OPLS-AA	124 POPC/5696 w/K22E	66×66×80	free run	300ns
60/64-K25E	Berger/OPLS-AA	124 POPC/5696 w/K25E	66×66×80	free run	300ns
60/64-K28E	Berger/OPLS-AA	124 POPC/5696 w/K28E	66×66×80	free run	300ns
34/34-WT	Berger/OPLS-AA	68 POPC/3180 w/WT	49.5×49.5×79	free run	600ns
34/34-K28E	Berger/OPLS-AA	68 POPC/3182 w/K28E	49.5×49.5×79	free run	600ns

CG PMF analysis of dimerization in water					
in-water-2WT	MARTINI	1684 w/2 WT/13 Na/ 23 Cl	59.5×59.5× 59.5	distance-restrained	2us for each distance
in-water-2K28E	MARTINI	1691 w/2 K28E/15 Na/ 21 Cl	59.5×59.5× 59.5	distance-restrained	2us for each distance
CG run for peptide self- association near membrane					
1-to-1-free-WT	MARTINI	256 POPC/5444 w /2WT/20Na/30Cl	92×92×118	free; initially one in water and one on membrane	100 × 800ns runs
1-to-1-free-K28E	MARTINI	256 POPC/5444 w/ 2 K28E/22 Na/28 Cl	92×92×118	free; initially one in water and one on membrane	100 × 800ns runs

* For the CG and AT PMF simulations, as well as the AT free runs, chloride ions, but not other ions, were added to adjust the total charge zero.

Table 2. Summary of PMF analysis

Simulation	Position of energy minimum relative to bilayer center (nm)	Depth of PMF well ± S.E. (kJ/mol)†	ΔG^{bind} ± S.E. (kJ/mol)*
CG-pmf-WT	2.35	-57.82 ± 0.74	-23.2 ± 0.28
CG-pmf-K8E	2.5	-55.19 ± 1.28	-21.7 ± 0.71
CG-pmf-K15E	2.35	-65.79 ± 0.50	-26.8 ± 0.25
CG-pmf-K20E	2.5	-57.86 ± 0.84	-23.3 ± 0.35
CG-pmf-K22E	2.35	-59.25 ± 1.31	-24.0 ± 0.66
CG-pmf-K25E	2.5	-49.48 ± 0.69	-18.1 ± 0.40
CG-pmf-K28E	2.35	-49.28 ± 0.41	-18.8 ± 0.22
AT-pmf-WT	1.7	-61.2 ± 4.5	n.t.
AT-pmf-K15E	1.7	-72.2 ± 4.7	n.t.
AT-pmf-K28E	2.1	-40.1 ± 5.0	n.t.

* n.t. = not tested

†For the AT series, the PMF depth relative to the PMF value at z = 3.8nm is shown. The mean force at this position was smaller than 3.0 kJ/nm and our estimation based on the CG PMF curve suggested that the systematic error in the PMF depth resulting from the ignoring the z = 3.8 - 5.0 nm range was smaller than 0.5 kJ/mol for all three peptides.

Table 3. Averaged peptide penetration depth based on the AT 60/64 simulation series

Peptide	COM from bilayer center ± S.D. (nm)	Trp residue COM from bilayer center ± S.D. (nm)	Trp residue COM from peptide COM ± S.D. (nm)
WT	1.84 ± 0.16	1.20 ± 0.16	-0.64 ± 0.06
K8E	1.88 ± 0.24	1.39 ± 0.32	-0.49 ± 0.12
K15E	1.70 ± 0.15	1.08 ± 0.17	-0.63 ± 0.06
K20E	1.62 ± 0.15	1.06 ± 0.18	-0.56 ± 0.11
K22E	1.69 ± 0.14	1.07 ± 0.17	-0.62 ± 0.09
K25E	1.90 ± 0.17	1.23 ± 0.17	-0.67 ± 0.06
K28E	1.84 ± 0.16	1.28 ± 0.19	-0.56 ± 0.09

Table 4. Analysis of the 1-to-1-free simulations.

Simulation	Peptide	Bound to pre-bound peptide	Bound to bilayer in *cis* configuration	Bound to the opposite side of bilayer	Remained in water
1-to-1-freeWT	WT	25	5	9	61
1-to-1-freeK28E	K28E	51	4	15	30

Legends for Figures

Figure 1. Van der Waals rendering of GsMTx4 structure and the simulation configuration. *Left*: a representative snapshot from an AT 60/64-WT free simulation of WT GsMTx4 and a POPC bilayer membrane. Trp residues are cyan, Phe residues are lime, other hydrophobic residues (Ala, Cys, Ile, Leu, Met, Pro and Val) are green, basic residues (Arg ad Lys) are blue, and acidic residues (Asp and Glu) are red. For the POPC head group, the nitrogen atoms are blue, phosphorus atoms are ocher, and carbonyl oxygen atoms are red spheres. The terminal carbon atoms of the lipid acyl tails are ice blue spheres. Water molecules and chloride ions are not shown. *Right:* a bottom and side view of WT GsMTx4 sampled from an in-water simulation. The bottom view illustrates the hydrophobic protrusion that contains W6. The graphical representation is similar to the panel on the left.

Figure 2. CG PMF profiles for WT and mutant peptides within the POPC bilayer.

Figure 3. Schematic representations of tilt angles for WT and mutant peptides in AT simulations. *Top:* WT peptide. Small grey boxes at the tip of the vertical bars indicate the mean z-position of the Lys Cγ atom. To represent the Cγ positions in 3-dimensions, grey vertical lines were anchored to the horizontal plane that represents the height of the COM for the peptide. The root positions of the bars are not accurate, but indicate that K8, K28, K25, K22 and K20 are arrayed in a counterclockwise order when viewed from the bottom, and that K22 and K15 are located somewhat internally compared to K20 and K25. *The remaining figures*: Results for each mutant are indicated by black arrows that are superimposed on the WT data. Arrows start from the Cγ position observed for WT (i.e., grey boxes) and end at the positions observed in the simulation of each mutant. Bold numbers denote native residues, whereas encircled numbers denote mutated residues. Italicized numbers denote the difference in z-position (Å) for values equal to or greater than 2 Å.

Figure 4. Dipole moment vectors for WT and mutant peptides in the normal membrane-bound state. Arrows indicate the dipole moment vectors calculated for representative WT and mutant peptides bound to the POPC bilayer in the AT simulations. Note that the maximum angle is shown; i.e., the peptides were rotated around the z-axis, such that the

arrows aligned onto the xz-plane. The starting point of each vector represents the time-averaged position (depth) of the COM over the AT simulations.

Figure 5. Three-dimensional representations of the averaged z-positions of phosphorus atoms of the upper and lower POPC monolayers over the AT simulations. Control (i.e., no peptide), 60/64-WT, and 60/64 K28E runs were analyzed. 2×2 Å^2 monolayer patches were analyzed, but for clarity, the mean value for 3×3 pixels^2 (the central pixel plus the surrounding 8 pixels) was plotted.

Figure 6. Representative snapshots of the 1-to-1 free runs for WT peptide. The first (pre-bound) peptide is orange and the second peptide (in water) is yellow. Dark blue spheres are NC3 particles. (A) An initial structure. (B) The cis-binding configuration. (C) The second peptide is bound to the first peptide.

Figure 7. Tension-induced changes in the penetration depth of WT peptide in the POPC bilayer. (A) CG WT/POPC bilayer. (B) CG WT /POPC bilayer with an applied tension of 60 mN/m. (C) MARTINI model of POPC. Atom names and, in parenthesis, atom types are shown. (D) CG WT dimer/POPC bilayer. (E) CG WT dimer/POPC bilayer with an applied tension of 60 mN/m.

Figure 1

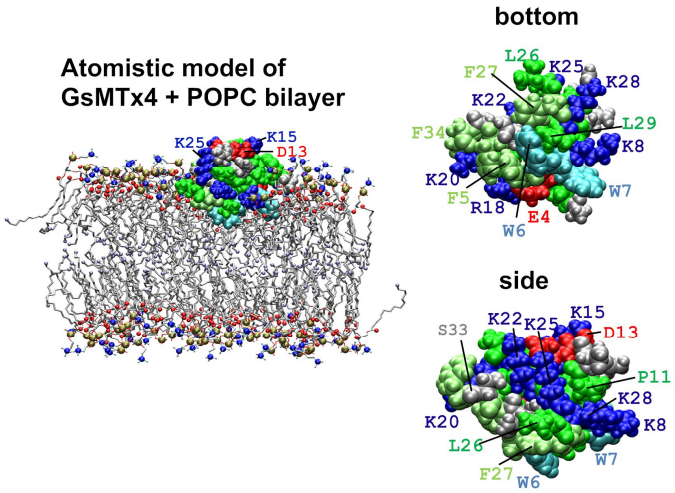

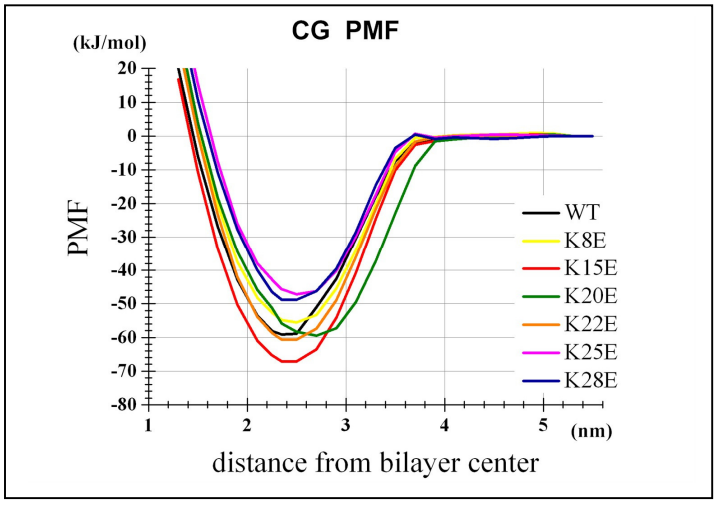

Figure 2

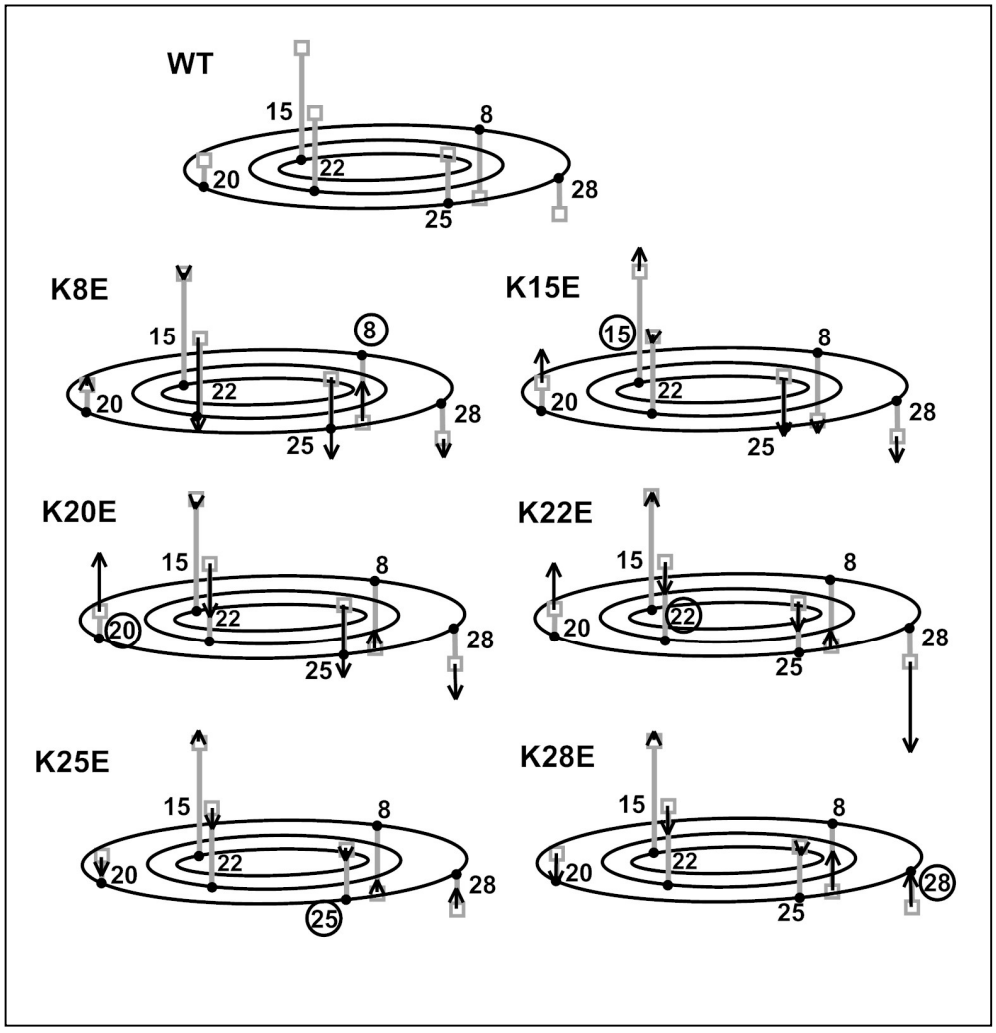

Figure 3

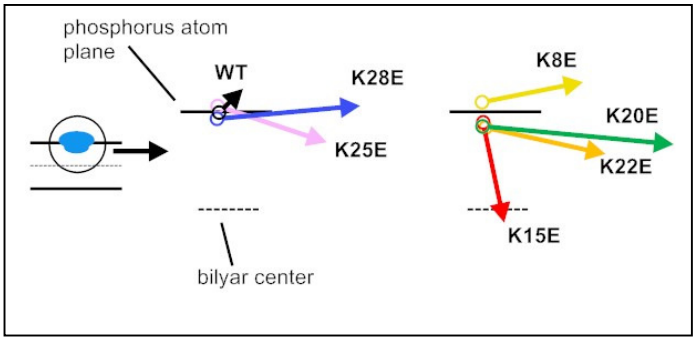

Figure 4

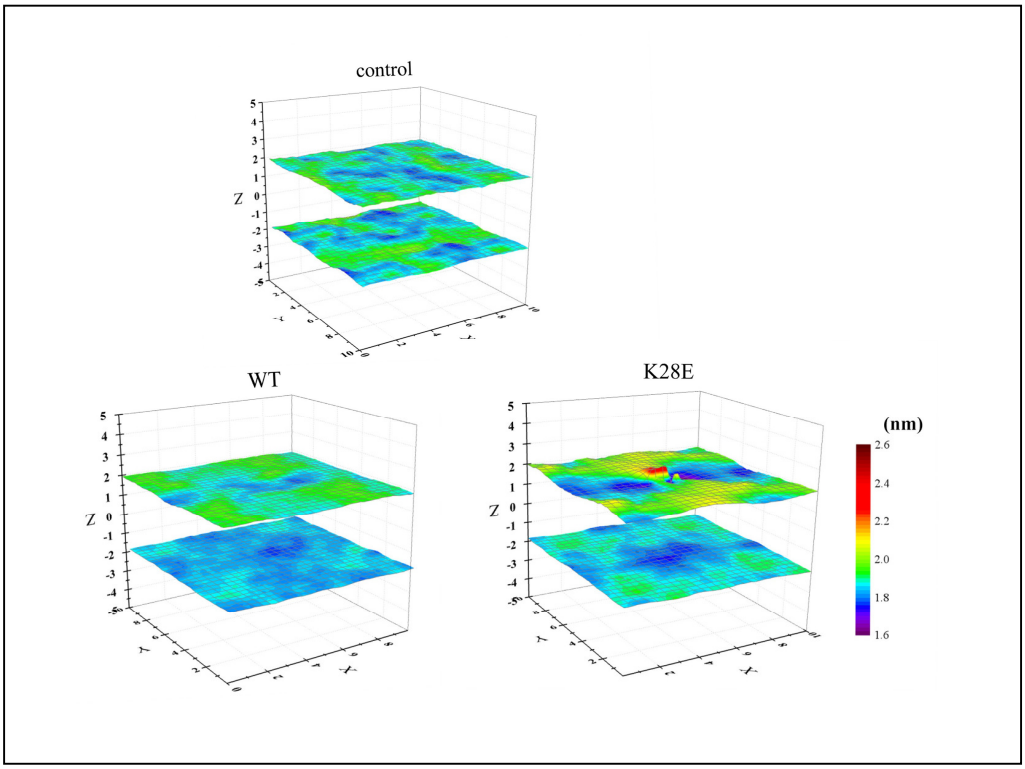

Figure 5

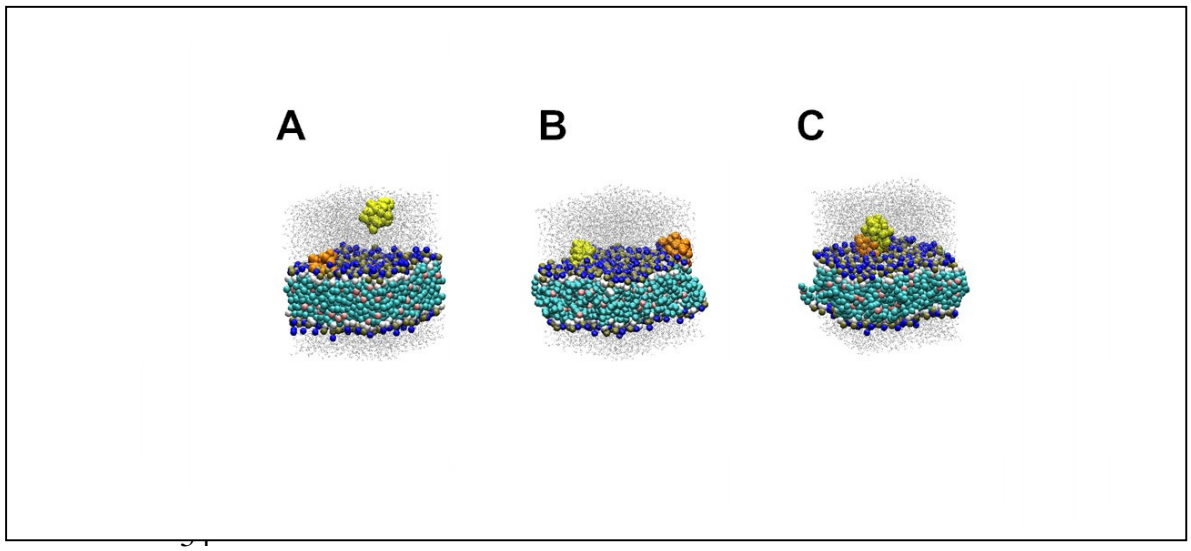

Figure 6

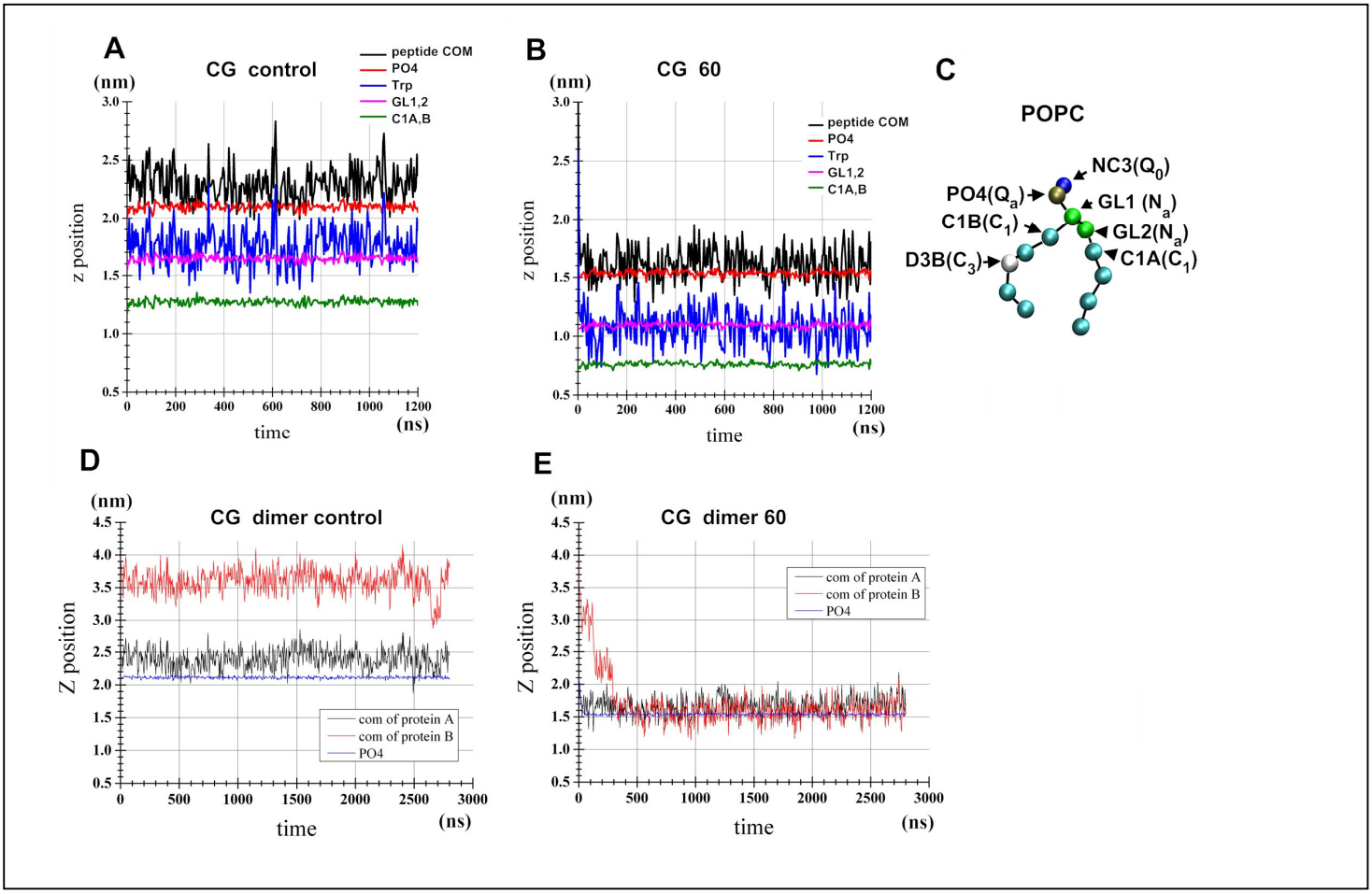
A
CG control
(nm)
peptide COM
PO4
Trp
GL1,2
C1A,B
z position
time
(ns)
B
CG 60
(nm)
peptide COM
PO4
Trp
GL1,2
C1A,B
z position
time
(ns)
C
POPC
NC3(Q0)
PO4(Qa)
GL1 (Na)
C1B(C1)
GL2(Na)
D3B(C3)
C1A(C1)
D
CG dimer control
(nm)
Z position
com of protein A
com of protein B
PO4
time
(ns)
E
CG dimer 60
(nm)
Z position
com of protein A
com of protein B
PO4
time
(ns)

Figure 7

Supplementary Material:

Effects of Lys to Glu mutations in GsMTx4 on membrane binding, peptide orientation, and self-association propensity, as analyzed by molecular dynamics simulations

by Nishizawa et al.

	AT analysis of Cγ z-position relative to peptide COM, Å (difference from WT)											
Simulation	Residue Number											
	8		15		20		22		25		28	
WT	-4.17		7.45		1.74		4.75		2.96		-2.29	
K8E	**-1.92**	**(2.25)**	7.34	(-0.10)	1.85	(0.10)	-0.63	*(-5.39)*	-1.84	*(-4.80)*	-3.78	*(-1.49)*
K15E	-4.69	(-0.52)	**8.46**	**(1.01)**	**4.04**	**(2.29)**	4.74	(-0.02)	-0.33	*(-3.29)*	-4.37	*(-2.08)*
K20E	-3.06	(1.11)	7.52	(0.07)	**5.64**	**(3.89)**	1.41	*(-3.35)*	-1.41	*(-4.38)*	-4.70	*(-2.41)*
K22E	-3.23	(0.93)	7.59	(0.14)	**5.56**	**(3.81)**	2.57	*(-2.18)*	0.81	*(-2.15)*	-8.38	*(-6.09)*
K25E	-3.42	(0.74)	7.80	(0.35)	0.97	(-0.78)	3.37	*(-1.39)*	2.63	(-0.34)	-1.34	(0.95)
K28E	**-1.53**	**(2.637)**	7.82	(0.378)	-0.15	*(-1.895)*	3.11	*(-1.641)*	2.79	(-0.170)	**0.12**	**(2.416)**

Table S1. Tilt angle analysis

Tilt analysis: z-positions of the Cγ atom of the indicated residues relative to the peptide COM. Bold values were greater than WT values, with margins wider than 1 Å. Underlined values were smaller than WT values, with margins wider than 1 Å. The SD of the z-position relative to the peptide COM fell within 0.5 to 1.7 Å.

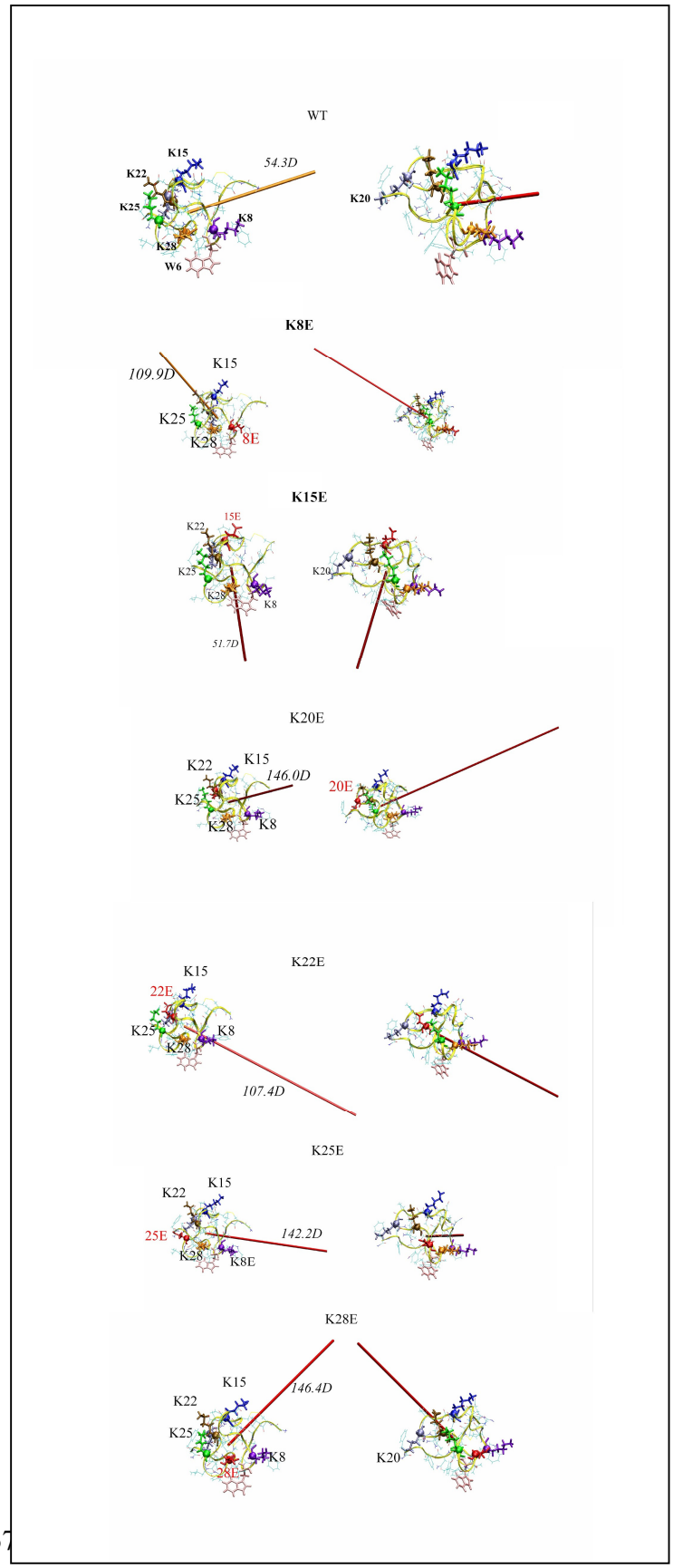

Figure S1. Dipole moment vector. The vector is represented by a red bar extending from the peptide COM. The dipole moment was calculated using the peptide structures sampled from in-water simulations. Two views, captured at slightly different rotations about the z-axis, are shown. For all panels, the hydrophobic protrusion was oriented downward.

Xerocytosis is caused by mutations that alter the kinetics of the mechanosensitive channel PIEZO1

Chilman Bae[a,b], Radhakrishnan Gnanasambandam[a,b], Chris Nicolai, Frederick Sachs[a,b,1], and Philip A. Gottlieb[a,b,1]

[a]Department of Physiology and Biophysics and [b]The Center for Single Molecule Biophysics, State University of New York at Buffalo, Buffalo, NY 14214

Edited by David E. Clapham, Howard Hughes Medical Institute, Children's Hospital Boston, Boston, MA, and approved February 5, 2013 (received for review November 13, 2012)

Familial xerocytosis (HX) in humans is an autosomal disease that causes dehydration of red blood cells resulting in hemolytic anemia which has been traced to two individual mutations in the mechanosensitive ion channel, PIEZO1. Each mutation alters channel kinetics in ways that can explain the clinical presentation. Both mutations slowed inactivation and introduced a pronounced latency for activation. A conservative substitution of lysine for arginine (R2456K) eliminated inactivation and also slowed deactivation, indicating that this mutant's loss of charge is not responsible for HX. Fitting the current vs. pressure data to Boltzmann distributions showed that the half-activation pressure, $P_{1/2}$, for M2225R was similar to that of WT, whereas mutations at position 2456 were left shifted. The absolute stress sensitivity was calibrated by cotransfection and comparison with MscL, a well-characterized mechanosensitive channel from bacteria that is driven by bilayer tension. The slope sensitivity of WT and mutant human PIEZO1 (hPIEZO1) was similar to that of MscL implying that the in-plane area increased markedly, by ~6–20 nm^2 during opening. In addition to the behavior of individual channels, groups of hPIEZO1 channels could undergo simultaneous changes in kinetics including a loss of inactivation and a long (~200 ms), silent latency for activation. These observations suggest that hPIEZO1 exists in spatial domains whose global properties can modify channel gating. The mutations that create HX affect cation fluxes in two ways: slow inactivation increases the cation flux, and the latency decreases it. These data provide a direct link between pathology and mechanosensitive channel dysfunction in nonsensory cells.

mechanical channels | PIEZO1 mutations | channel domains

Hereditary xerocytosis (HX) is an autosomal dominant disease characterized by dehydrated red blood cells (RBCs) and mild-to-moderate hemolytic anemia. Two familial HX mutations were identified recently in the gene encoding hPIEZO1, a mechanosensitive ion channel (MSC) (1).

Mouse PIEZO1 (mPIEZO1) cloned from Neuro2A cells contains ~2,500 amino acids predicted to have 24–36 transmembrane domains. Using crosslinking and photobleaching techniques, PIEZO1 was shown to assemble as a homotetramer (2, 3) with no other cofactors. Currently it is not known whether the pore is central to the tetramer (intermolecular) or whether each subunit conducts (intramolecular). mPIEZO1 is a cation-selective channel with a reversal potential near 0 mV. The conductance is ~70 pS and is reduced to 35 pS by increasing extracellular Mg^{+2} (3, 4). mPIEZO1, like other cationic MSCs, is inhibited by the peptide GsMTx4 (5) and nonspecifically by ruthenium red (2). Heterologous expression in HEK293 cells is efficient, and mechanical currents can be evoked in whole-cell mode or patches. In cell-attached patches at hyperpolarized potentials, mPIEZO1 activates with ~30 mmHg of pipette suction and inactivates within ~30 ms, a rate that slows with depolarization (2–4).

To explore the biophysical properties of human PIEZO1 (hPIEZO1) that produce HX, we cloned it from HEK293 cells and then duplicated the mutations identified with HX. The mutants had slower inactivation and developed a long latency for activation. We also observed that groups of channels could change kinetics together, implying that they normally exist in confining domains that can fracture with the applied force. We showed by coexpressing MscL from bacteria with hPIEZO1 and its mutants that both PIEZO1 and the mutants have similar dimensional changes during opening (6, 7). The half-maximal activation pressure ($P_{1/2}$) for two mutants was shifted to lower pressures, making them more sensitive in absolute terms. The data suggest that mutant hPIEZO1s cause symptoms by excess cation influx (8) from slow inactivation or by delayed activation resulting from increased latency.

Results

To understand the biophysical consequences of the HX mutations, we first cloned hPIEZO1 from HEK293 cells and then introduced the HX mutations at positions 2225 and 2456 (Fig. 1*A*). hPIEZO1 is 88% homologous to mPIEZO1. The HX mutation of M2225 is thought to reside on the extracellular side and R2456 on the intracellular side of the membrane (the full protein sequence is shown in Fig. S1). We characterized hPIEZO1's electrophysiology by transfection into HEK293 cells. In cell-attached patches, hPIEZO1 had an open time of ~40 ms when fit to a three-state linear model, shut-open-inactivated, with pressure sensitivity needed only in the shut-to-open rate constant (Fig. 1*B*). Cell-attached patches show little endogenous activity (5). Like mPIEZO1, inactivation slowed with depolarization (Fig. 1*C*), and activation was inhibited by GsMTx4 (Fig. 1*D*).

We evoked whole-cell mechanical currents by indenting the cells with a glass probe (2, 4, 9) (Fig. 2*A*). Both mutants, M2225R and R2456H, had slower inactivation kinetics than WT (Fig. 2), whereas GFP-transfected control cells produced no mechanically

Significance

Familial xerocytosis in humans, which causes dehydration of red blood cells and hemolytic anemia, was traced to mutations in the mechanosensitive ion channel, PIEZO1. The mutations slowed inactivation and introduced a pronounced latency for activation. Loss of inactivation and increased latency for activation could modify groups of channels simultaneously, suggesting that they exist in common spatial domains. The hereditary xerocytosis mutants affect red cell cation fluxes: slow inactivation increases them, and increased latency decreases them. These data provide a direct link between pathology and mechanosensitive channel dysfunction in nonsensory cells.

Author contributions: F.S. and P.A.G. designed research; C.B., R.G., and P.A.G. performed research; C.N., F.S., and P.A.G. analyzed data; and F.S. and P.A.G. wrote the paper.

The authors declare no conflict of interest.

This article is a PNAS Direct Submission.

Freely available online through the PNAS open access option.

Data deposition: The sequence for human PIEZO1 has been deposited in the National Center for Biotechnology Reference Sequence data bank (accession number KC602455).

[1]To whom correspondence may be addressed. E-mail: sachs@buffalo.edu or philgott@buffalo.edu.

This article contains supporting information online at www.pnas.org/lookup/suppl/doi:10.1073/pnas.1219777110/-/DCSupplemental.

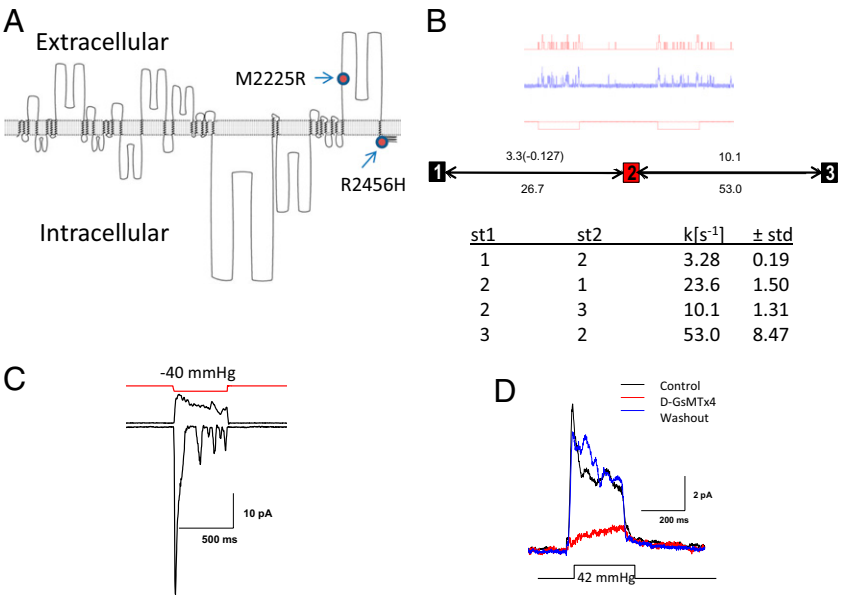

Fig. 1. Characterization of cloned hPIEZO1. (*A*) A diagram showing the putative transmembrane domains of hPiezo1 and intracellular and extracellular regions. The HX mutation sites are shown where M2455R is thought to be extracellular and H2456 is intracellular. (*B*) Kinetic data and a fitted model for hPIEZO1 with three states (closed-open-inactivated). The theoretical fit to the model shown in red provided the kinetic rate constants shown in the table. The pressure dependence is shown in parenthesis. (*C*) Voltage-dependent inactivation. At depolarized voltages (+40 mV) there is slow inactivation, and at hyperpolarized voltages (−110 mV) there is rapid inactivation. (*D*) hPIEZO1 is inhibited by the D enantiomer of GsMTx4 (2 μM, +50 mV holding potential).

activated current (Fig. S2*A*). These results illustrate both transfection specificity and the "mechanoprotection" of the endogenous channels. We explored the generality of whole-cell mechanoprotection by comparing these results with cells transfected with DNA for TREK-1, a K^+ selective MSC (10, 11). This transfection produced small whole-cell currents, but patches from the same cells had large currents (Fig. S2*B*) so that in the whole-cell configuration TREK-1 also was protected from stress, as we assume MSCs are in situ.

Single-channel recordings also showed kinetic differences between the mutants and WT (Fig. 3). A unique characteristic of the mutant channels, not seen in the WT, was a pronounced latency to activation (Fig. 3, compare *Insets*). For hundreds of milliseconds following the application of suction, there was no change in the current, followed by a sudden activation of many channels. We could not simulate this behavior with a Markov model even with many closed states, and we postulate that the latency reflects a stress-induced physical rupture of a domain containing the channels (see below).

We measured the dose–response curve (current vs. pressure fit to a Boltzmann distribution) for hPIEZO1 and the mutant channels. R2456H and R2456K exhibited a leftward shift of 13 and 8 mmHg, respectively, in the $P_{1/2}$, but M2225R was similar to the WT channel (Fig. 4*A*). The leftward shift may represent decreased stress within the resting channel protein or differences in local stress felt within a domain. In the case of TREK-1, it is known that transfection alone causes massive change to the cytoskeleton (12). In contrast to the changes we observed in $P_{1/2}$, the slope sensitivity α (the maximum slope of Popen vs. pressure) was similar for WT and the hPIEZO1 mutants (7–8 $mmHg^{-1}$). The constant α is proportional to the dimensional change between the closed and open conformations and suggests that the mutations did not affect the domains responsible for activation (13).

To provide an absolute measure of α, we cotransfected cells with MscL (14), a bacterial MSC known to be activated by bilayer tension and previously calibrated (7, 15, 16). The plots of peak current vs. pressure curves were fit to the sum of two Boltzmanns, one for the channel under test and one for MscL (Fig. 5). We performed this operation for hPIEZO1 (Fig. 5), two PIEZO1 mutants (Fig. S3), and TREK-1 (Fig. 5). The ratio of α for hPIEZO1 to MscL was 1.15 ± 0.14, $n = 5$, equivalent to a change of ~6–20 nm^2 in the in-plane area (6, 7) (assuming that both populations felt the same tension). The α was similar in the two mutant hPIEZO1 channels. However, for TREK-1, the α ratio was only 0.54 implying that this channel had a smaller dimensional change or that the local tension was about half that of

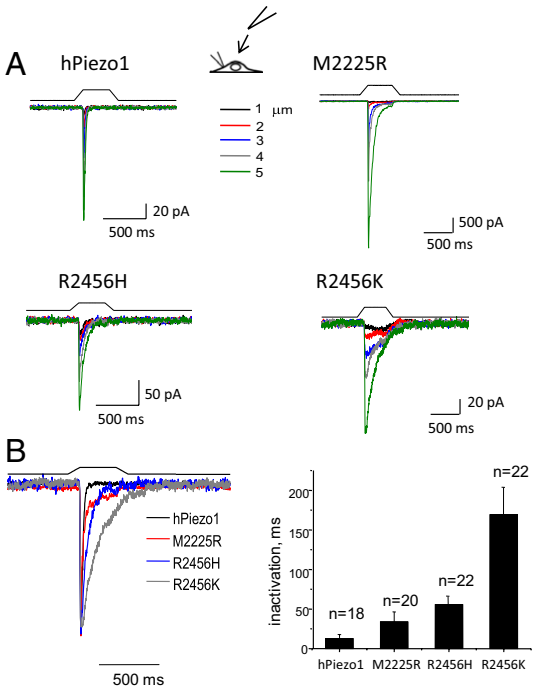

Fig. 2. The effect of HX mutations on whole-cell currents. The mutations were introduced at positions 2225 or 2456 (see sequence in Fig. S1). HEK293 cells were transfected with ~1 μg of DNA and measured 24–48 h later. (*A*) Whole-cell currents as a function of depth of the indenting probe. The stimulus waveform is shown above the current trace. (*B*) (*Left*) Average of repeated current traces showing the slowing of inactivation for both M2225R and R2456H. These traces have been normalized for kinetic comparison. The conservative mutation that replaced arginine with lysine at position 2456 (R2456K) was intended to measure the effect of residue charge. Despite maintaining charge, the mutation completely removed inactivation, suggesting that this site may be part of a hinge domain. (*Right*) The bar graph shows the mean response ± SD.

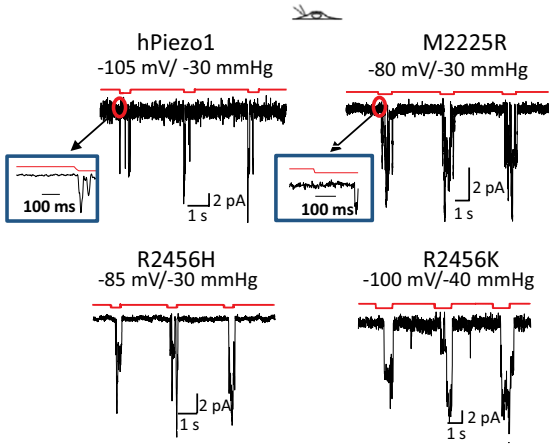

Fig. 3. hPIEZO1 mutations slow inactivation in cell-attached patches at single-channel resolution. M2225H and R2456H slow inactivation, and R24565 removes inactivation. (*Insets*) All three mutants introduced a profound latency for activation not seen in the WT.

the bilayer containing MscL, i.e., they resided in a different mechanical domain(s). These measurements provide an absolute measure of energetics of eukaryotic MSC gating.

Why did the mutations slow inactivation? R2456H resides near the cytoplasmic end of the C-terminal transmembrane span (Fig. 1*A*) and might be in the membrane electric field. To investigate whether the loss of charge associated with this mutation might account for the loss of inactivation, we substituted lysine for the arginine found in the WT. The resulting R2456K mutation did not inactivate and also exhibited slow deactivation (channel closing after removal of the stimulus) (Fig. 2 *A* and *B*). Residue charge did not appear to be involved. Interestingly, it is known that arginine can be modified posttranslationally, and the data from R2456K suggest such a biological change could shift the channel kinetics from phasic to tonic (17–19).

We observed some kinetic differences between cell-attached and excised patches suggesting that the cytoskeleton contributes to stress at the channel (20). In cell-attached mode, M2225R inactivated more slowly than in outside-out (O/O) patches (compare Fig. 6 and Fig. S4). The cell-attached response for a multichannel patch illustrating the loss of inactivation for mutant channels is shown in Fig. S4. Fig. 6 *A* and *B* shows data from O/O patches in which inactivation was restored almost completely in M2225R and was restored partially in R2456H. However, differences in the peak/steady-state current ratios remained, showing that the substitutions were not functionally identical. Fig. 6*B* shows a normalized average response, illustrating that the ratio of peak to steady-state current (an approximate assay for the relative rates of inactivation and recovery) is greater for mutants than for WT. We observed some small differences in activation kinetics between cell-attached and excised patches, but hPIEZO1 inactivated in both patch modes, and R2456K did not inactivate in either one (Fig. 6 *A* and *B*). GsMTx4 inhibited the WT and mutant channels in O/O patches (Fig. 7). Because the non-inactivating mutant R2456K was inhibited by GsMTx4, the peptide's ability to inhibit channel activity does not appear to involve the protein region needed for hPEIZO1 inactivation.

Both HX mutations were near the C terminal of hPIEZO1, so we examined the functionality of the whole region by removing it with a stop codon at position 2218 (G2218Stop). Fig. 8 shows that the truncation mutant behaved like R2456K, exhibiting a long latency, slowed or complete loss of inactivation, and very slow deactivation. Because the activation kinetics, other than latency, were largely unaffected, we conclude that the C-terminal region functions as an independent unit responsible for channel closure by inactivation or deactivation and that residue R2456 is a key locus in that region.

Discussion

We have characterized hPIEZO1 in an effort to understand its involvement in xerocytosis (1). The single point mutations slowed inactivation and introduced a long latency followed by activation of groups of channels (Fig. 8*B*). Might these changes lead to the symptoms of HX? One possibility is that they alter the mechanical sensitivity of the channel and thus change the flux of ions that accompanies mechanical stress, particularly as the RBC pass through capillaries. The relationship between cation leakage and hemolytic anemia has been observed for band 3 protein mutations (8). Although these pathways are different, band3 and PIEZO1 mutations may produce hemolytic anemia by the same mechanism.

An important feature of PIEZO1 that may contribute to the clinical presentation is its ability to pass calcium. The net cation flux through hPIEZO1 channels depends on the open time. All the mutations we tested had slower inactivation rates. R2456H had a leftward shift in activation so that it turned on at a lower stress, but M2555R did not. The slowing of the inactivation may be more important than the channel sensitivity to stress. A second, non-

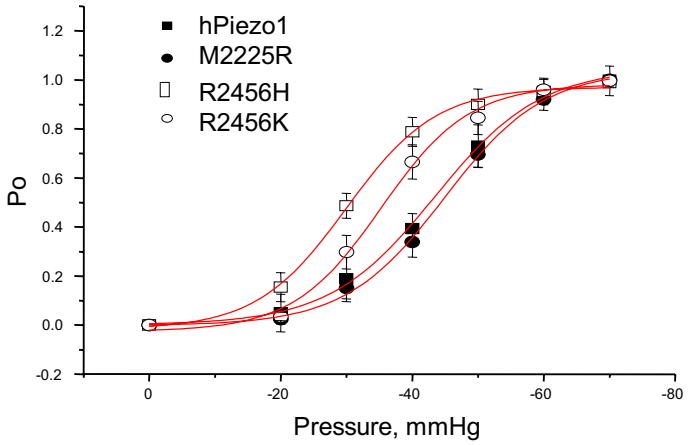

	$P_{1/2}$ (mmHg)	α (mmHg^{-1})	
hPiezo1	-43 ± 0.7	8.1 ± 0.7	n = 10
M2225R	-45 ± 0.6	7.6 ± 0.6	n = 6
R2456H	-30 ± 0.6	6.8 ± 0.4	n =11
R2456K	-35 ± 1.1	6.8 ± 0. 9	n = 7

Fig. 4. Comparison of mechanical sensitivities via peak current vs. suction and fit to a Boltzmann distribution. The mean values ± SD for $P_{1/2}$ and α are shown in the table. The α is approximately the same for the four channels, indicating they have a similar dimensional change between closed and open orientations. Mutations at position 2456 shifted $P_{1/2}$ but the mutation at 2225 did not.

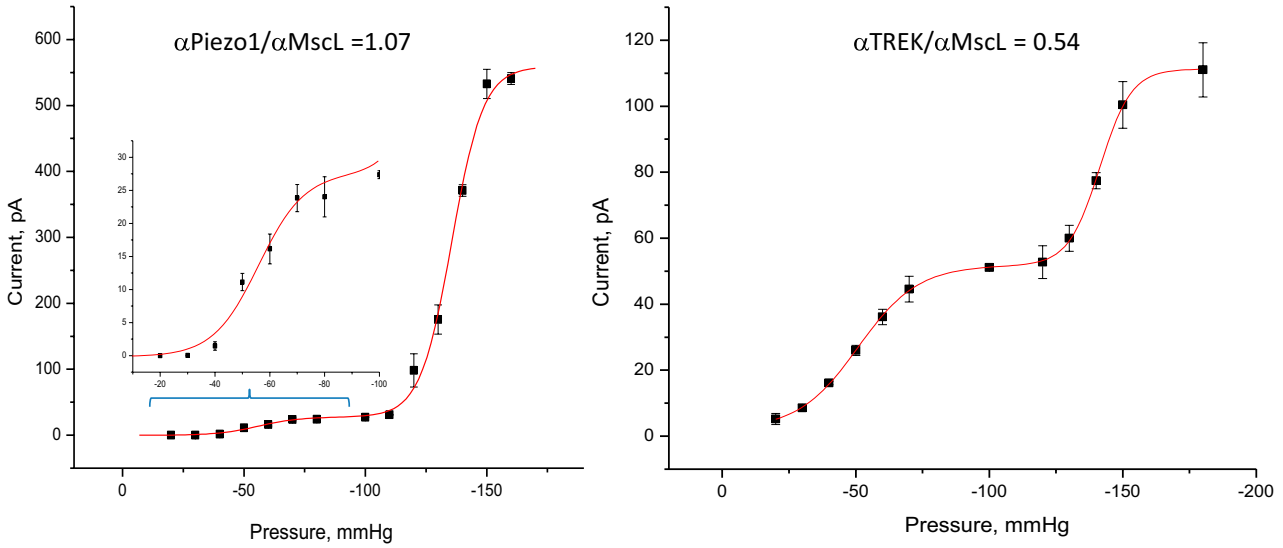

Fig. 5. Comparison of the bacterial channel MscL with Piezo1 or TREK using cotransfection. (*Left*) Current vs. suction for hPIEZO1 and MscL in the same patch. (*Inset*) An expanded view of the hPIEZO1 response curve. (*Right*) The same measurement but using TREK-1. In contrast to hPIEZO1, TREK-1 had a lower ratio of $\alpha_{\text{channel/MscL}}$ indicating either that TREK-1 has smaller dimensional changes or that the local tension around TREK-1 is smaller, as might occur if TREK-1 were in a different domain from PIEZO1.

exclusive possibility is that because of the latency, mutant channels do not activate when needed during capillary transit.

Hydrostatic pressure has been shown to change RBC shape, membrane composition and volume, and to alter the blood flow in small vessels. An influx of Ca^{2+} might alter the stiffness of RBCs (21). The short open-channel lifetime of WT hPIEZO1 restricts significant ion fluxes to the immediate vicinity of the channel, and it is unclear whether such localization is significant.

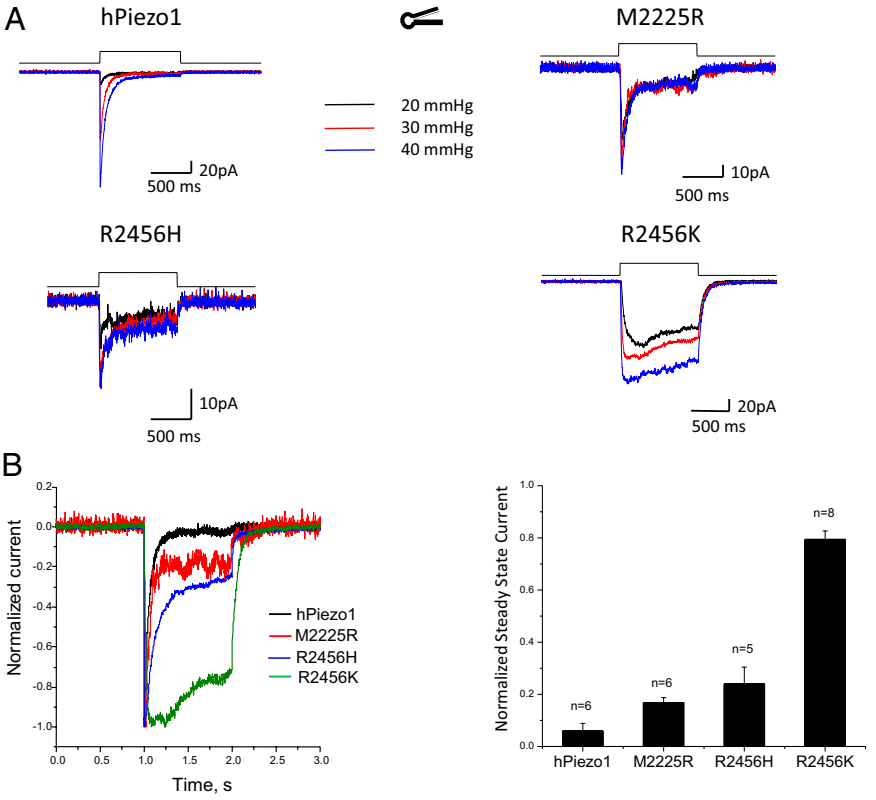

Fig. 6. Response of O/O patches. (*A*) The difference between WT and mutants. M2225R and R2456H have partially restored inactivation; R2456H remains slow; R2456K does not inactivate at all. (*B*) The traces normalized for kinetic comparison. The ratio of peak to steady-state current (bar graph with SD) illustrates that, even with the partial restoration of inactivation, M2225R and R2456H transfer more permeant charge than WT during an opening because of the longer open time. Deactivation (closure upon release of stress) was fast in patches from WT but was slow in mutants.

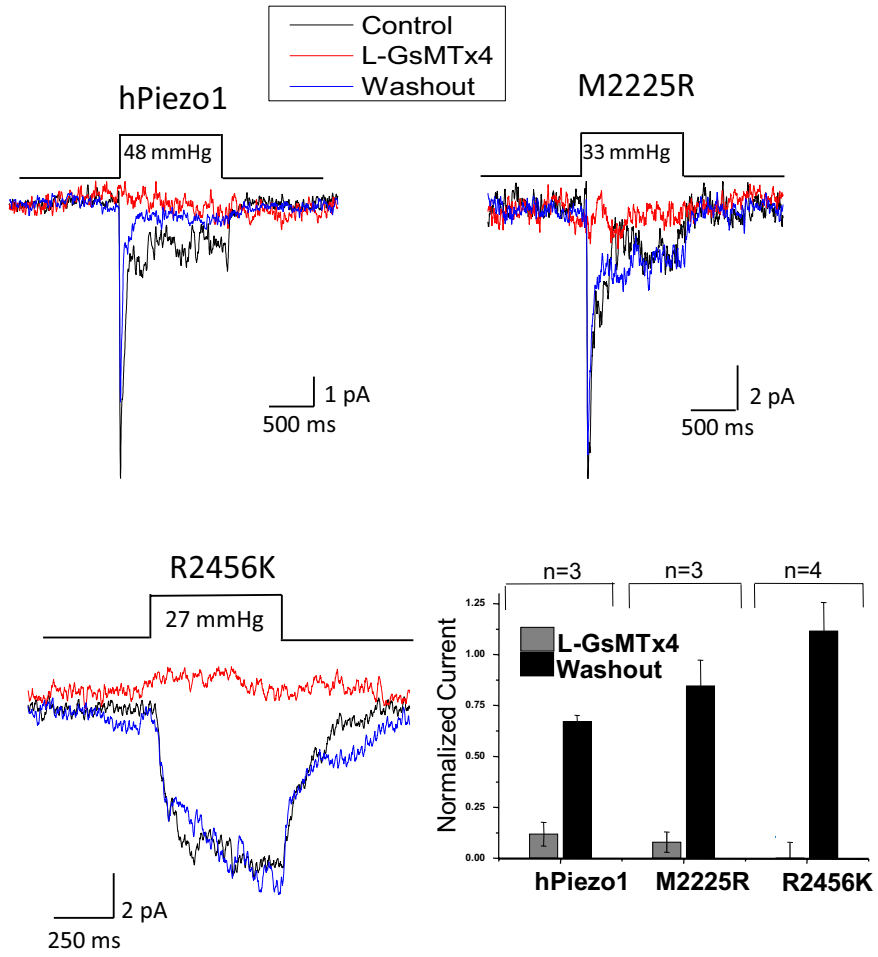

Fig. 7. The peptide L-GsMTx4 (10 μM) reversibly inhibits mutant hPIEZO1 channels in O/O patches from cells transfected with the indicated channels. The bar graph shows the average ± SEM from the indicated number of patches. Note that R2456K did not inactivate but was inhibited, implying that the peptide does not act upon the inactivation domain.

Thus, HX mutations might cause pathology either by too little or too much activation.

The experiments presented in this paper provide molecular details of hPIEZO1 function. Our measurements of α indicate that the dimensional changes associated with opening are similar to those reported for MscL, equivalent to 6–20 nm^2 of in-plane area or an ∼1-nm change in mean radius for a 10-nm diameter channel. If the dimensional changes associated with gating were not global but instead were movements of smaller regions, then there must be a proportionately larger movement to generate the equivalent free energy described by the Boltzmann curves. For the 2D model most commonly used for MSC gating, the free energy available for gating is TΔA where T is bilayer tension and ΔA is the change of area between the closed and open states. These dimensional constraints must be met for any molecular model of hPIEZO1 gating. Because MscL is known to be gated by bilayer tension, we might suppose the same is true for hPIEZO1. If, however, hPIEZO1 were gated by cytoskeleton stress in parallel with the bilayer, the stress on the channel will be decreased because the mean tension is shared. In this case the dimensional changes of hPIEZO1 would have to be larger than MscL to explain the comparable sensitivity. This particular constraint of the dimensional changes does not apply to all MSCs. TREK-1 is half as sensitive as hPIEZO1.

We were surprised that hPIEZO1 appeared to be in discrete physical domains separated from the common bilayer. Channel openings of multiple channels appeared suddenly following a long latency. The channels also often exhibited a collective loss of inactivation (figure 2 in ref. 4 and Fig. 8). As expected for the random sampling of the cell surface by the patch pipette, we occasionally did observe some patches that appeared to have sev-

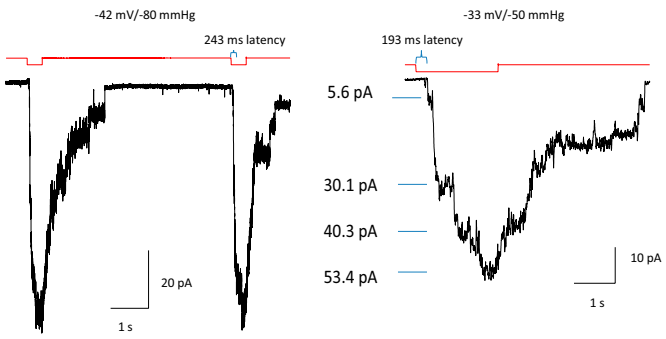

Fig. 8. Removal of the C terminus with a stop codon at position 2218 of hPIEZO1 leads to a non-inactivating form of the channel with pronounced latency, loss of inactivation, and extremely slow deactivation. The slow deactivation might represent the rate for mutant monomers to reassociate. *A* and *B* show the currents from many channels in cell-attached patches, and *B* shows the loss of inactivation in an expanded view. The unitary conductance at −33mV was 73 pS (0.5 mM Mg^{2+} in pipette).

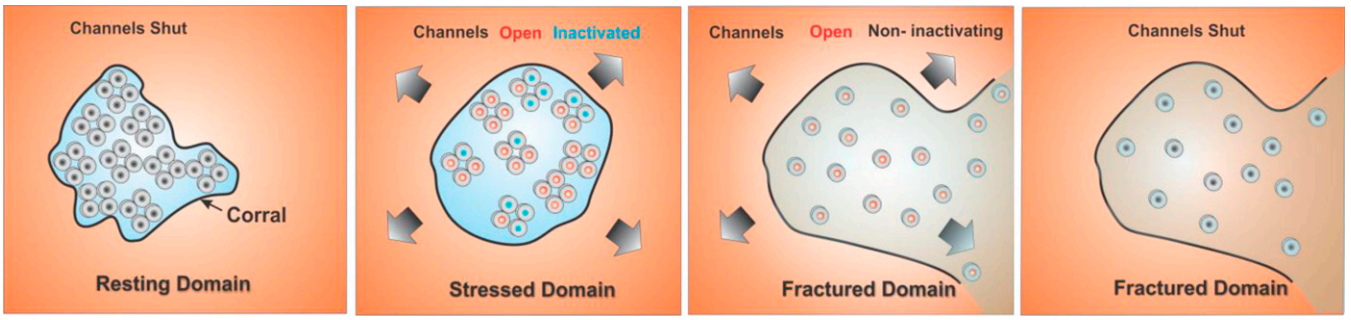

Fig. 9. Cartoon model of how domains might affect channel behavior. We arbitrarily modeled the domain as a cytoskeletal corral. The panel at the far left shows closed WT channels (black) in a domain with a flexible boundary that can transmit external stress without delay. In this domain the channels exist as tetramers. The second panel from the left shows the expansion of the flexible boundary with external tension causing channels to open (red) and to inactivate (blue). The panel third from the left shows what happens when high forces rupture the domain boundary. The channels diffuse outward into the bulk bilayer where the tension is sufficient to activate them, but the tetramers can dissociate. We postulate that inactivation requires channel–channel interactions so the diffusing channels do not inactivate quickly. The right panel shows deactivation in a ruptured domain after tension is removed. In this model, HX mutations would decrease the interchannel-binding energy, allowing easier dissociation. Although the cartoon shows the domain as a corral, the domain may be a lipid phase, caveolae, cytoskeletal structures, or even channel aggregates.

eral domains. In contrast to the mutants, WT hPIEZO1 channels activated without a measurable latency, so the domains of normal resting cells must be able to transmit the applied stimulus coming from the bilayer to the domain interior rapidly without spending time to reform the domain boundary. The collective loss of inactivation and introduction of latency has been observed previously with endogenous MSCs (4, 22). Extreme latencies (with durations in minutes) have been observed for whole-cell mechanically activated currents from heart cells (23). This transition between phasic and tonic kinetics probably represents global changes in the mechanical properties of the domains. However, with high and/or repeated stress the domain boundary can rupture, making the local tension closer to that of the mean bilayer. The modulation of ion channels by lipid microdomains has been described for other channels (24), and the clustering of channels has been noted for many channels such as in the endplate (25).

To simplify the discussion of how domain properties can alter channel kinetics, we made the cartoon model shown in Fig. 9. In this model, the resting domain boundary is folded so there is little line tension, and the external stress is transmitted rapidly to the interior, causing the channels to open and inactivate (second panel from the left). With excessive simulation, the domain ruptures allowing channels to diffuse into the external bilayer (third panel from the left). This diffusion might allow hPIEZO1 tetramers to dissociate, and, if we postulate that inactivation requires interchannel interactions, this dissociation would account for the observed collective loss of inactivation. The forces required for domain rupture are unknown but clearly are less than the lytic limit of the bilayer because the patch remained intact. The actual domains might be cytoskeletal lattices, caveolae, rafts, or other structures, and high-resolution imaging of labeled channels may permit the domains to be visualized (20).

As for the physiological utility of hPIEZO1 in the circulation, the role of hPIEZO1 can be acutely tested in animals using the specific inhibitor GsMTx4 (Fig. 7) (5, 26). A transgenic mouse in which the WT channel has been replaced with the non-inactivating mutant R2456K would make a very interesting test system. hPIEZO1 is one member of the larger PIEZO family (2, 3), and the two HX sites analyzed in this study are conserved in Piezo2 (Fig. 10). Piezo2 is highly expressed in dorsal root ganglia neurons, where its function has been associated with nociception (27). If that channel behaves like hPIEZO1, a transgenic mouse with the same mutations might create a model for chronic pain. Xerocytosis provides an example of how the altered biophysical properties of MSCs can create pathology and illuminates the potential role of these channels in nonsensory tissues.

```
                2225
                 |
hP1    LGGYEPLFTMSAQQPSIPFTA
hP2    LGGYQPIFTMSAQQSQLKIMD

                2456
                 |
hP1   SIVLVIGKFVRGFFSEISHSIMFEEL
hP2   SVVLVIGKFVREFFSGISHSIMFEEL
```

Fig. 10. Sequence comparison between human Piezo1 and Piezo2. The amino acids in Piezo1 involved in xerocytosis also are found in Piezo2. This homology suggests that mutations at these sites in Piezo2 lead to a loss or slowing of inactivation and potential increase in nociception.

Experimental Procedures

Electrophysiology. The bath solution contained (in mM) 145 NaCl, 5 KCl, 3 $MgCl_2$, 1 $CaCl_2$, 10 Hepes (pH 7.3, adjusted with NaOH). The pipette solution contained (in mM) 150 KCl, 0.5 $MgCl_2$, 0.25 EGTA, 10 Hepes (pH 7.3), or, alternatively 150 CsCl, 1 $MgCl_2$, 1 $CaCl_2$, 5 EGTA, 10 Hepes (pH 7.3). Patch pipettes had resistances of 2–5 MΩ. For studies of TREK-1, CsCl was replaced with KCl. The mechanical stimulus for patches was suction applied with a high-speed pressure clamp (HSFC-1; ALA Scientific Instruments) and controlled by QuBIO software (www.qub.buffalo.edu). HEK293 cells were transfected with 250 ng cDNA using Fugene (Roche Diagnostic) and were tested 24–48 h later. GsMTx4 was synthesized, folded, and purified as previously described (26, 28) and was applied to cells through an ALA perfusion system controlled by QuBIO (www.qub.buffalo.edu). All experiments were done at room temperature.

Whole-cell and patch-clamp experiments were performed using an Axopatch 200B amplifier (Axon Instruments) controlled by QuBIO, sampled at 10 kHz, and filtered at 2 kHz. The dose–response data for two different types of channels in a single patch were fit using the sum of two Boltzmann equations, one for each type of channel:

$$I = A + Im1^{*}\left[1 - \frac{1}{\left(1 + e^{\left(\frac{P1-P}{a1}\right)}\right)}\right] + Im2^{*}\left[1 - \frac{1}{\left(1 + e^{\left(\frac{P2-P}{a2}\right)}\right)}\right],$$

where *Imi* is the maximum available current for each channel type *i*, P_i is the pressure at half activation, α_i is the slope sensitivity, and *A* is an instrumental offset. Whole-cell mechanical stimulation used indentation with a fire-polished

glass pipette (tip diameter 2–4 μm) positioned at an angle of 45° to the coverslip. A computer-controlled micromanipulator (MP-285; Sutter Instruments Co.) with LabVIEW software provided coarse positioning of the probe to ∼30 μm from the cell. From there, a further rapid downward trapezoidal waveform of indentation was driven by a piezoelectric stage (P-280.20 XYZ NanoPositioners; Physik Instrumente). We define the mechanical threshold as the depth at which the probe visibly deformed the cell. The probe velocity was 0.56 μm/ms during the upward and downward movements, and the steady indentation was held constant for 400 ms. The stimulus was repeated with 0.5-μm increments every 6 s. The holding potential generally was −60 mV.

Molecular Cloning of HEK hPIEZO1. Total RNA was extracted from HEK293 cells using Quick-RNA MicroPrep (Zymo Research) and was converted to cDNA using the SuperScript III First Strand Synthesis System (Invitrogen). The hPIEZO1 gene was first amplified for 30 cycles using primers 5′-atggagccgcacgtgctcgg-3′ and 5′-ctactccttctcacgagtcc-3′ (designed from NM_001142864). A second round of amplification for 30 cycles used primers with 5′ linkers containing the Nt BbvCI sequence 5′-tcagcaagggctgagg-3′ and 5′-tcagcggaagctgagg-3′. The vector internal ribosome entry site 2 (IRES2)-EGFP was modified to include NtBbvCI sites according to the ligation-independent cloning method using nicking DNA endonuclease (29). Both the hPIEZO1 PCR product and the modified IRES2-EGFP were cut with NtBbvCI in one tube. After 8 h, the enzymes were deactivated by heating to 80 °C for 30 min and then were allowed to cool to room temperature. The DNA was transformed into Dh5Alpha cells (Invitrogen). The amplified DNA sequence of the WT hPIEZO1 cDNA was validated to ensure absence of unwanted mutations introduced by PCR amplification.

Mutagenesis of hPIEZO1. HEK-293 hPIEZO1 mutants M2225R, R2456H, and R2456K were made using the QuikChange XL site-mutagenesis kit (Agilent Technologies) according to the manufacturer's specifications. Primers used were M2225R forward, agccgctgttcaccaggagcgcccagcag; M2225R reverse, ggctgctgggcgctcctggtgaacagcgg; R2456H forward, tcggcaagttcgtgcacggattcttcagc; R2456H reverse, tctcgctaagaatccgtgcacgaacttgc; R2456K forward, tcggcaagttcgtgaagggattcttcagcgagatc; R2456K reverse, ctcgctgaagaatcccttcacgaacttgccgatgacc; G2218Stop forward, caccctgaagctgggctaatatgagccgctgttcacc; and G2218Stop reverse, ggtggacagcggctcatattagcccagcttcagggtg.

ACKNOWLEDGMENTS. We thank Dr. Steve Besch for help in the Boltzmann analysis, Joanne Pazik and Lynn Zeigler for expert technical assistance on the molecular biology, Julia Doerner from David Clapham's laboratory for sharing the eukaryotic vector for expression of the MscL channel, and Drs. Sidney Simon and Seth Alper for extensive editing. This work was supported by the National Institutes of Health, the Department of Defense, and the Children's Guild of Buffalo.

1. Zarychanski Y, et al. (2012) Mutations in the mechanotransduction protein PIEZO1 are associated with hereditary xerocytosis. *Blood* 120(9):1908–1915.
2. Coste B, et al. (2010) Piezo1 and Piezo2 are essential components of distinct mechanically activated cation channels. *Science* 330(6000):55–60.
3. Coste B, et al. (2012) Piezo proteins are pore-forming subunits of mechanically activated channels. *Nature* 483(7388):176–181.
4. Gottlieb PA, Bae C, Sachs F (2012) Gating the mechanical channel Piezo1: A comparison between whole-cell and patch recording. *Channels (Austin)* 6(4):282–289.
5. Bae C, Sachs F, Gottlieb PA (2011) The mechanosensitive ion channel Piezo1 is inhibited by the peptide GsMTx4. *Biochemistry* 50(29):6295–6300.
6. Chiang CS, Anishkin A, Sukharev S (2004) Gating of the large mechanosensitive channel in situ: Estimation of the spatial scale of the transition from channel population responses. *Biophys J* 86(5):2846–2861.
7. Sukharev SI, Sigurdson WJ, Kung C, Sachs F (1999) Energetic and spatial parameters for gating of the bacterial large conductance mechanosensitive channel, MscL. *J Gen Physiol* 113(4):525–540.
8. Bruce LJ, et al. (2005) Monovalent cation leaks in human red cells caused by single amino-acid substitutions in the transport domain of the band 3 chloride-bicarbonate exchanger, AE1. *Nat Genet* 37(11):1258–1263.
9. Gottlieb PA, Sachs F (2012) Piezo1: Properties of a cation selective mechanical channel. *Channels (Austin)* 6(4):214–219.
10. Dedman A, et al. (2009) The mechano-gated K(2P) channel TREK-1. *Eur Biophys J* 38(3):293–303.
11. Patel A, Honore E (2002) The TREK two P domain K+ channels. *J Physiol* 539(Pt 3):647.
12. Lauritzen I, et al. (2005) Cross-talk between the mechano-gated K2P channel TREK-1 and the actin cytoskeleton. *EMBO Rep* 6(7):642–648.
13. Markin VS, Sachs F (2004) Thermodynamics of mechanosensitivity. *Phys Biol* 1(1-2): 110–124.
14. Doerner JF, Febvay S, Clapham DE (2012) Controlled delivery of bioactive molecules into live cells using the bacterial mechanosensitive channel MscL. *Nature communications* 3:990.
15. Martinac B (2011) Bacterial mechanosensitive channels as a paradigm for mechanosensory transduction. *Cell Physiol Biochem* 28(6):1051–1060.
16. Moe P, Blount P (2005) Assessment of potential stimuli for mechano-dependent gating of MscL: Effects of pressure, tension, and lipid headgroups. *Biochemistry* 44(36):12239–12244.
17. Bedford MT, Richard S (2005) Arginine methylation an emerging regulator of protein function. *Mol Cell* 18(3):263–272.
18. Bedford MT, Clarke SG (2009) Protein arginine methylation in mammals: Who, what, and why. *Mol Cell* 33(1):1–13.
19. Koch-Nolte F, et al. (2006) ADP-ribosylation of membrane proteins: Unveiling the secrets of a crucial regulatory mechanism in mammalian cells. *Ann Med* 38(3): 188–199.
20. Suchyna TM, Markin VS, Sachs F (2009) Biophysics and structure of the patch and the gigaseal. *Biophys J* 97(3):738–747.
21. Barshtein G, Bergelson L, Dagan A, Gratton E, Yedgar S (1997) Membrane lipid order of human red blood cells is altered by physiological levels of hydrostatic pressure. *Am J Physiol* 272(1 Pt 2):H538–H543.
22. Hamill OP, McBride DW, Jr. (1997) Mechanogated channels in Xenopus oocytes: Different gating modes enable a channel to switch from a phasic to a tonic mechanotransducer. *Biol Bull* 192(1):121–122.
23. Bett GC, Sachs F (2000) Whole-cell mechanosensitive currents in rat ventricular myocytes activated by direct stimulation. *J Membr Biol* 173(3):255–263.
24. Dart C (2010) Lipid microdomains and the regulation of ion channel function. *J Physiol* 588(Pt 17):3169–3178.
25. Pan NC, Ma JJ, Peng HB (2012) Mechanosensitivity of nicotinic receptors. *Pflugers Arch* 464(2):193–203.
26. Suchyna TM, et al. (2004) Bilayer-dependent inhibition of mechanosensitive channels by neuroactive peptide enantiomers. *Nature* 430(6996):235–240.
27. Kim SE, Coste B, Chadha A, Cook B, Patapoutian A (2012) The role of Drosophila Piezo in mechanical nociception. *Nature* 483(7388):209–212.
28. Ostrow KL, et al. (2003) cDNA sequence and in vitro folding of GsMTx4, a specific peptide inhibitor of mechanosensitive channels. *Toxicon* 42(3):263–274.
29. Yang J, Zhang Z, Zhang XA, Luo Q (2010) A ligation-independent cloning method using nicking DNA endonuclease. *Biotechniques* 49(5):817–821.

Human PIEZO1: Removing Inactivation

Chilman Bae, Philip A. Gottlieb, and Frederick Sachs*
Department of Physiology and Biophysics and The Center for Single Molecule Biophysics, State University of New York at Buffalo, Buffalo, New York

ABSTRACT PIEZO1 is an inactivating eukaryotic cation-selective mechanosensitive ion channel. Two sites have been located in the channel that when individually mutated lead to xerocytotic anemia by slowing inactivation. By introducing mutations at two sites, one associated with xerocytosis and the other artificial, we were able to remove inactivation. The double mutant (DhPIEZO1) has a substitution of arginine for methionine (M2225R) and lysine for arginine (R2456K). The loss of inactivation was accompanied by ~30-mmHg shift of the activation curve to lower pressures and slower rates of deactivation. The slope sensitivity of gating was the same for wild-type and mutants, indicating that the dimensional changes between the closed and open state are unaffected by the mutations. The unitary channel conductance was unchanged by mutations, so these sites are not associated with pore. DhPIEZO1 was reversibly inhibited by the peptide GsMTx4 that acted as a gating modifier. The channel kinetics were solved using complex stimulus waveforms and the data fit to a three-state loop in detailed balance. The reaction had two pressure-dependent rates, *closed* to *open* and *inactivated* to *closed*. Pressure sensitivity of the opening rate with no sensitivity of the closing rate means that the energy barrier between them is located near the open state. Mutant cycle analysis of inactivation showed that the two sites interacted strongly, even though they are postulated to be on opposite sides of the membrane.

INTRODUCTION

PIEZO1 is a eukaryotic mechanosensitive cation-selective channel (1–3) of ~2500 amino acids containing 30 putative transmembrane domains (1,4,5). It has electrophysiological properties similar to many endogenous cationic mechanosensitive ion channels (MSCs), with a reversal potential around 0 mV, voltage-dependent inactivation, and inhibition by the peptide GsMTx4 (6,7). PIEZO1 forms homotetrameric aggregates (2), but it is not known whether the pore is located in the monomers or at the interfaces.

The channel is sensitive to its physical environment because the gating kinetics are not identical in patch and whole-cell recordings (8). The channels appear to exist in physical domains that can be fractured at stresses below the lytic strength of the bilayer (7). The domains might consist of clusters of channels, lipid phases, or cytoskeletal corrals (9).

Mutations (M2225R and R2456H) that produce human hereditary xerocytosis (an autosomal dominant anemia) have slower inactivation rates than wild-type (WT) (7,10,11) and an increased latency to activation (7). The longer open times due to slow inactivation will produce the larger cation fluxes that seem to be associated with hereditary xerocytosis (7,10,11), but longer latencies will reduce the flux for transient stimulations such as passage through capillaries. The mutations do not seem to act via changes in residue charge because the conservative mutation of arginine to lysine at position 2456 slowed inactivation.

A double mutant, DhPIEZO1, substitutes an arginine for a methionine at position 2225 (M2225R), which is associated with hereditary xerocytosis, and a lysine for an arginine at position 2456 (R2456K), which we created. The single-site mutants inactivated slower than WT (7), but the double mutant did not inactivate at all. To examine whether the two sites interacted to produce the loss of inactivation, we did a mutant cycle analysis and estimated the free energy for inactivation for WT, single-site mutants, and the double mutant. The analysis shows a strong interaction.

Other properties of DhPIEZO1 were similar to WT, including the near-zero Na/K reversal potential and inhibition by GsMTx4. The gating curves (the Boltzmann relationship of open probability vs. pressure) showed that the dimensional change between closed and open states was similar to WT, although the midpoint of the gating curve was shifted to lower pressures. The channel kinetics of all channel types, even for complex stimuli, could be fit with a simple three-state closed loop model (closed–open–inactivated) in detailed balance with only two pressure-dependent rates.

MATERIALS AND METHODS

The bath solution contained (in mM) 150 NaCl, 5 KCl, 1 $MgCl_2$, 2.5 $CaCl_2$, 10 HEPES, pH 7.4 (adjusted with NaOH). The pipette solution contained (in mM) 150 CsCl, 10 HEPES, 5.0 EGTA, 1.0 $MgCl_2$, 1.0 $CaCl_2$, pH 7.3 (adjusted with CsOH), or 150 KCl, 10 HEPES, 0.25 EGTA, 0.5 $MgCl_2$, pH 7.3 (adjusted with KOH). Patch pipettes had resistances of 2–5 MΩ. The mechanical stimulus for patches was pipette suction for cell-attached patches and pipette pressure for outside-out patches. All pressure stimuli were applied by a high-speed pressure clamp (ALA Scientific Instruments, Farmingdale, NY). Whole-cell and patch-clamp currents were recorded using an Axopatch 200B amplifier (Axon Instruments), sampled at 10 kHz,

Submitted May 8, 2013, and accepted for publication July 16, 2013.

*Correspondence: Sachs@buffalo.edu

Editor: Michael Pusch

0006-3495/13/08/0880/7 $2.00

http://dx.doi.org/10.1016/j.bpj.2013.07.019

and low pass filtered at 1 kHz. Patch capacitance and conductance were measured as previously described (12,13) using an EG&G 5208 two-phase lock-in analyzer (Oak Ridge, TN).

The dose–response data were fit to a Boltzmann relationship, and when we had two different types of channels in a patch, the data were fit to the sum of two Boltzmann functions:

$$I = A + Im_1 \times \left[1 - \frac{1}{1 + e^{(q_1 \times (p_1 - p))}}\right] + Im_2 \times \left[1 - \frac{1}{1 + e^{(q_2 \times (p_2 - p))}}\right],$$

where Im_i is the maximum available current for channel type i, p_i is the pressure at half activation, q_i is the slope sensitivity, and A is an instrumental offset.

Whole-cell mechanical stimulation used a fire-polished glass pipette (diameter of 2–4 μm) positioned at an angle of 30° with respect to the cover glass to press on voltage clamped cells. The probe was coarsely positioned ~15 μm above the cell; from that position, we applied a trapezoidal downward waveform with a piezoelectric stage (P-280.20 XYZ NanoPositioner, Physik Instrumente). The indentation depth with 40-nm resolution was controlled using LabVIEW. The probe velocity was 0.15 μm/ms during transitions, and the indentation was held constant for 300 ms. Currents were generally recorded at a holding potential of −60 mV at room temperature. Hypotonic swelling was initiated by adding distilled water in equal volume to the bath solution.

To compute the channel kinetics, we applied a series of square suction pulses with variable off times (3.0, 2.0, 1.0, 0.5, 0.25, 0.1 s, and the reverse) usually in the cell-attached mode. These multichannel currents were analyzed using the MAC routine of QuB software (www.qub.buffalo.edu).

HEK-293 cells were transfected with 750 ng cDNA using Fugene (Roche Diagnostic, Indianapolis, IN) according to manufacturer's specification and transfected cells were tested 24–48 h later. The peptide GsMTx4 was synthesized, folded, and purified as previously described (14) and applied through an ALA perfusion system. Data acquisition and stimulation were all controlled by QUBIO software (www.qub.buffalo.edu).

RESULTS

Whole-cell data

At a given membrane potential, the currents increased with indentation depth (Fig. 1, *A* and *B*). In contrast to the WT channel (Fig. 1 *A*) and the single-site mutants (M2225R and R2456K) (7) that displayed faster or slower inactivation, respectively, DhPIEZO1 produced a steady-state current with sustained indentation (Fig. 1 *B*). DhPIEZO1 currents are mechanically sensitive, have no inactivation, and relative to WT, the channels are sensitized toward the open state. The fact that the DhPIEZO1 current persisted in steady state suggests that in the domains containing the channels there is no time-dependent adaptation of the local stimulus (13,15).

Osmotic pressure is often applied as an alternative stimulus to direct mechanical stimulation, but much of the osmotic stress is contained in the deep cytoskeleton, not the bilayer (16), so osmotic pressure is not an equivalent stimulus to direct stress. Nonetheless, we have found that hypoosmotic

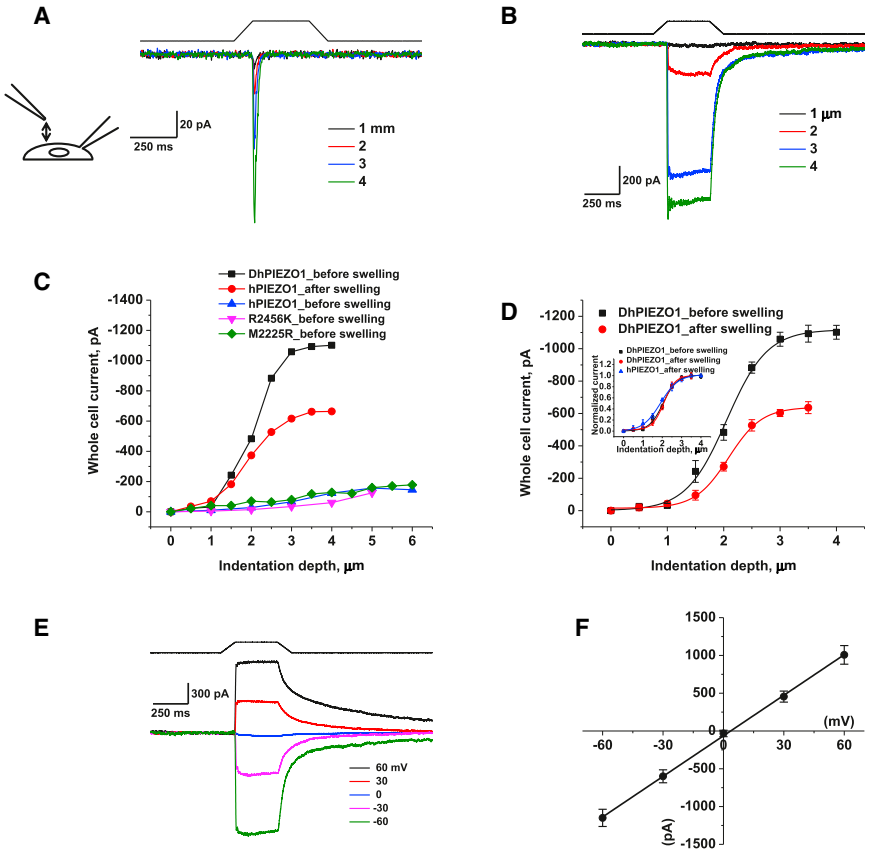

FIGURE 1 DhPIEZO1 does not inactivate. *(A)* Whole-cell currents of WT hPIEZO1 rapidly inactivate. *(B)* Whole-cell currents of DhPIEZO1 as a function of indentation depth showed no inactivation. Note the slow rate of deactivation after the stimulus is removed. *(C)* WT channels are sensitive to hypotonic swelling. Prior to swelling, there was less current for the same incremental indentation than after swelling. Also shown is the response of DhPIEZO1 prior to swelling. *(D)* Comparison of DhPIEZO1 responses before and after hypotonic swelling with 50% osmolarity. The inset shows the same data normalized. The sensitivity to indentation is similar, suggesting that the channels are already near a saturated level of stress in the resting state. *(E)* Deactivation is extremely slow and voltage independent. Deactivation for this channel may represent the kinetics of domain reformation rather than channel kinetics. *(F)* The I/V curve of peak currents shows a reversal potential near 0 mV for DhPIEZO1, indicating that the mutations do not affect the pore.

pressure increased the sensitivity of WT hPIEZO (Fig. 1 *C*) similar to results reported for the mouse channel (mPIEZO1) (8). In contrast, DhPIEZO1 proved insensitive to cell swelling, even when 50% distilled water was added to the bath (Fig. 1, *C* and *D*). This implies that the resting stress in the channel (prestress) is nearly saturated.

Because the rate of inactivation in WT and single-site mutants is voltage sensitive (1,6–8), we examined DhPIEZO1 from −60 to +60 mV. Fig. 1 *E* shows that the rate of inactivation was close to zero at all potentials. DhPIEZO1 *deactivation* was extremely slow relative to that of single-site mutants and WT, suggesting a structural correlation between inactivation and deactivation. All channel types had a similar ionic selectivity with a Na/K reversal potential of ~0 mV (Fig. 1 *F*), so that the mutations are not likely to be located near the pore.

Patch data

Cell-attached patches of DhPIEZO1 are mechanically sensitive and showed no inactivation, but had an increased latency for activation. The steady-state gating curve of DhPIEZO1 (Fig. 2 *A*) in patches was well fit by a Boltzmann function of $I = A + I_{max} \times (1 - 1/(1 + \exp(q \times (p - p_{1/2}))))$, where I_{max} is the maximum available current, p is the pressure, $p_{1/2}$ is the pressure at half activation, and q is the slope sensitivity to pressure. For DhPIEZO1, $p_{1/2} = -9.9 \pm 0.6$ mmHg, and the slope sensitivity, q, was 0.15 ± 0.01 mmHg^{-1} (*SD*, $n = 12$). For WT, the midpoint $p_{1/2} = -38.1 \pm 0.4$ mmHg and $q = 0.15 \pm 0.01$ mmHg^{-1} (*SD*, $n = 18$) comparable to previously measured values (7). The q-values of all channel types were the same, implying that the dimensional changes between the closed and open states are the same. The decrease in $p_{1/2}$ with constant q implies that the mutations added resting stress to the structure (prestress), favoring the open state. In terms of energy, the data indicate that the mutations decreased the energy of the open state while maintaining the difference in energy between the closed state and the barrier peak.

To calibrate the absolute sensitivity of DhPIEZO1, we cotransfected cells with a eukaryotic-expressing bacterial MSC called MscL that has been calibrated in bilayers (17,18). These cotransfection data were fit to the sum of two Boltzmanns, simultaneously solving for q and $p_{1/2}$ for both channels in the same patch (see *inset* in Fig. 2 *B*). The ratio of slope sensitivities for DhPIEZO1 to MscL was 0.98 ($n = 5$), so that both channels had similar dimensional changes between the closed and open states, equivalent to 20 nm^2 of in-plane area (17,19).

DhPIEZO1 was highly sensitive to the absolute level of pressure as a result of the leftward shift of the dose–response curve for pressure. A typical single-channel recording (Fig. 3 *A*) shows that a 3-mmHg change of suction, from −12 to −15 mmHg, resulted in a significant change in the number of active channels. These data were fit to a

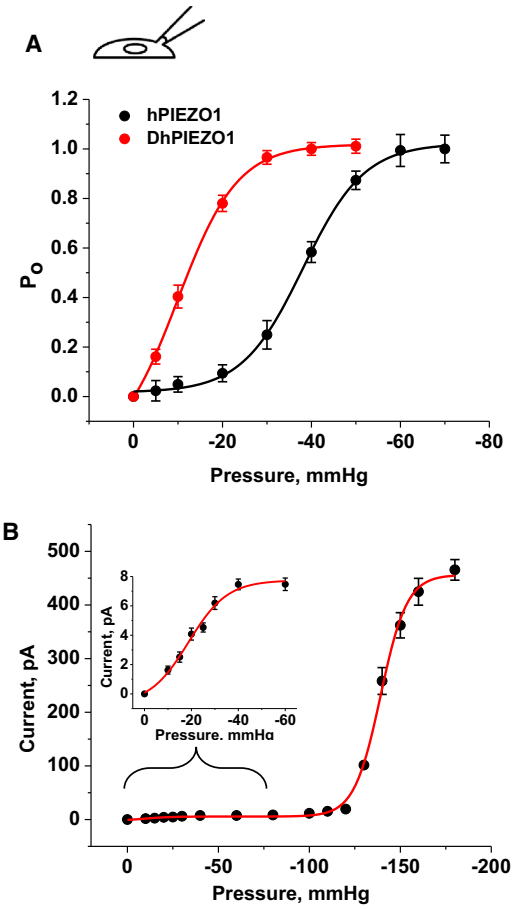

FIGURE 2 *(A)* The gating curve as a function of pressure fit to a Boltzmann. $p_{1/2}$ and the slope sensitivity q are indicated in the table. q is a measure of the dimensional change between closed and open states. q is the same for DhPIEZO1 ($n = 12$), WT ($n = 18$), and the single-site mutants, implying that the mutations have no effect on the key activation processes. However, $p_{1/2}$ was left-shifted relative to WT, representing a change in the intrinsic stress of the channel environment favoring the opening state. *(B)* To calibrate the absolute stress sensitivity, we cotransfected cells with bacterial MscL (7) and DhPIEZO1. Fit to a sum of two Boltzmanns, the slope sensitivities of both channels were nearly identical ($n = 5$), meaning that the dimensional changes of both channels are similar and also similar to WT and single-site mutants. The dimensional changes are equivalent to an in-plane area change of 20 nm^2.The inset shows an expansion of the region containing DhPIEZO1's response.

two-state model with a pressure-dependent opening rate and the same slope sensitivity as WT (Fig. 3 *A*). This extreme sensitivity is interesting considering that the resting patch is already under a large resting tension on the order of 1 to 2 mN/m because of adhesion of the gigaseal (15,20,21). Consistent with the higher absolute sensitivity of DhPIEZO1, we observed an increase in spontaneous openings (Fig. 3 *B*).

In contrast to WT channels that had no measurable latency for activation, DhPIEZO1 had a pronounced latency of ~250–350 ms followed by sudden activation (Fig. 3, *B* and *C*). The kinetics of the activation cannot be fit by simply adding more closed states prior to opening. We have proposed that the observed latency represents the time required

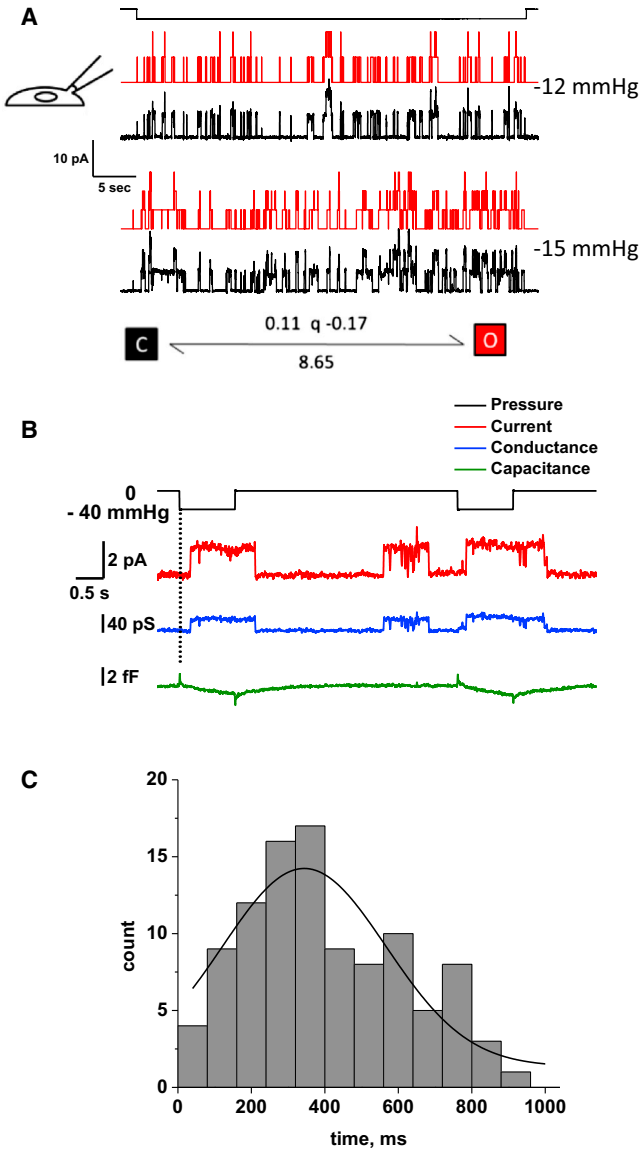

FIGURE 3 *(A)* DhPIEZO1 single-channel currents show high pressure sensitivity because of the left shift in the gating curve. The current trace is shown in black and the theoretical fit is in red. With a change of only 3 mmHg, there is a significant increase in the number of open channels. The kinetics are well fit by a two-state model with only the activation rate being pressure dependent. *(B)* Single-channel currents of DhPIEZO1 have a pronounced latency for activation, and this occurs with no significant change in patch capacitance, suggesting that the latency does not arise from large changes in the patch structure. The capacitance measuring noise level was 0.12 fF RMS, equivalent to ~0.012 μm^2 (assuming a specific capacitance of 1 $\mu F/cm^2$, or 10 $fF/\mu m^2$). Note the spontaneous (background) channel openings of DhPIEZO1 during the recording that is a result of its higher absolute sensitivity and tension from the gigaseal. *(C)* The distribution of latencies fit to a Gaussian gives a mean latency of 344 ± 133 ms. We attribute these latencies to the time required for domain fracture under stress.

for the domain boundary to fracture and to change the stress on the channels (7). A change in the domain, such as fracturing a caveolus, might produce a change in area and hence a change in patch impedance. We tried to measure such a change (12,13) but we observed none (Fig. 3 *B*). The measurement noise level placed an upper limit on any area change to $< 0.01\ \mu m^2$. This suggests that the domain fracture probably did not involve opening of a vesicular structure such as a caveolus.

Inhibition by GsMTx4

PIEZO1 currents are reversibly inhibited by the D-enantiomer of GsMTx4, a specific inhibitor of cationic MSCs (6,22). The lower graph of Fig. 4 *A* shows whole-cell peak

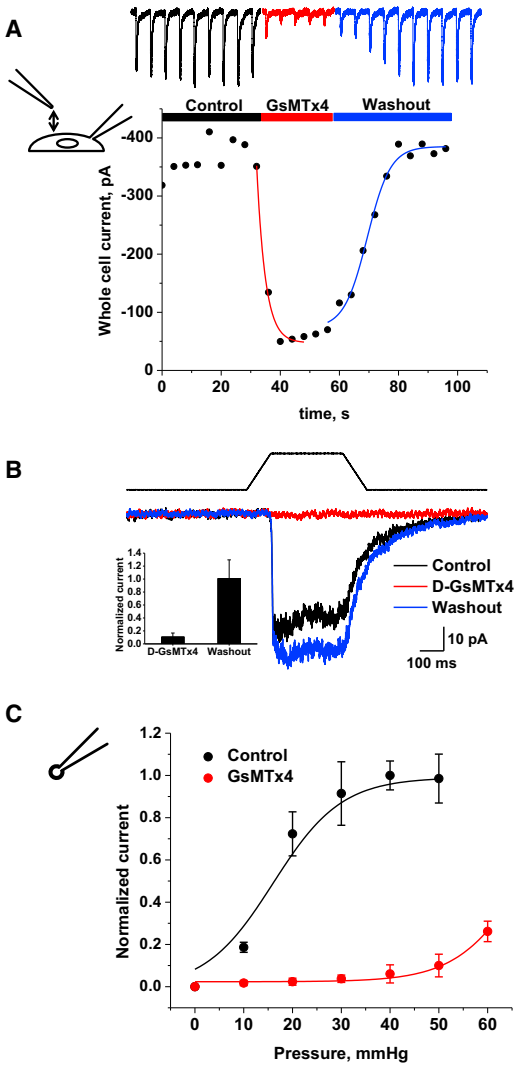

FIGURE 4 DhPIEZO1 channels in whole-cell patches were reversibly inhibited by 10 μM extracellular D-GsMTx4. *(A)* By fitting exponentials, we extracted a mean association time constant of 3.0 ± 0.6 s and a mean dissociation time constant of 13.4 ± 0.8 s ($n = 4$). The estimated association and dissociation rates are $2.6 \times 10^4\ M^{-1}\ s^{-1}$ and $0.08\ s^{-1}$, respectively, and the equilibrium constant calculated from the ratio is K_D ~3 μM. *(B)* D-GsMTx4 inhibition of DhPIEZO1 in the absence of inactivation. This suggests that the mechanism of action of D-GsMTx4 does not involve inactivation domains. The bar graph *(inset)* shows the average peak currents ± *SD* ($n = 3$) illustrated in Fig. 4 *B*. *(C)* The dose–response relationship shifts to higher stress with GsMTx4, as expected for a gating modifier (12).

currents as a function of time from GsMTx4 exposure through washout. From single exponential fits, the association time constant was 3.0 ± 0.63 s and the dissociation time constant was 13.4 ± 0.76 s. The ratio gives an equilibrium affinity of ~3 μm. Fig. 4 *B* shows that D-GsMTx4 inhibition occurs in the absence of inactivation so that the peptide does not seem to interact with the inactivation domain(s) of the channel. At −60 mV, 10 μM GsMTx4 caused an 89% reduction in peak current (Fig. 4 *B*). In outside-out patches (Fig. 4 *C*), the inhibition was >90%. GsMTx4 is a gating modifier acting on closed channels (6), and we estimated its efficacy to be equivalent to ~60 mmHg by the increase of suction required to obtain equal channel activity with and without GsMTx4.

Channel kinetics: Cell-attached patches

We stimulated the patch with a series of square suction pulses with varying time intervals between them (typically 3.0, 2.0, 1.0, 0.5, 0.25, 0.1 s, and the reverse). The response to the entire sequence could be fit using the MAC routine of QuB (www.qub.buffalo.edu). This nonstationary approach has many advantages over traditional single- or double-step analyses in that the responses need not reach equilibrium before the next pulse is applied. Furthermore, the fit is a global optimum for the entire sequence (i.e., the series is treated as a single stimulus; see Fig. 5 *A*).

DhPIEZO1 kinetics were fit with a simple three-state loop model (closed, open, and inactivated) in detailed balance (at all stimuli). To simplify comparison of the kinetics to WT and single-site mutations that required three states, we fit the DhPIEZO1 kinetics to the three-state model even though it had no inactivation. Detailed balance in a loop requires a minimum of two pressure-dependent rates, and we found we could satisfy that constraint with a pressure-dependent opening rate and inactivated-closed rate (Fig. 5 *B*). One of the most striking results of the kinetic analysis was that all channel types had identical slope sensitivities, q = 0.15 ± 0.005 $mmHg^{-1}$ (Fig. 5 *B*) so that the conformational change between the closed and open states of all channels was identical. Furthermore, all the channels had to be in domains with similar local stress. The preexponential coefficients of the activation rates were 10×10^{-3} s^{-1}, 4.62×10^{-3} s^{-1}, 6.13×10^{-3} s^{-1}, and 3.28×10^{-3} s^{-1} in hPIEZO1, M2225, R2456K, and DhPIEZO1, respectively, at −60mV. The mutations had little or no effect on the

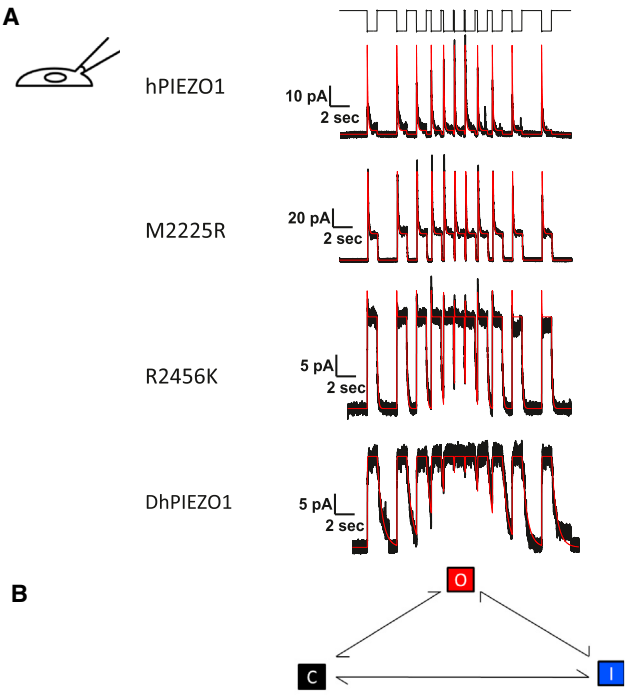

st1 →	st2	hPIEZO1	M2225R	R2456K	DhPIEZO1
C	O	0.01 q -0.16	4.62e-3 q -0.15	6.13e-3 q -0.15	3.28e-3 q -0.15
O	C	1.12	1.45	8.86	2.06
O	I	8.59	12.19	2.84	5.40E-04
I	O	1.19	4.40	115.1	141.46
I	C	73.77 q 0.16	153.40 q 0.15	4408.20 q 0.15	1888.80 q 0.15
C	I	3.28	1.35	0.08	1.22E-05

FIGURE 5 Channel kinetics. *(A)* Multichannel currents for different types of channels. The stimulus was a series of square pressure pulses applied with varying off intervals (typically 3.0, 2.0, 1.0, 0.5, 0.25, 0.1 s, and the reverse, *top trace*). Pressure pulses were 0 to −70 mmHg for HPIEZO1, 2555R PIEZO1, and 2456K PIEZO. For DhPIEZO1, they were 0 to –40 mmHg. The data trace is in black and the QuB fit in red. Notice how hPIEZO1 effectively summed currents from the applied stresses at short off-times of the stimulus. However, the mutant M2225R tended to accumulate inactivation in the same part of the stimulus (lower peaks at shortest resting intervals), but this can be accounted for simply by a change in the rate constants and requires no additional states. The kinetic parameters that characterize the behavior of all channels are presented in *(B)*. *(B)* Tabulation of the quantified kinetics with the three-state loop in detailed balance. The states are named C =closed state, O = open state, and I = inactivated state. Although DhPIEZO1 does not appear to have an inactivated state, we included it for consistency to better compare the models. The pressure dependence for all channel types is contained in the opening rate and the inactivated-closed rate. The pressure sensitivity of the rates is indicated by the parameter q [$mmHg^{-1}$]. q was consistent across all types of channels at ~0.15 so that the conformation associated with opening in all channel types is identical. The DhPIEZO1 trace ends with a jump that is probably closure of the last open channel.

0-mmHg opening rates (the preexponential coefficients). Because the preexponential term contains the entropy of activation, we infer that the mutations also did not change that component of the free energy.

Inactivation is fast in hPIEZO1, M2225R, and R2456K (12.7 s^{-1}, 9.8 s^{-1}, 12.4 s^{-1} at −60 mV, respectively), and DhPIEZO1 effectively did not inactivate ($< 1.6 \times 10^{-6}$ s^{-1} at −60 mV). When we examined deactivation, hPIEZO1 and M2225R were faster than the pressure clamp's response time, but R2456K was slow enough to measure (6.2 s^{-1}), and DhPIEZO1 was even slower (2.4 s^{-1}). Deactivation represents the process of going from open to closed and is characterized by the energy difference between the open state and the energy barrier between the open and closed state. If the change in deactivation rate was due to a change in barrier height, we would expect that the slope sensitivity for opening, q, would also change, but it did not, so the change in deactivation rate appears to represent changes in the open state energy. Slow deactivation of DhPIEZO1 may represent reforming of the domain, the inverse of fracturing. The C-terminal domain, where the mutations are located, is presumably involved in domain creation (7).

To explore whether the two mutation sites were independent, we did a mutant cycle analysis of inactivation (23). If the two sites were independent, the free energy difference for inactivation of DhPIEZO1 should be the sum of the energies of the single mutants. However, the data showed that the energy of the dual mutant is much larger than the sum of the two single mutant energies, so they must be interacting. The basic calculation is as follows, where ΔG_i is the free energy with mutation of residue i, and $\Delta\Delta G_i$ is the free energy changes with mutation of residue i.

$$\begin{aligned}
\Delta\Delta G_{2225} &= \Delta G_{2225} - \Delta G_{\mathrm{WT}}.\\
\Delta\Delta G_{2456} &= \Delta G_{2456} - \Delta G_{\mathrm{WT}}.\\
\Delta\Delta G_{\mathrm{DhPIEZO1}} &= \Delta G_{\mathrm{DhPIEZO1}} - \Delta G_{\mathrm{WT}}.
\end{aligned}$$

$$\begin{aligned}
\Delta G &= \Delta\Delta G_{\mathrm{DhPIEZO1}} - (\Delta\Delta G_{2225} + \Delta\Delta G_{2456})\\
&= \Delta G_{\mathrm{DhPIEZO1}} + \Delta G_{\mathrm{WT}} - \Delta G_{2225} - \Delta G_{2456}\\
&= -k_B T \times \left[\ln\left(\frac{5.4 \times 10^{-4}}{141.46}\right) + \ln\left(\frac{8.59}{1.19}\right)\right.\\
&\quad \left. - \ln\left(\frac{12.19}{4.40}\right) - \ln\left(\frac{2.84}{115.10}\right)\right]\\
&= 7.82\ k_B T.
\end{aligned}$$

The difference of free energy $\Delta G = 7.82\ k_B T$ shows that the sites are not independent despite on apparently opposites sides of the bilayer (7).

DISCUSSION

A striking feature of activation is that the slope sensitivity q was identical for all channel types. This means that the energy between the closed and open states was identical. Perhaps even more surprising is that this also implies that the local stresses sensed by the channel were identical: The domains were similar enough that the internal stresses were the same. The free energy of gating is well approximated by $\Delta G = T\Delta A$, where T is the local tension and ΔA is the change of in-plane area so that a change in T will produce a change in ΔG. The data on DhPIEZO1 also show that activation is effectively uncoupled from inactivation.

The kinetics of all mutants could be fit with the three-state loop model with the same two pressure-dependent rates so that the mutations did not appear to introduce any new states (Fig. 5). The fact that the kinetics of all the channels could be fit with a pressure-sensitive opening rate and a pressure-independent closing (deactivation) rate means that the energy barrier between the states is located close to the open state.

Because the slope sensitivity for activation was constant across all mutations, slowing the inactivation rate increases the channel open time for a transient stimulus. We have previously shown that PIEZO1 inactivates and does not adapt (8). To slow inactivation, one elevates the energy barrier between the open and inactivated states. But because the slope sensitivity for activation, q, was unchanged among the mutants, the difference in energy between the closed state and the barrier peak has to remain constant. Thus, the slowing of inactivation appears to represent a lowering of the energy of the open state.

The fact that the mutations caused changes in both the inactivation rate and the deactivation rate suggests that the two processes are coupled. A channel with fast inactivation, such as the WT, also has fast deactivation. When inactivation is slow (DhPIEZO1), then deactivation is slow. We previously suggested that inactivation may reflect an increased interaction between monomers to form clusters (domains) and that the regions of the channel altered by the mutations are also involved in intermonomer binding (7). DhPIEZO1 channels with no inactivation and slow deactivation may exist in loose, easily fractured clusters. The DhPIEZO1 kinetic behavior is quite similar to what we observed with the removal of the C-terminal domain (7).

Mutant cycle analysis of inactivation using WT, single-site mutants, and DhPIEZO1 (23) showed that the two sites interacted with ~8 $k_B T$ of energy (Fig. 6). What is the mechanism of coupling? It could be part of a common flexible region of the channel or possibly affect binding to the cytoskeleton and extracellular matrix, but that is doubtful given that we have previously demonstrated that disruptors of the cytoskeleton, such as CytochalasinD, disrupt whole-cell currents. However, we know that the channels are still present because patches from those cells show functional channels. The cytoskeletal disruptors probably do not affect the channel itself but more likely the mechanical pathways that affect the local distribution of stress (8). A lack of interaction with cytoskeletal proteins is supported by

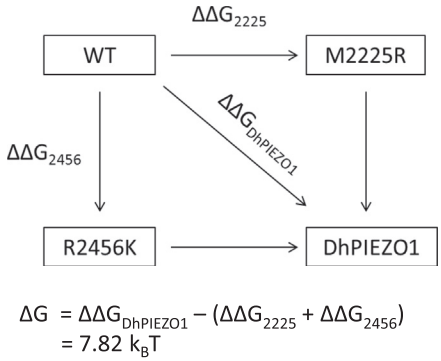

FIGURE 6 Mutant cycle analysis. The energy difference between open and inactivated states for WT, single-site mutants, and DhPIEZO1. The free energy change in DhPIEZO1 ($\Delta\Delta G_{\mathrm{DhPIEZO1}}$) is larger than the sum of free energy changes for the two single mutants by ~8 k_BT, showing that the sites are not independent but exhibit positive cooperativity.

mass-spectrum analysis of mPIEZO1 that shows no additional proteins bound to the purified channel (2).

DhPIEZO1 may be a good candidate for developing a high throughput screen for inhibitors of PIEZOs. Given that it lacks inactivation, a persistent mechanical stimulus to DhPIEZO1 will induce a persistent calcium influx, making the assay insensitive to variations in the rates of inactivation. Furthermore, inhibition by the specific reagent GsMTx4 is a positive control.

This work was supported by the National Institutes of Health, Department of Defense, and the Children's Guild of Buffalo. We are grateful to Joanne Pazik and Lynn Zeigler for expert technical assistance on the molecular biology and Julia Doerner from David Clapham's laboratory for sharing the eukaryotic vector for expression of the MscL.

REFERENCES

1. Coste, B., J. Mathur, …, A. Patapoutian. 2010. Piezo1 and Piezo2 are essential components of distinct mechanically activated cation channels. *Science.* 330:55–60.
2. Coste, B., B. Xiao, …, A. Patapoutian. 2012. Piezo proteins are pore-forming subunits of mechanically activated channels. *Nature.* 483:176–181.
3. Kim, S. E., B. Coste, …, A. Patapoutian. 2012. The role of Drosophila Piezo in mechanical nociception. *Nature.* 483:209–212.
4. Gottlieb, P. A., and F. Sachs. 2012. Piezo1: properties of a cation selective mechanical channel. *Channels (Austin).* 6:214–219.
5. Nilius, B., and E. Honoré. 2012. Sensing pressure with ion channels. *Trends Neurosci.* 35:477–486.
6. Bae, C., F. Sachs, and P. A. Gottlieb. 2011. The mechanosensitive ion channel Piezo1 is inhibited by the peptide GsMTx4. *Biochemistry.* 50:6295–6300.
7. Bae, C., R. Gnanasambandam, …, P. A. Gottlieb. 2013. Xerocytosis is caused by mutations that alter the kinetics of the mechanosensitive channel PIEZO1. *Proc. Natl. Acad. Sci. USA.* 110:E1162–E1168.
8. Gottlieb, P. A., C. Bae, and F. Sachs. 2012. Gating the mechanical channel Piezo1: a comparison between whole-cell and patch recording. *Channels (Austin).* 6:282–289.
9. Rawicz, W., B. A. Smith, …, E. Evans. 2008. Elasticity, strength, and water permeability of bilayers that contain raft microdomain-forming lipids. *Biophys. J.* 94:4725–4736.
10. Albuisson, J., S. E. Murthy, …, A. Patapoutian. 2013. Dehydrated hereditary stomatocytosis linked to gain-of-function mutations in mechanically activated PIEZO1 ion channels. *Nat. Commun.* 4:1884.
11. Andolfo, I., S. L. Alper, …, A. Iolascon. 2013. Multiple clinical forms of dehydrated hereditary stomatocytosis arise from mutations in PIEZO1. *Blood.* 121:3925–3935, S1–S12.
12. Suchyna, T. M., S. R. Besch, and F. Sachs. 2004. Dynamic regulation of mechanosensitive channels: capacitance used to monitor patch tension in real time. *Phys. Biol.* 1:1–18.
13. Suchyna, T. M., and F. Sachs. 2007. Mechanosensitive channel properties and membrane mechanics in mouse dystrophic myotubes. *J. Physiol.* 581:369–387.
14. Ostrow, K. L., A. Mammoser, …, P. A. Gottlieb. 2003. cDNA sequence and in vitro folding of GsMTx4, a specific peptide inhibitor of mechanosensitive channels. *Toxicon.* 42:263–274.
15. Suchyna, T. M., V. S. Markin, and F. Sachs. 2009. Biophysics and structure of the patch and the gigaseal. *Biophys. J.* 97:738–747.
16. Spagnoli, C., A. Beyder, …, F. Sachs. 2008. Atomic force microscopy analysis of cell volume regulation. *Phys. Rev. E Stat. Nonlin. Soft Matter Phys.* 78:031916.
17. Chiang, C. S., A. Anishkin, and S. Sukharev. 2004. Gating of the large mechanosensitive channel in situ: estimation of the spatial scale of the transition from channel population responses. *Biophys. J.* 86:2846–2861.
18. Nomura, T., C. G. Cranfield, …, B. Martinac. 2012. Differential effects of lipids and lyso-lipids on the mechanosensitivity of the mechanosensitive channels MscL and MscS. *Proc. Natl. Acad. Sci. USA.* 109:8770–8775.
19. Sukharev, S. I., W. J. Sigurdson, …, F. Sachs. 1999. Energetic and spatial parameters for gating of the bacterial large conductance mechanosensitive channel, MscL. *J. Gen. Physiol.* 113:525–540.
20. Ursell, T., A. Agrawal, and R. Phillips. 2011. Lipid bilayer mechanics in a pipette with glass-bilayer adhesion. *Biophys. J.* 101:1913–1920.
21. Opsahl, L. R., and W. W. Webb. 1994. Lipid-glass adhesion in gigasealed patch-clamped membranes. *Biophys. J.* 66:75–79.
22. Bowman, C. L., P. A. Gottlieb, …, F. Sachs. 2007. Mechanosensitive ion channels and the peptide inhibitor GsMTx-4: history, properties, mechanisms and pharmacology. *Toxicon.* 49:249–270.
23. Horovitz, A. 1996. Double-mutant cycles: a powerful tool for analyzing protein structure and function. *Fold. Des.* 1:R121–R126.

Orientation-based FRET sensor for real-time imaging of cellular forces

Fanjie Meng and Frederick Sachs*

Center for Single Molecule Biophysics, Department of Physiology and Biophysics, The State University of New York at Buffalo, 3435 Main Street, Buffalo, NY 14214, USA

*Author for correspondence (sachs@buffalo.edu)

Accepted 26 September 2011
Journal of Cell Science 125, 743–750

doi: 10.1242/jcs.093104

Summary

Mechanical stress is an unmapped source of free energy in cells. Mapping the stress fields in a heterogeneous time-dependent environment like that found in cells requires probes that are specific for different proteins and respond to biologically relevant forces with minimal disturbance to the host system. To meet these goals, we have designed a genetically encoded stress sensor with minimal volume and high sensitivity and dynamic range. The new FRET-based sensor, called cpstFRET, is designed to be modulated by the angles between the donor and acceptor rather than the distance between them. Relative to other probes, it is physically smaller and exhibits a greater dynamic range and sensitivity and expresses well. For in vivo testing, we measured stress gradients in time and space in non-erythroid spectrin in several different cell types and found that spectrin is under constitutive stress in some cells but not in others. Stresses appear to be generated by both F-actin and tubulin. The probe revealed, for the first time, that spectrin undergoes time-dependent force modulation during cell migration. cpstFRET can be employed in vitro, in vivo and in situ, and when incorporated into biologically expressed extracellular polymers such as collagen, it can report multidimensional stress fields.

Key words: Fluorescence resonance energy transfer, Optical probe, Sensor, Mechanical stress, Spectrin, Cytoskeleton, Migration

Introduction

Physiological processes generate and are modulated by mechanical stress (Kumar and Weaver, 2009; Shyu, 2009; Wallace and McNally, 2009). Of the three free energy sources available to cells, chemical, electrical and mechanical, the latter is mostly unmapped due to a lack of probes. To begin opening this field we developed the original FRET-based stress probe called stFRET. It used an α-helix (a molecular spring) to link two GFP mutants (Meng and Sachs, 2008; Meng et al., 2008). We then developed sstFRET, which matched the mechanical compliance of common hosts by substituting a spectrin repeat for the linker (Meng and Sachs, 2011a). Grashoff and colleagues created another FRET sensor, TSMod, using a domain from spider silk as the linker (Grashoff et al., 2010). Iwai and Uyeda developed a strain sensor based on proximity imaging (PRIM) with GFP dimers (Iwai and Uyeda, 2008). These force sensors share a uniform mechanism for interpreting force: tension in the host induces strain in the linker, leading to increased distance between the donor and acceptor. The dynamic range of these sensors is limited by the nearly linear relationship between FRET efficiency and strain (Meng et al., 2008). These sensors are also relatively large, >70 kDa, and potentially perturb host function. This paper describes a new probe that uses angular orientation as the dominant variable and is physically smaller than previous probes. It expresses well in cells, making it a general tool for studying cell mechanics. We demonstrated probe efficacy by mapping stress gradients in spectrin in different cell types and demonstrated, for the first time, that stress in spectrin is modulated during cell migration.

Use of the angular dependence of FRET, as expressed in the orientation factor κ^2, can provide a wide dynamic range compared with FRET sensors modulated by distance that have a much smaller dynamic range and slope sensitivity (Meng and Sachs, 2008; Meng et al., 2008). κ^2 can vary from 0–4 depending upon the angle between donor and acceptor (Dale et al., 1979), whereas the FRET efficiency with strain is offset to the resting linker length and only linear in strain. When two GFPs are oriented side by side, κ^2 can vary from ~0 to 1 (1 when they are parallel and 0 when they are orthogonal). Thus, if the angles can be modulated by force, the probe has a wide dynamic range.

To build such a probe, we closely linked a donor–acceptor pair from a screen of circularly permutated stFRET (cpstFRET) (Baird et al., 1999). The selected monomers, cpCerulean and cpVenus, were derived from Cerulean and Venus (Nagai et al., 2002; Rizzo et al., 2004). The spectroscopic properties of the fluorophores were unaffected by the mutations. We linked them tightly together to form a FRET pair and named it cpstFRET. cpstFRET exhibited high sensitivity to stresses of 5–10 pN generated by DNA springs (Tseng et al., 2009). In solution, unstressed cpstFRET had 75% efficiency (relative to theoretical maximum of 100%), supporting the assumption of a near-parallel orientation of the chromophores. The short linker of cpstFRET reduced the probe molecular weight to 54 kDa, reducing the likelihood of adverse effects on the host.

To test the in vivo efficacy of the probe, we labeled non-erythroid spectrin, a cytoskeletal protein traditionally associated with the cell cortex. The α- and β-spectrin monomers assemble into functional dimers and these further dimerize into

higher-order oligomers. The oligomers bind to F-actin through two CH domains and crosslink to the transmembrane protein ankyrin through spectrin repeat domains 14 and 15 in the β-subunit (Baines, 2009). In the erythrocyte, erythroid cortical spectrin plays a key role in establishing the elastic properties of the cell (Discher et al., 1994). Johnson and others demonstrated that physiological shear stress might unfold spectrin with picoNewton forces (Johnson et al., 2007; Randles et al., 2007). In other cell types, notably those with a three-dimensional cytoskeleton, the stresses in spectrin have never been measured. To expand the knowledge base, we incorporated cpstFRET into the linker region of spectrin between repeat domains 10 and 11 of the α-subunit. To serve as a stress-free control, we attached cpstFRET to the C-terminal, where it is expected to dangle freely. The data show that, in general, spectrin is under resting stress and that this stress is modulated during cell migration.

To test the general applicability of the probe, we measured the stress in different cell types and found constitutive stress in bovine aortic endothelial cells (BAECs) and Madin-Darby canine kidney (MDCK) cells but not in human embryonic kidney (HEK) cells. We demonstrated in BAECs that spectrin is functionally linked to the actin–tubulin cytoskeleton because pharmacologic disruption of those components reduced stress. We found in BAECs that the constitutive stress in spectrin is not constant but varies in time and space during migration.

In this article, to avoid confusion with the traditional notation of a FRET ratio, we inverted the ratio so that increased '$_{Inv}$FRET' refers to increased tension in the host.

Results

Circularly permutated Cerulean and Venus and cpstFRET constructs

We circularly permutated Cerulean and Venus by opening the loop between two adjacent β-strands (Fig. 1A; supplementary material Fig. S1A). The new variants named cpCerulean and cpVenus had the N- and C-termini located at amino acid position 174. The original N- and C-termini were connected by a poly(G) peptide linker (Fig. 1A). cpCerulean and cpVenus retained their parental spectroscopic properties (Table 1; supplementary material Fig. S2). The quantum yield for both mutants declined slightly relative to the parents but the extinction coefficient increased, with the net result that cpCerulean is brighter than Cerulean and cpVenus is slightly dimmer than Venus. The emission and excitation peaks remained at the same wavelength. The methodology for data acquisition and processing followed the procedures we published previously (Meng and Sachs, 2011a).

cpstFRET consists of closely linked cpVenus and cpCerulean and it exhibited the robust energy transfer expected for nearly parallel dipoles (Fig. 1B–D). On the basis of a comparison of cpstFRET with the other six FRET sensors constructed to date (Fig. 1B), the barrels should be nearly parallel at rest. The probe I27stFRET has the lowest FRET (FRET ratio of 0.8) due to the long I27 linker (Rief et al., 1997). Similarly, sstFRET had a low FRET (ratio 1.0; Fig. 1C,D). For comparison, stFRETVCcp and stFRETVcpC are tandem-linked Venus and cpCerulean, and cpVenus and Cerulean, respectively (Fig. 1B; supplementary

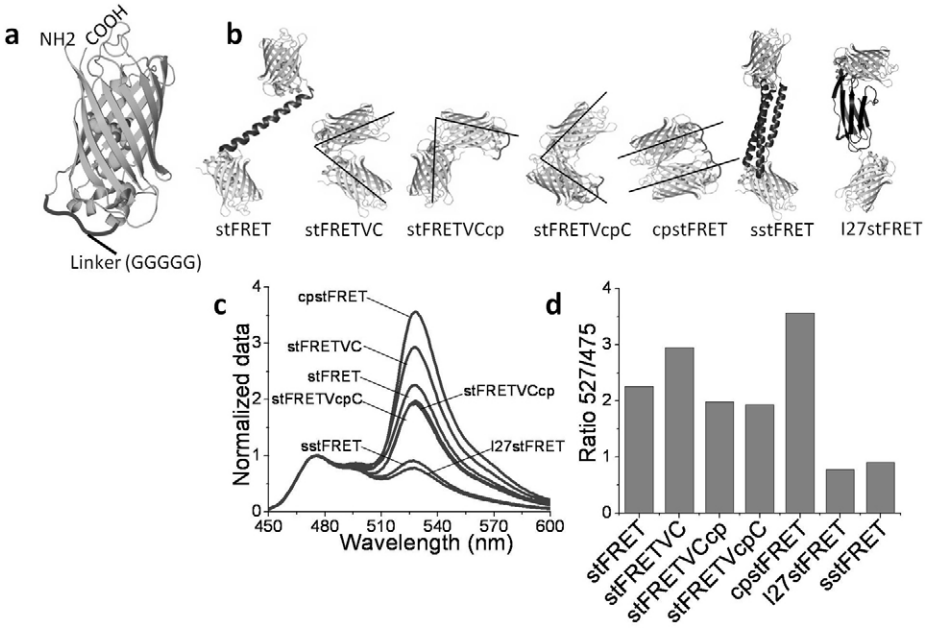

Fig. 1. FRET-based sensor constructs. (**A**) Circularly permutated donor (cpVenus) and acceptor (cpCerulean) in which the original N- and C-termini are linked by a five glycine peptide. New N- and C-termini were created at amino acid position 174. (**B**) Seven different FRET sensors that we developed. stFRET consists of Venus and Cerulean separated by a 5 nm α-helix. stFRETVC consists of Venus and Cerulean linked in tandem; substituting Cerulean by cpCerulean generates stFRETVCcp; substituting Venus by cpVenus generates stFRETVcpC, and substituting both with circularly permutated variants generates cpstFRET. sstFRET contains Venus and Cerulean separated by a spectrin repeat domain. I27stFRET contains the I27 domain from titin as the linker between Venus and Cerulean. (**C**) Spectra from purified proteins of all sensors with excitation at 433 nm and emission scan at 450 nm–600 nm. Spectra show one peak at 475 nm representing the maximum emission from Cerulean or cpCerulean, another at 528 nm representing FRET, with the maximum emission from Venus or cpVenus. All spectra were normalized to the 475 nm peak to emphasize peak shape. (**D**) Comparison of the FRET ratio (527 nm/475 nm) of seven force sensors.

Table 1. Fluorescent properties of CFP and YFP variants

Fluorescent protein*	Excitation (nm)†	Emission (nm)†	Extinction coefficient ($M^{-1}cm^{-1}$)‡	Quantum yield‡	Brightness (% of EGFP)§	p*Ka*	Photostability (wide field)
EYFP	514	527	83,400	0.61	151	6.9	60
Venus	515	528	92,200	0.57	156	6.0	15
cpVenus	515	528	158,600	0.26	122	n.d.	n.d.
ECFP	439	476	32,500	0.40	39	4.7	n.d.
Cerulean	433	475	43,000	0.62	79	4.7	36
cpCerulean	433	475	77,300	0.49	112	n.d.	n.d.

*Spectroscopic parameters determined from purified proteins (>95% homogeneity) as previously described (Meng and Sachs, 2011a; Meng and Sachs, 2011b).
†Excitation and emission wavelengths from peaks.
‡Extinction coefficients (ε) and quantum yield were determined as previously described (Meng and Sachs, 2011b).
§Brightness was calculated as the product of ε and quantum yield divided by the brightness of EGFP.
n.d., not determined.

material Fig. S1B). Despite the fact that the distance between monomers in stFRET is greater than that in stFRETVCcp or stFRETVcpC, their FRET ratio of 1.9 is less than the value of 2.2 for stFRET, which suggests that κ^2 plays a major role. Details about κ^2 applied to stFRET geometry have been published (Meng et al., 2008). The two fluorophores in stFRETVCcp and stFRETVcpC are closely fixed in distance but at unfavorable angles. We found that the closely linked pair stFRETVC (Venus and Cerulean in tandem) exhibited strong energy transfer (FRET ratio 2.9) suggesting proximity and a near parallel orientation. However, the most robust FRET occurred in cpstFRET (FRET ratio 3.8), and by analogy to the presumed parallel dimer structure of tandem GFP–cpGFP (Iwai and Uyeda, 2008), cpstFRET should also position the donor and acceptor to be nearly parallel. Force applied to the N- and C-termini of cpstFRET should disturb this nearly optimal configuration, leading to lower FRET, and thus cpstFRET can serve as a force sensor.

In vitro characterization of cpstFRET as a force sensor

To calibrate the sensitivity, we applied stress to cpstFRET in solution using a DNA spring (Wang and Zocchi, 2009; Meng and Sachs, 2011a). We covalently attached a 60mer of single-stranded DNA (ssDNA) to two locations in cpstFRET protein as previously described (Fig. 2A) to form a floppy loop. Despite the high compliance of ssDNA, simply attaching ssDNA to

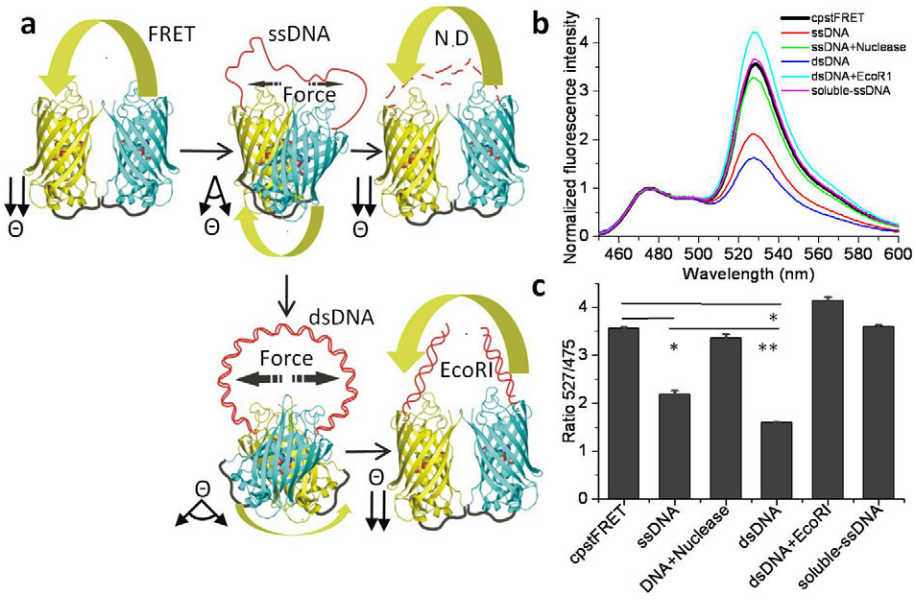

Fig. 2. Sensitivity of cpstFRET to molecular force. (**A**) ssDNA and dsDNA apply significant force to cpstFRET, leading to FRET changes. The donor is cpCerulean (cyan) and the acceptor cpVenus (yellow). Θ is the angle between donor and acceptor dipoles. At rest, a parallel orientation of donor and acceptor cpstFRET leads to robust energy transfer. Attachment of ssDNA applies <<10 pN and gently twists the monomers to an unfavorable angle causing a decrease in FRET. Complementary ssDNA anneals to the bound ssDNA and forms dsDNA that is much stiffer, further shifting the angle and decreasing FRET. Nuclease digestion (ND) breaks ssDNA and restores the control FRET with its parallel alignment. *Eco*R1 cleaves the dsDNA, releasing the force, and returns FRET to control levels. (**B**) Spectra of each of the complexes shown in A. Spectra were normalized to the cpCerulean emission 475 nm peak and scanning parameters were set as in Fig. 1. (**C**) FRET ratio of cpstFRET under DNA stretching (higher force, lower FRET ratio). Solution cpstFRET was stretched by ssDNA (ssDNA) and then digested by nuclease (DNA+Nuclease). cpstFRET was stretched by dsDNA (dsDNA) and then cleaved by *Eco*R1 (dsDNA+EcoR1). Comparison of the mixture of ssDNA and cpstFRET protein served as another control (soluble-ssDNA). Results represent mean + s.e.m. (n=3); *P<0.05, **P<0.05 (one-way ANOVA, post-hoc Tukey test).

cpstFRET led to a moderate decline in the FRET ratio from 3.6 to 2.2 (Fig. 2B,C). This suggests that the probe is sensitive to picoNewton forces. Cleavage of the bound ssDNA by nuclease restored the original (~ parallel) orientation of the donor and acceptor and fully recovered the FRET ratio. Adding complementary DNA (cDNA) to the complex created the stiffer double-stranded DNA (dsDNA) generating a force of 5–7 pN (Tseng et al., 2009). This exerted more force on the sensor and reduced the ratio to 1.5, a 60% decrease from stress-free cpstFRET. This force could be relieved with the restriction enzyme *Eco*RI that cuts through both strands of dsDNA, restoring the high FRET ratio (Fig. 2B,C). As a control for non-specific effects of DNA binding, we mixed cpstFRET protein and ssDNA in solution (soluble-ssDNA) and found no change of FRET. Thus, cpstFRET is more sensitive (60% decrease) than our previous sensor, sstFRET, which showed a 25% decrease (Meng and Sachs, 2011a). The dynamic range of FRET sensors is determined by the span from maximum to minimum FRET efficiency (E) so that cpstFRET with E=75% provides the largest dynamic range of available sensors.

We examined probe stability by exposing cpstFRET protein to denaturing concentrations of urea (supplementary material Fig. S3) and extreme pH (supplementary material Fig. S4). The monomers and cpstFRET were resistant to 8 M urea. However, pH below 6.5 decreased the fluorescence. Venus fluorescence decreased ~50% at pH 6.0 and 70% at pH 5.0 and showed a slight increase from pH 7.0 to 9.0 (supplementary material Fig. S4A). Cerulean decreased ~16% at pH 6.0 and 30% at pH 5.0 and also showed a slight increase from pH 7.0 to 9.0 (supplementary material Fig. S4B). pH also affected the FRET ratio of cpstFRET such that acidic pH 6.5 reduced FRET (emission at 527 nm) and there was almost no FRET at pH 5.0. Alkaline pH from 7.0 up to pH 10 led to a slight increase in FRET (supplementary material Fig. S4C). These results remind us that GFP-based FRET probes, in general, are sensitive to more than a single input and, ideally, the data should be obtained at different levels of acidity to check for crosstalk.

Forces in non-erythroid spectrin in living cells

We inserted cpstFRET at amino acid position 1201 in non-erythroid spectrin (Fig. 3A). The chimeric spectrin (spectrin–cpstFRET, referred to here as Spec) should not be much longer than the wild-type spectrin because the N- and C-termini of the sensor are adjacent to each other. Because both termini are located at the top of the two β-barrels, most of the sensor appears to lie perpendicular to the spectrin axis. Again, as a control, we made a spectrin tagged at the C-terminal (spectrin-C–cpstFRET, referred to here as Spec-C) where there should be no tension (Fig. 3B). We transiently expressed the chimeric spectrin constructs, free cpstFRET and a 1:1 mixture of cpCerulean and cpVenus (C+V) in BAECs (Fig. 3C,D), MDCK (Fig. 3E) and HEK cells (Fig. 3F). In cells expressing the mixture of monomers, the average distance between the two probes was large and hence exhibited negligible quenching of the donor and thus showed the highest average $_{Inv}$FRET ratio of 0.33 (donor emission intensity/acceptor emission intensity, see Materials and Methods). In Fig. 3C, $_{Inv}$FRET varied between cells due to the random amounts of cpCerulean and cpVenus DNA taken up by individual cells. The average $_{Inv}$FRET ratio from many cells approached that of a 1:1 protein mixture in solution. Cells expressing free cpstFRET showed little cell-to-cell variation and

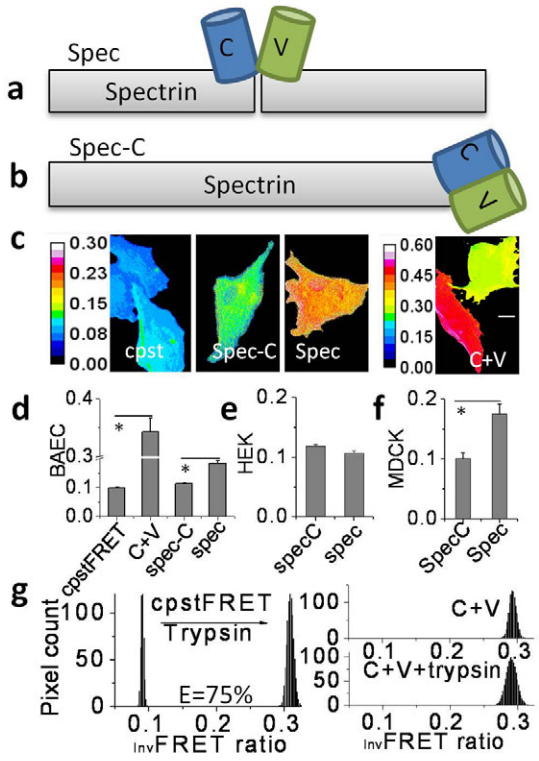

Fig. 3. Forces in non-erythroid spectrin. (**A**) Spectrin chimeric construct with cpstFRET inserted at amino acid 1201 (Spec). Donor is cpCerulean (C) and acceptor is cpVenus (V). (**B**) Spectrin tagged by cpstFRET on the C-terminal (Spec-C). (**C**) $_{Inv}$FRET images of BAECs transfected by cpstFRET (cpst), Spec, Spec-C and a 1:1 mixture of cpCerulean and cpVenus (C+V). Images were pseudo-colored using a 16-color lookup table. Scale bar: 5 µm. (**D**) $_{Inv}$FRET of BAECs expressing cpstFRET (n=20), C+V (n=15), Spec-C (n=20) and Spec (n=20). (**E**) $_{Inv}$FRET ratio of HEK cells expressing Spec-C (n=28) and Spec (n=28). (**F**) $_{Inv}$FRET of MDCK cells expressing Spec-C (n=20) and Spec (n=20). (**G**) $_{Inv}$FRET of cpstFRET and C+V in solution; pixel count distribution of $_{Inv}$FRET ratios obtained from microscopy images from donor and acceptor channels. Trypsinization eliminated FRET by cutting the linker between donor and acceptor. Based on equations developed previously (see Materials and Methods), the efficiency E reached 75%. *P<0.5 (ANOVA, post-hoc Tukey test).

a low $_{Inv}$FRET (0.10, characteristic of low stress) characteristic of robust energy transfer and a highly quenched donor signal (Fig. 3C,D). Note that in cells containing labeled spectrin, endogenous wild-type and mutant spectrin molecules might form heterotetramers, changing the observed stress. The $_{Inv}$FRET ratio seen in images is an average across all the molecules in the optical voxel. It does not represent the stress in a single molecule because there is likely to be heterogeneity in chemical composition and local stress.

In BAECs expressing labeled spectrin, $_{Inv}$FRET was 0.27, indicating the presence of significant resting stress. The host control, with cpstFRET at the C-terminal (Spec-C), sensed no force corresponding to lower $_{Inv}$FRET (0.12), similar to cells transfected with free cpstFRET (Fig. 3C,D). The algorithm to calculate $_{Inv}$FRET is insensitive to bleed-through and the inverse notation is such that a higher ratio corresponds to a larger donor signal and higher stress (Meng and Sachs, 2011a). The data shows that in BAECs spectrin bears significant constitutive stress. There was >55% increase in $_{Inv}$FRET relative to the free

sensor or to the C-terminal label, demonstrating the wide dynamic range and sensitivity of the sensor.

We measured the consistency of the microscope image analysis to the more tightly controlled fluorimeter by imaging solutions of purified proteins (Fig. 3G). The cpstFRET protein solution showed $_{Inv}$FRET of 0.10, the same as that in cells expressing free cpstFRET. After 5 minutes of trypsin cleavage of the linking region at room temperature, $_{Inv}$FRET increased to 0.30, close to that observed in cells coexpressing cpCerulean and cpVenus. Assuming force in the host can twist the transition dipoles closer to perpendicular, $_{Inv}$FRET could increase to ~0.30, a threefold change from resting to high stress, a value expected from cells. Based on our measurements of the lower and upper limits of $_{Inv}$FRET, the FRET efficiency of ~75% was the same in the image as in the spectrometer. The detailed algorithm for calculating efficiency is contained in our previous work (Meng and Sachs, 2011a). As controls for the effects of trypsin on fluorescence of the monomers, we treated a 1:1 mixture of cpCerulean and cpVenus (C+V) in solution with trypsin and found no effect, showing that the fluorophores were insensitive to trypsin (Fig. 3G, supplementary material Fig. S5B). Trypsin eliminated FRET from cpstFRET within 30 seconds by cutting the linker, and the donor signal recovered dramatically from quenching (supplementary material Fig. S5A,B).

We examined the stress in spectrin in two other cell lines, HEK and MDCK (Fig. 3E,F). HEK cells expressing Spec and Spec-C exhibited $_{Inv}$FRET of 0.11, suggesting that in these cells spectrin is stress-free. MDCK cells exhibited a higher $_{Inv}$FRET (0.18) than cells expressing Spec and a lower $_{Inv}$FRET than the control cells expressing Spec-C, indicating the presence of constitutive stress. Erythroid spectrins in red blood cells are reported to be stressed (Johnson et al., 2007). The authors used cysteine labeling and quantitative mass spectrometry of spectrin to detect unfolding induced by shear stress. They discovered that there is a significant component of unfolded spectrin at 37℃, even in resting cells, so that resting stress in erythroid spectrin probably plays an active role in determining cell shape. Further studies are clearly warranted to establish the variability of stress in spectrins and other cytoskeletal proteins in different cell types at different phases of the cell cycle, during migration, following pharmacologic perturbation, etc.

To assess the intrusive effects of probe insertion on the spectrin host we compared the histological distribution of chimeric spectrin with that of the commonly used terminal GFP tag (supplementary material Fig. S6). We found that the protein distribution and cell morphology were indistinguishable for the three constructs. We then examined the physiology by measuring the cell migration speed (supplementary material Fig. S7). Using the centroid of the cell as a marker for cell position, we found no difference between cells expressing Venus, cpstFRET, Spec or Spec-C. All cells tended to slow down with time under observation, possibly as a result of photodamage (supplementary material Fig. S7A–E). We conclude that integrating the probe into spectrin does not significantly alter cell physiology.

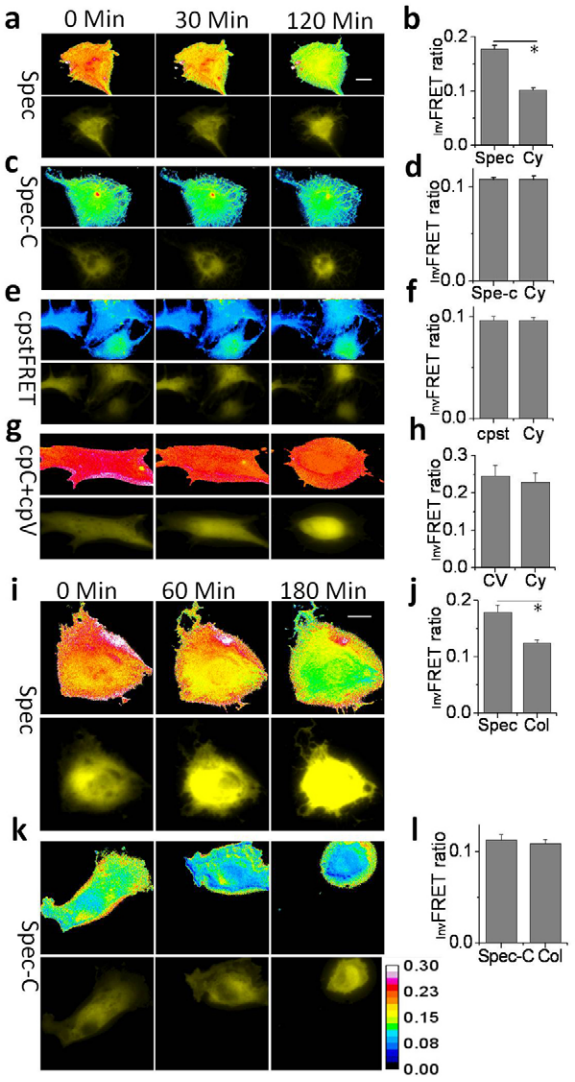

Fig. 4. Releasing molecular forces in spectrin. (**A**) Effect of treatment with cytochalasin D and latrunculin B on BAECs expressing Spec. Upper panels show $_{Inv}$FRET ratio images and lower panels show donor cpVenus in the YFP channel. (**B**) $_{Inv}$FRET of BAECs expressing Spec without treatment and after 120 minutes of treatment with 30 µM cytochalasin D and 20 µM latrunculin B (Cy). (**C**) Same as B, but for BAECs expressing Spec-C. (**D**) $_{Inv}$FRET of BAECs expressing Spec-C and the ratio after 120 minutes (P>0.1). (**E**) Same as B, but for BAECs expressing cpstFRET. (**F**) $_{Inv}$FRET of BAECs expressing cpstFRET (cpst) and the ratio after 120 minutes (P>0.1). (**G**) Same as B, but for BAECs coexpressing cpCerulean and cpVenus in a 1:1 ratio (cpC+cpV). (**H**) $_{Inv}$FRET of BAECs coexpressing cpCerulean and cpVenus (CV) and the ratio after 120 minutes (P>0.1). (**I**) Effect of treatment with 50 µM colchicine on BAECs expressing Spec. (**J**) $_{Inv}$FRET of BAECs expressing Spec and the ratio after 180 minutes of colchicine treatment (Col). (**K**) Same as I, but for BAECs expressing Spec-C. (**L**) $_{Inv}$FRET of BAECs expressing Spec-C and the ratio after 180 minutes in colchicine (P>0.1). $_{Inv}$FRET images were displayed in ImageJ using a 16-color map (bottom right). Scale bars: 10 µm. Bar graphs show means + s.e.m. (n=20); *P<0.05 (one-way ANOVA, post-hoc Tukey test).

Cytoskeleton and the forces coupling to spectrin

We examined the two major cytoskeleton components, F-actin and microtubules. We treated BAECs expressing Spec with a mixture of cytochalasin D and latrunculin B to disrupt F-actin and recorded a time series of images (Fig. 4A, supplementary material Movie 1). Within 20 minutes there was a gradual decrease in $_{Inv}$FRET, reflecting lower stress in spectrin. After 2 hours the average $_{Inv}$FRET ratio fell to the unstressed value of 0.10 (Fig. 4B, Figs 1, 3). As controls, we performed the same

studies on cells expressing Spec-C, free cpstFRET and cpCerulean plus cpVenus (Fig. 4C–H, supplementary material Movie 1). Spec-C and cpstFRET showed no change, with an $_{Inv}$FRET of ~0.10 and there were only minor changes after 2 hours. The mixture neither sensed stress nor detected changes induced by the drugs. We conclude that F-actin probably generates the constitutive force in spectrin.

Although actin fibers are known to have a direct contact to spectrin, what about the microtubules that have no such association? To answer this, we treated cells with colchicine and again recorded a time series (Fig. 4I–L; supplementary material Movie 2). During the first hour, $_{Inv}$FRET declined slowly and after 3 hours $_{Inv}$FRET decreased to 0.12, indicating reduced stress. The control, Spec-C, showed no change. Apparently, microtubules also contribute to constitutive stress in spectrin. We anticipate that other cytoskeletal proteins will show similar coupling.

The stress in cells varies during migration so we analyzed their movement over time (Fig. 5, supplementary material Movie 3). Cells expressing Spec showed large time-dependent fluctuations in $_{Inv}$FRET, indicating dynamic changes in stress. In Fig. 5A, the 'Spec' panels show two adjacent cells in the same field. At the beginning of the time series, the bottom cell showed a high $_{Inv}$FRET (~0.20, indicating high stress) and the upper one showed a lower $_{Inv}$FRET (0.12, indicating low stress). Both cells migrated to the left during the first 3 hours. $_{Inv}$FRET (stress) in the upper cell did not change whereas the bottom cell contracted and displayed a dramatic drop in $_{Inv}$FRET (supplementary material Movie 3, Fig. 5A). After 4 hours these two cells diverged. The bottom cell reversed its migration direction and started moving to the right. However, $_{Inv}$FRET and stress continued dropping to a level equal to the upper cell, which remained at low stress and maintained the same migration direction. With the upper cell serving as an internal control for the lower cell, the data showed that simple cell morphology is not a good indicator of internal stresses.

As additional controls, we monitored the migration of cells expressing Spec-C and free cpstFRET (Fig. 5A). Consistent with the absence of force, $_{Inv}$FRET remained constant throughout the 6-hour time series (Fig. 5B). We examined the data statistically for correlations between resting stress and time-dependent changes. Cells expressing Spec, with high constitutive stress, showed decreasing stress with time; cells with low constitutive stress tended to remain at constant stress over time. The average $_{Inv}$FRET of cells expressing cpstFRET and Spec-C remained low (~0.10; Fig. 5B). The data illustrate the heterogeneity of the stresses in cells and reaffirms that one cannot estimate these stresses from cell shape or traction stress on substrates.

Discussion

The design principle of cpstFRET is that the FRET depends strongly on angular orientation of the donor and acceptor. In a previous study, we deliberately changed κ^2 by varying the α-helical linker length in stFRET to produce large changes in angle with small changes in length (Meng et al., 2008). Later that year, Iwai and Uyeda reported that cpGFP and GFP joined in tandem form parallel dimers (Iwai and Uyeda, 2008). Modeling that experiment, as we reduced the length of our linker we expected a robust energy transfer but, surprisingly, neither cpCerulean–Venus nor Cerulean–cpVenus generated high FRET. However, by screening mutants we created cpstFRET that exhibited high energy transfer, implying a near-parallel orientation at rest (Fig. 1, supplementary material Fig. S1). The rigid structure of the fluorophores and our tight linker limited the variation of distance between donor and acceptor but not the angles. As we have shown, forces <10 pN can twist the structure to unfavorable orientations and cause a decrease in FRET (increase in $_{Inv}$FRET). Our improved sensitivity is demonstrated by the experiments in which the force generated with DNA springs led to larger changes with cpstFRET than with sstFRET or stFRET (Fig. 2). In an ideal case, forces in the host could rotate the angles from parallel to perpendicular so that FRET could vary from ~ 75% to 0%. cpstFRET is smaller than other probes because it has no linker domain as used in stFRET, sstFRET and TSMod (Meng et al., 2008; Grashoff et al., 2010; Meng and Sachs, 2011a). The smaller size should minimize perturbations to the host and this is supported by the data showing that cells expressing chimeric spectrin displayed normal morphology and physiological activity (supplementary material Figs S6, S7). As with most probes, the specificity of cpstFRET fluorescence is not perfect for stress alone because it displays some sensitivity to pH (supplementary material Fig. S4C). The user needs to remain aware of potential crosstalk between stimulus modalities.

We wish to emphasize that the probe does not provide an absolute measure of local stress, i.e. the absolute tension in spectrin. In a light microscope, the effective voxel size is on the order of a cubic micrometer and, within that volume, there are likely to be many labeled molecules, heterogeneity of composition (dimers of labeled, unlabeled and bilabeled hosts) and variations in local stress. The images only provide estimates

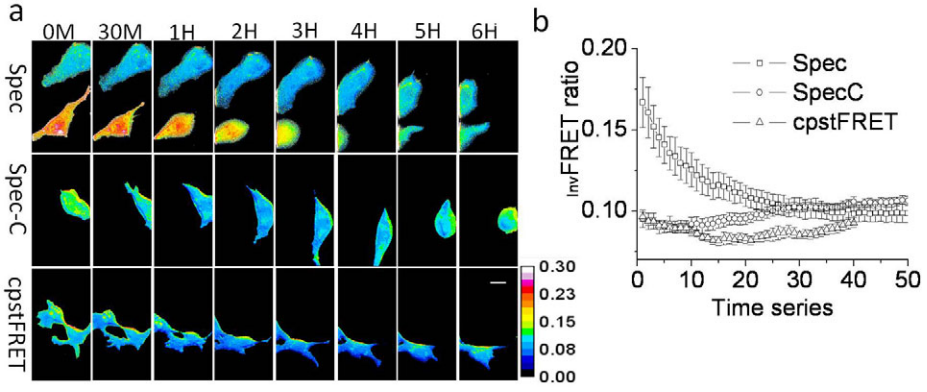

Fig. 5. Forces across spectrin network during cell migration. (**A**) $_{Inv}$FRET time series of migrating BAECs expressing Spec, Spec-C and cpstFRET. $_{Inv}$FRET images were pseudo-colored using a 16-color map (bottom right). Frames shown are spanning 0, 0.5, 1, 2, 3, 4, 5 and 6 hours. Scale bar: 20 μm. (**B**) Time series of $_{Inv}$FRET of migrating BAECs expressing Spec (n=8), Spec-C (n=8) and cpstFRET (n=6). Time series was 50 time points with 10 minute intervals. Values represent mean ± s.e.m.

of the mean stress and not the stress that one might measure in a single-molecule experiment (Oberhauser et al., 2001; Brown et al., 2007). The probes are most useful for examining gradients of stress and sources of modulation.

The constitutive stresses in spectrin appear to originate from F-actin and microtubules (Fig. 4). Even though spectrin is anchored to the cell membrane through ankyrin and transmembrane protein complexes (Baines, 2009), the bilayer itself does not appear to exert detectable force on spectrin because in HEK cells spectrin was unstressed. The variation of constitutive stress (Fig. 3E) shows that generalizing between cell types is unwise. The cytoskeleton in HEK cells and BAECs are morphologically different. Decorated by labeled α-actinin, HEK cells have fine actin fibers although BAECs have robust fibers (Meng and Sachs, 2011a). In migrating BAECs, the mean stress in spectrin decreased with time to a basal constitutive level. However, in the same culture dish there were cells exhibiting low stress, and these remained at low stress over time except for a few cells that showed increased stress after ~6 hours (supplementary material Movie 4). This heterogeneity emphasizes that we are still far from understanding the basics of cell biology because the mechanical changes were not obviously correlated with easily observable changes in cell morphology, and fixed tissue no longer has in vivo mechanical properties. Some of the variability of results in many different types of experiments might correlate with variable stresses correlated with uncontrolled culture conditions, passage number, serum or cell hereditary. We know that stresses in the cell cortex of endothelial and epithelial cells are readily modified by fluid shear stress and that these forces are probably a major factor affecting differentiation (Johnson et al., 2007; Weinbaum et al., 2010). Our data show that mechanical stress in cells should not be treated as a static variable. Mechanical signal transmission has been demonstrated to occur over long distances at the speed of nerve conduction (Na et al., 2008).

cpstFRET is a reliable and sensitive probe for studying intra- or extracellular fibrous proteins (Meng and Sachs, 2011b; Meng et al., 2011) and can be utilized with acute transfection or probably in transgenic animals. Applicable to tissue engineering, labeled matrix proteins such as collagen produced by transgenic animals could be used to create three-dimensional matrices that can report the distribution of local stress in real time.

Materials and Methods

Gene construction and protein purification

pEYFP-C1 Venus and pECFP-C1 Cerulean plasmids were generous gifts from David W. Piston, Vanderbilt University, Nashville, TN. Based on Venus and Cerulean, we constructed circularly permutated cpVenus and cpCerulean. For cpVenus, we first subcloned the gene fragments of 175Gly–239Lys from Venus into pET-52b (+) vector (Novagen, Gibbstown, NJ) by primers 5′-GGG-TACCAGGATCCATGGGCGGCGTGCAGC-3′ with *Bam*HI and 5′-GAACAGC-TCCTCGCCCTTGCTCACCCCGCCACCGCCGCCGAATTCCTTGTAC-3′ with *Eco*RI. Then we subcloned the gene fragments of 1Met–174Asp and connected them to the C-terminal of the first fragment (supplementary material Fig. S1). Five glycines were added between them to give flexibility. Primers were: 5′-GTACAAGGAATTCGGCGGCGGTGGCGGGGTGAGCAAGGGCGAGGAGC-TGTTC-3′ with *Eco*RI and 5′-CCAGAGCGAGCTCGTCCTCGATGTTG-TGGCGGATC-3′ with *Sac*I. We generated cpCerulean similarly except that a different primer was used for fragment 175Gly–239Lys, which was 5′-GGTACCAGGATCCATGGGCAGCGTGCAGC-3′ with *Bam*HI. For eukaryotic cell expression, we subcoloned cpVenus and cpCerulean into pEGFP vector with EGFP removed beforehand. Primers used were: sense 5′-CAGATCCG-CTAGCATGGGCAGCGTGCAGCTCGC-3′ with *Nhe*1 for cpCerulean, and 5′-CAGATCCGCTAGCATGGGCGGCGTGCAGCTCG-3′ with *Nhe*I for cpVenus; anti-sense 5′-CCCGCGGTACCTTAGTCCTCGATGTTGTGGCGGATC-3′ for both constructs. pET-cpstFRET was created by connecting cpVenus to the C-terminal of cpCerulean in pET-52b(+) vector; primers used were: 5′-GGC-GGCAGATCTATGGGCAGCGTGCAGCTCGCC-3′ with *Bgl*II and 5′-CCAGA-GCGAGCTCGTCCTCGATGTTGTGGCGG-3′ with *Sac*I. Fore eukaryotic cell expression of cpstFRET, we subcloned it into pEGFP vector by primers 5′-CAGATCCGCTAGCCAGGGACCCGGGGTACCAGGATCC-3′ with *Nhe*I and 5′-GATCCCGGGCCCTTTAACTACCGCGTGGCAC-3′ with *Apa*I.

To create chimeric gene constructs of α-spectrin, we subcloned the gene encoding spectrin into pEGFP-C1 vector from which the EGFP gene was removed beforehand. The primers and restriction enzyme sites introduced into PCR products for subcloning spectrin were: sense, 5′-CTAGCGCTACCGGTA-TGGACCCAAGTGGGGTCAAAGTGC-3′ with *Age*I and anti-sense, 5′-CGGG-CCCGCGGTACCGTTCACGAAAAGCGAGCGGGTGAAC-3′ with *Sac*II. cpst-FRET was inserted into spectrin at amino acid position 1200, which located in the linker domain between the 10th and 11th spectrin repeat domains by restriction sites *Sal*I and *Not*I. The restriction enzyme sites were introduced into the host proteins by a site-directed mutagenesis kit from Stratagene (La Jolla, CA) with the host protein amino acid unchanged. We also tagged spectrin with cpstFRET or EGFP on the C-terminal as negative controls. Spectrin-EGFP can show the distribution of spectrins in cells. All construct sequences were confirmed by DNA sequencing at Roswell-Park Cancer Institute (Buffalo, NY). Protein purification followed protocols previously described (Meng et al., 2008).

Protein-DNA complex synthesis and in vitro DNA stretching

As described previously (Meng and Sachs, 2011a), a 60mer DNA, [AminoC6]GAGTGTGGAGCCTAGACCGTGAATTCCTGGCAGTGGTGCGA-CCGACGTGGAGCCTCCCT[AmC7Q], and the complementary strand were purchased from Operon (Huntsville, AL). The oligo has an amino modification on both ends and an *Eco*R1 cutting site in the middle. The sequence was selected on the basis of a previously published study (Wang and Zocchi, 2009). The DNA–crosslinker construct was then incubated with 1.5 nmol of purified cptFRET protein in conjugation buffer, with a total volume of 50 µl. Both donor and acceptor in cptFRET have two free sulfhydryls at Cys48 and Cys70. The 70 position is concealed inside the β-barrel and inaccessible, and the 48 position is only partially exposed. To speed the reaction of the maleimides of the DNA–crosslinker to sulfhydryls at position 48, we incubated the mixture at 37℃ for 30 minutes. Because DNA does not interfere with FRET measurements, no further purification was necessary. To further stretch cpstFRET, 15 nmol of cDNA was added to the protein–ssDNA complex. The solution was left at room temperature overnight to complete the annealing.

Cell imaging and $_{Inv}$FRET ratio calculation

As described in our previous publication (Meng and Sachs, 2011a), imaging was performed on an inverted Zeiss Axio Observer A1 equipped with an Andor Ixon DV897 back-illuminated cooled CCD camera. The images at the donor emission and acceptor emission were recorded through a Dual View (Photometrics) splitter with double band excitation filters. A LED light engine from Lumencor (Lumencor, San Francisco, CA) was used for excitation at wavelengths of 433 nm for the donor and 515 nm for acceptor. The light engine used electronic shutters to switch excitation wavelengths so there was no mechanical movement over the time series.

We calculated the $_{Inv}$FRET ratio using the relationship:

$$InvFRET\ ratio = I_d/I_a.$$

where I_a is the acceptor emission intensity with acceptor excitation and I_d is the donor emission intensity with donor excitation. The $_{Inv}$FRET ratio denotes the inverted FRET ratio and positively correlates to mechanical force. The acceptor intensity scales with protein concentration and the donor signal scales with both protein concentration and quenching due to FRET. The FRET ratio directly correlated to stress: high stress, low FRET because of less quenching and thus a higher signal from the donor. We derived the FRET efficiency E from the FRET ratio as done for sstFRET (Meng and Sachs, 2011a) yielding E=75%.

For time series image acquisition and processing, we used NIH ImageJ with Micromanager software that controlled a Lumencor illuminator, Zeiss Axio Observer A1 and Ludl motorized stage. The 433 nm and 515 nm excitation power was set at 25% maximum with an exposure time of 100 milliseconds for each time point. We used 5 or 10 minute intervals between frames of the time series. The experimental span was 250 or 500 minutes.

Spectrometry and FRET ratio calculation

We used a fluorescence spectrometer (Aminco–Bowman series 2) to measure the fluorescence of purified proteins in solution. All purified proteins were exchanged into 10 mM Tris-HCl buffer before further processing. The measurements were performed at room temperature with 200 µl of 1 µM protein. The spectrometer settings were: 4 nm bandpass, 1 nm step size, and 450–600 nm emission scan

range with excitation at 433 nm. We have used the FRET ratio as the energy transfer index: FRET ratio = I_{527nm}/I_{475nm} where I_{527nm} is the acceptor emission signal (FRET) of cpstFRET and $I_{475\ nm}$ is the donor emission signal.

Cell culture, transfection and protein expressing

BAECs, HEK cells and MDCK cells were cultured in Dulbecco's modified Eagle's medium (Gibco, Invitrogen, Carlsbad, CA) supplemented with 10% fetal bovine serum and antibiotics. Cells were spread on coverslips and allowed to grow for 24 hours. Fugene 6 (Roche, Indianapolis, IN) was used to deliver 2.0 μg per coverslip of plasmid DNA to the cells. The cells were studied 24–36 hours following transfection.

Acknowledgements

We thank David Piston (Vanderbilt University) for providing the mVenus and mCerulean vectors, Thomas Suchyna for thoughtful discussion, Phil Gottlieb for advice on the chemistry, Yuexiu Wang for preparing DNA and cells, and Mary Teeling for cell culture.

Funding

This work was supported by grants from the National Institutes of Health (R01HL054487) and The Children's Guild of Buffalo to F.S. Deposited in PMC for release after 12 months.

Supplementary material available online at
http://jcs.biologists.org/lookup/suppl/doi:10.1242/jcs.093104/-/DC1

References

Baines, A. J. (2009). Evolution of spectrin function in cytoskeletal and membrane networks. *Biochem. Soc. Trans.* **37**, 796-803.

Baird, G. S., Zacharias, D. A. and Tsien, R. Y. (1999). Circular permutation and receptor insertion within green fluorescent proteins. *Proc. Natl. Acad. Sci. USA* **96**, 11241-11246.

Brown, A. E. X., Litvinov, R. I., Discher, D. E. and Weisel, J. W. (2007). Forced unfolding of coiled-coils in fibrinogen by single-molecule AFM. *Biophys. J.* **92**, L39-L41.

Dale, R. E., Eisinger, J. and Blumberg, W. E. (1979). The orientational freedom of molecular probes. The orientation factor in intramolecular energy transfer. *Biophys. J.* **26**, 161-193.

Discher, D. E., Mohandas, N. and Evans, E. A. (1994). Molecular maps of red cell deformation: hidden elasticity and in situ connectivity. *Science* **266**, 1032-1035.

Grashoff, C., Hoffman, B. D., Brenner, M. D., Zhou, R., Parsons, M., Yang, M. T., McLean, M. A., Sligar, S. G., Chen, C. S., Ha, T. et al. (2010). Measuring mechanical tension across vinculin reveals regulation of focal adhesion dynamics. *Nature* **466**, 263-266.

Iwai, S. and Uyeda, T. Q. (2008). Visualizing myosin-actin interaction with a genetically-encoded fluorescent strain sensor. *Proc. Natl. Acad. Sci. USA* **105**, 16882-16887.

Johnson, C. P., Tang, H. Y., Carag, C., Speicher, D. W. and Discher, D. E. (2007). Forced unfolding of proteins within cells. *Science* **317**, 663-666.

Kumar, S. and Weaver, V. M. (2009). Mechanics, malignancy, and metastasis: the force journey of a tumor cell. *Cancer Metastasis Rev.* **28**, 113-127.

Meng, F. and Sachs, F. (2008). stFRET, a novel tool to study molecular force in living cells and animals. *Proquest* **Dissertation 1757060081**, 143.

Meng, F. and Sachs, F. (2011a). Visualizing dynamic cytoplasmic forces with a compliance-matched FRET sensor. *J. Cell Sci.* **124**, 261-269.

Meng, F. and Sachs, F. (2011b). Measuring strain of structural proteins in vivo in real time. In *Cardiac Mechano-Electric Coupling and Arrhythmia: From Pipette to Patient* (ed. P. Kohl, F. Sachs and M. R. Franz). Oxford: Oxford University Press.

Meng, F., Suchyna, T. M. and Sachs, F. (2008). A fluorescence energy transfer-based mechanical stress sensor for specific proteins in situ. *FEBS J.* **275**, 3072-3087.

Meng, F., Suchyna, T., Lasalovitch, E., Gronostajski, R. M. and Sachs, F. (2011). Real time FRET based detection of mechanical stress in cytoskeletal proteins. *Cell. Mol. Bioeng.* **4**, 148-159.

Na, S., Collin, O., Chowdhury, F., Tay, B., Ouyang, M. X., Wang, Y. X. and Wang, N. (2008). Rapid signal transduction in living cells is a unique feature of mechanotransduction. *Proc. Natl. Acad. Sci. USA* **105**, 6626-6631.

Nagai, T., Ibata, K., Park, E. S., Kubota, M., Mikoshiba, K. and Miyawaki, A. (2002). A variant of yellow fluorescent protein with fast and efficient maturation for cell-biological applications. *Nat. Biotechnol.* **20**, 87-90.

Oberhauser, A. F., Hansma, P. K., Carrion-Vazquez, M. and Fernandez, J. M. (2001). Stepwise unfolding of titin under force-clamp atomic force microscopy. *Proc. Natl. Acad. Sci. USA* **98**, 468-472.

Randles, L. G., Rounsevell, R. W. and Clarke, J. (2007). Spectrin domains lose cooperativity in forced unfolding. *Biophys. J.* **92**, 571-577.

Rief, M., Gautel, M., Oesterhelt, F., Fernandez, J. M. and Gaub, H. E. (1997). Reversible unfolding of individual titin immunoglobulin domains by AFM. *Science* **276**, 1109-1112.

Rizzo, M. A., Springer, G. H., Granada, B. and Piston, D. W. (2004). An improved cyan fluorescent protein variant useful for FRET. *Nat. Biotechnol.* **22**, 445-449.

Shyu, K. G. (2009). Cellular and molecular effects of mechanical stretch on vascular cells and cardiac myocytes. *Clin. Sci. (Lond.)* **116**, 377-389.

Tseng, C.-Y., Wang, A., Zocchi, G., Rolih, B. and Levine, A. J. (2009). Elastic energy of protein-DNA chimeras. *Phys. Rev. E Stat. Nonlin. Soft Matter Phys.* **80**, 061912.

Wallace, G. Q. and McNally, E. M. (2009). Mechanisms of muscle degeneration, regeneration, and repair in the muscular dystrophies. *Annu. Rev. Physiol.* **71**, 37-57.

Wang, A. and Zocchi, G. (2009). Elastic energy driven polymerization. *Biophys. J.* **96**, 2344-2352.

Weinbaum, S., Duan, Y., Satlin, L. M., Wang, T. and Weinstein, A. M. (2010). Mechanotransduction in the renal tubule. *Am. J. Physiol. Renal Physiol.* **299**, F1220-F1236.

Actin stress in cell reprogramming

Jun Guo[a,1], Yuexiu Wang[b,1], Frederick Sachs[c], and Fanjie Meng[c,2]

[a]Department of Biochemistry, Nanjing Medical University, Nanjing, Jiangsu 210029, China; [b]Department of Physiology, Capital Medical University, Beijing 100069, China; and [c]Physiology and Biophysics Department, Center for Single Molecule Studies, University at Buffalo, The State University of New York at Buffalo, Buffalo, NY 14214

Edited* by Martin Chalfie, Columbia University, New York, NY, and approved October 31, 2014 (received for review June 23, 2014)

Cell mechanics plays a role in stem cell reprogramming and differentiation. To understand this process better, we created a genetically encoded optical probe, named actin–cpstFRET–actin (AcpA), to report forces in actin in living cells in real time. We showed that stemness was associated with increased force in actin. We reprogrammed HEK-293 cells into stem-like cells using no transcription factors but simply by softening the substrate. However, Madin-Darby canine kidney (MDCK) cell reprogramming required, in addition to a soft substrate, Harvey rat sarcoma viral oncogene homolog expression. Replating the stem-like cells on glass led to redifferentiation and reduced force in actin. The actin force probe was a FRET sensor, called cpstFRET (circularly permuted stretch sensitive FRET), flanked by g-actin subunits. The labeled actin expressed efficiently in HEK, MDCK, 3T3, and bovine aortic endothelial cells and in multiple stable cell lines created from those cells. The viability of the cell lines demonstrated that labeled actin did not significantly affect cell physiology. The labeled actin distribution was similar to that observed with GFP-tagged actin. We also examined the stress in the actin cross-linker actinin. Actinin force was not always correlated with actin force, emphasizing the need for addressing protein specificity when discussing forces. Because actin is a primary structural protein in animal cells, understanding its force distribution is central to understanding animal cell physiology and the many linked reactions such as stress-induced gene expression. This new probe permits measuring actin forces in a wide range of experiments on preparations ranging from isolated proteins to transgenic animals.

actin | force probe | stem cell | reprogramming | cell mechanics

Cells have only three sources of free energy—chemical, electrical, and mechanical potential (1)—and life is driven by the flow of energy between them. The flow of mechanical energy has not been well studied in living cells outside of muscle, yet all cells are subject to endogenous and exogenous mechanical forces. The lack of progress in measuring these forces (stress) has primarily been due to a lack of suitable probes, but that has now been remedied with the development of genetically coded FRET-based force sensors (2). The literature shows many macroscopic effects of mechanical stress on cellular processes including cell motility, embryogenesis, stem cell replication and differentiation (3, 4), bone and muscle homeostasis, gene expression, protein folding (5), and membrane potential (6). However, these studies lacked the ability to measure stress in specific structural proteins, and the analyses have tended to treat cytoskeletal stresses as uniform, which we now know is not true (2, 7). We, and other groups (8), have shown that the distribution of forces is nonuniform in both time and space and protein specificity (9).

The force sensors consist of a FRET pair (typically CFP/YFP) connected by a protein linker, a biological analog of a mechanical spring (2, 8, 10). We have used a variety of different linkers and some that match the compliance of the host protein (7, 11, 12). All of the published work on force probes has required a host protein that is linear, so the probes can be coded into the DNA of the host protein. However, several key fibrous structural proteins, such as actin and tubulin, have multimeric structures, so a new approach was required to insert the sensors. Here we present, to our knowledge, the first probe to measure force in a polymeric protein, f-actin, that fulfills many structural and motor functions in cells. For example, f-actin forms filaments that bridge chromatin domains in the nucleus to the cell membrane and the extracellular matrix, providing a path for the well-known effects of mechanical stress on gene expression (13), stem cell differentiation, and mobility (14, 15).

Our actin probe, named actin–cpstFRET (circularly permuted stretch sensitive FRET)–actin (AcpA), consists of a dipole orientation-based FRET sensor called cpstFRET flanked with β-actin monomers. The sensor consists of a pair of tandemly connected circularly permutated CFP/YFPs (cpCerulean/cpVenus; Fig. 1, *Inset*) (7). Mechanical loading twists the dipole orientation from near parallel to diagonal, decreasing FRET efficiency. The angular sensor has a much wider dynamic range and higher sensitivity than the sensors with linear linkers that use the distance dependence of FRET (7). The sensor shows ~80% energy transfer at rest and reductions as low as 20% with physiologically relevant forces (7). Perhaps because the sensor somewhat resembles the structure of actin dimers, the actin probe AcpA expresses well and labels f-actin efficiently, presumably at random locations. For imaging purposes, we found that, as previously published, polarized FRET (16–18) reduces bleed-through corrections and provides increased contrast.

The actin probe appeared nontoxic, as we were able to establish multiple stable cell lines expressing the probe. Furthermore, the anatomy of stable cell lines and the founders was similar. We expressed the actin probes in HEK, Madin-Darby canine kidney (MDCK), 3T3, and bovine aortic endothelial (BAEC) cells and compared the actin distributions to the cells expressing Actin–GFP. Actin–GFP is a widely accepted standard

Significance

Mechanical signaling plays many roles in cell physiology, including stem cell differentiation and reprogramming. To better understand the roles of mechanical forces in stem cells, we created genetically coded probes for actin that enables the direct measurement of forces in actin in living cells. This is the first force probe created for oligomeric proteins. We reprogrammed HEK-293 and Madin-Darby canine kidney cells into stem-like cells by culturing them on a soft substrate without using transcription factors. The mechanical properties of the microenvironment, and thus the local forces, promote cell reprogramming. Surprisingly, the cells showed close association of stemness to high tension in actin. Given the universal presence of actin in animal cells, the actin force probes have broad applications in biology.

Author contributions: F.S. and F.M. designed research; J.G., Y.W., and F.M. performed research; J.G., Y.W., and F.M. analyzed data; and F.S. and F.M. wrote the paper.

The authors declare no conflict of interest.

*This Direct Submission article had a prearranged editor.

[1]J.G. and Y.W. contributed equally to this work.

[2]To whom correspondence should be addressed. Email: fmeng2@buffalo.edu.

This article contains supporting information online at www.pnas.org/lookup/suppl/doi:10.1073/pnas.1411683111/-/DCSupplemental.

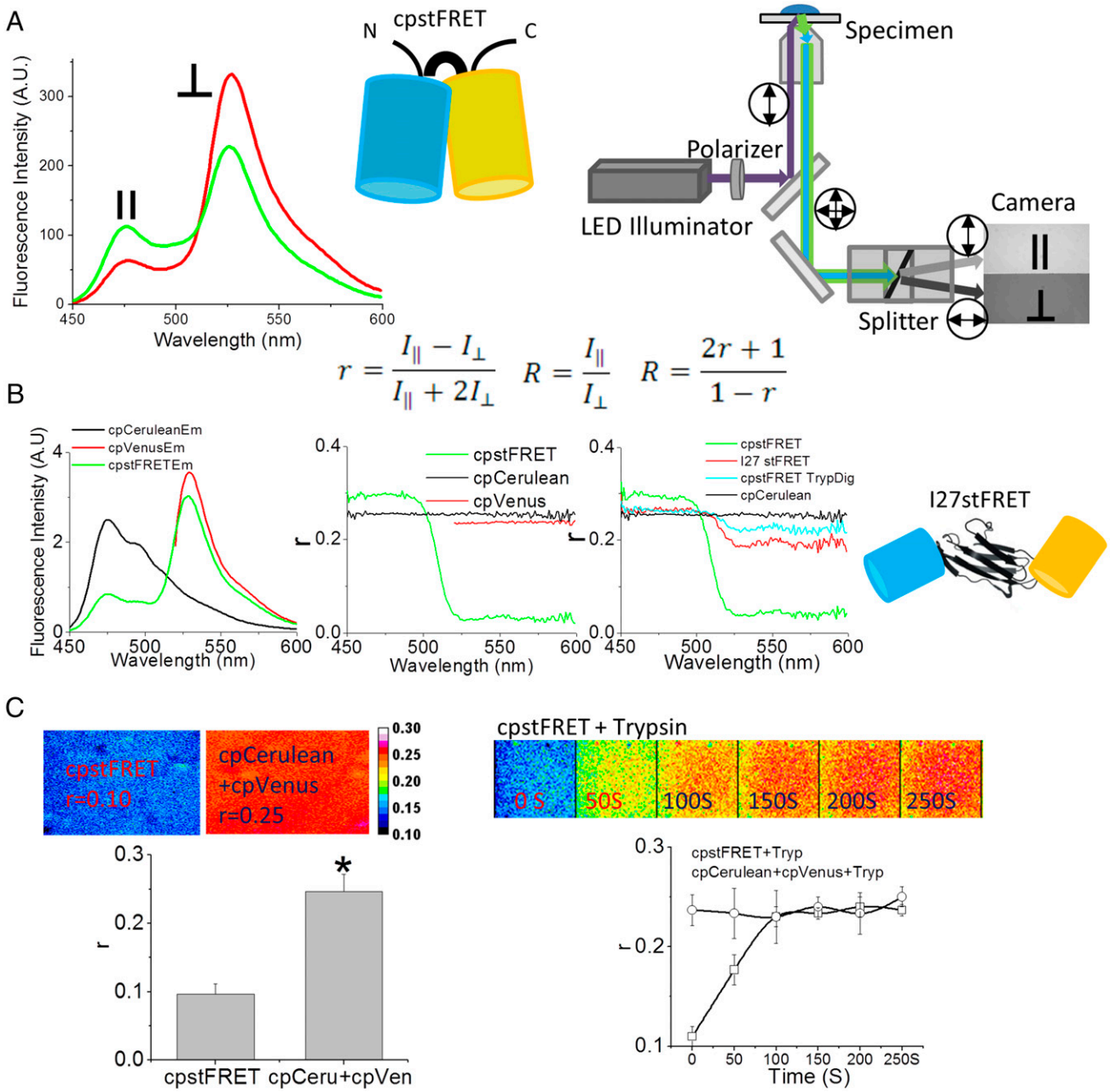

Fig. 1. Fluorescence anisotropy is a sensitive method to detect FRET changes in cpstFRET. (*A*) Schematic diagram of the cpstFRET force sensor and the microscope setup. (*Left*) cpstFRET anisotropy scanned by a spectrofluorimeter; ||, emission parallel to excitation; ⊥, emission perpendicular to excitation. (*Middle*) The cyan barrel represents cpCerulean, and the yellow barrel represents cpVenus. (*Right*) The wide-field fluorescence microscope setup for anisotropy measurements. Double-headed arrows indicate the polarization in the light path. (*Equation Inset*) *R*, anisotropy FRET ratio; *r*, anisotropy. (*B*) Anisotropy measured by spectrofluorimeter. (*Left*) The emission spectra of a purified protein solution of cpstFRET (green), cpVenus (red), and cpCerulean (black). (*Middle*) The emission spectral anisotropy of the three protein solutions. (*Right*) The anisotropy of cpCerulean (black), cpstFRET (green), cpstFRET after cleavage of the linker by trypsin for 20 s (cyan), and *I27stFRET* (red). Schematic diagram shows I27stFRET, with I27 as the linker between cpVenus and cpCerulean. (*C*) cpstFRET protein solution anisotropy measured in the microscope. (*Left*) FRET anisotropy, *r,* images of free-floating dilute probe *cpstFRET* ($r = 0.1$) and cpCerulean and cpVenus in a 1:1 ratio with no visible FRET ($r = 0.25$). (*Right*) *R* images of cpstFRET protein with linker cleaved by trypsin up to 250 s. All images were processed and pseudocolored by the 16-color map of ImageJ. The calibration bar was set from 0.08 to 0.30.

for mapping actin, and functional studies and histology showed our labeled actin distribution was similar. We observed dynamic changes in the force in actin upon applying reversible, physiologically relevant, mechanical, and pharmaceutical perturbations including reprogramming. We were easily able to reprogram our stable cell lines into stem-like cells by softening the substrate (19). Mechanical cues such as matrix stiffness, surface topology, and cell shape are known to play critical roles in stem cell self-renewal and linage differentiation (3, 4). Counter to our intuition, we found that reprogramming increased tension in f-actin relative to the parent. The increased tension was reversible upon replating the cells on coverslips, suggesting that increased force in actin may be essential to reprogramming and retaining stemness. The actin probe has broad applicability in biology, as actin is so common and it permits the cross-correlation of actin forces with biochemical and electrical activities in living cells.

Results

Anisotropy Measurements of FRET in Stress Probes. FRET efficiency depends on both the distance and the dipole angular orientation between donor and acceptor. In most FRET experiments, the donor/CFP and acceptor /YFP spectral emission overlap, and that requires cross-talk corrections. However, as proposed by Piston's group, fluorescence anisotropy provides a straightforward way to minimize those errors (16); FRET emission is more depolarized than donor or acceptor emission, as the dipole orientations are not the same and the dual lifetimes allow more Brownian motion. The measurement of polarized FRET uses polarized excitation and paired orthogonally polarized emission for the acceptor. This ratio is typically parameterized as fluorescence anisotropy or polarization (16, 17).

To verify the correlation of fluorescence anisotropy and traditional FRET efficiency, we used purified cpstFRET protein solutions and examined them in a spectrofluorimeter (Fig. 1, *Inset*) and in a microscope (Fig. 1*A*). In the spectrofluorimeter, we recorded orthogonal and parallel emission spectra using vertically polarized donor excitation (Fig. 1*A*, *Left*). In the microscope, equipped with a dual-band filter set, and a polarized dual-view splitter, we recorded the perpendicular and parallel polarized signals simultaneously (Fig. 1*A*, *Right*). The anisotropy *r* and the FRET ratio *R* were calculated using the equations shown in the *Inset* of Fig. 1.

We scanned the protein solution spectra of cpstFRET, cpVenus, and cpCerulean using the spectrofluorimeter. Fig. 1 *B*, *Left* shows their emission spectra from 450–600 nm. The *Middle* panel shows the anisotropy *r*. cpVenus and cpCerulean showed high *r* values between 0.23 and 0.24 across the spectra, corresponding to a high polarization of emission and little Brownian motion during the fluorescence lifetime. For cpstFRET, *r* was high (0.27) for cpCerulean donor emission (between 450 and 500 nm) and low (0.05) for the FRET from acceptor emission, 525–600 nm—increased anisotropy of the quenched cpCerulean and low anisotropy of FRET. To test the correlation of anisotropy to FRET, we cleaved the sensor linker with trypsin and measured *r*. We also measured changes with a probe called I27stFRET, which uses the I27 domain of titin as a physiological linker, and that had 10–15% efficiency (Fig. 1*B*, *Right*). With no link, the fluorophores float randomly and eliminate FRET. Twenty seconds of trypsin digestion cleaved cpstFRET into donors and acceptors and eliminated FRET. The anisotropy *r* increased from 0.05 to 0.23 over 525–600 nm because the fluorescence came from the directly excited donor. Between 450 and 500 nm, *r* decreased from 0.27 to 0.24 due to the elimination of the quenching of cpCerulean, which increased the lifetime. I27stFRET had $r = 0.20$ between 525 and 600 nm.

In the microscope, cpstFRET had $r = 0.10$, and a 1:1 mixture of donor and acceptor (essentially zero FRET) also gave $r = 0.25$ (Fig. 1 *C*, *Left*), matching the data from the spectrofluorimeter. As with the spectrofluorimeter, trypsin digestion of cpstFRET led to a rapid increase of *r* of the FRET channel from 0.10 to 0.25 as FRET efficiency decreased from 80 to 0. Trypsin had no effect on a mixture of unlinked donors and acceptors (Fig. 1*C*, *Right*). Thus, as previously published, anisotropy is a sensitive method to measure changes in FRET efficiency.

AcpA Probe Reports Force in Actin. To estimate the intrinsic stress sensitivity of the probe, we used DNA springs (20) to push apart the two fluorophores of the sensor. We covalently linked 60 mer of single-stranded DNA between the donor and acceptor GFPs using the natural peripheral cysteines. Single-stranded DNA is like a floppy string with a short persistence length (~1 nm) and thus exerts minimal force on the probe. Adding the complementary strand created dsDNA that is much stiffer (persistence length, ~50 nm) to push apart the donor and acceptor with forces of 7–20 pN (7, 21), and this caused a significant reduction in FRET. Although we do know roughly the absolute sensitivity of the probe, optical images have a voxel resolution of ~1 μm^3 that averages over many proteins, labeled and unlabeled, that may be under different levels of stress. The most important results from these probes are the gradients of force in time and space and the factors that modulate these forces.

To create chimeric actin (Fig. 2*A*), we flanked cpstFRET with β-actin to allow it to integrate naturally into microfilaments, and we named the construct AcpA. As a force-free control to test for possible environmental effects on FRET aside from those induced by forces, we created a version of cpA that had only had one actin monomer, and this left the other end of the probe dangling free and the probe devoid of tension. To generalize our results, we created covalent cpstFRET actinin, an actin cross-linker that forms antiparallel homodimers and cross-links parallel microfilaments (22). We inserted cpstFRET between spectrin repeat domains 3 and 4 toward the middle of actinin and created what we called actinin–M–cpstFRET. We also created the force-free version with C-terminal tagged actinin: actinin–C–cpstFRET (Fig. 2*A*). Once expressed in cells, the actin probe could incorporate into f-actin filaments, bridge adjacent filaments, or bind to other actin binding proteins, but it appeared to us that the majority incorporated into f-actin.

To measure the forces in actin and actinin in living cells, we introduced the construct's DNA into MDCK and HEK cells and used the simple anisotropy FRET ratio *R* (the ratio of the two orthogonal dual-view polarized images) to measure changes in FRET (Fig. 2*B* and Fig. 1*A* equation). *R* is monotonic with *r* and force; high *R* equals high stress and low *R* equals low stress. We compared the properties of purified cpstFRET in the microscope and chimeric actinin in cells (Fig. 2*B*). The donor (CFP) emission (CFPex, CFPem) and acceptor (YFP) emission (YFPex, YFPem) in solution were similar to that in cells, with $R = 2.7$ and $R = 2.5$, consistent with results from the spectrofluorimeter. In solution, at basal/zero force, the FRET channel (CFPex, YFPem) yielded $R \sim 1.4$. In MDCK cells, *R* of the actinin chimera increased to ~1.7, showing constitutive stress. Actinin and actin both exhibited resting stress in MDCK and HEK cells (Fig. 2 *C* and *D*). The force-sensitive actinin–M–cpstFRET and AcpA cells showed high *R*, 1.63–1.72, meaning high stress, whereas the control cells containing the force-free probes cpA, cpstFRET, or Actinin–C–cpstFRET showed low stress, $R \sim 1.4$. Both cell lines had spatial heterogeneity of the resting forces in actin and actinin. This highlights the requirement that mathematical models of mechanics not assume uniform stress. The fact that *R* was lower in cells than the probes in free solution means that there was resting tension on the probes, as we have shown for multiple chimeras in previous publications. We have found no floppy filamentous proteins in cells, and this may be particularly significant for communication purposes. Wang and coworkers (23) showed that the cytoskeleton can transmit information much faster than chemical messengers, and like the tin can telephone, this communication requires tension in the linker.

To show the proper targeting of actin probes, we expressed Actin–GFP in HEK, MDCK, 3T3, and BAEC cells. The histological distribution of Actin–GFP was similar to the actin force probes (AcpA and cpA) in all these cells (Fig. 2*E*). HEK and MDCK cells expressing Actin–GFP, AcpA, and cpA did not show clear stress fibers. Actin networks in these cells tend to be diffuse, and the cells usually do not show stress fibers. In contrast, BAEC and 3T3 cells expressing Actin–GFP and the actin probes showed clear stress fibers (Fig. 2*E*), demonstrating the correct integration of the probes into f-actin. The *R* images also showed resting force in actin in BAEC and 3T3 cells (Fig. 2*E*).

Force Modulation in Actin in Response to External Stimuli. Actin is a major part of the cell cortex and helps define cell shape. External stimuli will modify structural protein stresses, and to measure

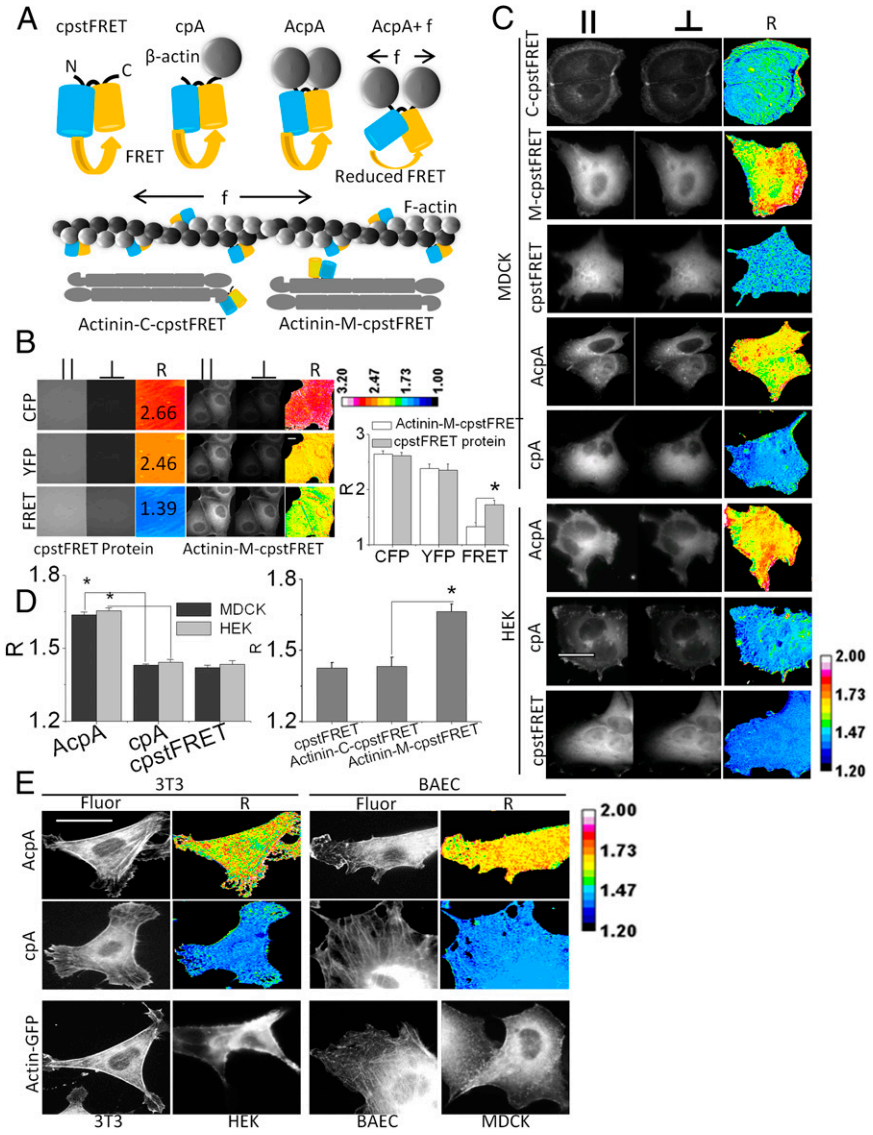

Fig. 2. Actin–cpstFRET–Actin and actinin–M–cpstFRET report force in actin and the actin cross-linker actinin. (*A*) Schematic diagram of actin–cpstFRET and actinin–cpstFRET chimeric constructs. cpA, cpstFRET–β-actin with one actin molecule attached to the C-terminal of cpstFRET; AcpA, Actin–cpstFRET–Actin with one actin molecule attached on each end of cpstFRET. *f* indicates force, which expands the structure of cpstFRET and leads to a reduction of FRET. The f-actin cartoon only presents what we expect to be the dominant configuration of probe incorporation and does not intend to exclude incorporation into cross-links. Actinin–C–cpstFRET/C–cpstFRET represents C-terminal–tagged actinin (force-free); Actinin–M–cpstFRET/M–cpstFRET represents actinin with the sensor incorporated in the middle of the host. (*B*) Comparison of the anisotropy ratio *R* of purified cpstFRET protein in solution and in the actinin host in MDCK cells. *R* is calculated from parallel and perpendicular polarizations using the equations shown in Fig. 1. The *R* images are presented in a 16-pseudocolor map with a range from 1.0 to 3.2. (Scale bar, 20 μm.) Histograms show *R* from cpstFRET protein and actinin–M–cpstFRET, $n \geq 3$. $P < 0.05$ by Student *t* test. (*C*) cpstFRET reporting constitutive tension in actin and actinin in HEK and MDCK cells. MDCK cells expressed Actinin–M–cpstFRET, Actinin–C–cpstFRET, cpstFRET, AcpA, and cpA. HEK expressed cpstFRET, AcpA, and cpA. High *R* means high stress and vice versa. (*D*) Histogram plot of *R* for HEK and MDCK cells. $P < 0.05$ by Student *t* test. (*E*) 3T3 and BAEC cell expressing force-free cpA or AcpA and HEK, MDCK, 3T3, and BAEC expressing Actin–GFP. Fluor, YFP fluorescence channel acquired from acceptor Venus *R* ratio image indicates force levels. *R* images are presented in ImageJ 16-pseudocolor map with a range of 1.2–2.0. (Scale bar, 20 μm.)

these effects, we challenged transfected MDCK and HEK cells with a variety of mechanical and pharmaceutical stimuli (Fig. 3) (more details of the stimuli are presented in *Materials and Methods*). For direct mechanical stimuli, we pressed AcpA and cpA MDCK cells with a fire-polished micropipette (Fig. 3*A* and Fig. S1). MDCK cells showed an immediate increase in local stress, and the stress increased across the cell and intensified over the next minute and a half. This may represent the viscoelastic properties of the cytoskeleton in vivo or an effect of mechanosensitive ion channels (MSCs) letting in calcium. The increases in force were nonuniform in space and propagated through the cell. The stress returned to basal levels within 2 min after lifting the pipette, and some regions fell below resting levels (green areas). MDCK cells expressing the force-free cassette cpA did not show any change of *R* (Fig. S1) so that any possible biochemical alterations on the probe were ruled out.

As another form of mechanical stimulation, we challenged the cells with hypo-osmotic stress by switching the bath from saline to distilled water (it may be surprising to realize that many nucleated cells do not lyse under these conditions). The cells swelled as expected, and the tension in actin reached the maximum within 5 min. Returning the bath to saline returned the

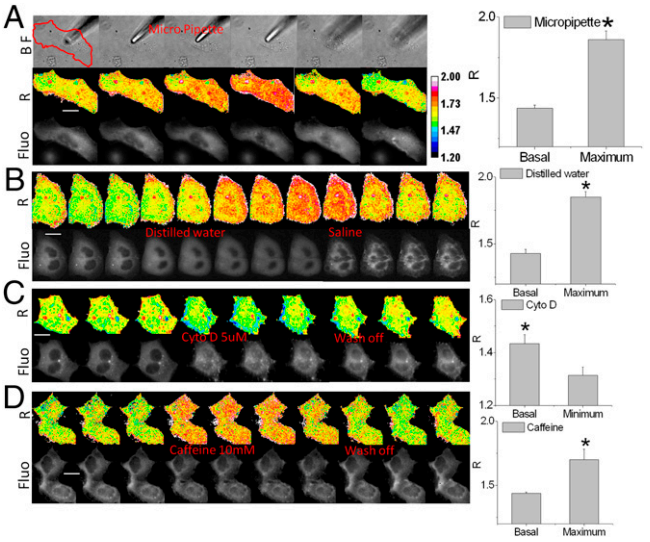

Fig. 3. cpstFRET reports changes in actin force in response to mechanical and chemical stimuli. (*A*) MDCK cells expressing AcpA were indented by a micropipette; the red line outlines the cell. Fluo, FRET image of the cell; *R*, anisotropy ratio images showing force in actin. (The experiments were repeated $n \geq 5$.) Histograms show maximum changes in the ratio *R* ($P < 0.05$ by Student *t* test). (*B*) MDCK cells challenged by anisotonic osmotic pressure. Replacing Hepes buffer with distilled water swelled the cells and increased force in actin, and returning them to saline shrank the swollen cells and lowered stress below resting levels in places (green). (*C*) HEK AcpA cells treated with 5 μM of cytochalasin D. (*D*) HEK AcpA cells treated with 10 mM of caffeine to elevate calcium Ca^{+2} and induce contraction. Each experiment was repeated $n \geq 5$. Histograms on the right show the maximum ratio *R* changes under each condition. $P < 0.05$ by Student's *t* test, calibration bar with 16-color map. (Scale bar, 20 μm.)

stress to basal levels, and the cell shrank (Fig. 3*B*). Control probes showed no change in *R* (Movie S1). These data confirm the tight coupling of cell volume to cytoskeletal stress in three dimensions throughout the cell volume rather than being confined to the cell cortex (24) and back up the predictions from atomic force microscopy studies (24).

Disrupting f-actin in HEK AcpA cells with cytochalasin D (5 μM) released the basal tension (Fig. 3*C*). Actin tension in AcpA HEK cells fell within 10 min of CytoD treatment and recovered within 10 min of washout. Again, force-free cpA controls did not show any changes (Movie S2), showing that the changes in FRET are not biochemically mediated but driven by forces. We also treated the cells with 10 mM of caffeine (Fig. 3*D*) to elevate calcium Ca^{+2}. Within 1 min, *R* increased dramatically, and washout rapidly returned the forces to basal levels. The *R* of control cells was unaffected (Movie S3). These simple stimuli have in common changes in mechanical force within the actin network, and we presume those changes will lead to activation of downstream messenger cascades.

Increased Cytoskeletal Forces in Reprogrammed Cells. Mechanical and physical factors affect stem cell renewal and differentiation (3). Varying the mechanical properties of the extracellular matrix can redirect stem cell linage commitment (19). Other mechanical cues correlated with fate commitment of mesenchymal stem cells are cell shape and the mean stress in the cytoskeleton (15). Because actin transfers physical cues between the cell exterior and interior, it likely plays a major role in stem cell linage commitment (14, 25). However, there have been no measurements available on the forces in specific structural proteins in adult cell reprogramming and dedifferentiation. We have now made those measurements for actin and actinin.

Transient expression of the probes proved inconvenient because the cells gradually lost the plasmids over time and the fluorescence faded. We therefore created stable cell lines expressing probe chimeras (Fig. 4, Fig. S2, and Table S1). These "prelabeled" HEK and MDCK cell lines underwent regular cell cycles and the proliferation, showing that the probes were not toxic (Movies S4 and S5). We also observed no morphological differences relative to the wild-type cells.

Specialized somatic cells can be reprogrammed to pluripotent stem cells (PSCs), induced pluripotent stem cells (IPS) with a combination of four transcription factors (TFs) (26, 27), and there has been much effort to reduce the number of potentially carcinogenic TFs by using chemical compounds (28, 29). Remarkably, HEK cell reprogramming requires no TFs but simply culturing on low-adhesion soft substrates such as agarose (30), emphasizing again the critical role of physical cues in reprogramming. To create labeled cells exhibiting stemness, we cultured stable HEK cell lines on soft polydimethylsiloxane (PDMS) (Fig. 5*A*). Within 3 d, the majority of cells formed tightly packed multicellular spherical embryonic bodies (EBs). These cells were alkaline phosphatase (AP) positive, as expected for EB stem cells. Some cells remained attached on PDMS and did not show AP activity (Fig. 5*A*, arrowheads). There was no AP activity in HEKs cultured on glass. These data support the critical role of mechanics in dedifferentiation. The majority of cells in EBs showed much higher actin tension than cells cultured on glass, suggesting increased force may be essential to HEK cell reprogramming. As a repeated control for biochemical effects on the chromophores, we found that cells expressing stress-free cpA had low basal *R* values and showed no changes between the cells in EBs and cells attached to glass. Also surprising was that EBs did not show a significant force increase in *actinin* (Fig. S3*A*). This visibly demonstrates that cytoskeletal stress is not uniform, even for actin and its cross-linkers, and one cannot reliably generalize about the forces in one protein from forces in another.

As another test for stemness and actin force, we examined the behavior of a different cell line, MDCK. MDCK cells cultured on PDMS also aggregated into clumps (Fig. 5*B*), but these cells did not form spheroidal EBs. In contrast to HEK lines, these

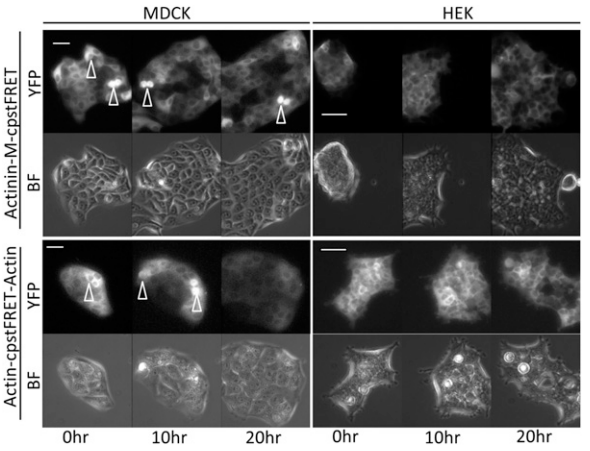

Fig. 4. Stable cell lines expressing actin-sensor and actinin-sensor chimeras show normal cell physiology. We created 13 cell lines (Table S1). The MDCK and HEK stable cell lines were cultured in media in a 5% CO_2 chamber on a heated stage. A 20-h time lapse sequence from each cell line was used to monitor cell proliferation (BF, bright field; YFP, YFP channel signal from cpVenus). Using the Zeiss Definite Focus, we monitored at least five cell colonies simultaneously. Arrowheads indicate the dividing cells. All cells went through mitosis and proliferation. (Scale bar, 50 μm.)

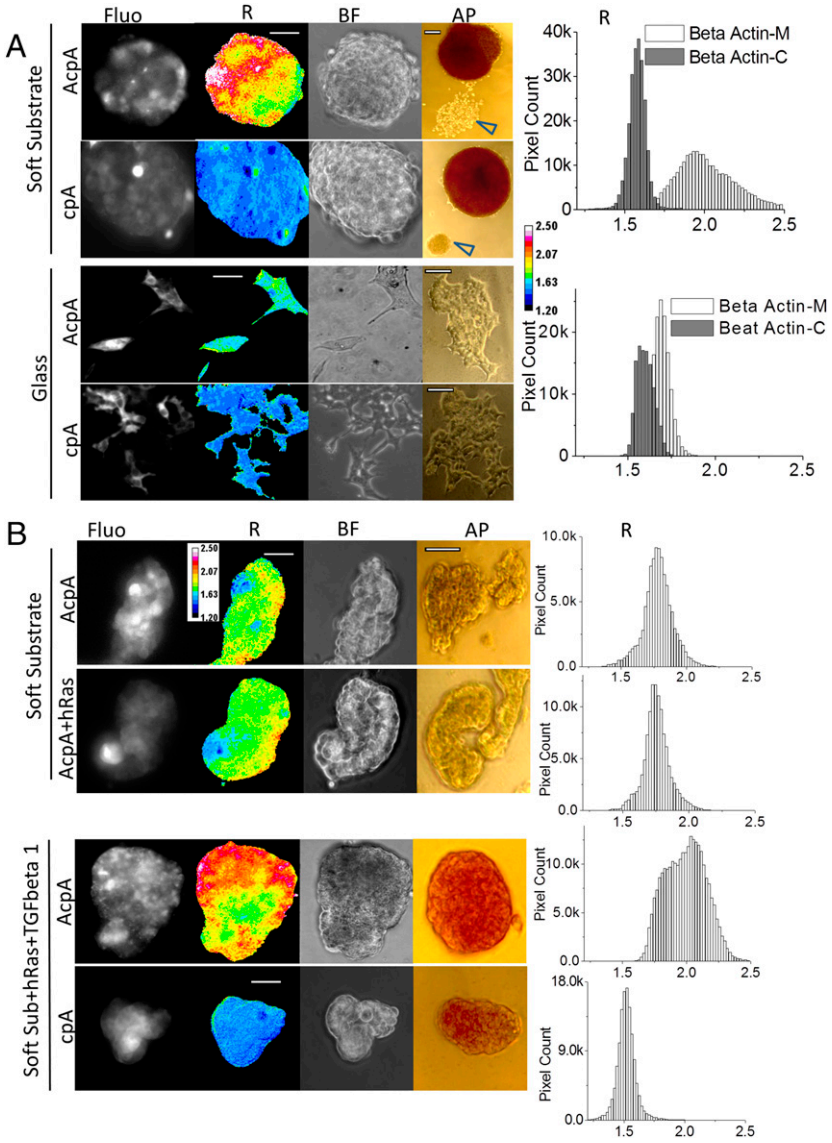

Fig. 5. Actin force elevation in stem-like cells reprogrammed from HEK and MDCK stable cell lines. (*A*) HEK actin stable cell lines cultured on soft substrate (PDMS) and glass. AcpA, HEK stable line expressing actin–cpstFRET–actin; AP, alkaline phosphatase staining of EBs and cells; BF, bright-field images of EBs and cells; cpA, HEK stable line expressing cpstFRET–actin; Fluo, FRET signal; *R*, anisotropy ratio representing tension in actin. Arrowheads indicate HEK cells attached to the substrate showing no AP activity, and these cells were not reprogrammed. Pixel count distribution plots on the right were generated from all pixels from >10 *R* images. *R* images are presented with a 16-color map of 1.20–2.50. (Scale bar, 50 μm.) (AP scale bar, 100 μm.) (*B*) MDCK actin stable cell lines cultured on soft substrate (PDMS). AcpA, MDCK stable line expressing *actin*–cpstFRET–actin cassette; cpA, MDCK stable line expressing cpstFRET–actin; +hRas, MDCK stable cell lines expressing hRas gene; +TGFbeta 1, cell cultures were supplied with 5 μg/mL TGF-β1. hRas MDCK stable lines were derived from MDCK AcpA or cpA stable cell lines. Pixel count distribution plots on the right were created using all pixel values from at least 10 *R* images. *R* images are presented with a 16-color map of Image J with a range of 1.20–2.50. (Scale bar, 50 μm.) (AP scale bar, 100 μm.)

clumps of AcpA-labeled cells did not show increased force in actin compared with cells cultured on glass (Fig. 5*B* and Fig. S3*B*). AP staining was also negative, indicating that the lumps did not contain stem cells. TGF-β1 and Harvey rat sarcoma viral oncogene homolog are reported to potentiate the epithelial–mesenchymal transition (EMT) of MDCK cells (31, 32). Human mammary epithelia cells undergoing EMT show stem cell properties and the expression of stem cell markers (33). Therefore, we introduced hRas into MDCK AcpA and cpA cell lines and created more cell lines with stable expression of hRas (Table S1). The hRas–MDCK–AcpA cells cultured on soft PDMS aggregated to clumps, but they exhibited no increase in actin stress or AP activity (Fig. 5*B*). However, when we added TGF-β1 to hRas MDCK cells, and cultured them on a soft substrate, both MDCK AcpA and cpA cells transformed to stem-like cells, and AcpA cells displayed elevated force in actin and had AP activity (Fig. 5*B*). Control cells with force-free cpA showed no FRET differences relative to the parents cultured on glass (Fig. S3*B*). On glass, the TGF-β1–treated hRas MDCK cells showed fibroblast-like morphology, probably as a result of EMT. None of the cells cultured on glass showed AP activity (Fig. S3). Both HEK and MDCK, with different mechanisms of reprogramming, showed elevated force in actin when they exhibited stemness. These cell lines may reside in intermediate states between highly specialized cells and PSCs, and a high force in actin may shift the balance toward pluripotent states, whereas low force may reverse the balance.

To further show the stemness of cells on soft substrates, we examined the up-regulation of two other key marker proteins of

stem cells, transcription factor OCT4 and Nanog[29,30] (Fig. 6*A*). HEK cells cultured on glass coverslips showed little or no OCT4 and Nanog expression, whereas the EBs generated by 3 d culturing on soft PDMS showed strong OCT4 and Nanog immunostaining. We confirmed the immunostaining data with real-time RT-PCR (Fig. 6*B*). Both OCT4 and Nanog expression were up-regulated in HEKs cultured on soft PDMS. The OCT4 expression on PDMS increased 5–7-fold over HEKs cultured on coverslips, whereas the Nanog expression increased more than 150-fold. We also checked the neuron progenitor marker neurofilament-M. HEK cells showed high expression of the protein, which is consistent with them being closely related to neurons (34), and we found robust staining of neurofilament-M in glass-attached HEK cells (Fig. 6*A*). When cultured on soft PDMS and forming EBs, the cells had much lower immunostaining of neurofilament-M, indicating the soft, low-adhesion substrate induced morphological as well as genomic transitions.

Forces Promote Cell Reprogramming and Retaining Stemness. After 4 d of culture on soft PDMS, HEK AcpA and cpA stable cell lines dedifferentiated into stem-like cells with nearly 100% efficiency (Fig. 7 *A* and *B*). The cells proliferated and attached to each other to form EBs within 24 h. Actin tension in EBs increased at the same time. Force-free cpA probe in control cells under the same culture conditions did not show any change in *R*. Hydrophobic surfaces with low adhesion, such as soft PDMS, can trigger HEK cell reprogramming, and reprogramming is associated with increased tension in actin. Transferring the EBs to glass coverslips shifted the cells toward differentiated states (Fig. 7*C*). After 2 d of culturing, cells from trypsinized HEK EBs reattached to glass and displayed typical HEK morphology. Intact EBs cultured on coverslips (with no trypsin treatment) started spreading on the surface at the periphery of the EBs. Trypsin treatment to loosen the cells had its own effects, which may apply whenever cells are trypsinized. After 2 d in culture, 30 out of 96 cells obtained from EBs without trypsin treatment retained high stress in actin, whereas only one out of 52 cells from trypsinized EBs retained high stress.

We treated the reprogrammed cells with drugs that might alter actin tension. HEK AcpA cells on PDMS were treated with 5 mM of caffeine to elevate calcium Ca^{+2} (to likely enhance forces in actin; Fig. 3*D*) or 5 μM of cytochalasin D (to reduce forces in actin; Fig. 3*C*). After 2 d, cells grown in caffeine media formed EBs and showed elevated actin tension characteristic of stemness. CytoD-treated cells did not form EBs but accumulated in clusters of cells with lower force as differentiated cells. These data imply that high forces in actin may be required for cells to retain stemness.

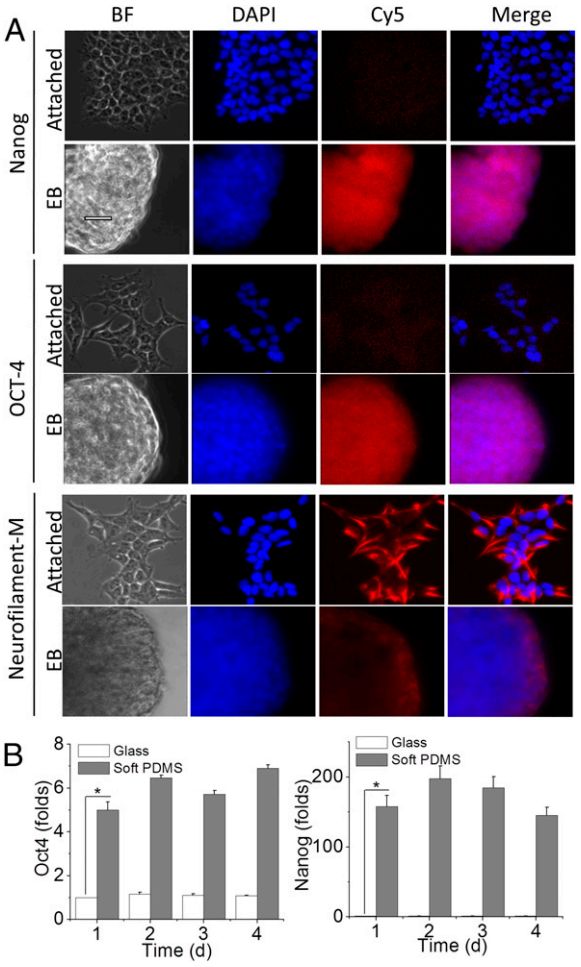

Fig. 6. Stem cell markers in HEK-derived EBs. (*A*) HEK cells cultured on a coverslip (attached) and PDMS (EB, embryonic body) were immunostained with anti-Nanog, OCT4, and Neurofilament-M antibodies. Then, the cells were treated with secondary antibodies conjugated with Cy5. The nuclei were stained with DAPI. BF, bright field. (Scale bar, 50 μm.) (*B*) Real-time RT-PCR of HEK cultured on coverslip glass and soft PDMS for 1, 2, 3, and 4 d. The histogram shows the average fold of increase of OCT4 and Nanog from three sets of independently prepared samples at each time point (*$P < 0.05$ by Student *t* test).

Discussion

Mechanical forces affect all life forms, but until recently there had been no reliable method to track mechanical forces in specific proteins in living cells. This changed with the development of genetically coded FRET-based force probes (2, 10). To calibrate the intrinsic force sensitivity of these probes, we used DNA springs to stretch the probes in solution and showed that the probes responded clearly to forces in the range of 10 pN (7, 10, 11). We have calibrated the strain sensitivity of the earlier linear linked probes and showed FRET to be linear as predicted (2). (In the strain experiment, we attached the probes at each end to a rubber sheet and biaxially stretched the sheet while performing FRET.) We have explored a variety of fluorescence imaging techniques to improve FRET imaging and reduce cross-talk, and we have found, as previously suggested (16, 17), that fluorescence anisotropy provided the most sensitive measurement (Figs. 1, 2, and 3) and is simple to implement.

Our FRET images do not explicitly report the stress in individual proteins, as the microscope resolution is the order of a cubic micrometer, much larger than a single molecule. Thus, our images are averages across the voxel and can include force gradients. The probes are most useful in reporting stress gradients in time and space. Although the DNA spring calibration showed that the probe was readily modulated with stress in the range of 10 pN, the most significant measure of sensitivity comes from the fact that we could observe changes in FRET with reversible perturbations that are physiologically relevant.

The cpstFRET angular force probe (7) used here has a wider dynamic range and smaller molecular weight than the earlier linear linker probes. The angular probe uses the dipole orientation dependence of FRET, allowing FRET efficiencies, in principle, from 0% to 100% (2, 8, 11). The dimeric structure of cpstFRET mimics the dimer subunit structure of many multimeric cytoskeleton proteins such as actin and tubulin (Figs. 1 and 2). As we have shown for a variety of stimulation modalities and stem cell reprogramming, the probes appear to be applicable to all physiological variables (35).

We reprogrammed HEK and MDCK cell lines into stem-like cells and examined how actin forces correlate with stemness (Fig. 5).

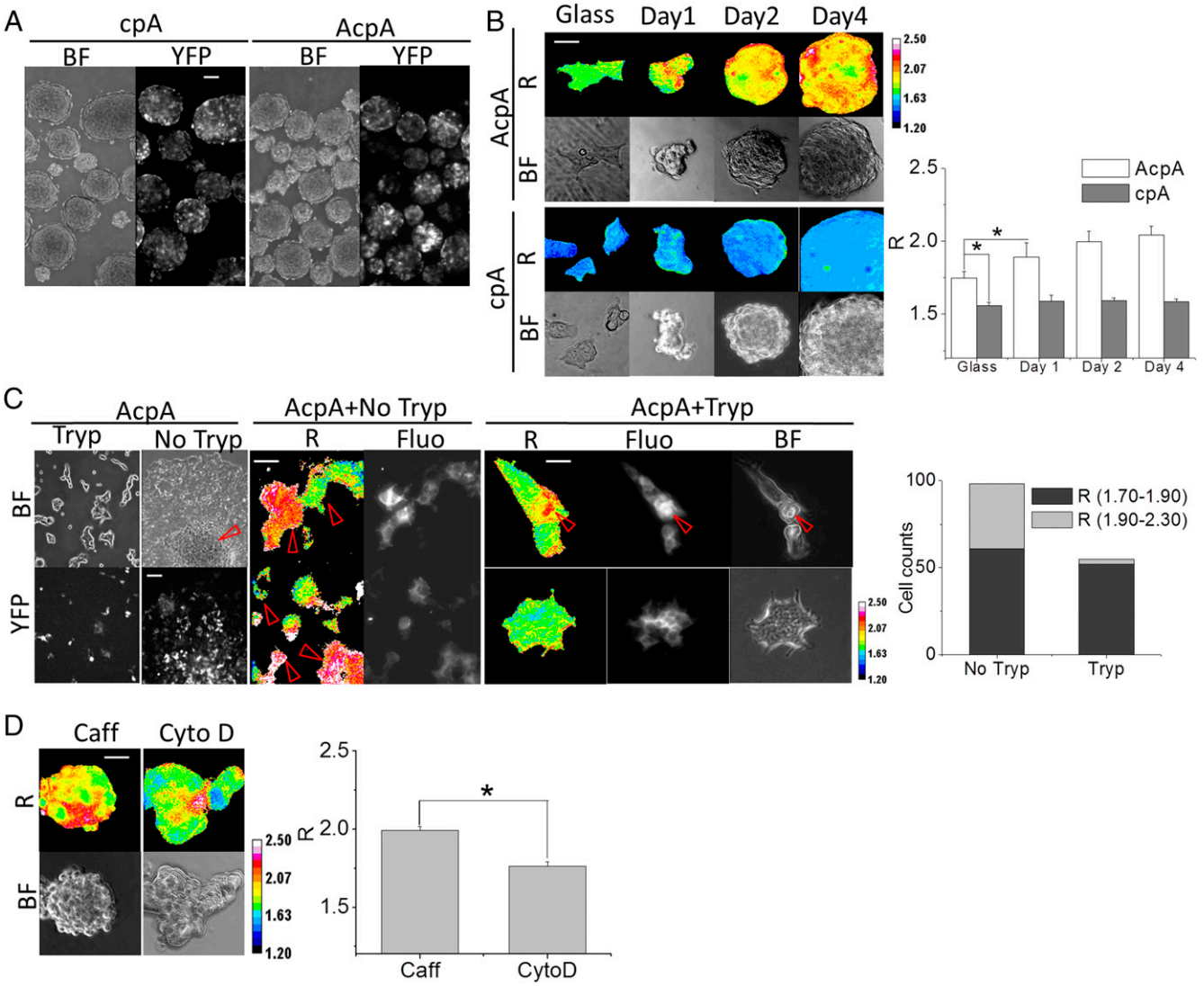

Fig. 7. Actin stress in dedifferentiated HEK cells and stemness retention. (*A*) HEK force-free cpA and AcpA cultured on PDMS for 3 d (BF, bright field; YFP, YFP channel fluorescence). (Scale bar, 100 μm.) (*B*) Time course of *R* in HEK cpA and AcpA cells. *R*, the anisotropy ratio is positively correlated to force. Histograms show the average *R* of five images at each time point. (Scale bar, 50 μm.) $P < 0.05$ by Student *t* test. (*C*) HEK AcpA cells cultured on a coverslip. AcpA HEK EBs were transferred to coverslips with (Tryp) or without trypsin (No Tryp) treatment. BF and YFP channels show the attached cells and fluorescence. AcpA+NoTryp displays *R* in attached cells derived from EBs without trypsin digestion; AcpA+Tryp displays *R* of two clusters of HEK cells differentiated from cells from trypsinized EBs. (Scale bar, 50 μm.) The histogram gives the proportion of high-force versus low-force cells from the two groups of HEK cells derived from trypsinized and nontrypsinized EBs. (*D*) HEK AcpA cells cultured on PDMS and supplied with Caff (caffeine) and CytoD (cytochalasin D). The histogram shows the average *R* of five images from each condition. (Scale bar, 50 μm.) $P < 0.05$ by Student *t* test. All *R* images have a 16-color map of 1.20–2.50.

The PDMS substrate was sufficient for HEK and MDCK cell reprogramming. Even though HEK cells are called human embryonic kidney cells, they did not exhibit AP activity, a marker of stemness, or other marker genes such as OCT4 and Nanog. PDMS is hydrophobic as well as soft, and we do not yet know which of these properties promoted cell reprogramming. Engler et al. performed the first evaluation of the role of substrate stiffness in the fate commitment of human mesenchymal stem cells, and they kept the surface chemistry of substrate the same while varying the stiffness. After several weeks in culture, the cells committed to lineages specified by substrate stiffness, hinting that the softness of the substrate in our experiments, rather than hydrophobicity, might be the key factor in dedifferentiation (19). We found that the mechanical effects on reprogramming were reversible by placing EBs on glass or placing individual cells isolated from EBs on glass (Fig. 7).

Induced PSCs (iPSCs) reprogrammed by viral introduction of OSKM TFs have potential for regenerative medicine. However, two issues have limited the utility of patient-orientated human iPSCs: (*i*) The integration of viral transgenes and the oncogenes c-MYC and KLF4 TFs into the genome poses a high risk of tumorigenesis, and (*ii*) the reprogramming efficiency is low with the four TFs (26, 36). Substantial effort has been devoted to reduce the number of required TFs using additional pharmaceuticals (28, 29, 37). Tested drugs include those that manipulate levels of histone methylation, acetylation, DNA methylation, and MAPK/ERK pathways (29), but these studies all omitted the influence of mechanical factors. We have now demonstrated dramatic changes in actin forces associated with reprogramming and dedifferentiation, so the probes promise to be useful as assay tools to screen for mechanical modifying drugs.

The probes permit researchers to study the role of mechanics under normal and pathologic conditions in cells, tissues, organs,

and animals. The probes are nontoxic based on the stability of labeled cell lines and transgenic animals (38) so that transgenic animals can be readily created, providing prelabeled tissues of all kinds (Fig. 4, Fig. S2, and Table S1). Although we have emphasized physiologically relevant perturbations, the results are transferrable directly to pathology. There is probably no disease that does not involve a change in the shape of some cells, and that can only occur through changes in force. These induced changes can have direct effects, as in athletic injuries, traumatic brain injury, or muscular dystrophy, or indirectly, as in the mechanical changes noted for metastatic cancer cells (39) or in anemia (40, 41).

Materials and Methods

cDNA Cloning and Plasmid Construction. We created the angular-dependent FRET force sensor cpstFRET by tandemly linking circularly permutated YFP/Venus and at the same position circularly permutated CFP/Cerulean at position 174 (7). The cpstFRET gene was incorporated into pEGFP-C1 vector (Clontech) with the EGFP gene preremoved from the plasmid. Then, we cloned human β-actin from an HEK cDNA library and incorporated the gene at the C-terminal of cpstFRET, creating pEG–cpstFRET–β-actin (cpA). We inserted another actin gene at the N-terminal of cpstFRET and created pEG–β-Actin–cpstFRET– β-actin (AcpA). For human alpha-actinin constructs, we purchased pEGFP-N1 alpha-actinin plasmid from Addgene (Plasmid 11908). We created pEG–actinin–sstFRET with sstFRET inserted between two spectrin repeats in actinin and pEG–Actinin–C–sstFRET with sstFRET tagged to the C-terminal of actinin (11). We replaced sstFRET with cpstFRET and created pEG–Actinin–cpstFRET and pEG–Actinin–C–cpstFRET. We also subcloned cpstFRET, cpCerulean, and cpVenus into pET-52b (+) vector (Novagen) for prokaryotic protein expression. A detailed list of primers and restriction enzyme sites is provided in Table S2.

Production and Purification of Recombinant Proteins. Recombinant proteins were expressed in the BL21(DE3) strain (Novagen) of *Escherichia coli* after induction with 1 mM isopropyl β-d-thiogalactopyranoside at 16 °C for 24 h. The proteins were purified using Ni-NTA agarose, and bacteria were lysed with BugBuster Protein Extraction Reagents (EMD Millipore) according to the manufacturer's instructions. The purified protein solutions were dialyzed to remove imidazole and extra salts.

Spectrometry and Microscopy Measurements of Fluorescence Polarization. We diluted the protein solution in 10 mM Tris·HCl to 10 μg/mL, pH 7.4, in a 50-μL quartz cuvette and recorded emission spectra with a PTI spectrofluorimeter (Photon Technology International). For *cpstFRET*, we fixed the excitation at 433 nm and recorded emission from 450 nm to 600 nm; for *cpCerulean*, we used 433-nm excitation and recorded emission from 450 nm to 600 nm, and for the *cpVenus* protein, we set excitation at 515 nm and recorded emission from 520 nm to 600 nm. We measured fluorescence polarization by exciting the protein solutions with vertically polarized light and scanned the parallel and perpendicular emission spectra. We calculated the anisotropy, *r*, or the simpler intensity ratio *R* using the equations shown in Fig. 1; both are negatively correlated to FRET efficiency but positively correlated with force.

We used a wide-field fluorescence microscope to image fluorescence polarization. Cells or protein solutions were imaged on an inverted Zeiss Axio Observer A1 equipped with an Andor Ixon DV897 back-illuminated cooled CCD camera. The light source was a LED light engine, model 6-LCR-XA (Lumencor), which uses electronic shutters to switch excitation wavelengths for CFP or YFP. We positioned a polarizing filter (Chroma) in front of the light engine to generate polarized excitation. For epifluorescence imaging, we used an ET-Dual CFP/YFP filter cube set (430/24x, 500/20x, 470/24m, 535/30m) (Chroma Technology). The excitation filter passes 433 nm and 515 nm of light, and the emission filter passes 475 nm of CFP emission (polarized) and 527 nm of acceptor emission/FRET (depolarized). For CFP channel recording, we used 433 nm of Ex and recorded 475 nm of Em; for YFP channel recording, we used 515 nm of Ex and recorded 525 nm of Em; for FRET channel recording, we used 433 nm of Ex and recorded 475 nm + 525 nm of Em. The total recorded FRET signals are the sum of polarized CFP and depolarized FRET signals. The ratio of the two changes with FRET efficiency. We used the Duel View (Photometrics) image splitter to separate the vertical and horizontal polarized images. The anisotropy value *r* or ratio *R* was calculated using the equations shown in Fig. 1. Because of the different N.A. of 63× objectives used for individual cells and the 20× objectives for imaging EBs and clusters of cells, the ratio *R* from 20× objectives is 0.2 higher than that obtained with 63× objectives.

Cell Culture and Gene Expression. MDCK and HEK cells were cultured in DMEM (Invitrogen) supplemented with 10% (vol/vol) FBS and antibiotics. Cells were spread on 35-mm coverslips and allowed to grow for 24 h. Fugene 6 (Promega) was used to deliver 0.5–1 μg of plasmid DNA per coverslip to the cells. Gene expression was examined on the microscope 24–36 h following transfection. Cells on coverslips were mounted on a stage equipped with a Bioptechs temperature controller to keep the cells at 37 °C. Because of strong autofluorescence (433 nm of Ex, 527 nm of Em) from serum containing media, the culture media was substituted with 37 °C prewarmed saline Hepes buffer, pH 7.4, for all FRET measurements.

Mechanical and Biochemical Acute Stimuli. A micromanipulator (SENSAPEX) was used to indent cells. The micropipette tips were fire-polished and sealed. To place the pipette on top of the MDCK AcpA and cpA cells, we focused the microscope to the top of the cells and lowered the micropipette until a shadow of the tip appeared. The micropipette was then lowered into direct contact with the cell, producing a visible deformation. FRET and bright-field (BF) images were taken at 30-s intervals. We treated HEK cells with 10 mM of caffeine in Hepes buffer and made images every 60 s. The caffeine was washed out with buffer after 5 min. We treated HEK cells with 5 μM of cytochalasin D and acquired images at 10-min intervals. We stimulated cells with cycles of hypotonic and isotonic solutions by simply exchanging the buffer with distilled water and returning to saline and taking images every 60 s. All FRET signals were acquired using 433-nm excitation and the dual-band emission (475 nm + 527 nm) filter cube and the Dual View outfitted with a polarizing splitter. The resulting vertical and horizontal polarized images were used to calculate the anisotropy ratio *R* and anisotropy *r*.

Stable Cell Line Development. We developed multiple cell lines with various genes (Table S1). The founder cell lines, genes, and antibiotics used for screening are listed in Table S1. The founder cell lines were spread on 35-mm polystyrene tissue culture Petri dishes and then transfected after 24 h in culture. For each cell line, four nontransfected dishes were used to determine the proper concentration of antibiotics. We set a concentration and then added 1×, 2×, 3×, and 4× of that to the nontransfected dishes. The concentration causing 70–80% cell death within 2–3 d was used for screening. Two days after transfection, antibiotics were added to the dishes, and they were placed in an incubator until the cells reached confluence. Cells were then trypsinized and transferred to 50-mL cell culture flasks (BD, Falcon). The same concentration of antibiotics was applied, and cells were allowed to grow to confluence. The cells were subcultured using a 1:10 dilution for three rounds. We checked cell fluorescence, and if 80–90% of the cells were fluorescent, we used these lines with multiple cloning. If the fluorescent cells were less than 30% of the population, we did further screening using 96-well flat-bottom Corning Costar cell culture plates (Invitrogen). We counted and diluted the cells to 150/10 mL of media and then added 100 μL per well. The majority of the wells had 1–2 cells. The culture plates were incubated for 15 d and individual colonies developed from single-cell cultures. We screened the colonies under the microscope and picked ones with relatively bright fluorescence and grew up the cells. The resulting cell lines are single cloning stable lines with nearly 100% identical genotype and phenotype.

Stem Cell Reprogramming and Culture. We reprogrammed HEK and MDCK to have stemness properties. For HEK, trypsinized cells were spread on PDMS-coated coverslips or 35-mm Petri dishes. PDMS was prepared from the SYLGARD 184 Silicone Elastomer Kit (DOW Corning) with an elastomer base to curing agent ratio of 25:1. The cells growing on PDMS formed EBs in 1–4 d. Strong autofluorescence from the serum containing media required us to transfer cells to saline for imaging. The EBs were collected and centrifuged at 200 *g* for 5 min. After removing the supernatant, the pellets were washed once with Hepes buffered saline. The pellets were resuspended and transferred to 35-mm tissue culture Petri dishes with a glass bottom for imaging. For MDCK cells, we first introduced the hRas gene to transform them using the pBabe–puro Ras V12 (Plasmid 1768, Addgene). After a cell line with stable expression of hRas was established, cells were trypsinized and plated on PDMS-coated 35-mm Petri dishes supplied with TGF-β1 (5 ng/mL). Cells were cultured for 7 d, and ∼10% of the cells turned into EBs.

Quantitative Real-Time PCR Analysis. Total RNA was extracted from HEK293 cells using TRIzol reagent (Invitrogen). The cDNA was synthesized by reverse transcription of the RNA using a High Capacity cDNA Archive kit (Invitrogen, USA) with random hexamers. The expression levels of the target genes were quantified by quantitative RT-PCR with the SYBR Green PCR Master Mix and

the 7300 Real-Time PCR system (Applied Biosystems). GAPDH was used as an internal expression control, and all data were analyzed using the GAPDH gene expression as a reference.

Statistical Analysis. All data are expressed as mean ± SD or ± SEM as noted. Each experiment was repeated at least three times, and >5 cells were imaged and analyzed under each condition. We evaluated statistical significance with the Student's *t* test for comparison between two mean values. The *R* of EBs is presented as pixel count distribution from >10 EBs. $P < 0.05$ was considered significant.

ACKNOWLEDGMENTS. We thank Dr. Thomas Suchyna for thoughtful discussion, Dr. Phil Gottlieb for advice on the chemistry, Mary Teeling for cell culture, and Joanne Pazik for plasmid DNA constructs. This work was supported by grants from the National Institutes of Health, US Department of Defense, and The Children's Guild of Buffalo.

1. Bustamante C, Chemla YR, Forde NR, Izhaky D (2004) Mechanical processes in biochemistry. *Annu Rev Biochem* 73:705–748.
2. Meng F, Suchyna TM, Sachs F (2008) A fluorescence energy transfer-based mechanical stress sensor for specific proteins in situ. *FEBS J* 275(12):3072–3087.
3. Li D, et al. (2011) Role of mechanical factors in fate decisions of stem cells. *Regen Med* 6(2):229–240.
4. Discher DE, Janmey P, Wang YL (2005) Tissue cells feel and respond to the stiffness of their substrate. *Science* 310(5751):1139–1143.
5. Johnson CP, Tang HY, Carag C, Speicher DW, Discher DE (2007) Forced unfolding of proteins within cells. *Science* 317(5838):663–666.
6. Kung C (2005) A possible unifying principle for mechanosensation. *Nature* 436(7051): 647–654.
7. Meng F, Sachs F (2012) Orientation-based FRET sensor for real-time imaging of cellular forces. *J Cell Sci* 125(Pt 3):743–750.
8. Grashoff C, et al. (2010) Measuring mechanical tension across vinculin reveals regulation of focal adhesion dynamics. *Nature* 466(7303):263–266.
9. Guo J, Sachs F, Meng F (2014) Fluorescence-based force/tension sensors: A novel tool to visualize mechanical forces in structural proteins in live cells. *Antioxid Redox Signal* 20(6):986–999.
10. Meng F, Suchyna TM, Lazakovitch E, Gronostajski RM, Sachs F (2011) Real time FRET based detection of mechanical stress in cytoskeletal and extracellular matrix proteins. *Cell Mol Bioeng* 4(2):148–159.
11. Meng F, Sachs F (2011) Visualizing dynamic cytoplasmic forces with a compliance-matched FRET sensor. *J Cell Sci* 124(Pt 2):261–269.
12. Borghi N, et al. (2012) E-cadherin is under constitutive actomyosin-generated tension that is increased at cell-cell contacts upon externally applied stretch. *Proc Natl Acad Sci USA* 109(31):12568–12573.
13. Heisenberg CP, Bellaïche Y (2013) Forces in tissue morphogenesis and patterning. *Cell* 153(5):948–962.
14. Connelly JT, et al. (2010) Actin and serum response factor transduce physical cues from the microenvironment to regulate epidermal stem cell fate decisions. *Nat Cell Biol* 12(7):711–718.
15. McBeath R, Pirone DM, Nelson CM, Bhadriraju K, Chen CS (2004) Cell shape, cytoskeletal tension, and RhoA regulate stem cell lineage commitment. *Dev Cell* 6(4): 483–495.
16. Rizzo MA, Piston DW (2005) High-contrast imaging of fluorescent protein FRET by fluorescence polarization microscopy. *Biophys J* 88(2):L14–L16.
17. Rizzo V (2007) Lights, camera, actin! The cytoskeleton takes center stage in mechanotransduction. Focus on "Mapping the dynamics of shear stress-induced structural changes in endothelial cells." *Am J Physiol Cell Physiol* 293(6):C1771–C1772.
18. Choy JS, et al. (2010) DNA methylation increases nucleosome compaction and rigidity. *J Am Chem Soc* 132(6):1782–1783.
19. Engler AJ, Sen S, Sweeney HL, Discher DE (2006) Matrix elasticity directs stem cell lineage specification. *Cell* 126(4):677–689.
20. Tseng CY, Wang A, Zocchi G, Rolih B, Levine AJ (2009) Elastic energy of protein-DNA chimeras. *Phys Rev E Stat Nonlin Soft Matter Phys* 80(6 Pt 1):061912.
21. Wang Y, Wang A, Qu H, Zocchi G (2009) Protein-DNA chimeras: Synthesis of two-arm chimeras and non-mechanical effects of the DNA spring. *J Phys Condens Matter* 21(33):335103.
22. Sjöblom B, Salmazo A, Djinović-Carugo K (2008) Alpha-actinin structure and regulation. *Cell Mol Life Sci* 65(17):2688–2701.
23. Na S, et al. (2008) Rapid signal transduction in living cells is a unique feature of mechanotransduction. *Proc Natl Acad Sci USA* 105(18):6626–6631.
24. Spagnoli C, Beyder A, Besch S, Sachs F (2008) Atomic force microscopy analysis of cell volume regulation. *Phys Rev E Stat Nonlin Soft Matter Phys* 78(3 Pt 1):031916.
25. Treiser MD, et al. (2010) Cytoskeleton-based forecasting of stem cell lineage fates. *Proc Natl Acad Sci USA* 107(2):610–615.
26. Takahashi K, Yamanaka S (2006) Induction of pluripotent stem cells from mouse embryonic and adult fibroblast cultures by defined factors. *Cell* 126(4):663–676.
27. Yu J, et al. (2007) Induced pluripotent stem cell lines derived from human somatic cells. *Science* 318(5858):1917–1920.
28. Huangfu D, et al. (2008) Induction of pluripotent stem cells from primary human fibroblasts with only Oct4 and Sox2. *Nat Biotechnol* 26(11):1269–1275.
29. Shi Y, et al. (2008) A combined chemical and genetic approach for the generation of induced pluripotent stem cells. *Cell Stem Cell* 2(6):525–528.
30. Su G, et al. (2013) The effect of forced growth of cells into 3D spheres using low attachment surfaces on the acquisition of stemness properties. *Biomaterials* 34(13): 3215–3222.
31. Nicolás FJ, Lehmann K, Warne PH, Hill CS, Downward J (2003) Epithelial to mesenchymal transition in Madin-Darby canine kidney cells is accompanied by down-regulation of Smad3 expression, leading to resistance to transforming growth factor-beta-induced growth arrest. *J Biol Chem* 278(5):3251–3256.
32. Oft M, et al. (1996) TGF-beta1 and Ha-Ras collaborate in modulating the phenotypic plasticity and invasiveness of epithelial tumor cells. *Genes Dev* 10(19):2462–2477.
33. Mani SA, et al. (2008) The epithelial-mesenchymal transition generates cells with properties of stem cells. *Cell* 133(4):704–715.
34. Shaw G, Morse S, Ararat M, Graham FL (2002) Preferential transformation of human neuronal cells by human adenoviruses and the origin of HEK 293 cells. *FASEB J* 16(8): 869–871.
35. Bowman CL, Gottlieb PA, Suchyna TM, Murphy YK, Sachs F (2007) Mechanosensitive ion channels and the peptide inhibitor GsMTx-4: History, properties, mechanisms and pharmacology. *Toxicon* 49(2):249–270.
36. Park IH, et al. (2008) Reprogramming of human somatic cells to pluripotency with defined factors. *Nature* 451(7175):141–146.
37. Zhu S, et al. (2010) Reprogramming of human primary somatic cells by OCT4 and chemical compounds. *Cell Stem Cell* 7(6):651–655.
38. Meng F, Suchyna TM, Lazakovitch E, Gronostajski RM, Sachs F (2011) Real time FRET based detection of mechanical stress in cytoskeletal and extracellular matrix proteins. *Cell Mol Bioeng* 4(2):148–159.
39. Bastatas L, et al. (2012) AFM nano-mechanics and calcium dynamics of prostate cancer cells with distinct metastatic potential. *Biochim Biophys Acta* 1820(7):1111–1120.
40. Bae C, Gnanasambandam R, Nicolai C, Sachs F, Gottlieb P (2013) Xerocytosis is caused by mutations that alter the kinetics of the mechanosensitive channel PIEZO1. *Proc Natl Acad Sci USA* 110(12):E1162–E1168.
41. Stewart AK, et al. (2011) Loss-of-function and gain-of-function phenotypes of stomatocytosis mutant RhAG F65S. *Am J Physiol Cell Physiol* 301(6):C1325–C1343.